THE UNIVERSITY OF CHICAGO

OPTIMIZATION-BASED IMAGE RECONSTRUCTION FOR X-RAY CT WITH MULTISPECTRAL DATA

A DISSERTATION SUBMITTED TO
THE FACULTY OF THE DIVISION OF THE BIOLOGICAL SCIENCES
AND THE PRITZKER SCHOOL OF MEDICINE
IN CANDIDACY FOR THE DEGREE OF
DOCTOR OF PHILOSOPHY

COMMITTEE ON MEDICAL PHYSICS

BY
BUXIN CHEN

CHICAGO, ILLINOIS
JUNE 2017

To my wife, Yunyi Wang, and my parents, Liqun Chen and Xiaomin Shentu,

for their selfless love and support

No idea is worth anything at all unless you can get it out of your head and put it *more or less intact* into other heads ... if possible, in a form that will stimulate additional thoughts in the other head.

– Charles Metz

TABLE OF CONTENTS

LIST OF FIGURES

LIST OF TABLES

ACKNOWLEDGMENTS

First and foremost, I would like to thank my advisor, Dr. Xiaochuan Pan, for the mentorship and encouragement throughout the academic journey of mine as a Ph.D. student and, especially, through this dissertation work. He is as kind and caring as he is knowledgeable and scholarly. His passion and tenacity are invigorating and exemplifying, and eventually become contagious. He is also as wholeheartedly dedicated to student's personal success as to the tireless pursuit of scientific rigor, which can be evidenced by countless hours of discussion we have carried and piles of manuscript draft versions we have exchanged with each other. I am indebted to him for the growth I have gained as a researcher.

I also wish to express my gratitude to the rest of my dissertation committee members, Dr. Chin-Tu Chen, Dr. Charles Pelizzari, and Dr. Emil Sidky. Dr. Chin-Tu Chen took me in when I first arrived in Chicago in the summer of 2011 with tremendous trust and support and led me into the research of medical imaging. Although I did not end up working on the dissertation in his lab, Dr. Chen is always available for advice and guidance. Dr. Emil Sidky's vast knowledge and deep understanding on image reconstruction and optimization problems have been a great resource, from which I have sought constant help. Dr. Charles Pelizzari has helped me learn the CT system instrumentation and integration, and provided real data for validating the proposed method in the work. It is without doubt that this dissertation work could not have been accomplished without the generous support from my committee members. My gratitude is also extended to other faculty members in the GPMP program who have been instrumental in my research projects, including Dr. Ingrid Reiser whose resourcefulness and kindness have truly inspired me.

Throughout my Ph.D. career, I have been fortunate to be surrounded by talented and compassionate individuals and lab members. The list of names includes, but is not limited to, Sean Rose, Andrew Davis, Dr. Adrian Sanchez, Dr. David Rigie, Dr. Zheng Zhang, Dr. Xiao Han, Dr. Erik Pearson, Dr. Junguo Bian, and Dr. Dan Xia. I am grateful for the

numerous discussions I have had with each one of them and the friendships I have gained. My appreciation also go to the GPMP program for its collective support to the students and the intellectual environment it creates, led by Dr. Maryellen Giger and Dr. Samuel Armato, as former and current department chairs, and Ruth Magana and Julie Hlavaty, as program administrators.

Last but not least, special thanks are reserved for my family. My wife, Yunyi, has been there for me since the beginning of this journey. Her love, support, patience, and confidence in me are what make it all possible. My parents, Liqun and Xiaomin, have encouraged me to embark on this long journey of scientific pursuit and inspired me with examples of their own achievements. Their continued support has carried me through ups and downs, while a simple phone call with them could often diminish any frustration and obstacle in the work.

ABSTRACT

Computed tomography (CT) has grown into a major workhorse in radiology since its emergence in the 1970's, for its noninvasiveness, three-dimensional information, and superior contrast resolution. There had been a number of major advances in the CT technology, including optimization-based reconstruction methods, which can be designed to reduce image artifacts and enable flexible scanning configuration design. More recently, there has been a renewed interest in exploring the energy information in CT imaging using multispectral scans. A number of commercial scanners are available to acquire dual-energy scan data for a range of clinical applications. On the other hand, a common limitation shared by almost all commercial dual-energy CT scanners is the significant addition of special hardware to conventional diagnostic CT, adding on to the already-expensive cost of CT systems. Part of the reason for the dependence on the special hardware to acquire dual-energy or multispectral CT data is the need to conform to the data conditions required by the reconstruction methods that include either data-domain or image-domain decomposition and the failure to take advantage of the design flexibility enabled by fully-modeled, optimization-based reconstruction methods, such as the one-step inversion methods for multispectral CT.

In this dissertation work, we aim to propose a one-step, optimization-based reconstruction method and enable novel, non-standard scan configurations of potential practical significance for multispectral CT that can be readily implemented on existing conventional CT scanners with no or minimum system modification. We start with the development of the method, including a non-linear data model, a non-convex optimization program, and an algorithm for numerically solving the program, and applied the method to both simulated and real data collected from standard, full-scan and non-standard, partial-scan configurations. The results suggest that fast, low-dose, and low-cost multispectral CT can be enabled by the proposed optimization-based reconstruction and the ASD-NC-POCS algorithm.

CHAPTER 1

INTRODUCTION

1.1 Background

Computed tomography (CT) has grown into a major workhorse in radiology since its emergence in the 1970's [1–3], for its noninvasiveness, three-dimensional information, and superior contrast resolution [4, 5]. Through the research and development for almost fifty years, today, CT is used in a wide range of clinical applications, including cancer screening [6–9], disease diagnosis [10–13], and treatment guidance [14–16], for almost all the human body parts, including head [11, 17, 18], heart [19–21], breast [22–24], lung [25–28], liver [29–31], bowel [32–34], blood vessels [35–37], and extremity [38–40]. Along with its increasing popularity, there has been a number of major advances in both hardware and software in the CT technology, including the introduction of helical scans with the slip ring design [4, 5], multi-row detectors [4, 5], and optimization-based iterative reconstruction methods.

1.1.1 Background on CT image reconstruction

Analytic-based reconstruction algorithms, such as filtered backprojection (FBP) [4], have been widely used for clinical CT systems [41] with fan-beam, helical cone-beam [42,43], and circular cone-beam [44] configurations. For the last one, an algorithm as a modification to the FBP algorithm was developed by Feldkamp, Davis, and Kress [44] (thus named FDK) for approximate image reconstruction from circular cone-beam data, and has dominantly been the go-to algorithm for commercial cone-beam CT scanners. The analytic-based reconstruction algorithms are based upon a linear continuous-to-continuous (CC) data model, either the Radon transform or the X-ray transform [45]. For the fan-beam or helical cone-beam configurations, mathematically exact algorithms can be derived in closed form to invert the data model [4,42,43], while no exact inversion of the X-ray transform from circular cone-beam data

exists according to Tuy's data sufficiency condition [46]. Nevertheless, the FDK algorithm are still popular owing to its robust performance in practical scanning conditions [47–50].

Optimization-based reconstruction algorithms, on the other hand, are based on a linear discrete-to-discrete (DD) data model, which links a vector of unknown to a vector of measurement simply through a system matrix [4, 45]. Many iterative algorithms have been proposed and developed to invert the large-scale matrix and solve for the unknown, including projection-onto-convex-sets (POCS) (also known as the Kaczmarz method or the algebraic reconstruction technique (ART) [51]) and simultaneous algebraic reconstruction technique (SART) [52]. Other algorithms assume a transmission model that is based on the linear DD model and optimize the likelihood function, such as expectation-maximization (EM) algorithms [53–56]. More recent advances in optimization-based reconstruction allow the incorporation of prior information, as constraints or penalties into the optimization problem, that are designed to address physical factors such as noise and under-sampling [57–59].

The advantages of optimization-based reconstruction algorithms over analytic-based ones are various and can be summarized into two main points - artifacts reduction and flexible scanning design. The optimization-based reconstruction algorithms can be designed to reduce metal artifacts [60, 61] (caused by photon starvation and non-linear partial volume effect), cone-beam artifacts [62] (caused by the non-exactness of the FDK algorithm in the off-middle planes), truncation artifacts [63] (caused by filtering of non-continuous data), and beam-hardening artifacts [64,65] (caused by the polychromatic nature of the conventional X-ray tube that are not modeled in the linear CC data model). Meanwhile, with optimization-based reconstruction algorithms, scanning configurations are not limited to circular source trajectory or dense angular sampling. As a result, a number of investigations have been done with non-circular source trajectory [66,67], sparse- or few-view sampling [68–73], and limited-angle tomography [74,75]. On the other hand, it shall also be noted that optimization-based reconstruction algorithms are more computationally costly and take longer time than the

analytic-based ones, although such gap is being significantly reduced by the technological advancement in CPU clock speed and graphical processor unit (GPU) [76, 77].

1.1.2 Background on multispectral CT

Conventionally, image reconstruction in CT adopts a linear model, assuming monochromatic X-ray spectrum and energy-independent linear attenuation coefficient. In multispectral CT, a non-linear model is used that takes into account the polychromatic nature of X-ray spectrum from Bremsstrahlung radiation and the energy dependence of the linear attenuation coefficient. As a result, artifact reduction can be done through a more realistic physics modeling and material differentiation can be improved by exploring the energy dependence of materials.

The idea of exploring the energy information for material differentiation was already mentioned in one of earliest publications on CT by Hounsfield in 1973 [1]. He described the "determination of atomic number of material" by having two pictures taken of the same slices at 100 and 140 KVp, respectively. A subtraction of the two pictures could then yield enhanced contrast at areas containing high atomic numbers, such as iodine ($Z = 53$) as compared to calcium ($Z = 20$). The earliest investigation on this topic was by Alvarez and Macovski in 1976 [78]. They described a theoretical framework within which a basis decomposition model was used and showed that "for any material, complete energy spectral information may be summarized by a few constants which are independent of energy".

More recently, there has been a renewed interest in exploring the energy information in CT imaging using multispectral scans [79–85]. One important reason was the introduction of Siemens' dual-source CT scanner [80], where a second pair of X-ray tube and detector is integrated into a diagnostic CT scanner. Since then, other major vendors have also released their own version of multispectral CT scanners. GE adopted a fast-KVp-switching technique, where the X-ray tube potential rapidly switches between low and high KVp [84, 86]. Philips

went with the dual-layer technique [79, 86]. With the availability of commercial scanners capable of acquiring multispectral data, a range of clinical applications have been developed to take the advantages [87, 88], including virtual non-contrast image (VNC) [89], virtual monochromatic image (VMI) [90, 91], automated material removal (including bone and calcium) [92, 93], pulmonary functional imaging [94–96], and kidney stone classification [97].

The image reconstruction problem for multispectral CT has been extensively studied with the focus on recovering the energy dependence of materials. There are three categories of methods, largely differentiated from one another by the relationship of reconstruction and decomposition in the method. The first category of methods use two or more spectral scans, while assuming a linear X-ray transform for image reconstruction from each of the scans. Images of different scans are reconstructed individually or jointly, and are then linearly combined to render material specific or pseudo-monochromatic images [81, 98–100]. These methods carry out first the reconstruction and then the decomposition in the image domain, and are thus often referred to as the image-domain decomposition methods. While some artifact reduction can be observed in the combined reconstructions, they often have lowered contrast-to-noise ratio (CNR) and more importantly retain strong beam hardening artifacts [101] as the methods cannot adequately correct for strong non-linear effects due to the fact that they use linear models for image reconstruction.

The second category of methods employs the non-linear data model and compensate approximately for the non-linear effect by decomposing the collected data from multiple spectral scans into X-ray transforms of individual basis images, or basis sinogram. Basis images are then reconstructed from the decomposed basis sinogram through the inversion of the X-ray transform [78, 82, 102–104]. Monochromatic images at any energy level can be formed by linear combination of the reconstructed basis images. These methods carry out the decomposition in the data domain, followed by the image reconstruction, and thus often referred to as the data-domain decomposition methods. The methods assume that rays from

different spectral scans are spatially perfectly registered, i.e., a ray-consistency condition [99], imposing stringent conditions on how the multispectral CT data can be collected.

The methods in the third category are commonly referred to as the one-step inversion approach, as they combine the reconstruction and decomposition together [65,105–110]. The methods also employ a non-linear data model and seek to reconstruct basis images directly from the collected data. The challenge for the methods is to adequately handle the non-linear effect in the reconstruction process. In contrast to the methods in the previous two categories, the one-step inversion approach methods address explicitly the non-linear spectral effect in basis-image reconstruction and remove the restrictive ray-consistency condition. Despite such a potentially high degree of flexibility in the scan configuration, the investigation of the one-step methods remains relative less active than those in the other two categories until recent, because of the complexity of the realistic, non-linear data model and the challenges to correct for the non-linear effect during the reconstruction step [110]. The one-step inversion approach may be exploited to reconstruct basis images and monochromatic images in multispectral CT from data collected with a variety of novel scan configurations or systems of potential practical significance.

1.2 Current implementations for multispectral CT

1.2.1 Photon-counting CT

Photon counting detectors with energy resolving capability can be used to acquire multispectral CT data [85,111]. Conventional CT detectors use scintillating crystals coupled with photodiodes and measure the total energy deposited in the crystal, essentially making it an energy-integrating detector [5]. Photon counting detectors can convert the energy deposited by each photon directly into charge pulses and measure the pulse height, which is proportional to the photon's energy, with a comparator. As a result, with multiple comparators,

photon counting detectors can detect and count photons into multiple energy windows. The resulting spectral separation as well as increased dose efficiency make the photon counting detector an ideal candidate for acquiring multispectral CT data. However, investigations of prototype systems also reveal many difficulties yet to overcome, such as energy calibration, gain calibration, and dealing with high flux rate [83, 112–114]. Besides, the current cost for photon counting detectors is too high for them to be widely implemented and utilized.

1.2.2 Dual-energy CT

In dual-energy CT, material-basis and/or monochromatic-energy images are reconstructed from data sets collected with two different spectra. There exist four distinctive methods currently for realizing dual-energy CT imaging. The first method, referred to as the slow-KVp-switch method, uses a single X-ray source and single set of detectors to collect dual-energy data sets by performing two consecutive full-rotation scans in which the source KVp is switched following the first full-rotation scan [86]. The second method, referred to as the fast-KVp-switch method, also uses a single X-ray source and a single detector for acquiring dual-energy data sets. The X-ray source rotates one full rotation in which the source invokes a rapid KVp switch at each effective view of the full-rotation scan between low and high KVp settings [84, 86]. The third method, referred to as the dual-source/detector method, employs two source-detector pairs of different spectra to collect dual-energy data sets within a full-rotation scan [80, 86]. The two sets of tube-detector pair are positioned with a 90° offset inside the gantry. The fourth method, referred to as the dual-layer-detector method, adopts a single X-ray source and a two-layer detector with each layer having a different energy response for collecting dual-energy data sets within a full-rotation scan [79, 86]. In addition, the top layer detector is used as a filtration and creates a hardened beam spectrum for the bottom layer detector.

While these methods are innovative, they are not without shortcomings. The fast-kVp-

switching method has limited spectral separation due to non-rectangular tube modulation and one-view mis-registration for low and high KVp rays. Low photon flux at lower KVp setting could also be a problem as the tube current can not modulate as fast as the KVp [5]. The dual-layer-detector also suffers from limited spectral separation. The dual-source one has cross-scatter contamination and is limited to image domain decomposition. In addition, the slow-KVp-switch method, while easy to implement without hardware addition, has a relative low temporal imaging capability and doubled radiation dose of a regular full-rotation scan, as it carries out two full-rotation scans. The fast-KVp-switch and dual-source/detector methods, while having improved temporal imaging resolution over the single-KVp-switch method, in essence also perform two scans within one full rotation, and thus may also double radiation dose of a regular full-rotation scan.

More importantly, the fast-KVp-switch, dual-source/detector, and dual-layer-detector methods all require significant hardware addition to a conventional diagnostic CT, thus considerably increasing CT system costs. Particularly, fast-KVp-switch method requires a unique, high performance X-ray tube capable of switching rapidly and repeatedly within a full rotation. The dual-source/detector method uses an additional pair of X-ray source and detector set, and the dual-layer-detector method uses a highly specialized detector technology. The cost of these might be a leading reason for the lack of their adoption especially in CT scanners other than diagnostic CT ones, such as C-arm cone-beam CT.

Overall, the current implementations of the dual-energy CT all conform to the data condition required by the reconstruction methods described above. For example, all of the four implementations require the performance of two or one full-rotation scans.

1.3 Motivation of the dissertation work

Observing the limitation of the current implementations for multispectral CT and the advantages of the one-step inversion approach, we are motivated in this dissertation work to

develop a one-step, optimization-based reconstruction method and use the developed method to enable novel scan configurations of potential practical significance for multispectral CT. Our approach is to focus on conventional energy-integrating detectors, and thus the existing conventional CT scanners, and to use algorithms to enable its capability for acquiring multispectral scans without the specialized hardware. As a result, we can provide a virtual hardware upgrade to current CT systems in service and make spectral CT applications accessible to a wide range of diagnostic CT scanners and cone-beam CT devices.

This thesis is organized as follows. In Chapter 2, we examine the data model based on which the optimization-based reconstruction algorithm is developed and derive a linearization approach that guides the development of the algorithm. In Chapter 3, we describe the optimization-based reconstruction method in detail, including a non-convex optimization program, a heuristic algorithm for numerically solving the non-convex program, and its optimality conditions. Chapter 4 consists of a verification study with consistent data that verifies the numerical convergence of the proposed algorithm in solving the non-convex optimization program and its computer implementation. In Chapters 5 and 6, we carry out characterization studies with inconsistent simulated data for both full-scan configuration and four non-standard scan configurations. In Chapter 7, we apply the developed optimization-based reconstruction algorithm to real data collected from a diagnostic scan and investigate two scan configurations for potentially fast, low-dose, and low-cost multispectral CT. Finally, Chapter 8 concludes the thesis with a summary and discussion on potential future directions.

CHAPTER 2

DATA MODEL FOR MULTISPECTRAL CT

2.1 Introduction

A data model sets up the unknown as the quantities of interest to be solved, establishes mathematical relationships between the unknown and the data, and, especially in the case of multispectral CT, determines how different spectral data sets are connected. Conventionally, the Radon transform or X-ray transform with the univariate $f(\vec{r})$ is the default data model for CT. With multispectral CT, we need to first set up the unknown to properly represent a bivariate attenuation coefficients $f(\vec{r}, E)$ and secondly organize all the measurements from multispectral data sets to be used in a combined manner. We set up the data model which can facilitate the development of image reconstruction methods, especially for non-standard scan configurations. Among other possible means, we focus on linearizing the data model, as the linear systems are much easier to deal with.

We derive a data model from the fundamental polychromatic model that enables more flexible scan configuration by combining the multispectral data sets jointly, while retaining the balance between the accuracy and complexity in the modeling.

2.2 Continuous-to-continuous data model

We describe first a continuous-to-continuous (CC) data model, based upon which a discrete-to-discrete (DD) data model is developed for optimization-based image reconstruction in multispectral CT. Let $\vec{r}_0(\lambda)$ denote a spatial trajectory of the X-ray source specified by parameter λ in a laboratory coordinate system and unit vector $\hat{\beta}$ the direction of a ray engendered from the source position $\vec{r}_0(\lambda)$. In multispectral CT, multiple sets of data are usually collected with different X-ray spectra or detector energy response. Therefore, we use $s \in \{1, \cdots, S\}$ to index a specific spectral data set, e.g., from a certain kVp setting

or a certain energy bin, and $Q^{[s]}(\lambda, \hat{\beta}, E)$ a generalized spectrum for ray $(\lambda, \hat{\beta})$ within data set s. The generalized spectrum, or simply referred to the X-ray spectrum, is a product of the incident X-ray spectrum and the detector energy response function. We note that $Q^{[s]}(\lambda, \hat{\beta}, E)$ can be ray-dependent, e.g., in the presence of a bow-tie filter in front of the X-ray source, and that multiple measurements can be made for a given ray, e.g., using multiple energy bins in photon counting detector.

When the polychromatic spectrum in CT imaging is considered, the linear attenuation coefficient $f(\vec{r}, E)$ is a function of not only spatial location $\vec{r}$ but also of X-ray photon energy E. The data model for the measurement of an X-ray with $\hat{\beta}$ in spectral set s is given by

$$I^{[s]}(\lambda, \hat{\beta}) = \int_0^\infty \mathrm{d}E \; Q^{[s]}(\lambda, \hat{\beta}, E) \exp\left(- \int_0^\infty \mathrm{d}t \; f(\vec{r}_0(\lambda) + t\hat{\beta}, E) \right), \tag{2.1}$$

and the measured intensity in an air scan with $f(\vec{r}_0(\lambda) + t\hat{\beta}, E) = 0$ is thus denoted by

$$I_0^{[s]}(\lambda, \hat{\beta}) = \int_0^\infty \mathrm{d}E \; Q^{[s]}(\lambda, \hat{\beta}, E). \tag{2.2}$$

A normalized X-ray spectrum function can be defined as

$$\tilde{q}^{[s]}(\lambda, \hat{\beta}, E) = \frac{Q^{[s]}(\lambda, \hat{\beta}, E)}{\displaystyle\int_0^\infty \mathrm{d}E \; Q^{[s]}(\lambda, \hat{\beta}, E)} = \frac{Q^{[s]}(\lambda, \hat{\beta}, E)}{I_0^{[s]}(\lambda, \hat{\beta})}, \tag{2.3}$$

with the normalization condition being

$$\int_0^\infty \mathrm{d}E \; \tilde{q}^{[s]}(\lambda, \hat{\beta}, E) = 1. \tag{2.4}$$

Combining (2.1)-(2.3), we define a data function as

$$\begin{aligned}\tilde{g}^{[s]}(\lambda,\hat{\beta}) =& -\ln\frac{I^{[s]}(\lambda,\hat{\beta})}{I_0^{[s]}(\lambda,\hat{\beta})}\\ =& -\ln\int_0^\infty \mathrm{d}E\ \tilde{q}^{[s]}(\lambda,\hat{\beta},E)\exp\left(-\int_0^\infty \mathrm{d}t\ f(\vec{r}_0(\lambda)+t\hat{\beta},E)\right).\end{aligned} \tag{2.5}$$

Note that, when $\tilde{q}^{[s]}(\lambda,\hat{\beta},E)=\delta(E-E_0)$, the CC data model becomes the conventional X-ray transform [115], in a linear form as

$$\tilde{g}_\delta^{[s]}(\lambda,\hat{\beta})=\int_0^\infty \mathrm{d}t\ f(\vec{r}_0(\lambda)+t\hat{\beta},E_0). \tag{2.6}$$

For the discussion of discretization of the CC-model, we consider below a parameterization of $\hat{\beta}$ in terms of physical parameters in an imaging experiment: a flat panel detector is assumed on which a Cartesian-coordinate system (u,v) is spanned by orthogonal unit vectors $\hat{\mathrm{e}}_u(\lambda)$ and $\hat{\mathrm{e}}_v(\lambda)$; unit vector $\hat{\mathrm{e}}_w(\lambda)$ denotes the normal-projection direction of the X-ray source pointing to the detector plane, and the normal-projection point on the detector plane is set as the origin of coordinate system (u,v). Unit vector $\hat{\beta}$, as the direction of a ray engendered from the X-ray source, can then be expressed as

$$\hat{\beta}(\lambda,u,v)=\frac{u\hat{\mathrm{e}}_u(\lambda)+v\hat{\mathrm{e}}_v(\lambda)+L(\lambda)\hat{\mathrm{e}}_w(\lambda)}{\sqrt{u^2+v^2+L(\lambda)^2}}, \tag{2.7}$$

where $L(\lambda)$ denotes the distance between the source and the origin of coordinate system (u,v). We then use $g^{[s]}(\lambda,u,v)$ and $q^{[s]}(\lambda,u,v,E)$ to denote the model-data function and normalized spectrum function in terms of parameterization λ, u, and v as

$$g^{[s]}(\lambda,u,v)=\tilde{g}^{[s]}(\lambda,\hat{\beta}), \tag{2.8}$$

$$q^{[s]}(\lambda,u,v,E)=\tilde{q}^{[s]}(\lambda,\hat{\beta},E). \tag{2.9}$$

where (u, v) are related to $\hat{\beta}$ through equation (2.7).

2.3 Discrete-to-discrete data model

2.3.1 Discretization of the CC data model

For each spectral data set s, we consider a discrete representation of data space $\{\lambda, u, v\}$ in which each ray is specified by

$$\lambda = \lambda_0 + j_\lambda \delta_\lambda,$$

$$u = u_0 + j_u \delta_u,$$

$$v = v_0 + j_v \delta_v,$$

where λ_0, u_0, v_0 denote the starting position and δ_λ, δ_v, δ_u the sampling intervals, along λ, u, and v, respectively. The integers j_λ, j_u, and j_v index the discrete samples and take the ranges as

$$j_\lambda \in \{0, \cdots, N_\lambda^{[s]} - 1\},$$

$$j_u \in \{0, \cdots, N_u^{[s]} - 1\},$$

$$j_v \in \{0, \cdots, N_v^{[s]} - 1\},$$

where $N_\lambda^{[s]}$, $N_u^{[s]}$, and $N_v^{[s]}$ denote the total numbers of samples along each axis in spectral data set s. We align data for all rays in a single spectral set into a 1D array of size $J^{[s]} = N_\lambda^{[s]} \times N_u^{[s]} \times N_v^{[s]}$ in a concatenate form in the order of j_u, j_v, and j_λ, indexed by

$$j = j_u + j_v \times N_u^{[s]} + j_\lambda \times N_v^{[s]} \times N_u^{[s]}.$$

The discrete form of $g^{[s]}(\lambda, u, v)$ for the jth ray in spectral data set s is thus defined as

$$g_j'^{[s]} = g^{[s]}(\lambda_0 + j_\lambda \Delta_\lambda, u_0 + j_u \Delta_u, v_0 + j_v \Delta_v). \tag{2.10}$$

The energy space is also discretized uniformly with $E = m\Delta_E$, with $m \in \{1, \cdots, M\}$ and Δ_E the energy sampling interval. The discretized form of the spectrum function of equation (2.9) is then defined as

$$q_{jm}^{[s]} = \Delta_E \, q^{[s]}(\lambda_0 + j_\lambda \Delta_\lambda, v_0 + j_v \Delta_v, u_0 + j_u \Delta_u, m\Delta_E), \tag{2.11}$$

and the normalization condition of the normalized spectrum function in equation (2.4) becomes the normalization condition of the discrete spectrum as

$$\sum_m q_{jm}^{[s]} = 1,$$

for each ray j in spectral data set s.

We next consider a voxel-based representation of three-dimensional (3D) space $\{\vec{r}\} = \{x, y, z\}$ by discretizing evenly along its x-, y-, and z-axis, with

$$x = x_0 + i_x \Delta_x,$$
$$y = y_0 + i_y \Delta_y,$$
$$z = z_0 + i_z \Delta_z,$$

where x_0, y_0, z_0 denote the starting positions and Δ_x, Δ_y, Δ_z the voxel sizes, along x-, y-, and z-axis, respectively. The integers i_x, i_y, and i_z index the voxels and take the ranges as

$$i_x \in \{0, \cdots, N_x - 1\},$$
$$i_y \in \{0, \cdots, N_y - 1\},$$
$$i_z \in \{0, \cdots, N_z - 1\},$$

where N_x, N_y, and N_z denote the total numbers of voxels. The voxels can be aligned into a 1D array of size $I = N_x \times N_y \times N_z$ in a concatenate form in the order of i_x, i_y, and i_z,

indexed by

$$i = i_x + i_y \times N_x + i_z \times N_y \times N_z.$$

Therefore, the discrete form of the linear attenuation coefficient $f(\vec{r}, E)$ is defined as

$$f'_{im} = f(x_0 + i_x \Delta x, y_0 + i_y \Delta y, z_0 + i_z \Delta z, m\Delta_E). \tag{2.12}$$

2.3.2 A discretized CC data model

Using equations (2.5)-(2.12), we obtain a discrete form of data function $g^{[s]}(\lambda, u, v)$ as

$$g_j'^{[s]}(f'_{im}) = -\ln \sum_m q_{jm}^{[s]} \exp\left(-\sum_i a_{ji}^{[s]} f'_{im}\right), \tag{2.13}$$

where $j \in \{0, \cdots, J^{[s]} - 1\}$ and $i \in \{0, \cdots, I-1\}$ index the discrete data samples (in spectral set s) and image voxels, respectively, and $a_{ji}^{[s]}$ denotes the intersection length of ray j in spectral set s with voxel i. Note that the integral over energy E is replaced by the summation over energy samples m and the line integral along a ray direction $\hat{\beta}$ is replaced by the summation of all $a_{ji}^{[s]}$ for ray j.

While equation (2.13) represents a DD data model for multispectral CT, it is difficult to directly reconstruct f'_{im}, or $f(\vec{r}, E)$, as a function of both spatial location and energy. Instead, in an attempt to address the difficulty, an expansion

$$f(\vec{r}, E) = \sum_k b_k(\vec{r}) \mu_k(E) \tag{2.14}$$

is often considered, where $k \in \mathbb{Z}^+$, $b_k(\vec{r})$ and $\mu_k(E)$ are the basis images and expansion coefficients. The basis images can be designed based upon material or interaction decomposition [78], and the expansion coefficients can be the energy-dependent cross sections of photon electric effect and Compton scattering, in the case of interaction decomposition, or

mass attenuation coefficients of materials, in the case of material decomposition. In both cases, the expansion coefficients can be assumed to be known. As a result, the problem of image reconstruction in multispectral CT is simplified to the determination of the basis images, which are functions of only the spatial variable $\vec{r}$.

2.3.3 A DD data model with basis decomposition

In this work, a basis decomposition is considered in which $b_k(\vec{r})$ and $\mu_k(E)$ are referred to as the kth basis image and its mass attenuation coefficient. Again, the voxel-based representation as described above is used to obtain a basis image in a discrete form and align the voxel values into a 1D array of size I in a concatenated form in the order of i_x, i_y, and i_z, with the ith element given by

$$b_{ki} = b_k(x_0 + i_x\Delta x, y_0 + i_y\Delta y, z_0 + i_z\Delta z), \tag{2.15}$$

where $i = i_x + i_y \times N_x + i_z \times N_y \times N_z$. Additionally, a discrete form of the mass attenuation coefficient is defined as

$$\mu_{km} = \mu_k(m\Delta_E). \tag{2.16}$$

Practically, a limited number of basis materials are to be considered, yielding a discrete form of equation (2.14) as

$$f'_{im} = f^K_{im} + \Delta f_{im} \tag{2.17}$$

where

$$f^K_{im} = \sum_{k=1}^{K} \mu_{km} b_{ki} \tag{2.18}$$

is referred to as the ith voxel of the monochromatic image at energy m, as a linear combination of basis images weighted by their expansion coefficients evaluated at energy m. K is the total number of basis materials considered and Δf_{im} the decomposition error.

Using equations (2.17) and (2.18) and ignoring the decomposition error term Δf_{im}, we obtain another DD data model as

$$g_j^{[s]}(\mathbf{b}) = -\ln \sum_m q_{jm}^{[s]} \exp\left(-\sum_k \mu_{km} \sum_i a_{ji}^{[s]} b_{ki}\right), \tag{2.19}$$

where $\mathbf{b}$ denotes a vector formed by concatenating individual basis image vectors $\mathbf{b}_k$, with b_{ki} as their elements, in the ascending order of k. We include $\mathbf{b}$ as a variable of this model data $g_j^{[s]}(\mathbf{b})$ to explicitly indicate that the reconstruction task is to determine $\mathbf{b}$ from knowledge of data measured. The DD data model in equation (2.19) is the base upon which the reconstruction algorithm for multispectral CT is designed and developed.

For the sake of clarity in the following sections, we define vectors and aggregate vectors based on the quantities as defined in equations (2.13)-(2.19), among which $\mathbf{b}$ and $\mathbf{b}_k$ are already introduced, and summarize in Table 2.1. The vectors in the middle column are simply

Table 2.1: Notations for vector and aggregate vector, and their sizes and corresponding elements as defined in equations (2.13)-(2.19).

element	vector	size	aggregate vector	size
b_{ki}	$\mathbf{b}_k$	I	$\mathbf{b}$	$I \times K$
f_{im}^K	$\mathbf{f}_m^K$	I		
f'_{im}	$\mathbf{f}'_m$	I		
$q_{jm}^{[s]}$	$\mathbf{q}_j^{[s]}$	M		
$g_j'^{[s]}$	$\mathbf{g}'^{[s]}$	$J^{[s]}$	$\mathbf{g}'$	$\sum_{s=1}^S J^s$
$g_j^{[s]}$	$\mathbf{g}^{[s]}$	$J^{[s]}$	$\mathbf{g}$	$\sum_{s=1}^S J^s$
$g_{\mathcal{M}j}^{[s]}$	$\mathbf{g}_{\mathcal{M}}^{[s]}$	$J^{[s]}$	$\mathbf{g}_{\mathcal{M}}$	$\sum_{s=1}^S J^s$

obtained by aligning their corresponding elements in the first column along the vanished index. For example, from b_{ki} to $\mathbf{b}_k$, i is the vanished index. the aggregate vectors on the third column, if available, are formed by simply concatenating their corresponding vectors

in the middle column together, in the ascending order of the vanished index. For example, $\mathbf{b} = (\mathbf{b}_1^\top, \mathbf{b}_2^\top, \cdots, \mathbf{b}_K^\top)^\top$ and $\mathbf{g} = (\mathbf{g}^{[1]\top}, \mathbf{g}^{[2]\top}, \cdots, \mathbf{g}^{[S]\top})^\top$. Note that at the last row of Table 2.1 there is a new quantity $g_{\mathcal{M}j}^{[s]}$, which denotes the measured data for ray j in spectral set s.

2.4 Linear and non-linear terms of the data model

The DD data model in equation (2.19) is non-linear, which makes the reconstruction, that is the inversion of the data model, difficult. Reconstruction for conventional CT is based on the linear Radon transform in equation (2.6), and thus can have analytic-based, closed-form algorithm for inversion, such as filtered back-projection (FBP) [45], or optimization-based, iterative algorithm based on a linear data model. Focusing on the latter, the optimization-based reconstruction method, for the image reconstruction for multispectral CT data, we first separate the DD data model in equation (2.19) into linear and non-linear terms, and treat the non-linear term as a perturbation to be corrected for.

2.4.1 Splitting the mass attenuation coefficient

Note that the non-linearity can be eliminated by either setting the spectrum $q_{jm}^{[s]}$ to the Kronecker delta function, as equation (2.6) shows, or having the linear attenuation coefficient μ_{km} be independent of energy m. We thus split mass attenuation coefficient μ_{km} in equation (2.19) for material k into

$$\mu_{km} = \bar{\mu}_k + \Delta\mu_{km}, \tag{2.20}$$

where $\bar{\mu}_k$ is independent of energy and $\Delta\mu_{km}$ is the the remaining error term that is still energy dependent. Substituting equation (2.20) into equation (2.19) yields

$$\begin{aligned} g_j^{[s]}(\mathbf{b}) = & \sum_k \bar{\mu}_k \sum_i a_{ji}^{[s]} b_{ki} \\ & + \\ & \left[-\ln \sum_m q_{jm}^{[s]} \exp\left(-\sum_k \Delta\mu_{km} \sum_i a_{ji}^{[s]} b_{ki} \right) \right], \end{aligned} \tag{2.21}$$

which is separated into a linear term $\sum_k \bar{\mu}_k \sum_i a_{ji}^{[s]} b_{ki}$ on the first line and a non-linear term that carries the summation over energy index m on the second line. To treat the non-linear term as a perturbation with small magnitude, we shall choose the energy-independent portion $\bar{\mu}_k$ such that the error between $g_j^{[s]}(\mathbf{b})$ and the linear term is minimized, which can be derived from

$$\begin{aligned} & \frac{\mathrm{d}}{\mathrm{d}\bar{\mu}_k} \left(g_j^{[s]}(\mathbf{b}) - \sum_k \bar{\mu}_k \sum_i a_{ji}^{[s]} b_{ki} \right)^2 \\ = & -2 \sum_i a_{ji}^{[s]} b_{ki} \left(g_j^{[s]}(\mathbf{b}) - \sum_k \bar{\mu}_k \sum_i a_{ji}^{[s]} b_{ki} \right) \\ = & \, 0. \end{aligned} \tag{2.22}$$

The above optimality condition is satisfied when

$$g_j^{[s]}(\mathbf{b}) - \sum_k \bar{\mu}_k \sum_i a_{ji}^{[s]} b_{ki} = 0. \tag{2.23}$$

But equation (2.23) as the optimality condition is obvious - when the linear term equals the data model, the non-linear term as the difference of the two is zero and obviously minimized! However, equation (2.22) does provide information that the absolute value of the non-linear term, or simply the non-linear error, can be minimized. Let $\bar{\mu}_k$ start from 0 and increase, the first derivative in equation (2.22) should be negative, meaning the non-linear

error is decreasing. When $\bar{\mu}_k$ is increased to large enough, the linear term $\sum_k \bar{\mu}_k \sum_i a_{ji}^{[s]} b_{ki}$ becomes large enough and greater than $g_j^{[s]}(\mathbf{b})$, so the first derivative becomes positive and the non-linear error starts to increase. Therefore, we re-visit equation (2.23) and derive an expression for $\bar{\mu}_k$ with some approximation. Substitution of the full expression of $g_j^{[s]}(\mathbf{b})$ in equation (2.19) into equation (2.23) yields

$$\begin{aligned} -\ln \sum_m q_{jm}^{[s]} \exp\left(-\sum_k \mu_{km} \sum_i a_{ji}^{[s]} b_{ki}\right) &= \sum_k \bar{\mu}_k \sum_i a_{ji}^{[s]} b_{ki} \\ \Rightarrow \quad \sum_m q_{jm}^{[s]} \exp\left(-\sum_k \mu_{km} \sum_i a_{ji}^{[s]} b_{ki}\right) &= \exp\left(-\sum_k \bar{\mu}_k \sum_i a_{ji}^{[s]} b_{ki}\right) \end{aligned} \tag{2.24}$$

Using a first-order Taylor expansion for the exponential function, we can approximate the condition in equation (2.24) as

$$\begin{aligned} \sum_m q_{jm}^{[s]} \left(1 - \sum_k \mu_{km} \sum_i a_{ji}^{[s]} b_{ki}\right) &= 1 - \sum_k \bar{\mu}_k \sum_i a_{ji}^{[s]} b_{ki} \\ \Rightarrow \quad \sum_k \sum_m q_{jm}^{[s]} \mu_{km} \sum_i a_{ji}^{[s]} b_{ki} &= \sum_k \bar{\mu}_k \sum_i a_{ji}^{[s]} b_{ki}, \end{aligned} \tag{2.25}$$

given the normalization condition of $q_{jm}^{[s]}$. Observing both sides on the second line of equation (2.25), we note that the equality can be satisfied when

$$\bar{\mu}_k = \sum_m q_{jm}^{[s]} \mu_{km}. \tag{2.26}$$

The result matches our intuitive guess that using the spectrum-weighted average as $\bar{\mu}_k$ best approximates μ_{km} [102, 116]. Given the dependence on ray j and set s of $q_{jm}^{[s]}$, we use a different notation for the energy-independent term and re-write equations (2.26) and (2.20) as

$$\mu_{km} = \bar{\mu}_{jk}^{[s]} + \Delta\mu_{jkm}^{[s]}, \tag{2.27}$$

where

$$\bar{\mu}_{jk}^{[s]} = \sum_m q_{jm}^{[s]} \mu_{km}, \tag{2.28}$$

and

$$\Delta\mu_{jkm}^{[s]} = \mu_{km} - \bar{\mu}_{jk}^{[s]}. \tag{2.29}$$

2.4.2 Separating the data model into linear and non-linear terms

Just as equation (2.21), substitution of equation (2.27) into (2.19) yields

$$g_j^{[s]}(\mathbf{b}) = \bar{g}_j^{[s]}(\mathbf{b}) + \Delta g_j^{[s]}(\mathbf{b}), \tag{2.30}$$

where

$$\bar{g}_j^{[s]}(\mathbf{b}) = \sum_k \bar{\mu}_{jk}^{[s]} \sum_i a_{ji}^{[s]} b_{ki} \tag{2.31}$$

and

$$\Delta g_j^{[s]}(\mathbf{b}) = -\ln \sum_m q_{jm}^{[s]} \exp\left(-\sum_k \Delta\mu_{jkm}^{[s]} \sum_i a_{ji}^{[s]} b_{ki} \right) \tag{2.32}$$

denote the linear (LI) and non-linear (NL) terms in the data model, respectively. The NL term determined in this way should be approximately the smallest in magnitude, according to the derivation from equations (2.22)-(2.26). As a matter of fact, we show in Figs. 2.1 and 2.2 the different selections of $\bar{\mu}_k$, in addition to the optimal one $\bar{\mu}_{jk}^{[s]}$, and how they impact $\Delta g_j^{[s]}$.

We form vectors and aggregate vectors from $\bar{g}_j^{[s]}(\mathbf{b})$ and $\Delta g_j^{[s]}(\mathbf{b})$, as defined in equations (2.31) and (2.32), in the same fashion as from $g_j^{[s]}$, and summarize in Table 2.2, as an addition to Table 2.1.

With the vectors defined in Tables 2.1 and 2.2, we expand the DD data model in equation (2.19) from a single measurement ray to all measurement rays in a matrix-vector form,

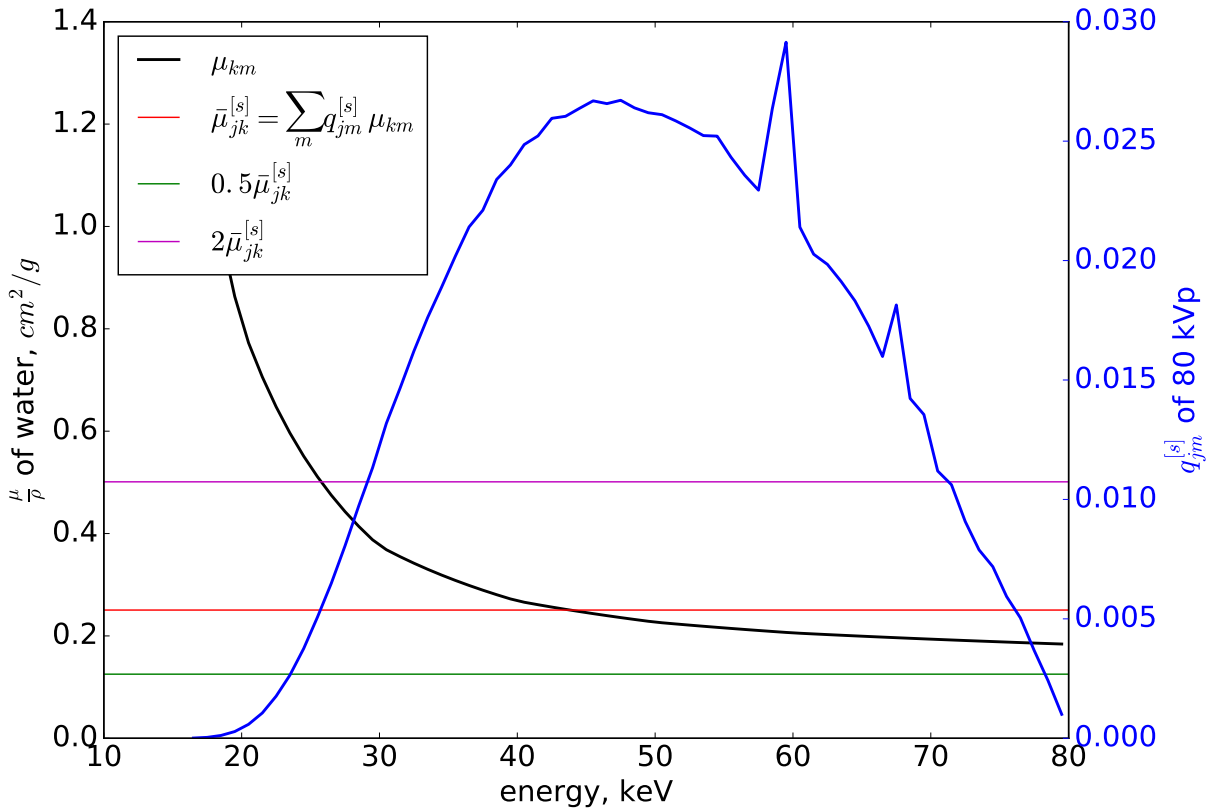

Figure 2.1: Plots of μ_{km} of water and different selections of $\bar{\mu}_k$ as compared to the optimal one calculated as the spectrum-weighted average (in red). A typical spectrum at 80 kVp is also plotted for reference.

as

$$\begin{aligned} \mathbf{g}(\mathbf{b}) &= \bar{\mathbf{g}}(\mathbf{b}) + \Delta\mathbf{g}(\mathbf{b}) \\ &= \mathcal{H}\,\mathbf{b} + \Delta\mathbf{g}(\mathbf{b}), \end{aligned} \tag{2.33}$$

where matrix $\mathcal{H}$ of size $\left(\sum_{s=1}^{S} J^s\right) \times (I \times K)$, is defined as

$$\mathcal{H} = \begin{pmatrix} \mathcal{U}_1^{[1]}\,\mathcal{A}^{[1]} & \mathcal{U}_2^{[1]}\,\mathcal{A}^{[1]} & \cdots & \mathcal{U}_K^{[1]}\,\mathcal{A}^{[1]} \\ \mathcal{U}_1^{[2]}\,\mathcal{A}^{[2]} & \mathcal{U}_2^{[2]}\,\mathcal{A}^{[2]} & \cdots & \mathcal{U}_K^{[2]}\,\mathcal{A}^{[2]} \\ \vdots & \vdots & \ddots & \vdots \\ \mathcal{U}_1^{[S]}\,\mathcal{A}^{[S]} & \mathcal{U}_2^{[S]}\,\mathcal{A}^{[S]} & \cdots & \mathcal{U}_K^{[S]}\,\mathcal{A}^{[S]} \end{pmatrix}, \tag{2.34}$$

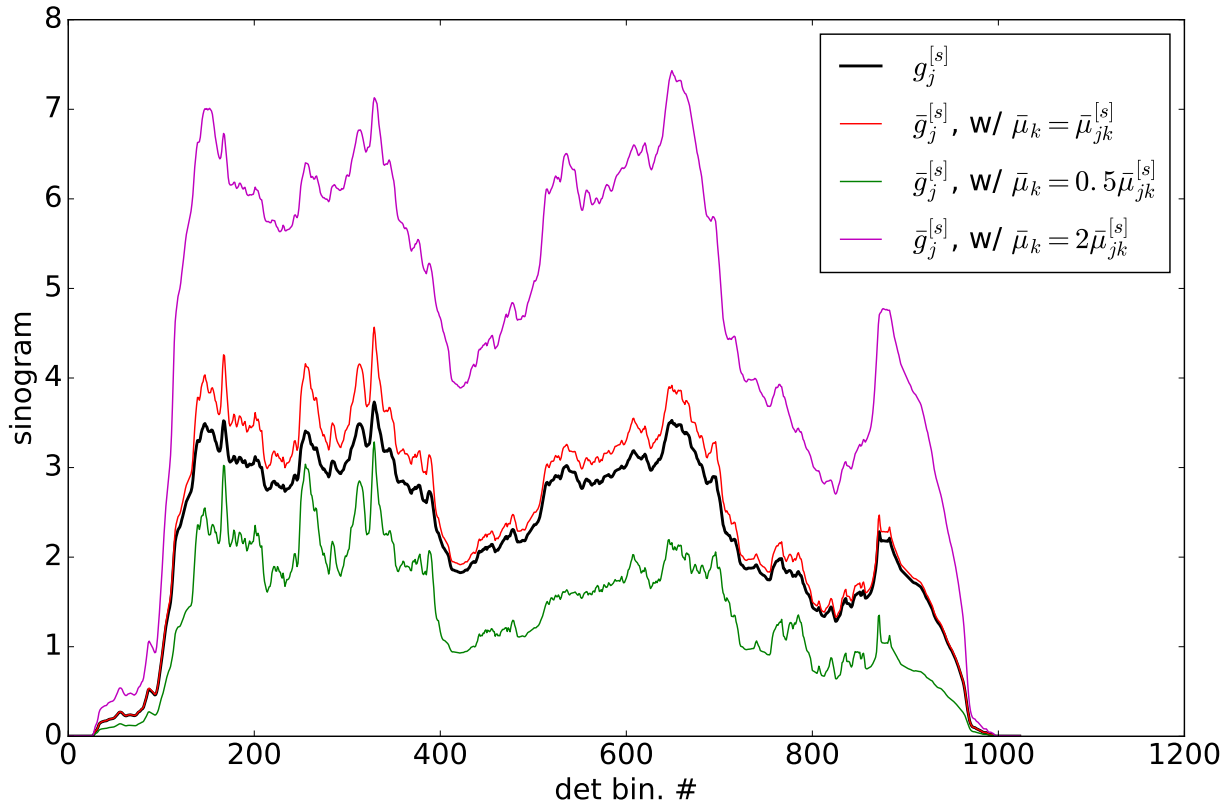

Figure 2.2: $g_j^{[s]}$ calculated from equation (2.19) with a simple simulation setup, and different linear terms $\bar{g}_j^{[s]}$ corresponding to the different selections of $\bar{\mu}_k$ in Fig. 2.1. It is evident in this case that choosing $\bar{\mu}_k$ as the spectrum-weighted average gives the smallest error between the sinogram and the linear term.

in which matrix $\mathcal{A}^{[s]}$, of size $J^{[s]} \times I$, has $a_{ji}^{[s]}$ as its elements and $\mathcal{U}_k^{[s]}$ a diagonal matrix of size $J^{[s]}$ with $\bar{\mu}_{jk}^{[s]}$ defined in equation (2.28) as its diagonal elements, as

$$\mathcal{U}_k^{[s]} = \begin{pmatrix} \bar{\mu}_{0k}^{[s]} & & & & \\ & \ddots & & & \\ & & \bar{\mu}_{jk}^{[s]} & & \\ & & & \ddots & \\ & & & & \bar{\mu}_{(J^{[s]}-1)k}^{[s]} \end{pmatrix}. \tag{2.35}$$

Table 2.2: Additional notations for vector and aggregate vector

element	vector	size	aggregate vector	size
$\bar{g}_j^{[s]}$	$\bar{\mathbf{g}}^{[s]}$	$J^{[s]}$	$\bar{\mathbf{g}}$	$\sum_{s=1}^{S} J^s$
$\Delta g_j^{[s]}$	$\Delta \mathbf{g}^{[s]}$	$J^{[s]}$	$\Delta \mathbf{g}$	$\sum_{s=1}^{S} J^s$

Note that $\mathcal{A}^{[s]}$, for $s \in \{1, \cdots, S\}$, denotes the discrete X-ray transform for spectral data set s, collected from a certain kVp setting or a certain energy bin.

While equation (2.33) is only a different form of the DD data model in equation (2.19), it reveals that it is NL term $\Delta \mathbf{g}(\mathbf{b})$ that results in the non-convexity of the data divergence and thus of the optimization program.

2.4.3 A linear DD data model

A linear DD data model can be formed by considering the linear term in equation (2.31) only as

$$g_j^{[s]}(\mathbf{b}) = \sum_k \bar{\mu}_{jk}^{[s]} \sum_i a_{ji}^{[s]} b_{ki}, \tag{2.36}$$

or in the matrix-vector form as

$$\mathbf{g}(\mathbf{b}) = \mathcal{H}\,\mathbf{b}, \tag{2.37}$$

where $\mathcal{H}$ is defined in equations (2.34) and (2.35). Just as the DD data model in equation (2.19) or (2.33), the linear DD data model described above can also be used to develop reconstruction algorithms for multispectral CT. Such algorithms are useful in reconstructing from consistent data with the linear model in an inverse-crime study. It can also be used to reconstruct from data generated using (2.19) and demonstrate the importance of considering the non-linear modeling in the reconstruction.

2.5 Discussion

In this chapter, we have established a DD data model in equation (2.19), based on which the optimization-based reconstruction is developed. The DD model was discretized from the CC data model, which describes a polychromatic integral over energy, and incorporated a basis decomposition model that reduces the dimensionality of the unknown in the inverse problem. More importantly, the DD data model was separated into linear and non-linear terms, which facilitated the development of the reconstruction algorithm. In addition, a second DD data model in equation 2.13 prior to the basis decomposition step was also introduced and is mainly used to generate inconsistent data with decomposition errors in simulation studies in Chapters 5 and 6.

The linearization of the DD data model was done by splitting the mass attenuation coefficient into a zero-order, energy-independent term and a residual, energy-dependent term. The splitting was introduced as, intuitively, the spectrum-weighted average over energy, and was validated by an approximated theoretical derivation. The current splitting scheme seems to yield the non-linear term small in magnitude, as shown in Fig. 2.2. However, for each ray measurement with a different spectrum, there could exist a different value of $\bar{\mu}_k$ that minimizes the non-linear term other than the spectrum-weighted average $\bar{m}u_{jk}^{[s]}$. It might be of interest to find a consistent way to split the mass attenuation coefficient that can yield smaller non-linear terms than the current method and to study the impact of the magnitude of the non-linear term to the convergence of the reconstruction algorithm.

There also exist other ways to linearize the DD data model, one of which is through Taylor expansion. Zhao et al [109] adopted such linearization method and developed extended algebraic reconstruction technique (E-ART) for dual spectral CT. In their work, the first-order Taylor expansion is used to establish a virtual hyper-plane at each iteration point and the ART algorithm was applied based on the virtual hyper-plane and used to move to the next iteration. While the interpretation of the method was novel, the resulting procedure is

the same as applying a gradient-based method to the non-linear data model directly, such as gradient descent or incremental method [117, 118], since the first-order Taylor expansion retains only the gradient.

CHAPTER 3

OPTIMIZATION-BASED RECONSTRUCTION METHOD

3.1 Introduction

There are three categories of methods for image reconstruction using multispectral CT data. Among the three, the image-domain decomposition methods start with a linear data model, so are not of interest to us. The data-domain decomposition methods do employ a non-linear data model, however also require ray-consistency condition which significantly limits how the multispectral data can be acquired. We thus choose the third category, one-step inversion methods, for its flexibility with ray distribution. The image reconstruction problem is thus tantamount to the determination of basis images by directly inverting the DD data model in equation (2.19). As the data model is non-linear, we turn to optimization-based reconstruction algorithm to iteratively solve the inversion.

An optimization-based reconstruction method consists of three components, a DD data model, an optimization program, and an algorithm. While the data model has been discussed in Chapter 2, we shall focus on the latter two in this chapter. Particularly, a constrained optimization program is designed. The image total-variation (TV) is used for dealing with challenging data sampling conditions from the novel, non-standard scan configurations of our interest and for its de-noising ability. An algorithm is then established for numerically solving the optimization program, i.e., taking to the designed solution specified by the optimization program. Such trailblazing property of the algorithm will be verified in Chapter 4. In this work where a non-linear, non-convex optimization program is adopted, we rely on the linearization of the data model to guide us in the development of the algorithm. In addition, we stress the importance of parameter selection in the reconstruction, as they can have a significant impact on the reconstruction results. We will discuss the selection of parameters in this work, including convergence conditions that are derived from necessary optimality

conditions.

3.2 Convex optimization program and ASD-POCS algorithm

3.2.1 Optimization program

We first form an optimization program based on the linear DD-data model in equation (2.37) as

$$\begin{aligned} \mathbf{b}^* = \ & \underset{\mathbf{b}}{\operatorname{argmin}}\ \Psi(\mathbf{b}) \\ \text{s. t.} \quad & \frac{||\mathcal{H}\mathbf{b} - \mathbf{g}_{\mathcal{M}}||_2}{||\mathbf{g}_{\mathcal{M}}||_2} \leq \epsilon, \\ & \mathbf{b} \succeq 0, \end{aligned} \tag{3.1}$$

where data constraint parameter $\epsilon > 0$, $\succeq$ denotes the vector-form inequality, which requires all elements of $\mathbf{b}$ to be non-negative, and $||\cdot||_2$ the ℓ_2-norm. The objective function is designed as

$$\Psi(\mathbf{b}) = \sum_k ||\mathbf{b}_k||_{\text{TV}} \tag{3.2}$$

where $||\cdot||_{\text{TV}}$ denotes the image total-variation (TV), defined as the ℓ_1-norm of the gradient magnitude image, i.e., $||\mathbf{b}_k||_{\text{TV}} = ||(|\nabla \mathbf{b}_k|)||_1$, with ∇ denoting the finite-differencing approximation to the gradient and $|\cdot|$ a spatial magnitude operator. The optimization program defined in equation (3.1) is convex, since the objective function is a convex function and both feasible sets defined by the constraints are convex sets.

3.2.2 Reconstruction algorithm

The adaptive-steepest-descent-projection-onto-convex-set (ASD-POCS) algorithm [57] is used to numerically solve the constrained TV-minimization program in equation (3.1). Different than the conventional ASD-POCS algorithm used for the conventional CT reconstruction as reported in the literature [68–73], the ASD-POCS algorithm in this work is adapted to

reconstruct basis image from multiple data sets. A key distinct step is the POCS procedure for lowering the data divergence, which is explicitly written as

$$\mathbf{b}_k^{(n+1)} = \mathbf{b}_k^{(n)} + \gamma^{(n)} \, \bar{\mu}_{jk}^{[s]} \frac{g_{\mathcal{M}j}^{[s]} - \mathbf{a}_j^{[s]\top} \sum_k \bar{\mu}_{jk}^{[s]} \mathbf{b}_k^{(n)}}{\sum_k (\bar{\mu}_{jk}^{[s]})^2 \mathbf{a}_j^{[s]\top} \mathbf{a}_j^{[s]}} \mathbf{a}_j^{[s]}, \tag{3.3}$$

where $\mathbf{a}_j^{[s]}$, a column vector, denotes the jth row of matrix $\mathcal{A}^{[s]}$, $\top$ matrix or vector transpose, and $0 < \gamma^{(n)} < 2$. The pseudo-code for the ASD-POCS algorithm is shown in Algorithm 1.

Algorithm 1 pseudo-code for the ASD-POCS algorithm

Initialize $\mathbf{b}_k^{(0)} \leftarrow 0$
repeat iterations
    - POCS update -
    for $s = 1$ to S **do**
        for $j = 0$ to $J^{[s]} - 1$ **do**
            for $k = 1$ to K **do**
                $\mathbf{b}_k^{(n+1)} = \mathbf{b}_k^{(n)} + \gamma^{(n)} \, \bar{\mu}_{jk}^{[s]} \frac{g_{\mathcal{M}j}^{[s]} - \mathbf{a}_j^{[s]\top} \sum_k \bar{\mu}_{jk}^{[s]} \mathbf{b}_k^{(n)}}{\sum_k (\bar{\mu}_{jk}^{[s]})^2 \mathbf{a}_j^{[s]\top} \mathbf{a}_j^{[s]}} \mathbf{a}_j^{[s]}$
            end for
        end for
    end for
    - TV descent update -
    for $t = 1$ to N_{TV} **do**
        for $k = 1$ to K **do**
            $\mathbf{b}_k^{(n+1)} \leftarrow \mathbf{b}_k^{(n+1)} - \alpha_k^{(n+1)} \nabla_{\mathbf{b}_k} \|\mathbf{b}_k^{(n+1)}\|_{\mathrm{TV}}$
        end for
    end for
until practical convergence conditions are satisfied

The ASD-POCS algorithm based on the linear DD-data model is the pedestal from which the reconstruction algorithm based on the non-linear DD-data model in equation (2.19) is developed.

3.3 Non-convex optimization program and ASD-NC-POCS algorithm

3.3.1 Optimization program

We form another optimization program based on the non-linear DD-data model in equation (2.19) as

$$\begin{aligned} \mathbf{b}^* = \ & \underset{\mathbf{b}}{\text{argmin}}\ \Psi(\mathbf{b}) \\ \text{s.t.} \quad & \Phi(\mathbf{b}; \mathbf{g}_{\mathcal{M}}) \leq \epsilon, \\ & \mathbf{b} \succeq 0. \end{aligned} \tag{3.4}$$

The objective function takes the same form in equation (3.2) as the sum of basis image TV, and the data-fidelity function is designed as

$$\Phi(\mathbf{b}; \mathbf{g}_{\mathcal{M}}) = D(\mathbf{g}(\mathbf{b}), \mathbf{g}_{\mathcal{M}}), \tag{3.5}$$

where $D(\mathbf{x}, \mathbf{y})$ denotes the *data divergence*, often in the form of ℓ_p-norm or Kullback-Leibler (KL) divergence, between vectors $\mathbf{x}$ and $\mathbf{y}$. We consider in this work a normalized ℓ_2-norm of vector difference between model data $\mathbf{g}(\mathbf{b})$ and measured data $\mathbf{g}_{\mathcal{M}}$, i.e.,

$$D(\mathbf{g}(\mathbf{b}), \mathbf{g}_{\mathcal{M}}) \ = \left(\frac{\sum_s ||\mathbf{g}^{[s]}(\mathbf{b}) - \mathbf{g}_{\mathcal{M}}^{[s]}||_2^2}{\sum_s ||\mathbf{g}_{\mathcal{M}}^{[s]}||_2^2} \right)^{1/2}, \tag{3.6}$$

where $\mathbf{g}(\mathbf{b})$ is the non-linearly modeled data as defined in equation (2.33). The data divergence $D(\mathbf{g}(\mathbf{b}), \mathbf{g}_{\mathcal{M}})$ is thus non-convex (NC) due to the non-linearity of the DD-data model. As a result, the feasible set formed by the data divergence constraint is non-convex and so is the constrained optimization program in equations (3.4)-(3.6).

3.3.2 Reconstruction algorithm

In the absence of a mathematically exact solver for the non-convex optimization program, we propose an heuristic algorithm for numerically solving the program.

Linear and non-linear terms of the data model

Recall equations (2.27)-(2.29), where the mass attenuation coefficient is splitted into a zero-order, energy-independent term and another energy-dependent, error term as

$$\mu_{km} = \bar{\mu}_{jk}^{[s]} + \Delta\mu_{jkm}^{[s]}, \tag{3.7}$$

where

$$\bar{\mu}_{jk}^{[s]} = \sum_{m} q_{jm}^{[s]}\, \mu_{km}, \tag{3.8}$$

and

$$\Delta\mu_{jkm}^{[s]} = \mu_{km} - \bar{\mu}_{jk}^{[s]}. \tag{3.9}$$

Recall, consequently, equations (2.30)-(2.32), where the DD-data model are separated into linear and non-linear terms as

$$g_j^{[s]}(\mathbf{b}) = \bar{g}_j^{[s]}(\mathbf{b}) + \Delta g_j^{[s]}(\mathbf{b}), \tag{3.10}$$

where

$$\bar{g}_j^{[s]}(\mathbf{b}) = \sum_{k} \bar{\mu}_{jk}^{[s]} \sum_{i} a_{ji}^{[s]} b_{ki} \tag{3.11}$$

and

$$\Delta g_j^{[s]}(\mathbf{b}) = -\ln \sum_{m} q_{jm}^{[s]} \exp\left(-\sum_{k} \Delta\mu_{jkm}^{[s]} \sum_{i} a_{ji}^{[s]} b_{ki} \right) \tag{3.12}$$

or, in a matrix-vector form for all the rays from the multiple spectral data sets as

$$\mathbf{g}(\mathbf{b}) - \Delta\mathbf{g}(\mathbf{b}) = \mathcal{H}\,\mathbf{b}. \tag{3.13}$$

While equation (3.13) is only a different form of the DD-data model in equation (2.19), it reveals that it is NL term $\Delta\mathbf{g}(\mathbf{b})$ that results in the non-convexity of the data divergence and thus of the optimization program.

A procedure for numerically lowering the non-convex data divergence

In an attempt to facilitate the derivation of the procedure, we first assume that NL term $\Delta\mathbf{g}(\mathbf{b})$ is known and denoted by $\widetilde{\Delta\mathbf{g}}$. Under this condition, the DD-data model in equation (3.13) becomes a linear equation, as

$$\mathbf{g}(\mathbf{b}) - \widetilde{\Delta\mathbf{g}} = \mathcal{H}\mathbf{b}, \tag{3.14}$$

and data divergence $D(\mathcal{H}\mathbf{b}, \mathbf{g}_{\mathcal{M}} - \widetilde{\Delta\mathbf{g}})$ and the optimization program consequently becomes convex, which can then be solved by use of a host of well-established algorithms [57–59], including the ASD-POCS algorithm described in Section 3.2.

The projection-onto-convex-sets (POCS) procedure can be used to lower convex $D(\mathcal{H}\mathbf{b}, \mathbf{g}_{\mathcal{M}} - \widetilde{\Delta\mathbf{g}})$ with the update step

$$\mathbf{b}_k^{(n+1)} = \mathbf{b}_k^{(n)} + \gamma^{(n)}\,\bar{\mu}_{jk}^{[s]} \frac{\left(g_{\mathcal{M}j}^{[s]} - \widetilde{\Delta g}_j^{[s]}\right) - \mathbf{a}_j^{[s]\top} \sum_k \bar{\mu}_{jk}^{[s]} \mathbf{b}_k^{(n)}}{\sum_k (\bar{\mu}_{jk}^{[s]})^2 \mathbf{a}_j^{[s]\top} \mathbf{a}_j^{[s]}} \mathbf{a}_j^{[s]}, \tag{3.15}$$

where $\widetilde{\Delta g}_j^{[s]}$ is the jth element within spectral set s of $\widetilde{\Delta\mathbf{g}}$. Notice that this POCS update step is similar to the one in the ASD-POCS algorithm in equation (3.3), except the measured

data is $\left(g^{[s]}_{\mathcal{M}j} - \widetilde{\Delta g}^{[s]}_j\right)$, instead of only $g^{[s]}_{\mathcal{M}j}$.

Using $\mathbf{b}^{(n)}$ in equation (3.12), one can calculate

$$\Delta g^{[s]}_j(\mathbf{b}^{(n)}) = -\ln \sum_m q^{[s]}_{jm} \exp\left(-\sum_k \Delta\mu^{[s]}_{jkm}\, \mathbf{a}^{[s]\top}_j \mathbf{b}^{(n)}_k\right). \tag{3.16}$$

We then propose to use $\Delta g^{[s]}_j(\mathbf{b}^{(n)})$ as an estimate of $\widetilde{\Delta g}^{[s]}_j$ in equation (3.15), and thus obtain an NC-POCS update step as

$$\mathbf{b}^{(n+1)}_k = \mathbf{b}^{(n)}_k + \gamma^{(n)}\, \bar{\mu}^{[s]}_{jk} \frac{\left[g^{[s]}_{\mathcal{M}j} - \Delta g^{[s]}_j(\mathbf{b}^{(n)}_k)\right] - \mathbf{a}^{[s]\top}_j \sum_k \bar{\mu}^{[s]}_{jk} \mathbf{b}^{(n)}_k}{\sum_k (\bar{\mu}^{[s]}_{jk})^2 \mathbf{a}^{[s]\top}_j \mathbf{a}^{[s]}_j} \mathbf{a}^{[s]}_j, \tag{3.17}$$

which has a form identical to that of the conventional POCS, except for that at iteration n, $\Delta g^{[s]}_j(\mathbf{b}^{(n)})$ is calculated to compensate for the NL effect [116, 119–121].

The ASD-NC-POCS algorithm for the non-convex program

Combining this NC-POCS procedure for lowering $D(\mathbf{g}(\mathbf{b}), \mathbf{g}_{\mathcal{M}})$ with the steepest descent (SD) for lowering the TV objective function, we obtain an *heuristic ASD-NC-POCS algorithm* for numerically solving the non-convex program specified by equations (3.4)-(3.6). Like the conventional ASD-POCS algorithm [57], the ASD-NC-POCS algorithm adaptively lowers the image TV and data divergence by use of the SD and NC-POCS procedures for image reconstruction in multispectral CT. The pseudo-code is shown in Algorithm 2. In a reconstruction, once the practical convergence condition on the data constraint is satisfied, we apply gradient descent steps to lowering data divergence so that other practical convergence conditions can be met rapidly [68]. While there is no proof whether the ASD-NC-POCS algorithm can mathematically solve the non-convex program considered, we devise below its necessary, convergence conditions.

Algorithm 2 pseudo-code for the ASD-NC-POCS algorithm

Initialize $\mathbf{b}_k^{(0)} \leftarrow 0$, $\hat{\mathbf{g}}^{(0)} \leftarrow \mathbf{g}_{\mathcal{M}}$
repeat iterations
    - POCS update -
    for $s = 1$ to S **do**
        for $j = 0$ to $J^{[s]} - 1$ **do**
            for $k = 1$ to K **do**
                $$\mathbf{b}_k^{(n+1)} = \mathbf{b}_k^{(n)} + \gamma^{(n)} \bar{\mu}_{jk}^{[s]} \frac{\hat{g}_j^{[s](n)} - \mathbf{a}_j^{[s]\top} \sum_k \bar{\mu}_{jk}^{[s]} \mathbf{b}_k^{(n)}}{\sum_k (\bar{\mu}_{jk}^{[s]})^2 \mathbf{a}_j^{[s]\top} \mathbf{a}_j^{[s]}} \mathbf{a}_j^{[s]}$$
            end for
        end for
    end for
    - TV descent update -
    for $t = 1$ to N_{TV} **do**
        for $k = 1$ to K **do**
            $\mathbf{b}_k^{(n+1)} \leftarrow \mathbf{b}_k^{(n+1)} - \alpha_k^{(n+1)} \nabla_{\mathbf{b}_k} \| \mathbf{b}_k^{(n+1)} \|_{\mathrm{TV}}$
        end for
    end for
    - NL term update step -
    for $s = 1$ to S **do**
        for $j = 0$ to $J^{[s]} - 1$ **do**
            $$\Delta g_j^{[s](n+1)} = -\ln \sum_m q_{jm}^{[s]} \exp\left(-\sum_k \Delta \mu_{jkm}^{[s]} \, \mathbf{a}_j^{[s]\top} \mathbf{b}_k^{(n+1)} \right)$$
            $\hat{g}_j^{[s](n+1)} \leftarrow g_{\mathcal{M}j}^{[s]} - \Delta g_j^{[s](n+1)}$
        end for
    end for
until practical convergence conditions are satisfied

3.4 Reconstruction parameters

There are two types of parameters involved in an optimization-based image reconstruction, which are referred to as *program* and *algorithm* parameters in the work. The former specify the optimization program in equation (3.4), including image voxel, spectra $\mathbf{q}_j^{[s]}$, system matrices $\mathcal{A}^{[s]}$, and parameter ϵ. Different choices of program parameters necessarily lead to different optimization programs and thus different designed solutions. In this work, we focus on the investigation of ϵ that impacts dominantly the reconstruction, while selecting image voxel, $\mathbf{q}_i^{[s]}$, and $\mathcal{A}^{[s]}$ similar to those used in practical applications. The algorithm parameters such as $\gamma^{(n)}$, N_{TV}, and $\alpha_k(n)$ control the algorithm path leading to the designed solution, including those in Algorithm 2. While they have no effect on the designed solutions, they can impact the numerical reconstructions especially for a non-convex program. In this study, we use the same algorithm parameters as those used in the conventional ASD-POCS algorithm [57].

We consider three necessary, mathematical convergence conditions for the ASD-NC-POCS algorithm:

$$\bar{D}(\mathbf{b}^{(n)}) = \frac{\left| D(\mathbf{g}(\mathbf{b}^{(n)}, \mathbf{g}_{\mathcal{M}}) - \epsilon \right|}{\epsilon} \to 0 \tag{3.18}$$

$$\bar{\Delta}\Psi(\mathbf{b}^{(n)}) = \frac{\left| \Psi(\mathbf{b}^{(n+1)}) - \Psi(\mathbf{b}^{(n)}) \right|}{\left| \Psi(\mathbf{b}^{(n+1)}) + \Psi(\mathbf{b}^{(n)}) \right|} \to 0 \tag{3.19}$$

$$c_\alpha(\mathbf{b}^{(n)}) = \hat{\mathbf{d}}_{\text{data}}^{\top}(\mathbf{b}^{(n)})\, \hat{\mathbf{d}}_{\text{TV}}(\mathbf{b}^{(n)}) \to -1, \tag{3.20}$$

as iteration number $n \to \infty$, where unit vectors $\hat{\mathbf{d}}_{\text{data}}(\mathbf{b}^{(n)})$ and $\hat{\mathbf{d}}_{\text{TV}}(\mathbf{b}^{(n)})$ are defined in Section 3.5 [57]. The second condition is for the optimality of the objective function, whereas the other two are the local optimality conditions, i.e., the Karush-Kuhn-Tucker (KKT) conditions [122] as shown in Section 3.5. While the mathematical convergence conditions cannot be met in practical reconstructions, they are used to devise practical convergence

conditions for each individual study in this work.

3.5 Optimality condition

Using equation (2.14), we can obtain monochromatic energy images as $\mathbf{f}_n = \sum_k \mu_{kn}\mathbf{b}_k$ at N energies, where $n = 1, 2, \cdots, N$. Lower- or upper-bound constraints on the monochromatic energy images can be written as

$$\sum_k \tilde{\mu}_{kn}\mathbf{b}_k + p_n \preceq 0 \qquad \text{for } n = 1, 2, \cdots, N, \tag{3.21}$$

where p_n is a scalar for specifying the upper or lower bound of the nth monochromatic image, and $\tilde{\mu}_{kn} = \pm\mu_{kn}$ with the negative sign used to impose a lower bound of image values, or simply non-negativity, on the monochromatic images. We can rewrite equation (3.21) in a linear form of $\mathbf{b}$ as

$$\mathcal{Q}_n\mathbf{b} + \mathbf{p}_n \preceq 0 \qquad \text{for } n = 1, 2, \cdots, N, \tag{3.22}$$

where

$$\begin{aligned} \mathcal{Q}_n &= (\tilde{\mu}_{1n}\mathcal{I}, \tilde{\mu}_{2n}\mathcal{I}, \cdots, \tilde{\mu}_{Kn}\mathcal{I}), \\ \mathbf{p}_n &= (p_n, p_n, \cdots)^\top, \end{aligned} \tag{3.23}$$

and $\mathcal{I}$ denotes the identity matrix of size $I \times I$.

We now consider an optimization program in the form of

$$\begin{aligned} \mathbf{b}^* = \ & \arg\min_{\mathbf{b}} \ \Psi(\mathbf{b}) \\ \text{s.t.} \ & \Phi^2(\mathbf{b}; \mathbf{g}_{\mathcal{M}}) \leq \epsilon^2, \\ & \mathcal{Q}_n\mathbf{b} + \mathbf{p}_n \preceq 0 \qquad \text{for } n = 1, 2, \cdots, N. \end{aligned} \tag{3.24}$$

and derive its first-order optimality conditions, i.e., the Karush-Kuhn-Tucker (KKT) conditions. It can easily be shown that the optimzation programs in equations (3.24) and (3.4)

are equivalent when $N = K$, $p_n = 0$, and $\tilde{\mu}_{kn} = -1$ for $k = n$ (0 otherwise). Therefore, the derived KKT conditions for the former are applicable to the latter.

The Lagrangian of the optimization problem above is given as

$$L(\mathbf{b}, \nu, \{\boldsymbol{\lambda}_n\}) = \Psi(\mathbf{b}) + \nu(\Phi^2(\mathbf{b}) - \epsilon^2) + \sum_n \boldsymbol{\lambda}_n^\top (\mathcal{Q}_n \mathbf{b} + \mathbf{p}_n), \tag{3.25}$$

where scalar ν and vectors $\{\boldsymbol{\lambda}_n\}$ are the Lagrangian multipliers. The KKT conditions can thus be expressed as

$$\Phi^2(\mathbf{b}^*) \leq \epsilon^2, \tag{3.26a}$$

$$\mathcal{Q}_n \mathbf{b}^* + \mathbf{p}_n \preceq 0,\ n = 1, 2, \cdots, N, \tag{3.26b}$$

$$\nu^* \geq 0, \tag{3.26c}$$

$$\boldsymbol{\lambda}_n^* \succeq 0,\ n = 1, 2, \cdots, N, \tag{3.26d}$$

$$\nabla_{\mathbf{b}} L(\mathbf{b}^*, \nu^*, \{\boldsymbol{\lambda}_n^*\}) = \nabla_{\mathbf{b}} \Psi(\mathbf{b}^*) + \nu^* \nabla_{\mathbf{b}} \Phi^2(\mathbf{b}^*) + \sum_n \mathcal{Q}_n^\top \boldsymbol{\lambda}_n^* = 0, \tag{3.26e}$$

$$\nu^*(\Phi^2(\mathbf{b}^*) - \epsilon^2) = 0, \tag{3.26f}$$

$$\boldsymbol{\lambda}_n^{*\top}(\mathcal{Q}_n \mathbf{b}^* + \mathbf{p}_n) = 0,\ n = 1, 2, \cdots, N \tag{3.26g}$$

where $\mathbf{b}^*$ and $(\nu^*, \{\boldsymbol{\lambda}_n^*\})$ are optimal variables and Lagrangian multipliers for the optimization problem. With the introduction of the linear format of the constraints on the monochromatic images and the Lagrangian multipliers, we summarize in Table 3.1 the additional symbols and their dimensions, in order to improve the readability of the following derivation.

Given the specific form $\mathcal{Q}_n$ takes in equation (3.23), the last part of the gradient of the

Table 3.1: Dimensions and representations of additional symbols introduced

symbol		dimension	representation
$\mathbf{b}_k$	vector	$I \times 1$	basis image of the kth material
$\mathbf{b}$	vector	$(K \times I) \times 1$	aggregate basis image of all materials
$\tilde{\mu}_{kn}$	scalar		expansion coefficients for the nth monochromatic images
$\mathcal{Q}_n$	matrix	$I \times (K \times I)$	matrix for the nth linear constraint
$\mathbf{p}_n$	vector	$I \times 1$	upper or lower bound for the nth linear constraint on the monochromatic image
ν	scalar		Lagrangian multiplier for the data constraint
$\boldsymbol{\lambda}_n$	vector	$I \times 1$	Lagrangian multipliers for the nth linear constraint

Lagrangian in equation (3.26e) can be simplified to

$$\sum_n \mathcal{Q}_n^\top \boldsymbol{\lambda}_n^* = \sum_n \begin{pmatrix} \tilde{\mu}_{1n}\mathcal{I} \\ \tilde{\mu}_{2n}\mathcal{I} \\ \vdots \\ \tilde{\mu}_{Kn}\mathcal{I} \end{pmatrix} \boldsymbol{\lambda}_n^* = \begin{pmatrix} \sum_n \tilde{\mu}_{1n}\boldsymbol{\lambda}_n^* \\ \sum_n \tilde{\mu}_{2n}\boldsymbol{\lambda}_n^* \\ \vdots \\ \sum_n \tilde{\mu}_{Kn}\boldsymbol{\lambda}_n^* \end{pmatrix}. \tag{3.27}$$

In general, for non-zero $\tilde{\mu}_{kn}$, equation (3.27) has zero entries wherever all $\{\boldsymbol{\lambda}_n^*\}$ have zeros at the same entries. Based on this observation, we turn to the complementary slackness in (3.26g), which follows

$$\begin{cases} \lambda_{ni}^* = 0 & \text{if } (\mathcal{Q}_n\mathbf{b}^*)_i + p_n > 0, \\ \lambda_{ni}^* > 0 & \text{if } (\mathcal{Q}_n\mathbf{b}^*)_i + p_n = 0, \end{cases} \tag{3.28}$$

for $i \in \{0, \cdots, I-1\}$. We use a vector $\mathbb{1}_n(\mathbf{b})$ of size I to denote an identity function, whose elements are

$$\mathbb{1}_n(\mathbf{b})_i = \begin{cases} 1 & \text{if } (\mathcal{Q}_n\mathbf{b})_i + p_n > 0, \\ 0 & \text{if } (\mathcal{Q}_n\mathbf{b})_i + p_n = 0, \end{cases} \tag{3.29}$$

and diag($\mathbf{x}$) a function that yields a diagonal matrix with the elements of vector $\mathbf{x}$ placed along the diagonal line, as

$$\text{diag}(\mathbf{x}) = \begin{pmatrix} x_0 & & & & \\ & \ddots & & & \\ & & x_i & & \\ & & & \ddots & \\ & & & & x_{I-1} \end{pmatrix}. \tag{3.30}$$

Consequently, considering all N constraints, we construct a matrix as the product of N diagonal matrices

$$\mathcal{D}(\mathbf{b}^*) = \prod_{n=1}^{N} \text{diag}(\mathbb{1}_n(\mathbf{b}^*)). \tag{3.31}$$

As a result, $\mathcal{D}(\mathbf{b}^*)$ is also diagonal of size I and it picks out those image pixels at which location the N linear constraints in equation (3.21) or (3.22) are strictly satisfied simultaneously. Finally, we use K identical $\mathcal{D}(\mathbf{b}^*)$ and place them in a diagonal line to form a bigger diagonal matrix $\mathcal{D}'(\mathbf{b}^*)$ of size $K \times I$ as

$$\mathcal{D}'(\mathbf{b}^*) = \begin{pmatrix} \mathcal{D}(\mathbf{b}^*) & & \\ & \ddots & \\ & & \mathcal{D}(\mathbf{b}^*) \end{pmatrix}. \tag{3.32}$$

Left-multiplying $\mathcal{D}'(\mathbf{b}^*)$ to both sides of equations (3.27) yields

$$\begin{aligned}
\mathcal{D}'(\mathbf{b}^*)\sum_n \mathcal{Q}_n^\top \boldsymbol{\lambda}_n^* &= \begin{pmatrix} \mathcal{D}(\mathbf{b}^*) & & \\ & \ddots & \\ & & \mathcal{D}(\mathbf{b}^*) \end{pmatrix} \begin{pmatrix} \sum_n \tilde{\mu}_{1n}\boldsymbol{\lambda}_n^* \\ \sum_n \tilde{\mu}_{2n}\boldsymbol{\lambda}_n^* \\ \vdots \\ \sum_n \tilde{\mu}_{Kn}\boldsymbol{\lambda}_n^* \end{pmatrix} \\
&= \begin{pmatrix} \mathcal{D}(\mathbf{b}^*)\sum_n \tilde{\mu}_{1n}\boldsymbol{\lambda}_n^* \\ \mathcal{D}(\mathbf{b}^*)\sum_n \tilde{\mu}_{2n}\boldsymbol{\lambda}_n^* \\ \vdots \\ \mathcal{D}(\mathbf{b}^*)\sum_n \tilde{\mu}_{Kn}\boldsymbol{\lambda}_n^* \end{pmatrix} \\
&= 0,
\end{aligned} \tag{3.33}$$

where, according to equations (3.28)-(3.31), the non-zero entries in $\mathcal{D}(\mathbf{b}^*)$ should match exactly with the zero entries in $\sum_n \tilde{\mu}_{kn}\boldsymbol{\lambda}_n^*$.

We can now simplify the first order optimality condition in equation (3.26e) as

$$\mathbf{d}_{\mathrm{TV}}(\mathbf{b}^*) + \mathbf{d}_{\mathrm{data}}(\mathbf{b}^*) = 0, \tag{3.34}$$

where

$$\mathbf{d}_{\mathrm{TV}}(\mathbf{b}^*) = \mathcal{D}'(\mathbf{b}^*)\nabla_{\mathbf{b}}\Psi(\mathbf{b}^*),$$

and

$$\mathbf{d}_{\mathrm{data}}(\mathbf{b}^*) = \nu^*\ \mathcal{D}'(\mathbf{b}^*)\nabla_{\mathbf{b}}\Phi^2(\mathbf{b}^*).$$

Now equation (3.26c) states that ν^* is non-negative (dual feasibility), and the complementary slackness in (3.26f) states that ν^* can only be zero when the data fidelity constraint is not

active. For practical solutions that are non-trivial, i.e., other than non-negative flat images, the data fidelity constraint shall always be active. Therefore, it is desired that $\nu^* > 0$ in practical situations, which leads to that $\mathbf{d}_{\mathrm{TV}}(\mathbf{b}^*)$ and $\mathbf{d}_{\mathrm{data}}(\mathbf{b}^*)$ shall be oppositely co-linear, or

$$c_\alpha \equiv \hat{\mathbf{d}}_{\mathrm{TV}}^{\top}(\mathbf{b}^*)\, \hat{\mathbf{d}}_{\mathrm{data}}(\mathbf{b}^*) = -1, \tag{3.35}$$

where

$$\hat{\mathbf{d}}_{\mathrm{TV}}(\mathbf{b}^*) = \frac{\mathbf{d}_{\mathrm{TV}}(\mathbf{b}^*)}{|\mathbf{d}_{\mathrm{TV}}(\mathbf{b}^*)|}$$

and

$$\hat{\mathbf{d}}_{\mathrm{data}}(\mathbf{b}^*) = \frac{\mathbf{d}_{\mathrm{data}}(\mathbf{b}^*)}{|\mathbf{d}_{\mathrm{data}}(\mathbf{b}^*)|}$$

are the normalized vectors.

For computing $\mathbf{d}_{\mathrm{TV}}(\mathbf{b}^*)$, where $\Psi(\mathbf{b})$ is defined in equaton (3.2) as the sum of basis image TV, it can be divided into the computation of TV gradients of each basis image, as

$$\nabla_{\mathbf{b}} \Psi(\mathbf{b}^*) = \sum_k \nabla_{\mathbf{b}} ||\mathbf{b}_k^*||_{\mathrm{TV}}, \tag{3.36}$$

where

$$\nabla_{\mathbf{b}} ||\mathbf{b}_k^*||_{\mathrm{TV}} = \begin{cases} \nabla_{b_i} ||\mathbf{b}_k^*||_{\mathrm{TV}} & \text{if } b_i \in \mathbf{b}_k, \\ 0 & \text{if } b_i \notin \mathbf{b}_k. \end{cases}$$

As the ℓ_1-norm function is non-smooth, TV gradients, or $\nabla_{\mathbf{b}_k} ||\mathbf{b}_k^*||_{\mathrm{TV}}$, are computed based on an approximation of a smoothed version [74].

On the other hand, for computing $\mathbf{d}_{\mathrm{data}}(\mathbf{b}^*)$, we have

$$\begin{aligned} \Phi^2(\mathbf{b}) &= (||\mathbf{g}_{\mathcal{M}}||_2)^{-1} \, ||\mathbf{g}(\mathbf{b}) - \mathbf{g}_{\mathcal{M}}||_2^2 \\ &= \left(\mathbf{g}_{\mathcal{M}}^{\top} \mathbf{g}_{\mathcal{M}}\right)^{-1} (\mathbf{g}(\mathbf{b}) - \mathbf{g}_{\mathcal{M}})^{\top} (\mathbf{g}(\mathbf{b}) - \mathbf{g}_{\mathcal{M}}). \end{aligned} \tag{3.37}$$

Taking its gradient yields

$$\nabla_{\mathbf{b}}\Phi^2(\mathbf{b}) = 2\left(\mathbf{g}_{\mathcal{M}}^{\top}\mathbf{g}_{\mathcal{M}}\right)^{-1} J(\mathbf{g}(\mathbf{b}),\mathbf{b})(\mathbf{g}(\mathbf{b})-\mathbf{g}_{\mathcal{M}}), \tag{3.38}$$

where the Jacobian matrix $J(\mathbf{y}(\mathbf{x}),\mathbf{x})$ is given by

$$\begin{aligned} J(\mathbf{y}(\mathbf{x}),\mathbf{x}) &= \begin{pmatrix} \nabla_{\mathbf{x}} y(\mathbf{x})_1, & \nabla_{\mathbf{x}} y(\mathbf{x})_2, & \cdots \end{pmatrix} \\ &= \begin{pmatrix} \dfrac{\partial y(\mathbf{x})_1}{\partial x_1}, & \dfrac{\partial y(\mathbf{x})_2}{\partial x_1}, & \cdots \\ \dfrac{\partial y(\mathbf{x})_1}{\partial x_2}, & \dfrac{\partial y(\mathbf{x})_2}{\partial x_2}, & \cdots \\ \vdots & \vdots & \ddots \end{pmatrix}, \end{aligned} \tag{3.39}$$

where $y(\mathbf{x})_j$ and x_i are the j-th and i-th elements of vectors $\mathbf{y}(\mathbf{x})$ and $\mathbf{x}$, respectively. Given the concatenated form of the aggregate basis image vector as $\mathbf{b} = (\mathbf{b}_1^{\top}, \mathbf{b}_2^{\top}, \cdots, \mathbf{b}_K^{\top})^{\top}$ and the dimension of vector $\mathbf{g}(\mathbf{b})$ being $J' \equiv \sum_s J^{[s]}$ (recall from Section 2.3 that $J^{[s]}$ is the size of data vector $\mathbf{g}^{[s]}(\mathbf{b})$ for spectral set s), the Jacobian in equation (3.38) can be re-expressed as

$$J(\mathbf{g}(\mathbf{b}),\mathbf{b}) = \begin{pmatrix} \nabla_{\mathbf{b}_1} g(\mathbf{b})_0, & \nabla_{\mathbf{b}_1} g(\mathbf{b})_1, & \cdots & \nabla_{\mathbf{b}_1} g(\mathbf{b})_{J'-1} \\ \nabla_{\mathbf{b}_2} g(\mathbf{b})_0, & \nabla_{\mathbf{b}_2} g(\mathbf{b})_1, & \cdots & \nabla_{\mathbf{b}_2} g(\mathbf{b})_{J'-1} \\ \vdots & \vdots & \ddots & \vdots \\ \nabla_{\mathbf{b}_K} g(\mathbf{b})_0, & \nabla_{\mathbf{b}_K} g(\mathbf{b})_1, & \cdots & \nabla_{\mathbf{b}_K} g(\mathbf{b})_{J'-1} \end{pmatrix}. \tag{3.40}$$

Recall equation (2.19), where the element of data vector $\mathbf{g}(\mathbf{b})$ is indexed by the spectral set index s and ray index j. In this derivation, instead, a single index j' is used for the aggregate data vector $\mathbf{g}(\mathbf{b})$, as $j' = j + (s-1) * J^{[s-1]}$ and

$$g_{j'}(\mathbf{b}) = g_j^{[s]}(\mathbf{b}) = -\ln \sum_m q_{jm}^{[s]} \exp\left(-\sum_k \mu_{km}\, \mathbf{a}_j^{[s]\top} \mathbf{b}_k\right), \tag{3.41}$$

As a result, the gradient of $g_{j'}(\mathbf{b})$ w.r.t. basis image $\mathbf{b}_k$ can be written as

$$\nabla_{\mathbf{b}_k} g_{j'}(\mathbf{b}) = \left(\sum_m t_{j'm} \right)^{-1} \left(\sum_m \mu_{km} t_{j'm} \right) \mathbf{a}_{j'}, \tag{3.42}$$

where

$$\begin{aligned} t_{j'm} &= q_{jm}^{[s]} \exp\left(- \sum_k \mu_{km} \, \mathbf{a}_j^{[s]\top} \mathbf{b}_k \right) \\ \mathbf{a}_{j'} &= \mathbf{a}_j^{[s]} \end{aligned} \tag{3.43}$$

Finally, replacing equations (3.40) and (3.42) into (3.38) yields

$$
\begin{aligned}
&\nabla_{\mathbf{b}}\Phi^2(\mathbf{b}) \\
=&2\left(\mathbf{g}_{\mathcal{M}}^{\top}\mathbf{g}_{\mathcal{M}}\right)^{-1} J(\mathbf{g}(\mathbf{b}),\mathbf{b})(\mathbf{g}(\mathbf{b})-\mathbf{g}_{\mathcal{M}}) \\
=&\frac{2}{\mathbf{g}_{\mathcal{M}}^{\top}\mathbf{g}_{\mathcal{M}}}
\begin{pmatrix}
\nabla_{\mathbf{b}_1} g(\mathbf{b})_0, & \nabla_{\mathbf{b}_1} g(\mathbf{b})_1, & \cdots & \nabla_{\mathbf{b}_1} g(\mathbf{b})_{J'-1} \\
\nabla_{\mathbf{b}_2} g(\mathbf{b})_0, & \nabla_{\mathbf{b}_2} g(\mathbf{b})_1, & \cdots & \nabla_{\mathbf{b}_2} g(\mathbf{b})_{J'-1} \\
\vdots & \vdots & \ddots & \vdots \\
\nabla_{\mathbf{b}_K} g(\mathbf{b})_0, & \nabla_{\mathbf{b}_K} g(\mathbf{b})_1, & \cdots & \nabla_{\mathbf{b}_K} g(\mathbf{b})_{J'-1}
\end{pmatrix}
\begin{pmatrix}
g_0(\mathbf{b}) - g_{\mathcal{M}0} \\
g_1(\mathbf{b}) - g_{\mathcal{M}1} \\
\vdots \\
g_{J'-1}(\mathbf{b}) - g_{\mathcal{M}(J'-1)}
\end{pmatrix} \\
=&\frac{2}{\mathbf{g}_{\mathcal{M}}^{\top}\mathbf{g}_{\mathcal{M}}}
\begin{pmatrix}
\sum_{j'} (g_{j'}(\mathbf{b}) - g_{\mathcal{M}j'}) \nabla_{\mathbf{b}_1} g_{j'} \\
\sum_{j'} (g_{j'}(\mathbf{b}) - g_{\mathcal{M}j'}) \nabla_{\mathbf{b}_2} g_{j'} \\
\vdots \\
\sum_{j'} (g_{j'}(\mathbf{b}) - g_{\mathcal{M}j'}) \nabla_{\mathbf{b}_K} g_{j'}
\end{pmatrix} \\
=&\frac{2}{\mathbf{g}_{\mathcal{M}}^{\top}\mathbf{g}_{\mathcal{M}}}
\begin{pmatrix}
\sum_{j'} \dfrac{(g_{j'}(\mathbf{b}) - g_{\mathcal{M}j'}) \sum_m \mu'_{1m} t_{j'm}}{\sum_m t_{j'm}} \mathbf{a}_{j'} \\
\sum_{j'} \dfrac{(g_{j'}(\mathbf{b}) - g_{\mathcal{M}j'}) \sum_m \mu'_{2m} t_{j'm}}{\sum_m t_{j'm}} \mathbf{a}_{j'} \\
\vdots \\
\sum_{j'} \dfrac{(g_{j'}(\mathbf{b}) - g_{\mathcal{M}j'}) \sum_m \mu'_{Km} t_{j'm}}{\sum_m t_{j'm}} \mathbf{a}_{j'}
\end{pmatrix}.
\end{aligned}
\tag{3.44}
$$

3.6 Discussion

In this chapter, we have developed an optimization-based reconstruction method including a non-convex optimization program, a heuristic algorithm, ASD-NC-POCS, for numerically solving the optimization program, and convergence conditions for the algorithm. First-order optimality conditions for constrained optimization programs, i.e., KKT conditions, were derived for the non-convex programs proposed in this work and are used as the necessary condition for achieving local optimality of the problem. The algorithm was based on the conventional ASD-POCS algorithm solving a convex optimization program, which was also introduced here and will be used in the verification study in Chapter 4.

Different optimization programs can lead to different reconstructions especially in the presence of data inconsistencies. In the proposed reconstruction program, the data divergence term takes the form of ℓ_2-norm. It would be worthwhile to investigate and prototype optimization programs of different forms, for example containing the Kullback-Leibler (KL) and other data divergences [58, 62, 123]. Further, different constrained or unconstrained optimization program designs can be investigated, such as minimizing data divergence, subject to a TV constraint. An advantage of having TV as a constraint, rather than the objective function, is the flexibility to specifically set the TV constraint parameter, which has a direct impact on the image visualization.

CHAPTER 4

VERIFICATION STUDY

4.1 Introduction

A verification study is a simulation study where consistent data are generated and used for the reconstruction. The "consistency" of the data refers to the fact that the forward model used to generate the data is exactly the same as the data model used in the optimization-based reconstruction. Verification studies are employed to verify the computer implementation of the method and to check the numerical convergence of the inversion algorithm.

In the development of conventional CT reconstruction based on linear data models, the verification study is often referred to as the inverse-crime study [70,71,124,125]. With a linear DD-data model, the data is generated by left-multiplying the system matrix, representing an X-ray transform, to the truth image vector, representing a numerical phantom. An appropriate design of an optimization program and its associated algorithm, together with a faithful implementation of the algorithm, should lead to an exact recovery (only within computer precision) of the truth image. As the truth image is known in the inverse-crime study, the appropriate design of the reconstruction and the algorithm, in other words, the numerical convergence of the algorithm, and the correct computer implementation of the algorithm can be verified by explicitly checking if the exact recovery condition is met. It should be noted that, for an algorithm with a proof for the mathematical convergence, such as gradient descent (GD) and maximum likelihood expectation maximization (ML-EM), only the computer implementation part is checked in the inverse-crime study. For heuristic algorithms such as the conventional ASD-POCS, the numerical convergence of the algorithm and the implementation are checked together in the inverse-crime study.

In this work, we focus on the ASD-NC-POCS algorithm for the multispectral CT reconstruction based on a non-linear model. While there is no proof for the mathematical

convergence of the algorithm, we demonstrate the numerical convergence, altogether with the computer implementation, in the verification study where consistent data are used. Furthermore, because the ASD-NC-POCS algorithm is developed based on the conventional ASD-POCS algorithm with a linear data model, we break up the verification study into two stages. The first stage is essentially an inverse-crime study, where the linear data model, as indicated by equation (2.31), is used to generate the consistent data and assumed to be the data model in the reconstruction. Basis images are then reconstructed from the consistent data and compared to the numerical truth. Most of the implementation of the ASD-NC-POCS algorithm, i.e., the ASD-POCS algorithm in Algorithm 1, except for the NL update step, is checked in this first stage of the verification study. After the first stage is completed, the second stage of the verification study is carried out, as data are generated with the full-scale DD-data model in equation (2.19) and are reconstructed from using the ASD-NC-POCS algorithm as described in Algorithm 2. The numerical convergence of the algorithm, as well as the implementation of the NC update step, can be verified as an exact recovery of the truth numerical basis images is expected.

It shall be noted that the two stages of the verification study in this work are not redundant compared to the inverse crime studies that have been investigated in the literatures for the conventional ASD-POCS algorithm [70–72]. First, even with a linear data model in the first stage, the ASD-POCS algorithm used in this work reconstructs basis images, instead of linear attenuation coefficient images in conventional CT, which lead to different implementations of the algorithm. Second, for the second stage, the non-linear modeling is employed in both the data generation and image reconstruction, which results in a different algorithm, ASD-NC-POCS, with a distinct NL update step. Therefore, the verification study is necessary, despite that inverse crime studies have been investigated in the literature.

Finally, the verification study with consistent data can provide a performance upper-bound for the reconstruction method or the scan configuration of interest. Although the

consistent data is ideal and unrealistic, which can sometimes yield "excessively optimistic expectations about the performance" [125], it is not unreasonable to assume that, if a reconstruction program and its associated algorithm fail to perform in the verification study, i.e., not having an exact recovery, it is unlikely that they would perform well in studies in which data contain inconsistencies, such as in real data cases. As a result, verification studies are used to guide the design of the optimization program and the scan configurations for multispectral data.

4.2 Inverse-crime study with a linear data model

We first carry out an inverse-crime study with a linear DD-data model. A convex, constrained TV-minimization problem is formed as the image reconstruction and the ASD-POCS algorithm is used to reconstruct basis images from the consistent data. Despite that there has been extensive studies in the literature for the conventional ASD-POCS algorithm and its numerical convergence in conventional CT reconstruction, a different implementation of the algorithm with multiple basis images and X-ray transforms in the system matrix is used here, as shown in Algorithm 1. Thus, we use the inverse-crime study to check the implementation of the ASD-POCS algorithm, based on which the ASD-NC-POCS algorithm is developed and implemented.

4.2.1 Study design

Data generation

A *full-scan* configuration is used in the inverse-crime study to provide sufficient angular sampling condition. In this fan-beam configuration over a circular trajectory, as shown in Fig. 4.1, low (thin, blue line) and high (thick, red line) KVp scans cover a full rotation each, with 300 overlapping views distributed evenly over 2π. The physical dimensions simulate

those in a standard diagnostic CT, and are summarized in Table. 4.1. As a result, the discrete data size of the low or high KVp scan is $J^{[1]} = J^{[2]} = 300 \times 224$.

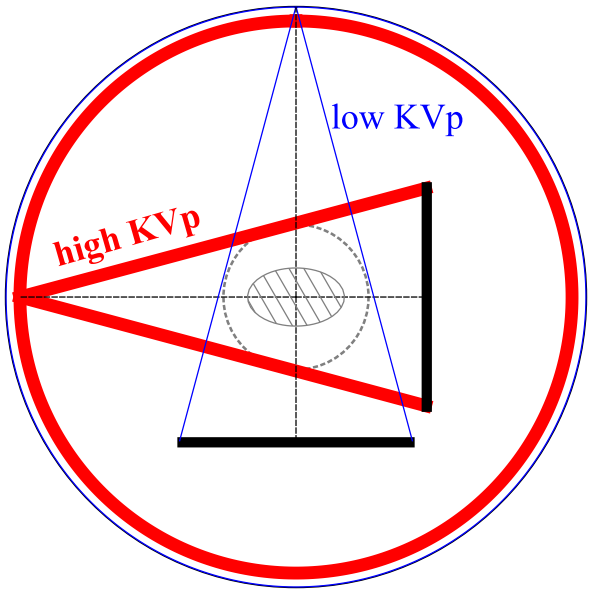

Figure 4.1: Full-scan configuration in which low (thin, blue line) and high (thick, red line) KVp scans are performed over a full rotation of 2π each.

Table 4.1: Physical dimensions of the scan configuration used in the inverse-crime study.

Physical quantity	dimension
source-to-detector distance	1072 mm
source-to-center-of-rotation distance	600 mm
detector length	920 mm
detector bin size	4.1 mm
detector bin samples	224
number of views	300

Two ($S = 2$) spectral data sets are collected with low ($s = 1$) and high ($s = 2$) spectra at 80 and 135 KVp. The incident spectra are multiplied with the detector energy response, which is modeled as a linear energy-integrating response, followed by a normalization to yield the X-ray spectrum, denoted by $q_m^{[s]}$. Note that no bow-tie filter is modeled so the X-ray spectrum is not ray-dependent. We plot the normalized discrete X-ray spectra in Fig. 4.2

with $\Delta_E = 1$ (KeV), where the spectral separation between the low (thin, blue line) and high (thick, red line) spectra are visible.

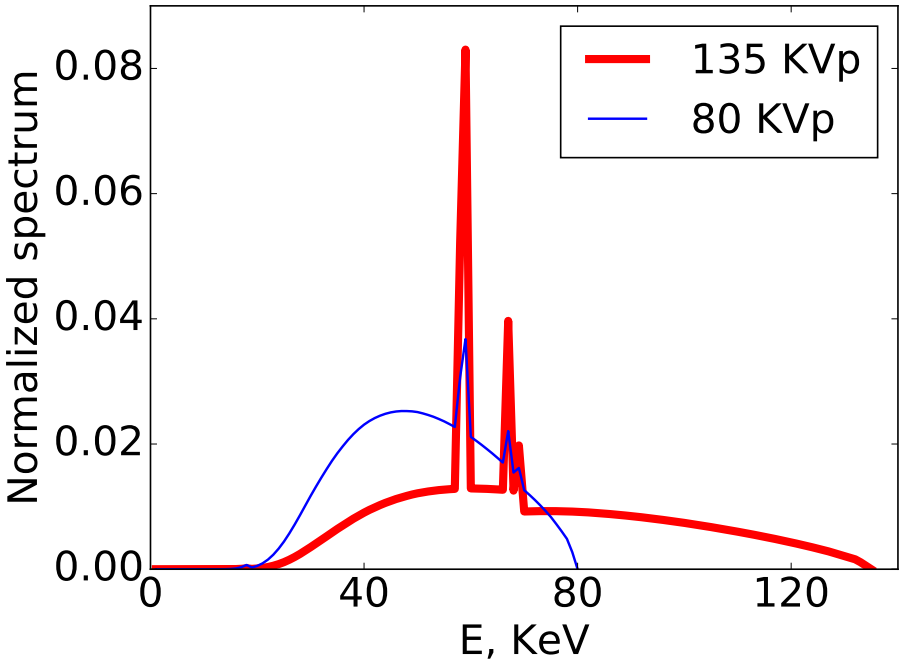

Figure 4.2: Normalized X-ray spectrum $q_m^{[s]}$, as a product of the incident beam spectrum and the linear energy-integrating detector response. Low (thin, blue line) and high (thick, red line) energy spectra at 80 and 135 KVp are used in the inverse-crime study.

A two-material ($K = 2$) basis decomposition model with water ($k = 1$) and bone ($k = 2$) is used. A numerical contrast-insert phantom, as shown in Fig. 4.3, is decomposed into water and bone basis images, as shown in the top row of Fig. 4.5. Both basis images are represented on an array of size $I = 128 \times 128$ with square pixels of size 2.73 mm. Note that it is the basis images that are the truth in the inverse-crime study from which the consistent data are generated, as to make sure no decomposition error is included.

Finally, considering the scan configuration, spectra, and truth basis images as described above, we generate consistent data by use of the linear DD-data model in equation (2.36) as

$$g_j^{[s]}(\mathbf{b}) = \sum_k \bar{\mu}_k^{[s]} \sum_i a_{ji}^{[s]} b_{ki}, \tag{4.1}$$

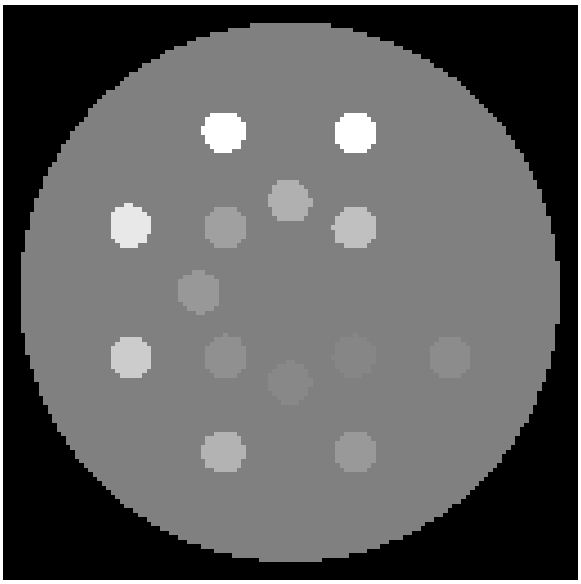

Figure 4.3: Monochromatic image at 80 KeV for the numerical contrast-insert phantom, from which the truth basis images are decomposed and used to generate data in the inverse-crime study. Display window: [-1000, 1000] HU

where $\bar{\mu}_k^{[s]} = \sum_m q_m^{[s]} \mu_{km}$ is not ray-dependent, just as the X-ray spectrum $q_m^{[s]}$. Alternatively, the linear data model can be expressed in an explicit matrix-vector form of equation (2.37) as

$$\begin{pmatrix} \mathbf{g}^{[1]}(\mathbf{b}) \\ \mathbf{g}^{[2]}(\mathbf{b}) \end{pmatrix} = \begin{pmatrix} \bar{\mu}_1^{[1]} \mathcal{A}^{[1]} & \bar{\mu}_2^{[1]} \mathcal{A}^{[1]} \\ \bar{\mu}_2^{[2]} \mathcal{A}^{[2]} & \bar{\mu}_2^{[2]} \mathcal{A}^{[2]} \end{pmatrix} \begin{pmatrix} \mathbf{b}_1 \\ \mathbf{b}_2 \end{pmatrix}, \tag{4.2}$$

where $\mathbf{b}^\top = (\mathbf{b}_1^\top, \mathbf{b}_2^\top)$. Note that, when the X-ray spectrum $q_m^{[s]}$, and consequently the energy-independent term of the mass attenuation coefficient $\bar{\mu}_k^{[s]}$, is not ray-dependent, the diagonal matrix $\mathcal{U}_k^{[s]}$ as defined in equation (2.35) is reduced to a scaled identity matrix with $\bar{\mu}_k^{[s]}$ being the scaling factor, as $\mathcal{U}_k^{[s]} = \bar{\mu}_k^{[s]} \mathcal{I}$, or

$$\mathcal{U}_k^{[s]} \mathcal{A}^{[s]} = \bar{\mu}_k^{[s]} \mathcal{I} \mathcal{A}^{[s]} = \bar{\mu}_k^{[s]} \mathcal{A}^{[s]}.$$

Image reconstruction

The convex optimization program in Section 3.2 is used for the image reconstruction in the inverse-crime study, re-written as

$$\begin{aligned} \mathbf{b}^* = \ & \underset{\mathbf{b}}{\operatorname{argmin}} \sum_{k=1}^{2} ||\mathbf{b}_k||_{\mathrm{TV}} \\ \text{s. t.} \quad & \frac{||\mathcal{H}\mathbf{b} - \mathbf{g}_{\mathcal{M}}||_2}{||\mathbf{g}_{\mathcal{M}}||_2} \leq \epsilon, \\ & \mathbf{b} \succeq 0. \end{aligned} \tag{4.3}$$

The ASD-POCS algorithm in Algorithm 1 are used to reconstruct water and bone basis images. In the inverse-crime study, most of the program parameters match the ones used in the the data generation, including image voxel size, spectra $q_m^{[s]}$, and system matrices $\mathcal{A}^{[s]}$. In addition, we select the data fidelity constraint parameter $\epsilon = 10^{-8}$ to form a tight feasible set for the optimization program. The limited computer precision prevents from selecting $\epsilon = 0$ practically. For the algorithm parameter, we use the same ones as those used in the conventional ASD-POCS algorithm [57], as

$$\begin{aligned} \gamma^{(n)} &= 0.95\,\gamma^{(n-1)}, \quad \text{with} \quad \gamma^{(1)} = 1.0, \\ \alpha_k^{(n)} &= 0.8\,\alpha_k^{(n-1)}, \quad \text{with} \quad \alpha^{(1)} = 0.2\,\Delta_{\mathbf{b}}^{(1)}, \\ N_{\mathrm{TV}} &= 20, \end{aligned} \tag{4.4}$$

where $\Delta_{\mathbf{b}}^{(1)}$ is the normalized ℓ_2 norm of the basis image vector difference before and after the POCS update in the first iteration.

Based on the mathematical convergence conditions defined in equations (3.18)-(3.20), we

design the practical convergence conditions for the inverse-crime study as

$$\bar{D}(\mathbf{b}^{(n)}) \leq 10^{-4}, \tag{4.5}$$

$$\bar{\Delta}\Psi(\mathbf{b}^{(n)}) \leq 10^{-4}, \tag{4.6}$$

$$c_{\alpha}(\mathbf{b}^{(n)}) \leq -0.99. \tag{4.7}$$

A convergent reconstruction is obtained when all of the convergence conditions above are satisfied. Because the truth basis images are known, we also devise a reconstruction-error metric

$$\bar{\Delta}_{\mathbf{b}}(\mathbf{b}^{(n)}) = \frac{||\mathbf{b}^{(n)} - \mathbf{b}_{\text{true}}||_2}{||\mathbf{b}_{\text{true}}||_2} \tag{4.8}$$

that denotes the normalized ℓ_2-distance between the truth and reconstructed basis images. This metric provides a quantitative indication as to whether and how the reconstructed basis image approaches the known truth.

4.2.2 Study results

Convergence plots

We display in Fig. 4.4 the convergence plot of the metric $\bar{D}(\mathbf{b}^{(n)})$ used in the practical convergence conditions and the plot of the reconstruction-error metric. Since we are checking the implementation, rather than the numerical convergence of the algorithm, the other two optimality-derived metrics are not shown here. It is observed that, while the data fidelity function is decreasing and approaching ϵ, the reconstructed images are also approaching the truth images.

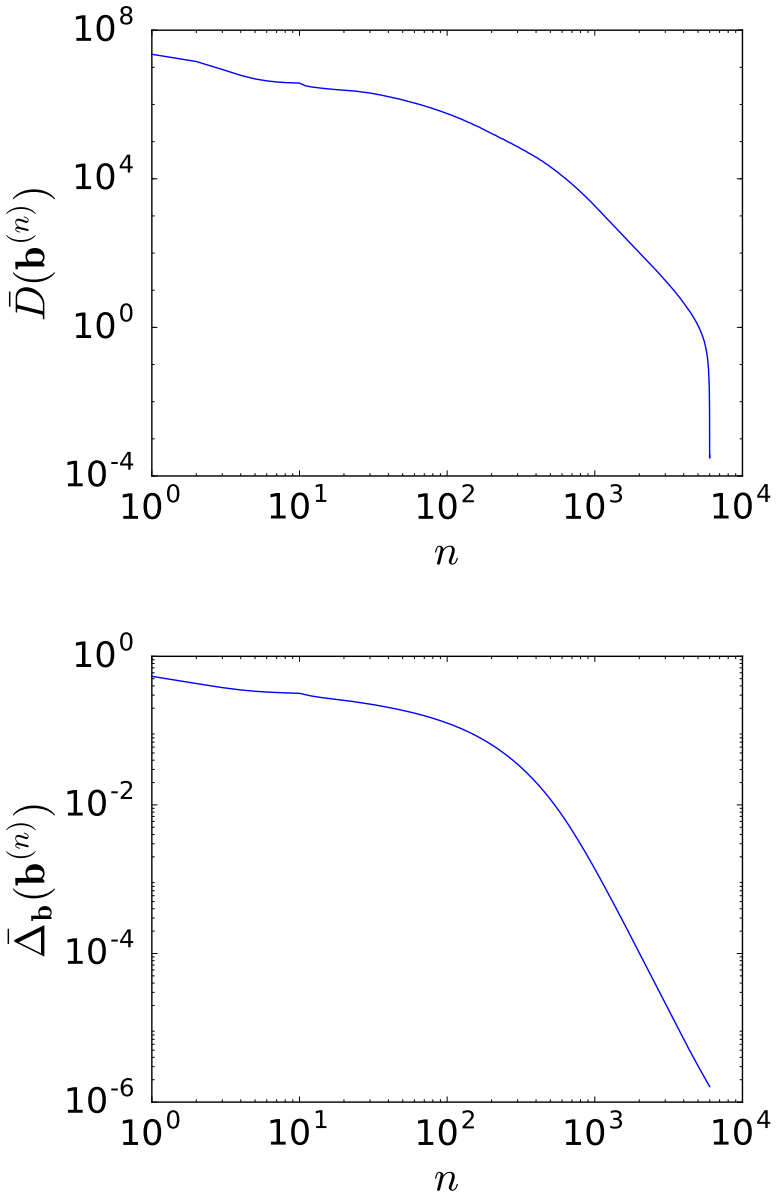

Figure 4.4: Practical convergence metric $\bar{D}(\mathbf{b}^{(n)})$ and reconstruction-error metric $\bar{\Delta}(\mathbf{b}^{(n)})$ as functions of iteration n in the inverse-crime study.

Reconstructed images

The basis images at the converged solutions are shown in Fig. 4.5 and compared to the truth phantom images. The two sets of basis images between the truth and the convergent solutions are visually identical. Their absolute differences, as shown in the bottom row of

Fig. 4.5, show no difference between the two in the small display window.

4.3 Verification study with a non-linear data model

Following the successful verification of the ASD-POCS algorithm implementation in the inverse-crime study, we carry out the verification study with a non-linear data model to verify the implementation of the code and that the ASD-NC-POCS algorithm can indeed lead to a local, or even global, optimal point. As a matter of fact, a total of two verification studies are conducted with two distinct phantoms that are structurally different.

4.3.1 Study design

Data generation

The first verification study is a continuation of the inverse-crime study, but with a different, non-linear data model. The full-scan configuration as shown in Fig. 4.1 and physical dimensions as summarized in Table 4.1 are used again. Similarly, the same spectra as shown in Fig. 4.2 and the same numerical basis image phantom are used to generate the data. The DD-data model in equation (2.19) is employed as

$$g_j^{[s]}(\mathbf{b}) = -\ln \sum_m q_m^{[s]} \exp\left(-\sum_k \mu_{km} \sum_i a_{ji}^{[s]} b_{ki}\right), \tag{4.9}$$

with ray-independent spectra $q_m^{[s]}$. The explicit matrix-vector form of the DD-data model can be expressed as

$$\begin{pmatrix} \mathbf{g}^{[1]}(\mathbf{b}) - \Delta\mathbf{g}^{[1]}(\mathbf{b}) \\ \mathbf{g}^{[2]}(\mathbf{b}) - \Delta\mathbf{g}^{[2]}(\mathbf{b}) \end{pmatrix} = \begin{pmatrix} \bar{\mu}_1^{[1]}\mathcal{A}^{[1]} & \bar{\mu}_2^{[1]}\mathcal{A}^{[1]} \\ \bar{\mu}_2^{[2]}\mathcal{A}^{[2]} & \bar{\mu}_2^{[2]}\mathcal{A}^{[2]} \end{pmatrix} \begin{pmatrix} \mathbf{b}_1 \\ \mathbf{b}_2 \end{pmatrix}, \tag{4.10}$$

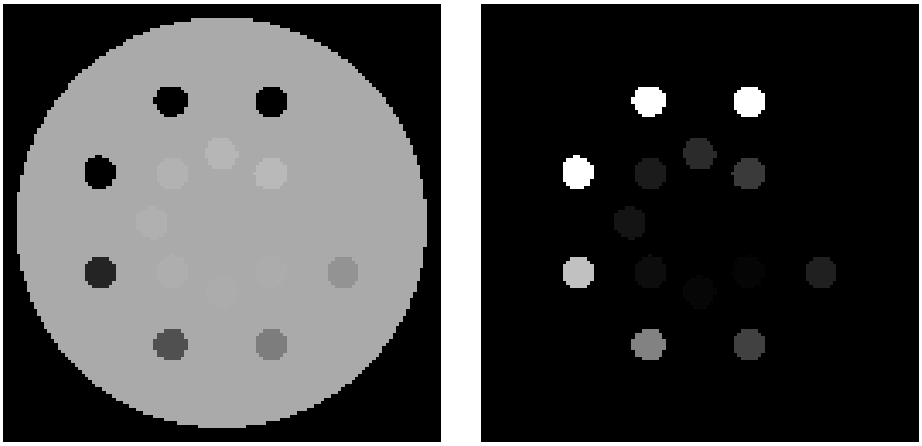

(a) water basis, truth

(b) bone basis, truth

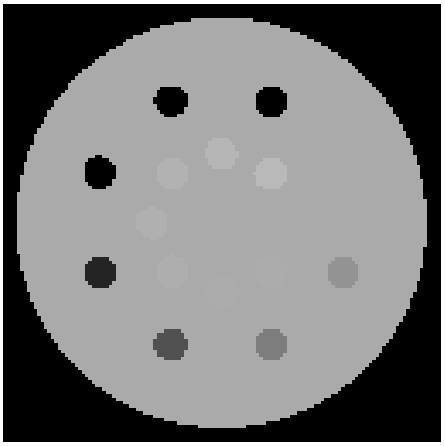

(c) water basis, reconstructed

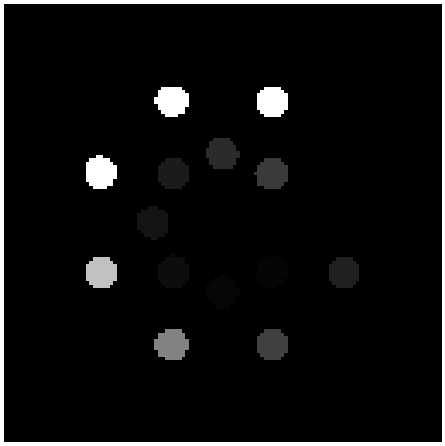

(d) bone basis, reconstructed

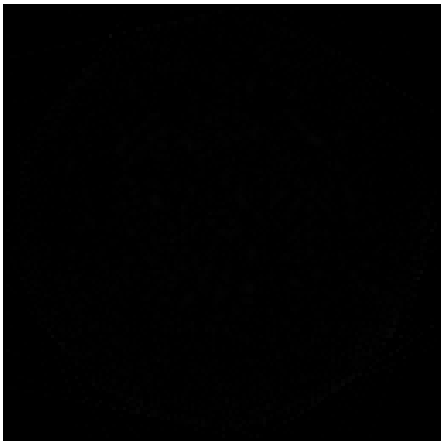

(e) water basis, absolute difference

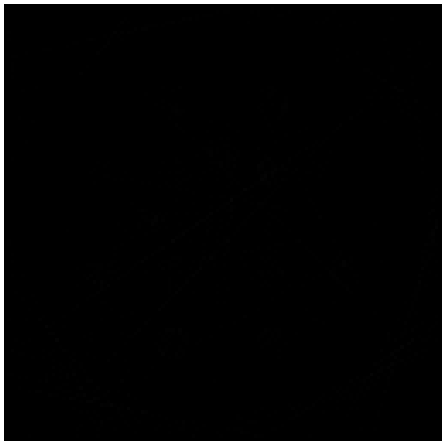

(f) bone basis, absolute difference

Figure 4.5: Truth (top row) and reconstructed (middle row) basis images of the numerical contrast-insert phantom from the inverse-crime study, with a display window of [0, 1.5], and their absolute difference image (bottom row), with a display window of $[0, 10^{-3}]$.

where $\mathbf{b}^\top = (\mathbf{b}_1^\top, \mathbf{b}_2^\top)$, $\bar{\mu}_k^{[s]} = \sum_m q_m^{[s]} \mu_{km}$, and the NL term $\Delta\mathbf{g}^{[s]}(\mathbf{b})$ is defined in equation (2.32).

For the second verification study, the full-scan configuration is used with 160 overlapping projection views distributed evenly over 2π for each rotation. The physical dimensions simulate those in a standard, on-board imager cone-beam CT (CBCT) employed in radiation therapy, and are summarized in Table 4.2.

Table 4.2: Physical dimensions of the scan configuration used in the verification study.

Physical quantity	dimension
source-to-detector distance	1500 mm
source-to-center-of-rotation distance	1000 mm
detector length	400 mm
detector bin size	1.56 mm
detector bin samples	256
number of views	160

Low and high spectra at 80 and 140 KVp are used as the incident spectra. A linear energy response function from an energy-integrating detector is modeled and multiplied with the incident spectra to yield the X-ray spectra. The normalized X-ray spectra used in the second verification study are plotted in Fig. 4.6.

A numerical lung phantom, as shown in Fig. 4.7, is used in the second verification study. The numerical lung phantom mimics the anatomical features and is not uniform or piece-wise constant as the contrast-insert phantom. It is used to demonstrate that, in the best case scenario, the designed non-convex, TV-constrained optimization program and the ASD-NC-POCS algorithm can lead to an optimal point from data generated from complex structure. The numerical lung phantom is decomposed water and bone basis images, as shown in the top row of Fig. 4.10, which are used as the truth to generate the consistent data. The images are represented on an array of size $I = 128 \times 128$ with square pixels of size 1.95 mm.

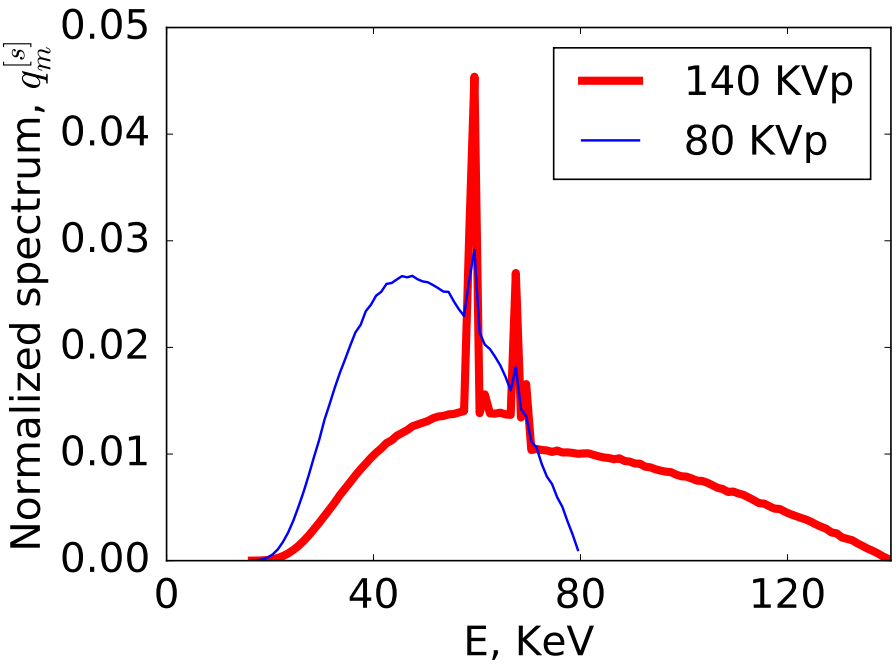

Figure 4.6: Normalized X-ray spectrum $q_m^{[s]}$. Low (thin, blue line) and high (thick, red line) energy spectra at 80 and 140 KVp are used in the verification study.

Image reconstruction

The non-convex optimization program described in Section 3.3 is used for the image reconstruction in the verification study, as

$$\begin{aligned} \mathbf{b}^* = \ & \underset{\mathbf{b}}{\operatorname{argmin}} \ \sum_{k=1}^{2} ||\mathbf{b}_k||_{\mathrm{TV}} \\ \text{s.t.} \quad & D(\mathbf{g}(\mathbf{b}), \mathbf{g}_{\mathcal{M}}) \leq \epsilon, \\ & \mathbf{b} \succeq 0, \end{aligned} \tag{4.11}$$

and the ASD-NC-POCS algorithm in Algorithm 2 is used for reconstructing water and bone basis images. We design the constrained optimization program above such that the solution would be numerically and visually close to the known, truth basis phantom images, by specifying the problem parameters. The data fidelity constraint parameter ϵ is set to 10^{-8}

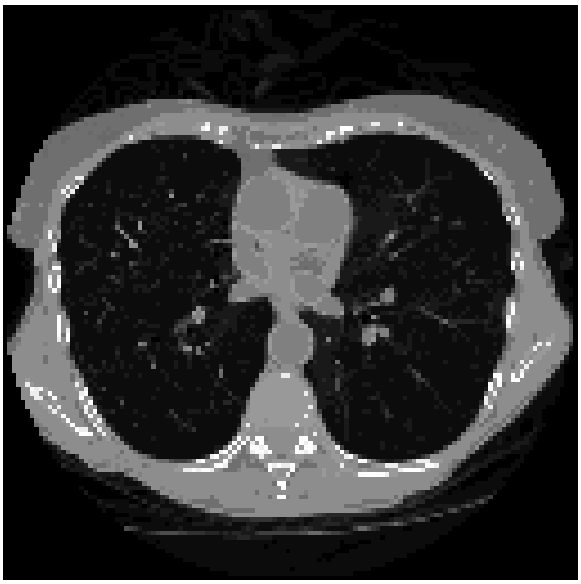

Figure 4.7: Monochromatic image at 80 KeV for the numerical lung phantom, from which the truth basis images are decomposed and used to generate data in the verification study. Display window: [-1000, 1000] HU

to form a tight feasible set for the optimization problem. All other program parameters match the ones used in generating the data, while the algorithm parameters are the same as those used in the inverse-crime study in equation (4.4).

Based on the mathematical convergence conditions defined in equations (3.18)-(3.20), we design the practical convergence conditions for the verification study as

$$\bar{D}(\mathbf{b}^{(n)}) \leq 10^{-4}, \tag{4.12}$$

$$\bar{\Delta}\Psi(\mathbf{b}^{(n)}) \leq 10^{-4}, \tag{4.13}$$

$$c_{\alpha}(\mathbf{b}^{(n)}) \leq -0.99. \tag{4.14}$$

A convergent reconstruction is obtained when all of the convergence conditions above are satisfied. We also observe the reconstruction-error metric $\bar{\Delta}_{\mathbf{b}}(\mathbf{b}^{(n)})$, as the image distance to the truth should approach zero.

4.3.2 Study results

Convergence plots

We first display in Figs. 4.8 and 4.9 the convergence plots of the metrics used in the practical convergence conditions. Only the results from the verification study with the numerical lung phantom are shown, as the numerical contrast-insert phantom ones are similar. It can be observed that all practical convergence conditions are met at the stopping iteration. In addition, the normalized image distance between the truth and the reconstructed basis images are quantitatively small.

Reconstructed images

The truth (top row) and reconstructed (middle row) basis images of the numerical contrast-insert phantom are shown in Fig. 4.10. They are visually identical to each other with the display window of [0, 1.5]. Their absolute differences as shown in the bottom row show no difference between the two in the small display window. Results from the numerical lung phantom are shown in Fig. 4.11 and same observations can be made.

4.4 Discussion

In this chapter, we have carried out a verification study to verify the numerical convergence of the ASD-NC-POCS algorithm and its computer implementation. As the ASD-NC-POCS algorithm was developed based on the ASD-POCS algorithm, an inverse-crime study using consistent data generated from the linear DD data model was first carried out to verify the computer implementation of most of the ASD-NC-POCS algorithm. Following the successful verification with the inverse-crime study, we used consistent data generated from the full non-linear DD data model and verified the numerical convergence of the ASD-NC-POCS, as well as the full implementation of the algorithm, as an exact recovery of the truth basis images

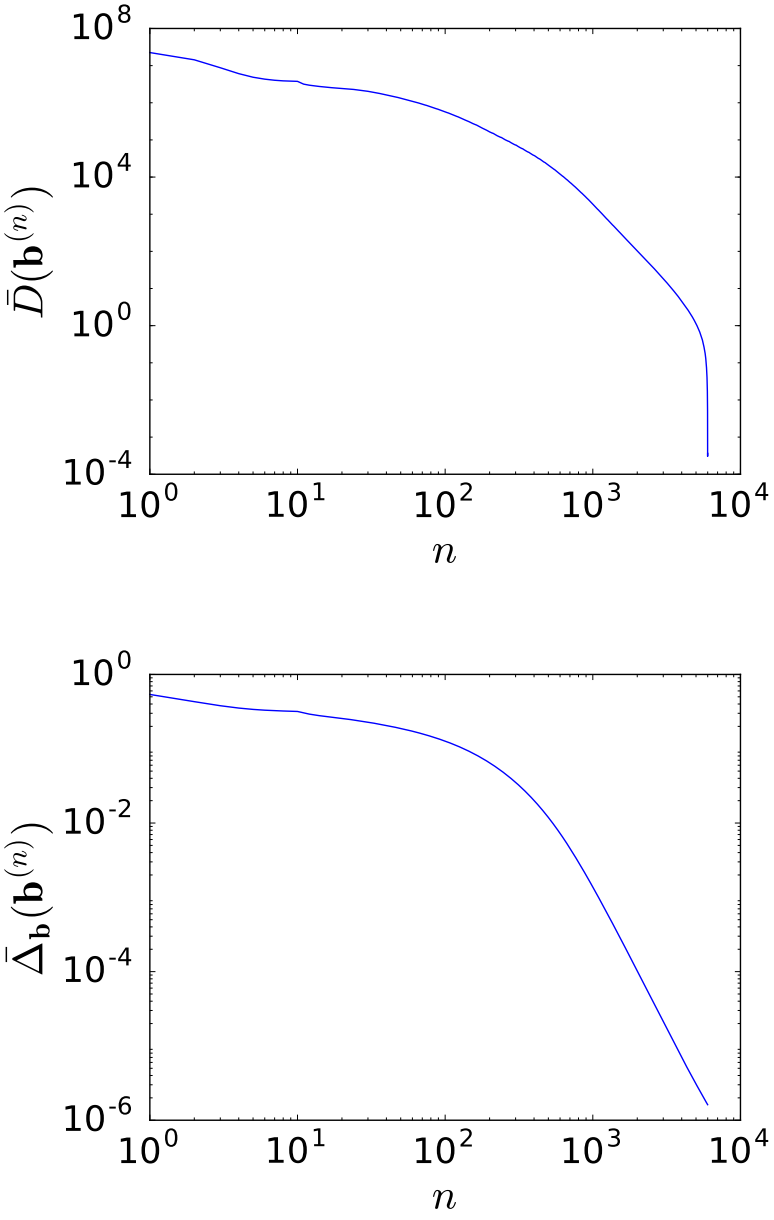

Figure 4.8: Practical convergence metric $\bar{D}(\mathbf{b}^{(n)})$ and reconstruction-error metric $\bar{\Delta}(\mathbf{b}^{(n)})$ as functions of iteration n in the verification study with the numerical lung phantom.

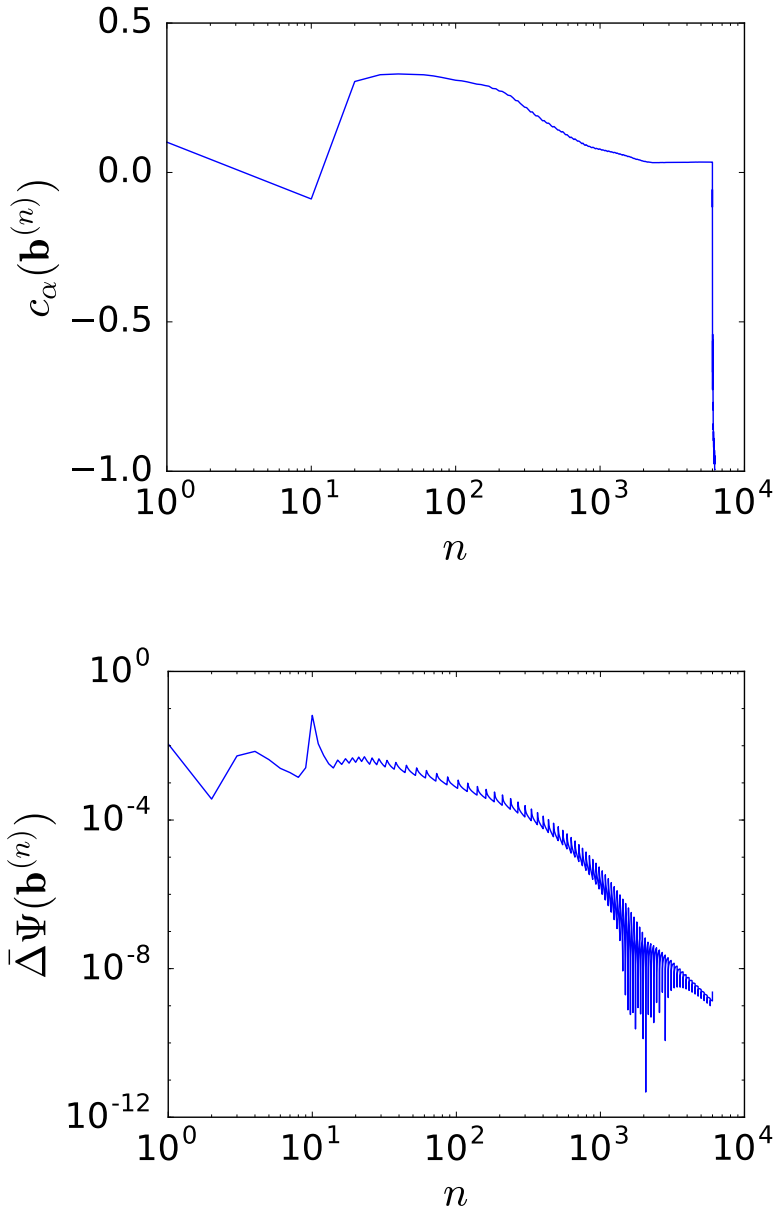

Figure 4.9: Practical convergence metric $c_\alpha(\mathbf{b}^{(n)})$ and $\Delta\Psi(\mathbf{b}^{(n)})$ as functions of iteration n in the verification study with the numerical lung phantom.

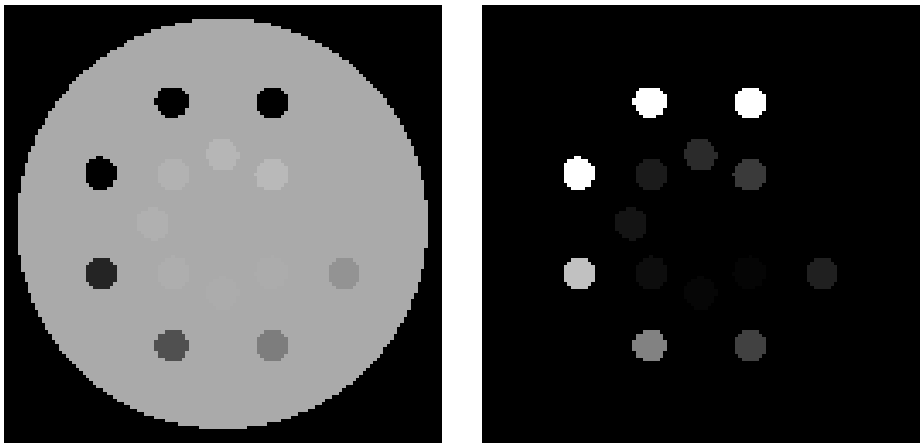

(a) water basis, truth

(b) bone basis, truth

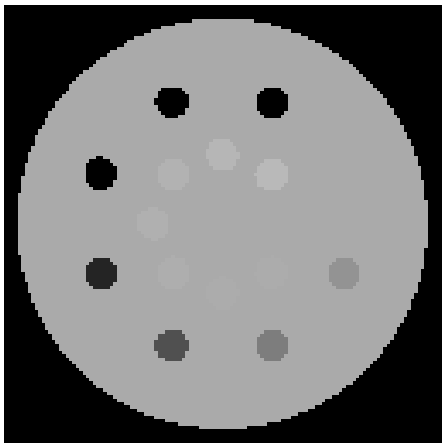

(c) water basis, reconstructed

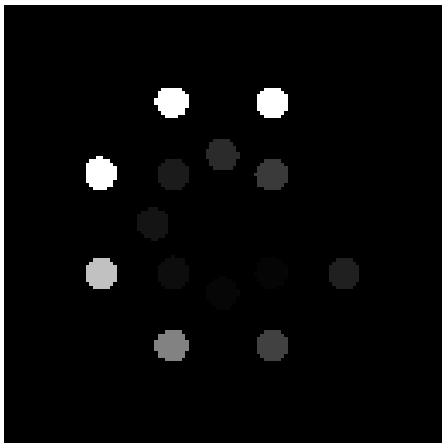

(d) bone basis, reconstructed

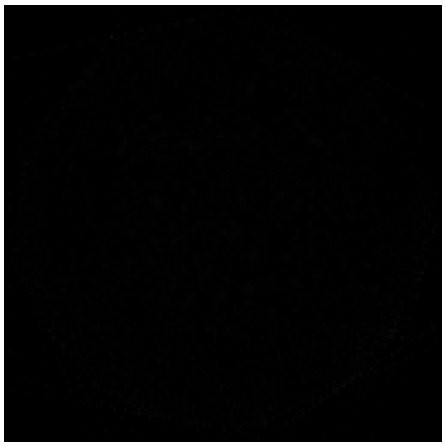

(e) water basis, absolute difference

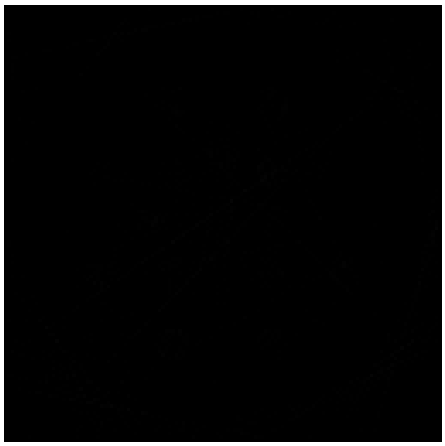

(f) bone basis, absolute difference

Figure 4.10: Truth (top row) and reconstructed (middle row) basis images of the numerical contrast-insert phantom from the verification study, with a display window of [0, 1.5], and their absolute difference image (bottom row), with a display window of $[0, 10^{-3}]$.

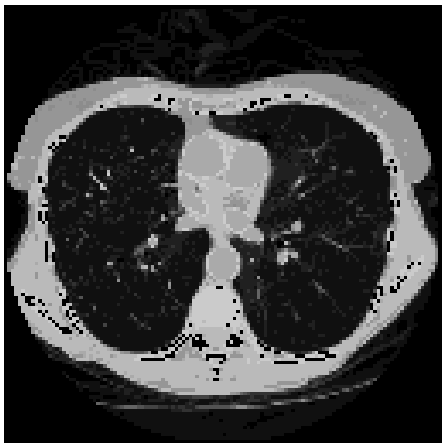

(a) water basis, truth

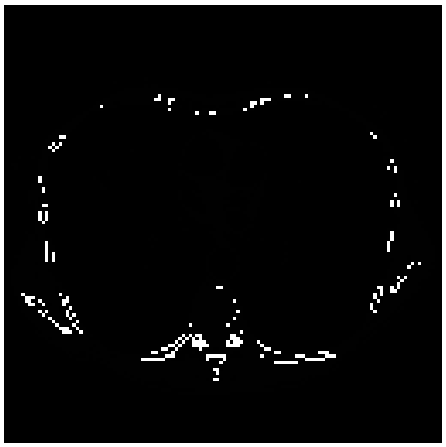

(b) bone basis, truth

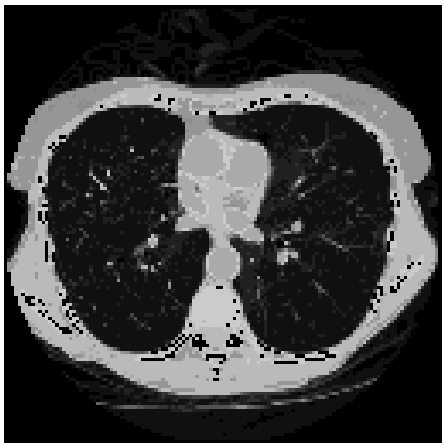

(c) water basis, reconstructed

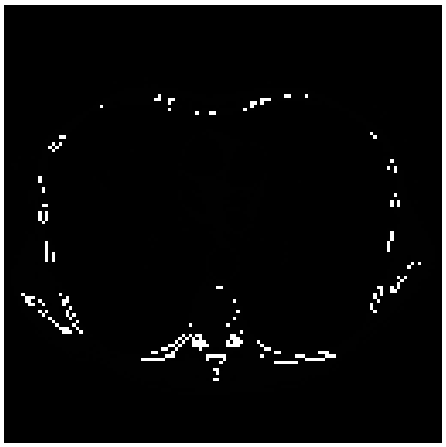

(d) bone basis, reconstructed

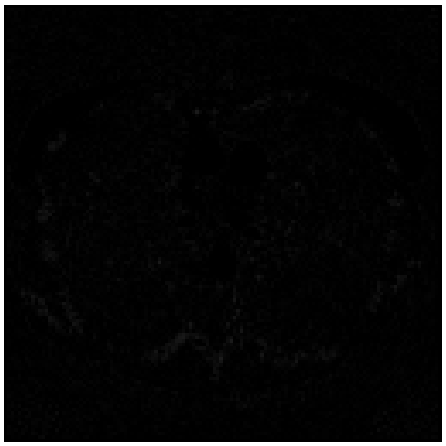

(e) water basis, absolute difference

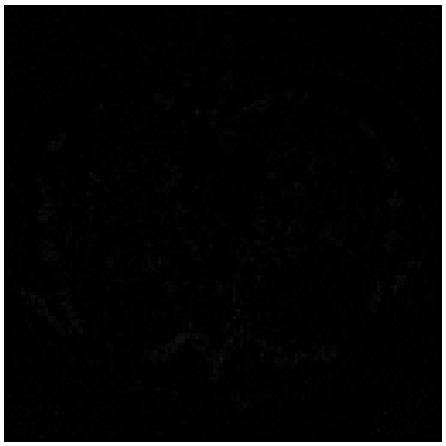

(f) bone basis, absolute difference

Figure 4.11: Truth (top row) and reconstructed (middle row) basis images of the numerical lung phantom from the verification study, with a display window of [0, 1.5], and their absolute difference image (bottom row), with a display window of [0, 10^{-3}].

was achieved.

The verification study by itself does not suggest any utility of the proposed method or the algorithm. However, it is an important step in the development of reconstruction methods and algorithms. Verification studies make sure that designed solutions by the optimization program could be achieved by the specific algorithm. Without the verification study, it would be difficult to interpret results, especially unexpected results such as artifacts, from the characterization studies with simulation and real data that follows.

CHAPTER 5

FULL SCAN CONFIGURATION SIMULATION STUDY

5.1 Introduction

Following the successful verification of the numerical convergence of the ASD-NC-POCS algorithm and its computer implementation, we next characterize the proposed optimization-based reconstruction method for multispectral CT data, including the optimization program, the ASD-NC-POCS algorithm, and reconstruction parameters, by using inconsistent data. The "inconsistency" of the data, as opposed to what was used in the verification study, refers to the fact that the forward model used to generate the data is not the same as the data model used in the optimization-based reconstruction. Real data collected in a physical experiment are inconsistent data, because the deterministic data model used in this work, i.e., equation (2.19), does not capture the stochastic nature of photon's interaction with matters. It is also sufficient to describe only dominant physical processes in a CT reconstruction model, thus leaving rooms for inconsistency when compared to measuring the real data. For simulation studies, most common inconsistencies are created by using a different model, e.g., a continuous-to-discrete data model, to generate data and/or adding some noise. An advantage of carrying out the characterization study using simulated inconsistent data is that the types and degree of inconsistencies can be controlled.

In this section, two sources of inconsistencies are considered - decomposition error and statistical noise. First, the decomposition error stems from the fact that the basis material decomposition model in equation (2.14) becomes an approximation when only a finite number of basis materials are used. For example, a two-basis-material decomposition model with water and bone is approximate, when the phantoms contain more than just these two materials, especially iodine and calcium, which gives rise to decomposition errors. Such inconsistencies are simulated by generating data with the DD data model prior to the de-

composition step, i.e., equation (2.13), while a different DD data model, i.e., equation (2.19), is used for the reconstruction. Second, Poisson noise is simulated, with a fluence level matching that in a clinical on-board imager (OBI) cone-beam CT scan. The normalized spectra $q_{jm}^{[s]}$ are scaled to the fluence level. The intensity measurements with the scaled spectra are taken as means in single Poisson realizations, followed by log-normalization with scaled "air scan" intensities, to generate the proper measured data.

We start the characterization study with the full scan configuration, so that potential issues caused by the decomposition error or noise can be isolated from the sampling condition. In addition, the full-scan configuration provides a performance benchmark for the following characterization studies with non-standard configurations that are enabled by the proposed reconstruction method. While the ASD-NC-POCS algorithm can reconstruct images from cone-beam data collected over standard and non-standard source trajectories, we demonstrate in this study its application to image reconstruction from data collected with a fan-beam configuration over a circular trajectory.

Another reason to start with the full scan configuration is that the data domain decomposition approach can be applied to the full-scan data, where the ray-consistency condition is satisfied for different KVp measurements. As one of the existing approaches for multispectral CT reconstruction, the data domain decomposition, in combination with the analytic-based reconstruction such as FBP, can also serve as a performance benchmark for the ASD-NC-POCS algorithm. In the development of optimization-based CT reconstruction methods of practical significance, we often expect the performance of the proposed algorithm, in this case the ASD-NC-POCS algorithm, to at least match, if not improve upon, the existing standard method, in this case the data domain decomposition with FBP, in the conventional situation, in this case the full scan configuration, before we move on to explore the enabling capability, if any, associated with the algorithm.

5.2 Data generation

5.2.1 Scanning configuration

We simulate data being generated from a standard cone-beam CT (CBCT) on-board imager (OBI) used in radiation therapy. The CBCT system has a source-to-center-of-rotation distance of 1000 mm. A linear detector of 400-mm in length is placed 1500 mm away from the source, consisting of 1024 bins of 0.39 mm in size. The scanning field-of-view (FOV) is thus formed as a circle of 265 mm in diameter. Further, for the full scan configuration used in the characterization study in this section, the X-ray tube rotates for a full rotation at the low KVp (thin, blue line) with 640 projection views evenly distributed over 2π, switches to the high KVp and rotates for another full rotation (thick, red line) with another 640 projections views at the same angular positions. Note that while the full-scan configuration in this characterization study is similar to the one employed in the verification study, the sampling and physical dimensions used here simulate those in the realistic scanning setting, and are thus different from those in the verification study. A schematic drawing of the full-scan configuration is shown in Fig. 5.1 and its physical dimensions are summarized in Table. 5.1. The data size of the low or high KVp scan in this study is $J^{[1]} = J^{[2]} = 640 \times 1024$.

Table 5.1: Physical dimensions of the scan configuration used in the full-scan study.

Physical quantity	dimension
source-to-detector distance	1500 mm
source-to-center-of-rotation distance	1000 mm
FOV	265 mm
detector length	400 mm
detector bin size	0.39 mm
detector bin samples	1024
number of views	640

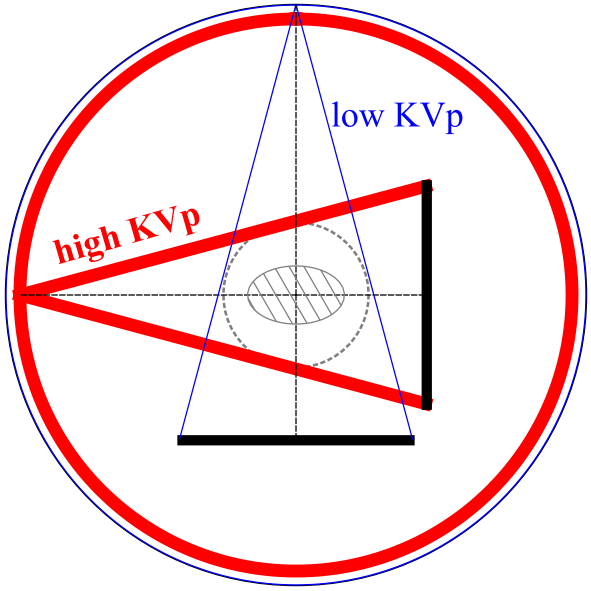

Figure 5.1: Full-scan configuration in which low (thin, blue line) and high (thick, red line) KVp scans are performed over a full rotation of 2π each.

5.2.2 Spectra

While the ASD-NC-POCS algorithm can be applicable to multispectral CT with multiple ($S \geq 2$) spectral data sets, we perform the full-scan characterization study using only two (i.e., $S = 2$) spectral data sets low ($s = 1$) and high ($s = 2$) spectra at 80 and 140 KVp. Typical X-ray spectra from a X-ray CT tube are generated using the TASMICS worksheet (v1.0) [126], assuming a tungsten anode and 5-mm-Al filter, and are used as the incident beam spectrum. The detector-energy response is modeled after an energy-integrating detector with a linear response. The X-ray spectra, $q_m^{[s]}$, are then taken as the product of the incident spectrum and detector-energy response after normalization. Fig. 5.2 shows the low (thin, blue line) and high (thick, red line) X-ray spectra at 80 and 140 KVp. No bow-tie filter is modeled, so the X-ray spectra shown in the figure is the same for all the rays while generating the data.

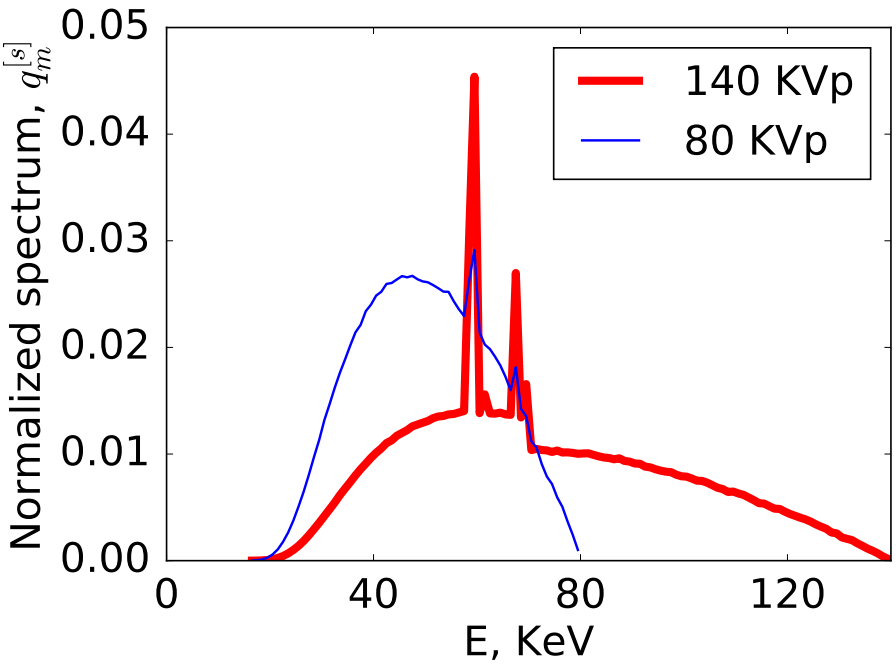

Figure 5.2: Normalized X-ray spectrum $q_m^{[s]}$. Low (thin, blue line) and high (thick, red line) energy spectra at 80 and 140 KVp are used in the verification study.

5.2.3 Phantoms

Two digital phantoms are used in the work, as shown in Fig. 5.3. The first simulates the standardized dual-energy contrast phantom with iodine and calcium solution inserts [127], and is referred to as the *DE-472* phantom. The second mimics human thoracic anatomy [110], and is referred to as the *lung* phantom. The DE-472 phantom contains iodine and calcium contrast inserts and can particularly characterize the material separation ability of the proposed reconstruction method for multispectral CT, while the lung phantom simulates anatomical structures that are more relevant in evaluating the potential of the proposed ASD-NC-POCS algorithm for patient scans.

Both phantoms are represented on an array of $I = 512 \times 512$ with square pixels of 0.49 mm. Therefore, the imaged subjects are completely within the FOV. Each image-pixel is labeled with a material type and its density, which can be translated into mass

Table 5.2: Non-water materials used in the composition of both digital phantoms employed in the studies. * indicates materials whose mass-attenuation coefficients are not readily available as tabulated data on NIST website and are thus computed with the XCOM program.

	DE-472 phantom		Lung phantom			
material	iodine solution*	calcium solution*	lung tissue	adipose tissue	skeleton muscle	cortical bone
density (g/ml)	0.002-0.02	0.05-0.6	0.1-0.6	0.88-0.95	1.11-1.21	1.53-2.05

attenuation coefficients at different energy levels. Table 5.2 summarizes the materials used in the composition of the phantoms, other than water with 1.0 g/ml density. For the lung phantom simulating various human tissues, the ICRU-44 standard was used for its materials, and the mass-attenuation coefficients are readily available as tabulated data on the NIST website [128]. For the DE-472 phantom, the mass-attenuation coefficients of the iodine and calcium solutions are calculated using the XCOM web program [129], also available on the NIST website, according to the specifications of the physical GAMMEX 472 Dual Energy CT phantom [127].

In addition, regions of interest (ROIs) are selected from each phantom for evaluation purpose and reconstruction parameter determination. For the DE-472 phantom, ROIs are drawn for each contrast inserts, as well as the two solid water inserts in the inner and outer circles that appear the same with the background, and two background regions at the center and in the peripheral. The total 18 ROIs are numbered, as shown in Fig. 5.4a. For the lung phantom, we instead use material masks to select the ROI. Three ROIs, corresponding to muscle, bone, and water masks, are selected, as shown in Figs. 5.4b, Figs. 5.4c, and Figs. 5.4d, respectively.

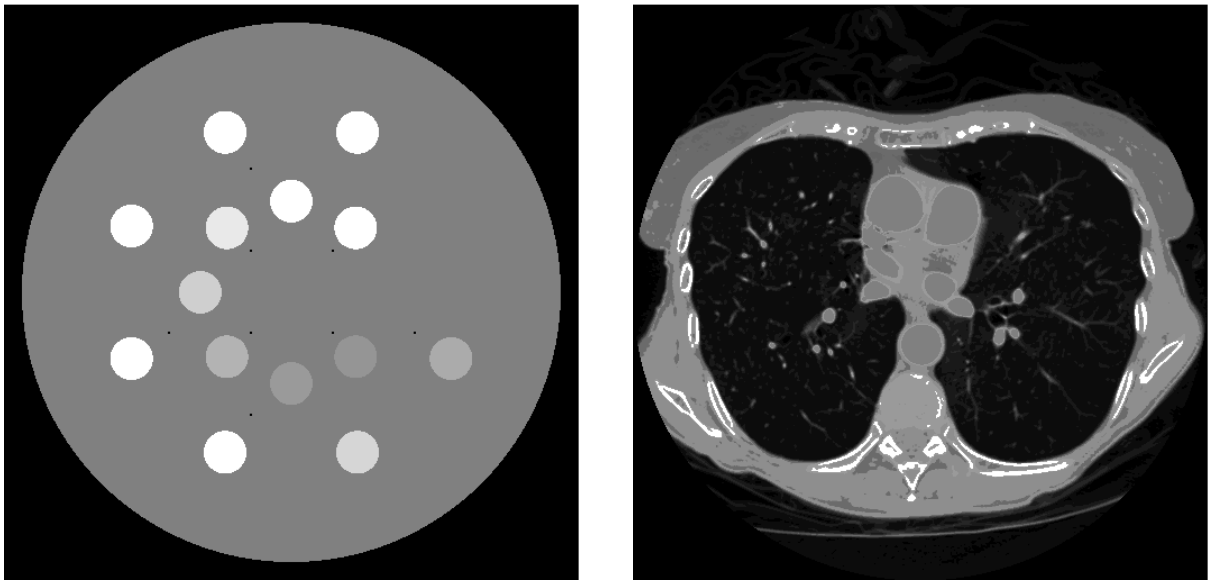

(a) DE-472 phantom (b) lung phantom

Figure 5.3: Monochromatic images of the DE-472 (a) and lung (b) phantoms as evaluated at 40 KeV, with display window of [-1000, 1000] HU.

5.2.4 Forward model

The DD data model with monochromatic images in equation (2.13), which is prior to the decomposition step, is used to generate the data as

$$g_j'^{[s]}(f'_{im}) = -\ln \sum_m q_m^{[s]} \exp\left(-\sum_i a_{ji}^{[s]} f'_{im}\right), \tag{5.1}$$

where $q_m^{[s]}$ denotes the ray-independent X-ray spectrum (shown in Fig. 5.2), $a_{ji}^{[s]}$ the intersection length of ray j in spectral set s with voxel i, also the elements in the jth row and ith column of the X-ray transform (shown in Fig. 5.1) matrix for spectral set s, and f'_{im} voxel i of the phantom monochromatic image at energy m. The data model above, instead of the one used in the verification study with the material decomposition already incorporated, is employed here in order to include the decomposition errors in the data for the full-scan characterization study, as such errors are unavoidable in the real data studies.

In addition, Poisson noise is added to data by scaling the spectra to yield $\phi = 2 \times 10^4$

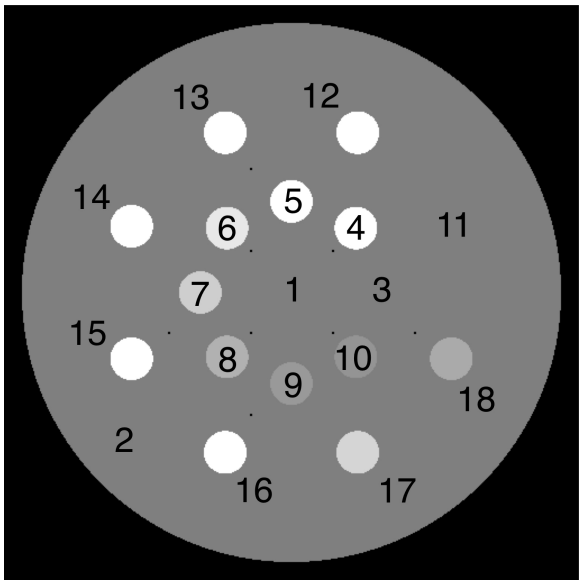

(a) DE-472 phantom

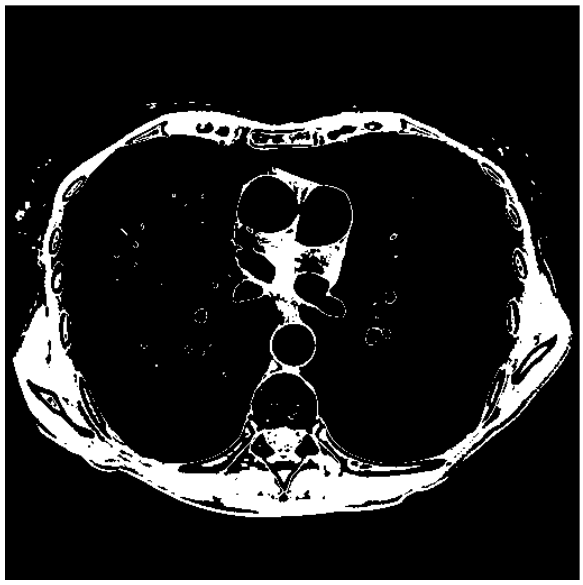

(b) Muscle mask

(c) Bone mask

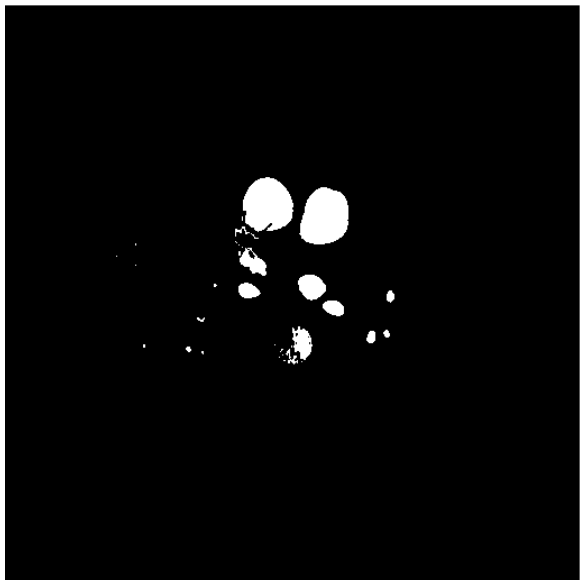

(d) Water mask

Figure 5.4: (a): 18 ROIs within the 16 circular inserts and 2 background areas of the DE-472 phantom numbered and highlighted from 1 to 18; (b), (c), (d): Material masks for the lung phantom to select ROIs, indicating muscle, bone, and water, respectively.

photons per ray in the air scan, which is a fluence level comparable to that in a OBI CBCT scan. As a result, the noisy data is generated according to the formula

$$\tilde{g}_j'^{[s]} = -\ln \frac{\sum_m \text{Poisson}\left[\phi\, q_m^{[s]} \exp\left(-\sum_i a_{ji}^{[s]} f'_{im}\right)\right]}{\phi \sum_m q_m^{[s]}}. \tag{5.2}$$

5.3 Image reconstruction

5.3.1 Basis and monochromatic images

We consider a two-basis-material decomposition model for both phantom studies with water ($k = 1$) and bone ($k = 2$). As a result, the DD data model in equation (2.33) can be re-expressed explicitly as

$$\begin{pmatrix} \mathbf{g}^{[1]}(\mathbf{b}) - \Delta\mathbf{g}^{[1]}(\mathbf{b}) \\ \mathbf{g}^{[2]}(\mathbf{b}) - \Delta\mathbf{g}^{[2]}(\mathbf{b}) \end{pmatrix} = \begin{pmatrix} \bar{\mu}_1^{[1]}\mathcal{A}^{[1]} & \bar{\mu}_2^{[1]}\mathcal{A}^{[1]} \\ \bar{\mu}_2^{[2]}\mathcal{A}^{[2]} & \bar{\mu}_2^{[2]}\mathcal{A}^{[2]} \end{pmatrix} \begin{pmatrix} \mathbf{b}_1 \\ \mathbf{b}_2 \end{pmatrix}, \tag{5.3}$$

where $\mathbf{b}^\top = (\mathbf{b}_1^\top, \mathbf{b}_2^\top)$ and $\bar{\mu}_k^{[s]} = \sum_m q_m^{[s]} \mu_{km}$. The data model above is thus used in the ASD-NC-POCS algorithm for reconstructing water and bone basis images for both phantom studies.

Using reconstructed basis images $\mathbf{b}_k$, along with knowledge of their mass attenuation coefficients, we can readily obtain monochromatic image $\mathbf{f}_m^K$ by linearly combing the basis images using equation (2.18) as

$$\mathbf{f}_m^K = \sum_{k=1}^{K} \mu_{km} \mathbf{b}_k. \tag{5.4}$$

In general, due to the presence of decomposition error, monochromatic image $\mathbf{f}_m^K$ differs from the linear attenuation coefficient $\mathbf{f}'_m$ from which the data are generated.

5.3.2 ASD-NC-POCS reconstruction

Optimization program

The non-convex optimization program described in Section 3.3 is used for the image reconstruction in the full-scan characterization study, as

$$\begin{aligned} \mathbf{b}^* = \ & \underset{\mathbf{b}}{\operatorname{argmin}} \sum_k ||\mathbf{b}_k||_{\mathrm{TV}} \\ \text{s. t.} \quad & D(\mathbf{g}(\mathbf{b}), \mathbf{g}_{\mathcal{M}}) \leq \epsilon, \\ & \mathbf{b} \succeq 0. \end{aligned} \tag{5.5}$$

As a reminder, the data fidelity constraint is specified by the normalized ℓ_2-norm as

$$D(\mathbf{g}(\mathbf{b}), \mathbf{g}_{\mathcal{M}}) = \left(\frac{\sum_s ||\mathbf{g}^{[s]}(\mathbf{b}) - \mathbf{g}^{[s]}_{\mathcal{M}}||_2^2}{\sum_s ||\mathbf{g}^{[s]}_{\mathcal{M}}||_2^2} \right)^{1/2},$$

and the model data vector $\mathbf{g}(\mathbf{b})$ has element

$$g_j^{[s]}(\mathbf{b}) = -\ln \sum_m q_{jm}^{[s]} \exp\left(-\sum_k \mu_{km} \sum_i a_{ji}^{[s]} b_{ki} \right).$$

Reconstruction parameter

The ASD-NC-POCS algorithm in Algorithm 2 is used for reconstructing water and bone basis images. The same algorithm parameters as those in the verification study are used as

$$\begin{aligned} \gamma^{(n)} &= 0.95\, \gamma^{(n-1)}, \quad \text{with} \quad \gamma^{(1)} = 1.0, \\ \alpha_k^{(n)} &= 0.8\, \alpha_k^{(n-1)}, \quad \text{with} \quad \alpha^{(1)} = 0.2\, \Delta_{\mathbf{b}}^{(1)}, \\ N_{\mathrm{TV}} &= 20, \end{aligned}$$

where $\Delta_{\mathbf{b}}^{(1)}$ is the normalized ℓ_2 norm of the basis image vector difference before and after the NC-POCS update in the first iteration.

Program parameters, such as image voxel size, X-ray spectra $q_m^{[s]}$, and system matrices $\mathcal{A}^{[s]}$, are selected to match the ones used in data generation, in which these parameters are already chosen as typically seen in practical applications like OBI CBCT. We note that in the full-scan characterization study the dimension of system matrices $\mathcal{A}^{[1]}$ and $\mathcal{A}^{[2]}$ are identical, as $J^{[1]} = J^{[2]} = 640 \times 1024$ and $I = 512 \times 512$. With the determination of program parameters including image pixel, spectra, and matrices, we now discuss the strategy for the selection of parameter ϵ in the characterization study.

Strategy for selection of parameter ϵ The determination of the parameter ϵ should be task-based. In the verification study with consistent data, the task is to verify the algorithm implementation and its numerical convergence by comparing to the truth images. Therefore, an infinitesimally small number ($\epsilon = 10^{-8}$) is selected to form a tight feasible set. For the characterization study where inconsistent data are used, it is no longer appropriate to set ϵ to be close to zero, as it needs to accommodate the inconsistencies between the measured, or generated, data and the model data. Instead, we propose to design evaluation metrics that are pertinent to the specific task of interest, and sample the metrics in the parameter space of ϵ to determine an optimal value for ϵ. In this study, we demonstrate how ϵ can be selected by designing the metrics below. We stress that it is by no mean a validation of the utility of the proposed optimization method for multispectral CT, nor is it a validation of the metrics used.

Because data are generated directly from linear attenuation coefficient $\mathbf{f}'_m$, we have no truth basis images in the characterization study, from which the reconstruction-error metric can be calculated. Instead, we design metrics based upon monochromatic images $\mathbf{f}_m$ for determination of parameter ϵ. We select R regions of interest (ROIs) in a monochromatic

image and calculate the "biases" and "standard deviations" within the ROIs as,

$$\theta_{rm} = \frac{1}{I_r} \sum_i |f_{im}^K - f'_{im}| \tag{5.6}$$

and

$$\sigma_{rm} = \left(\frac{1}{I_r - 1} \sum_i |f_{im}^K - \theta_{rm}|^2 \right)^{\frac{1}{2}}, \tag{5.7}$$

where $i \in I_r$ and I_r depicts the number of pixels within ROI r. Using θ_{rm} and σ_{rm}^2 computed at energies m_1 and m_2, we form two metrics for determination of parameter ϵ

$$\Theta = \frac{1}{R} \sum_r \left(\theta_{rm_1}^2 + \theta_{rm_2}^2 \right)^{\frac{1}{2}} \tag{5.8}$$

and

$$\Sigma = \frac{1}{R} \sum_r \left(\sigma_{rm_1}^2 + \sigma_{rm_2}^2 \right)^{\frac{1}{2}}. \tag{5.9}$$

For each phantom in the full-scan characterization study, we form monochromatic images $\mathbf{f}_m$ at $m_1 = 80$ KeV and $m_2 = 140$ KeV from reconstructed basis images for a number of ϵ values, compute Θ and Σ from the images, and then select ϵ that yields lowest Θ and Σ.

Practical convergence conditions We design practical convergence conditions for the full-scan characterization study as

$$\bar{D}(\mathbf{b}^{(n)}) < 10^{-3}, \tag{5.10}$$

$$\bar{\Delta}\Psi(\mathbf{b}^{(n)}) < 10^{-3}, \tag{5.11}$$

$$c_\alpha(\mathbf{b}^{(n)}) < -0.5. \tag{5.12}$$

The practical convergence conditions are looser than those in the verification study, as decomposition error and data noise need to be taken into consideration. In addition, our

previous experiences with the conventional ASD-POCS algorithm indicate that the third condition can often be relaxed to -0.5, instead of -0.99, with only imperceptible changes to the images [68, 69]. Using equation (5.4), we compose monochromatic image $\mathbf{f}_m^{K(n)}$ at iteration n. Also, in the simulation study, we have knowledge of truth monochromatic image $\mathbf{f}'_m$ and can thus calculate reconstruction-error metric

$$\bar{\Delta}_{\mathbf{f}}(\mathbf{f}_m^{K(n)}) = \frac{||\mathbf{f}_m^{K(n)} - \mathbf{f}'_m||_2}{||\mathbf{f}'_m||_2}, \tag{5.13}$$

which is the normalized ℓ_2-distance between the truth and reconstructed monochromatic images at energy m.

5.3.3 FBP reconstruction

In the full-scan characterization study, the ray-consistency condition for the data domain decomposition method is actually satisfied, in that each ray has both measurements with low and high KVp spectrum. As a result, we decompose the measured data into water and bone basis sinogram first and then reconstruct basis images directly from the basis sinogram using analytic-based FBP-like reconstruction algorithm. The basis and monochromatic image results, referred to as *FBP images*, from this method are taken as the benchmark and compared to those reconstructed using the ASD-NC-POCS algorithm, referred to as *ASD-NC-POCS images*.

Decomposition

We use a fix-point algorithm [102] to decompose measured sinogram to basis sinogram. First, we use L_{kj} to denote the basis sinogram of material k at ray j that has overlapping measurements from both spectral sets, which are simply the X-ray transform of the basis

image, as

$$L_{kj} = \sum_i a_{ji}^{[s]} b_{ki}. \tag{5.14}$$

Then, the DD data model in equation (2.30) can be re-expressed as a function of basis sinogram as

$$g_j^{[s]}(L_{kj}) = \bar{g}_j^{[s]}(L_{kj}) + \Delta g_j^{[s]}(L_{kj}), \tag{5.15}$$

where

$$\bar{g}_j^{[s]}(L_{kj}) = \sum_k \bar{\mu}_{jk}^{[s]} L_{kj} \tag{5.16}$$

and

$$\Delta g_j^{[s]}(L_{kj}) = -\ln \sum_m q_{jm}^{[s]} \exp\left(-\sum_k \Delta\mu_{jkm}^{[s]} L_{kj} \right). \tag{5.17}$$

In this full-scan study under consideration with two spectral sets ($S = 2$) and two basis materials ($K = 2$), we can re-write equation (5.15) as

$$\begin{pmatrix} g_j^{[1]}(L_{1j}, L_{2j}) - \Delta g_j^{[1]}(L_{1j}, L_{2j}) \\ g_j^{[2]}(L_{1j}, L_{2j}) - \Delta g_j^{[2]}(L_{1j}, L_{2j}) \end{pmatrix} = \begin{pmatrix} \bar{\mu}_1^{[1]} & \bar{\mu}_2^{[1]} \\ \bar{\mu}_2^{[2]} & \bar{\mu}_2^{[2]} \end{pmatrix} \begin{pmatrix} L_{1j} \\ L_{2j} \end{pmatrix}. \tag{5.18}$$

An update step of the fix-point algorithm can therefore be derived as, for the nth iteration,

$$\begin{pmatrix} L_{1j}^{(n)} \\ L_{2j}^{(n)} \end{pmatrix} = \begin{pmatrix} \bar{\mu}_1^{[1]} & \bar{\mu}_2^{[1]} \\ \bar{\mu}_2^{[2]} & \bar{\mu}_2^{[2]} \end{pmatrix}^{-1} \begin{pmatrix} g_{\mathcal{M}j}^{[1]} - \Delta g_j^{[1]}(L_{1j}^{(n-1)}, L_{2j}^{(n-1)}) \\ g_{\mathcal{M}j}^{[2]} - \Delta g_j^{[2]}(L_{1j}^{(n-1)}, L_{2j}^{(n-1)}) \end{pmatrix} \tag{5.19}$$

where $L_{1j}^{(0)}$ and $L_{2j}^{(0)}$ can take all zeros or simply from a "warm" start as

$$\begin{pmatrix} L_{1j}^{(0)} \\ L_{2j}^{(0)} \end{pmatrix} = \begin{pmatrix} \bar{\mu}_1^{[1]} & \bar{\mu}_2^{[1]} \\ \bar{\mu}_2^{[2]} & \bar{\mu}_2^{[2]} \end{pmatrix}^{-1} \begin{pmatrix} g_{\mathcal{M}j}^{[1]} \\ g_{\mathcal{M}j}^{[2]} \end{pmatrix}. \tag{5.20}$$

By definition, a converged solution for the fix-point algorithm for data decomposition is

achieved when there is no changes between the consecutive update steps, and the resulting basis sinogram are to be reconstructed into basis images.

Reconstruction

Analytic-based reconstruction algorithm, such as filtered-backprojection (FBP), is used to reconstruct basis images from basis sinogram. Equation (5.14) models the basis sinogram as a simply X-ray transform of the basis image. In the full-scan characterization study where angular samples are collected densely and uniformly around 2π, the FBP-like algorithm, with a smoothing Hanning window [4], should reconstruct basis images with reasonably good quality.

5.4 Study results

5.4.1 FBP reconstruction

Convergence plots

We first show in Fig. 5.5 the convergence plot of the fix-point algorithm used in the data domain decomposition. Using the lung phantom data as an example, the relative error between two consecutive updates are plotted as a function of iteration number n. It is shown that after about 60 iterations, the changes in the consecutive updates are almost zero (only at the computer precision level), indicating that the algorithm finds the "fixed-point" at about iteration 60. The result from the DE-472 phantom is consistent with Fig. 5.5.

Reconstructed images

Next, we show reconstructed basis images by use of FBP-like algorithm and their monochromatic energy images for both phantoms. A separate ROI for each phantom is selected and

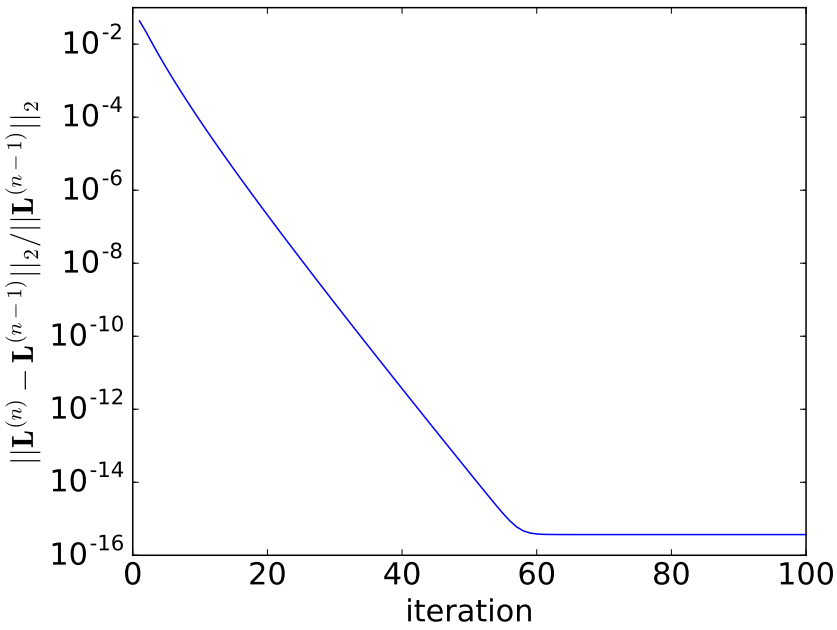

Figure 5.5: Relative error between consecutive updates as a function iteration n, using the fix-point algorithm for the data domain decomposition of the lung phantom data in the full-scan characterization study. $\mathbf{L}$ denotes the vector concatenated from the two basis sinogram vector $\mathbf{L}_1$ and $\mathbf{L}_2$.

zoomed-in for better visualization of the results. Further, for more quantitative analysis, profiles of monochromatic images composed from the basis images are plotted and compared to those from the truth monochromatic images.

DE-472 phantom results In Fig. 5.6, we display reconstructed basis images and their zoomed-in views of ROI images enclosed by the red rectangular boxes indicated in the full-size images in row 1, which contains two contrast inserts with the lowest concentration of iodine and calcium in the phantom and two air bubbles. The water and bone basis images are well decomposed by use of the data domain decomposition method, with the uniform water background appearing bright in the water basis image and almost all contrast inserts bright in the bone basis image. The ROI images show a significant noise level in both images, even with a smoothing Hanning window in the FBP-like reconstruction. The noise level is likely amplified in the data domain decomposition step, as the correlation between low and

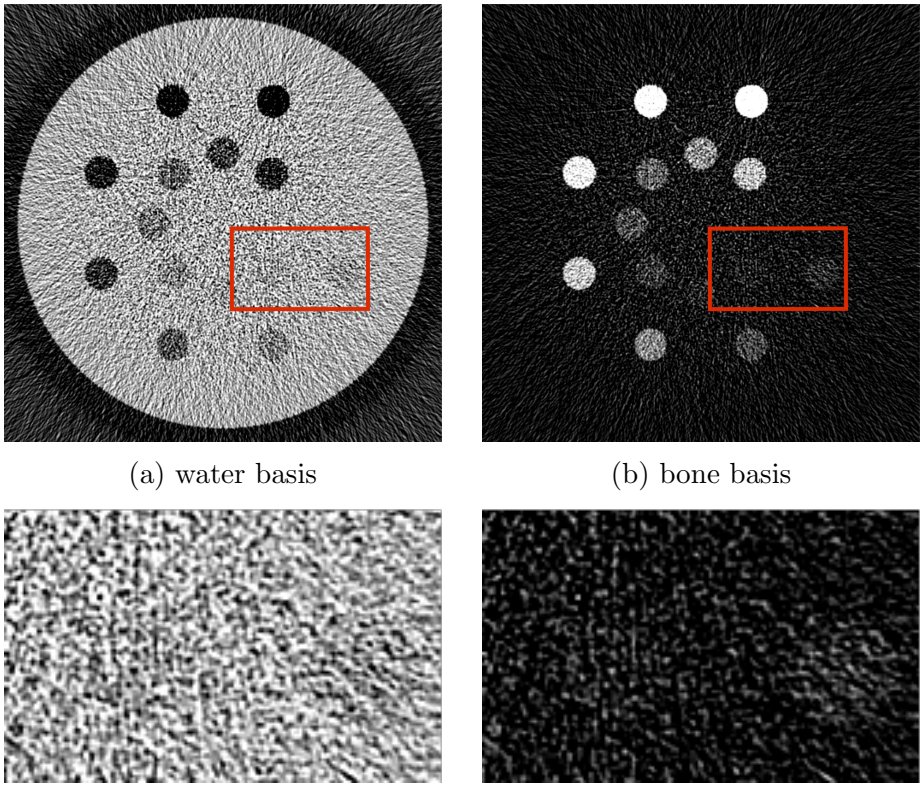

(a) water basis (b) bone basis

(c) water basis, zoomed-in (d) bone basis, zoomed-in

Figure 5.6: Water and bone basis FBP images (row 1) and zoomed-in views of ROI images (row 2) enclosed by red boxes in row 1, from full-scan data of the DE-472 phantom, with a display windows of [0, 1.5] for both rows.

high KVp sinogram are not considered in the decomposition.

Fig. 5.7 shows the monochromatic images at 40 and 120 KeV, the two energy levels that are often used for contrast enhancement and artifacts reduction, respectively, and their zoomed-in views of the same ROI as in Fig. 5.6. No significant cupping or banding artifacts are visible in the monochromatic images. Their ROIs, with a narrow display window of [-500, 500] HU, show both contrast inserts in the 40-KeV ROI image (Fig. 5.7c), but only the calcium insert in the 120-KeV one (Fig. 5.7d). Further, the air bubbles are obscured by the high noise level in both images and are not visible in either ROI image.

Fig. 5.8 shows the profile plots along the horizontal yellow line on the monochromatic images in row 1 of Fig. 5.7, for quantitative assessment of the FBP reconstruction. An overall

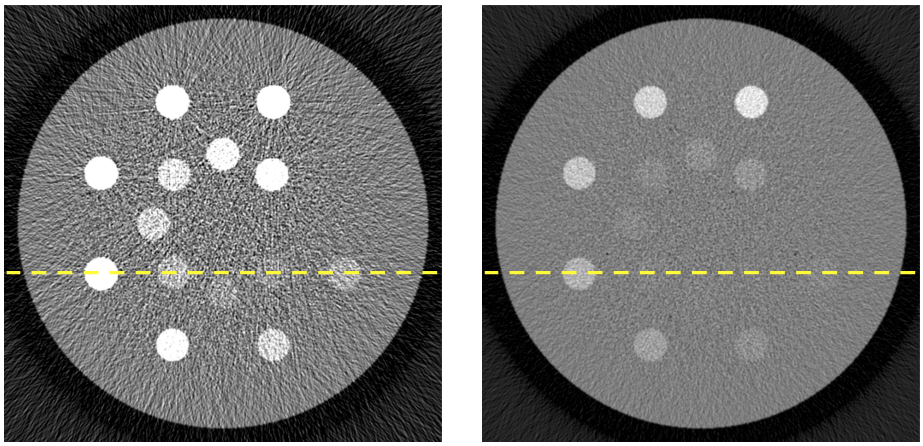

(a) 40-KeV image (b) 120-KeV image

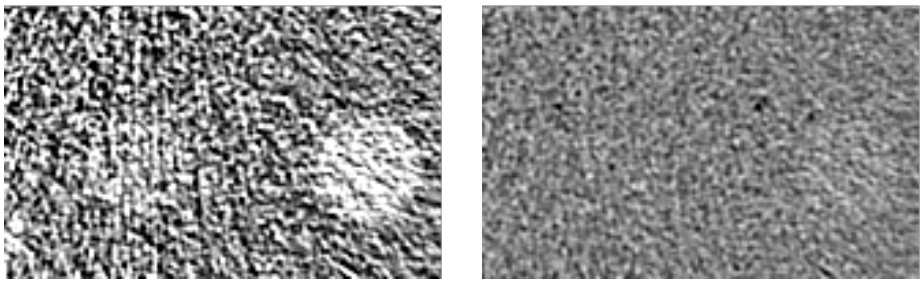

(c) 40-KeV zoomed-in (d) 120-KeV zoomed-in

Figure 5.7: 40 and 120 KeV monochromatic FBP images (row 1) and their zoomed-in views (row 2) of the same ROI as indicated by the red boxes in row 1 of Fig. 5.6, from full-scan data of the DE-472 phantom, with display windows of [-1000, 1000] HU (row 1) and [-500, 500] HU (row 2).

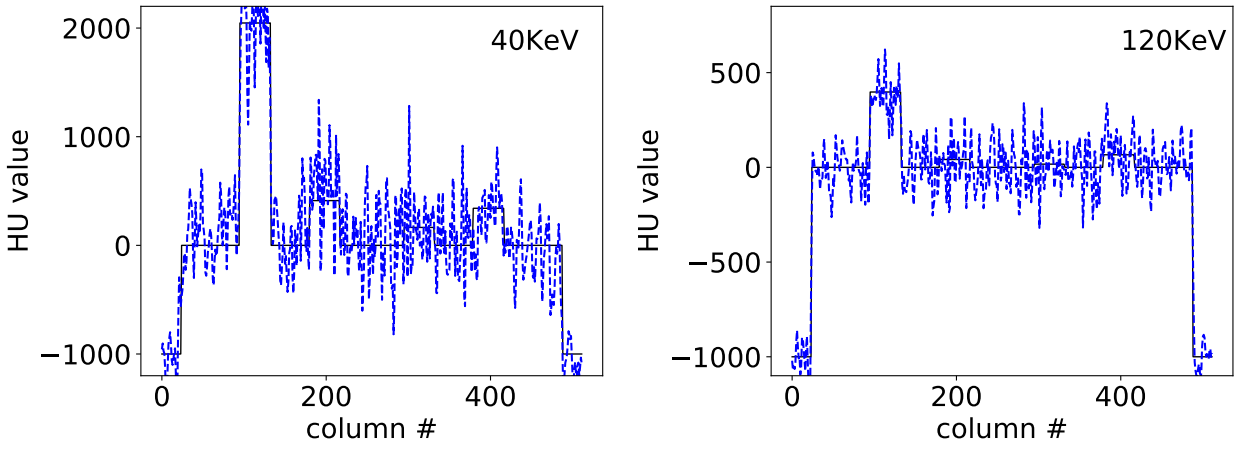

Figure 5.8: Profiles of FBP reconstructed (blue dashed) and truth (black solid) monochromatic images at 40 and 120 KeV along the horizontal yellow line indicated in row 1 of Fig. 5.7 from full-scan data of the DE-472 phantom

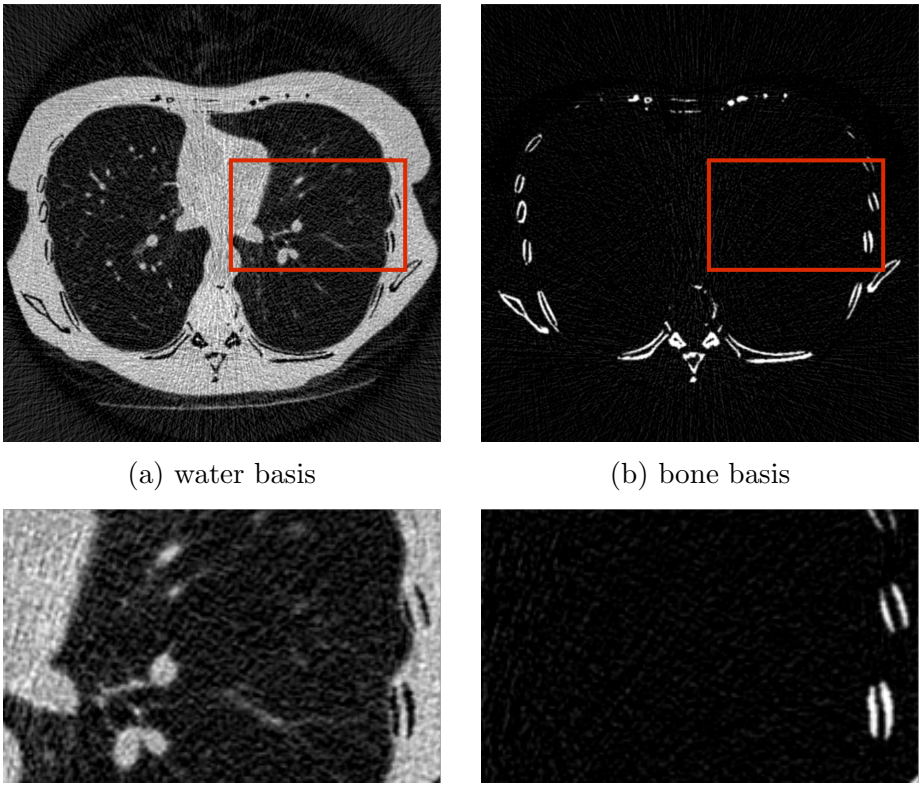

(a) water basis (b) bone basis

(c) water basis, zoomed-in (d) bone basis, zoomed-in

Figure 5.9: Water and bone basis FBP images (row 1) and zoomed-in views of ROI images (row 2) enclosed by red boxes in row 1, from full-scan data of the lung phantom, with a display windows of [0, 1.5] for both rows.

agreement in pixel HU values between the FBP reconstructed and truth monochromatic images at 40 and 120 KeV can be observed, although the high noise level present in the images prevents from further analysis of the quantitative accuracy from the profile plots.

Lung phantom results Similar to the DE-472 phantom results, we first display in Fig. 5.9 reconstructed basis images and their zoomed-in views of ROI images enclosed by the red rectangular boxes indicated in the full-size images in row 1 of the lung phantom results. The water and bone basis images are well separated, with the water image retaining most of the soft tissue structures and bone image the bony structures. The zoomed-in ROI images show complete decomposition of the two basis material, as the ribs on the right edge of the water ROI image (Fig. 5.9c) appear dark. However, it also shows some noise level in the dark

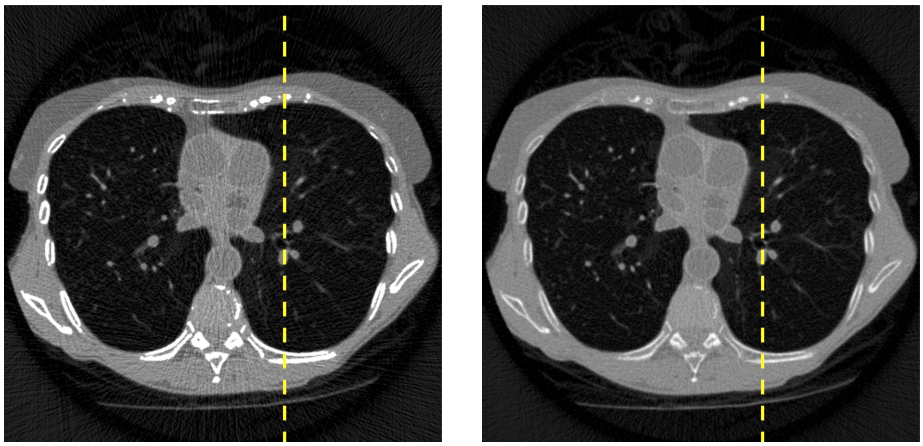

(a) 40-KeV image (b) 120-KeV image

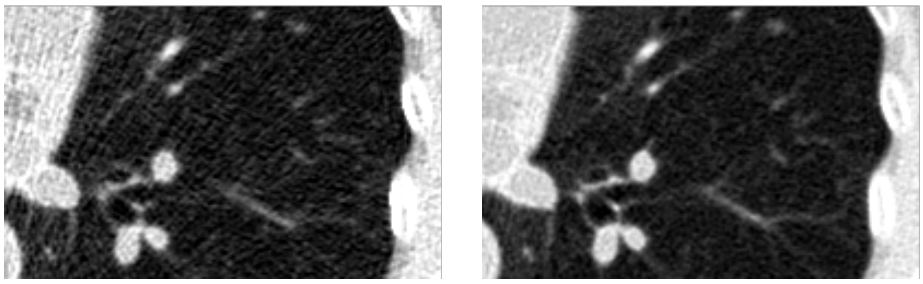

(c) 40-KeV zoomed-in (d) 120-KeV zoomed-in

Figure 5.10: 40 and 120 KeV monochromatic FBP images (row 1) and their zoomed-in views (row 2) of the same ROI as indicated by the red boxes in row 1 of Fig. 5.9, from full-scan data of the lung phantom, with display windows of [-1000, 1000] HU (row 1) and [-500, 500] HU (row 2).

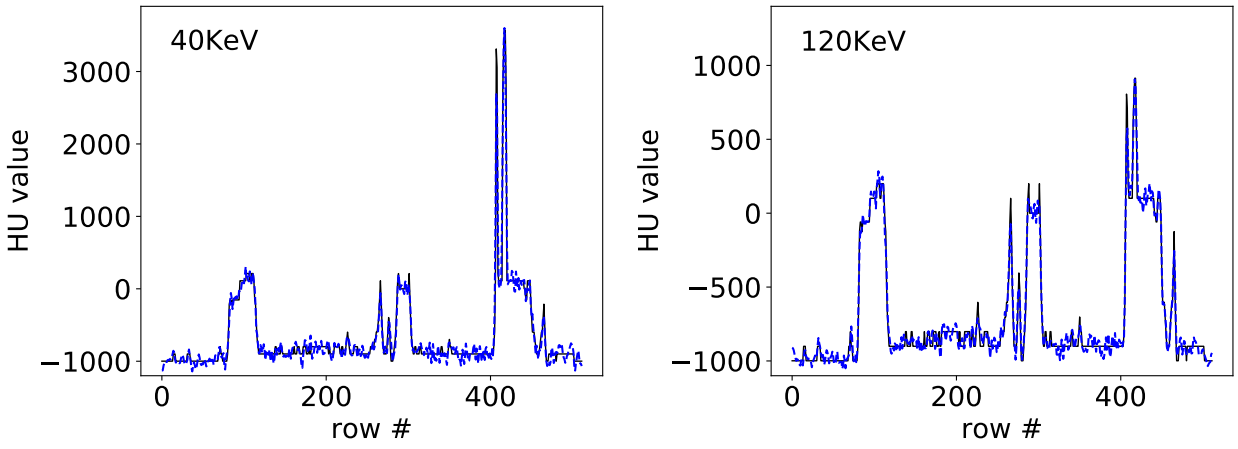

Figure 5.11: Profiles of FBP reconstructed (blue dashed) and truth (black solid) monochromatic images at 40 and 120 KeV along the vertical yellow line indicated in row 1 of Fig. 5.10 from full-scan data of the lung phantom

background of the water basis image.

Monochromatic images at 40 and 120 KeV and their zoomed-in views of the same ROI as in Fig. 5.9 are shown in Fig. 5.10. The bone contrast in the 40 KeV image (Fig. 5.10a) is visibly higher than the 120 KeV one, displayed with a same display window of [-1000, 1000] HU. No significant cupping or banding artifacts are visible in either images. Their ROIs are shown with a narrow display window of [-1000, 200] HU to highlight the lung nodules in the dark background. While the big nodules are visible in both ROI images, some tiny ones are buried in the noise. Fig. 5.11 shows the profile plots along the vertical yellow line on the monochromatic images in row 1 of Fig. 5.10. A good agreement in pixel HU values between the FBP reconstructed and truth monochromatic images at both energy levels can be observed.

5.4.2 ASD-NC-POCS reconstruction

Demonstration of reconstruction convergence

We first use a reconstruction from the DE-472 phantom data of the full-scan configuration to demonstrate that the practical convergence conditions in equations (5.10)-(5.12) can be met by the ASD-NC-POCS algorithm. The reconstruction is carried out with $\epsilon = 0.0170$, and we display in Figs. 5.12 and 5.13 convergence metrics $\bar{D}(\mathbf{b}^{(n)})$, $\bar{\Delta}\Psi(\mathbf{b}^{(n)})$, and $c_\alpha(\mathbf{b}^{(n)})$, and the reconstruction-error metric $\bar{\Delta}_{\mathbf{f}}(\mathbf{f}_m^{(n)})$, as functions of iteration number n. It can be observed that the ASD-NC-POCS algorithm converges to meet the practical convergence conditions.

Selection of parameter ϵ

For each of DE-472 and lung phantoms, we perform reconstructions from its data by using the ASD-NC-POCS algorithm for multiple values of ϵ, calculate metrics Θ and Σ, as defined

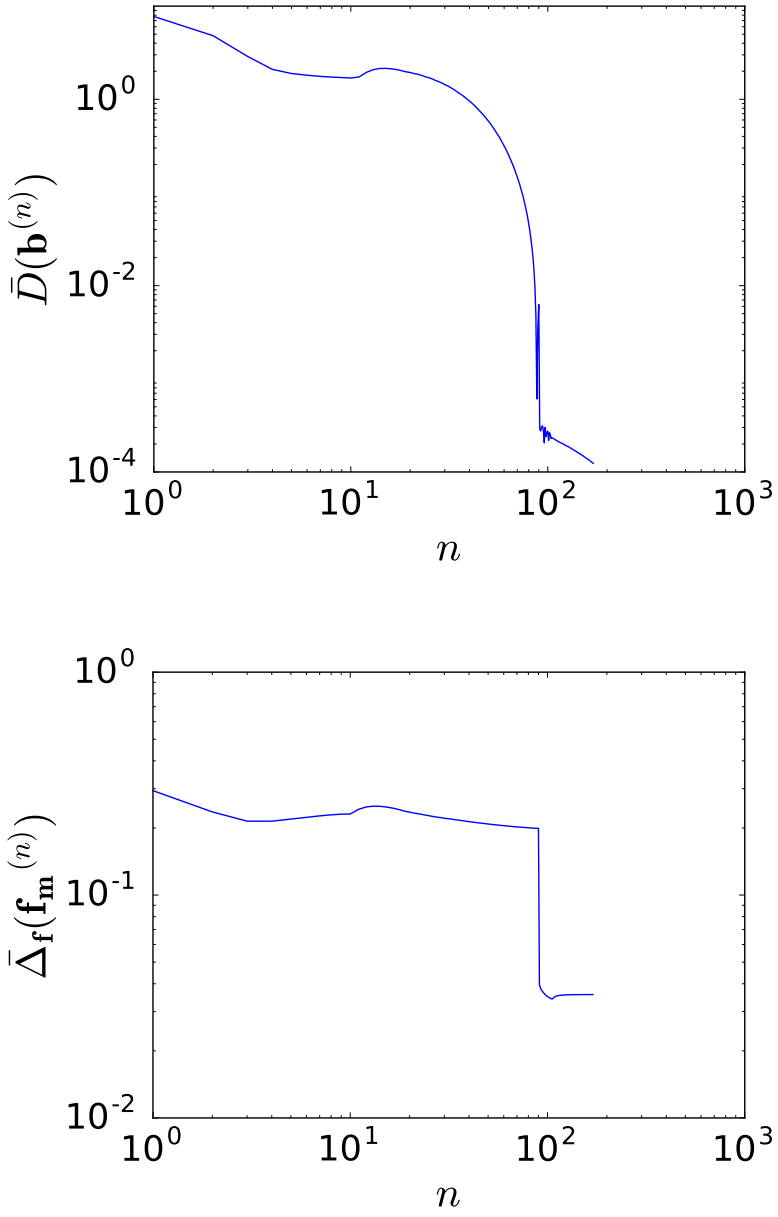

Figure 5.12: Convergence metric $\bar{D}(\mathbf{b}^{(n)})$ and reconstruction-error $\bar{\Delta}_{\mathbf{f}}(\mathbf{f}_m^{(n)})$ of 80-KeV monochromatic image as functions of iteration number n, obtained with $\epsilon = 0.0170$ for the DE-472 phantom data in the full-scan characterization study.

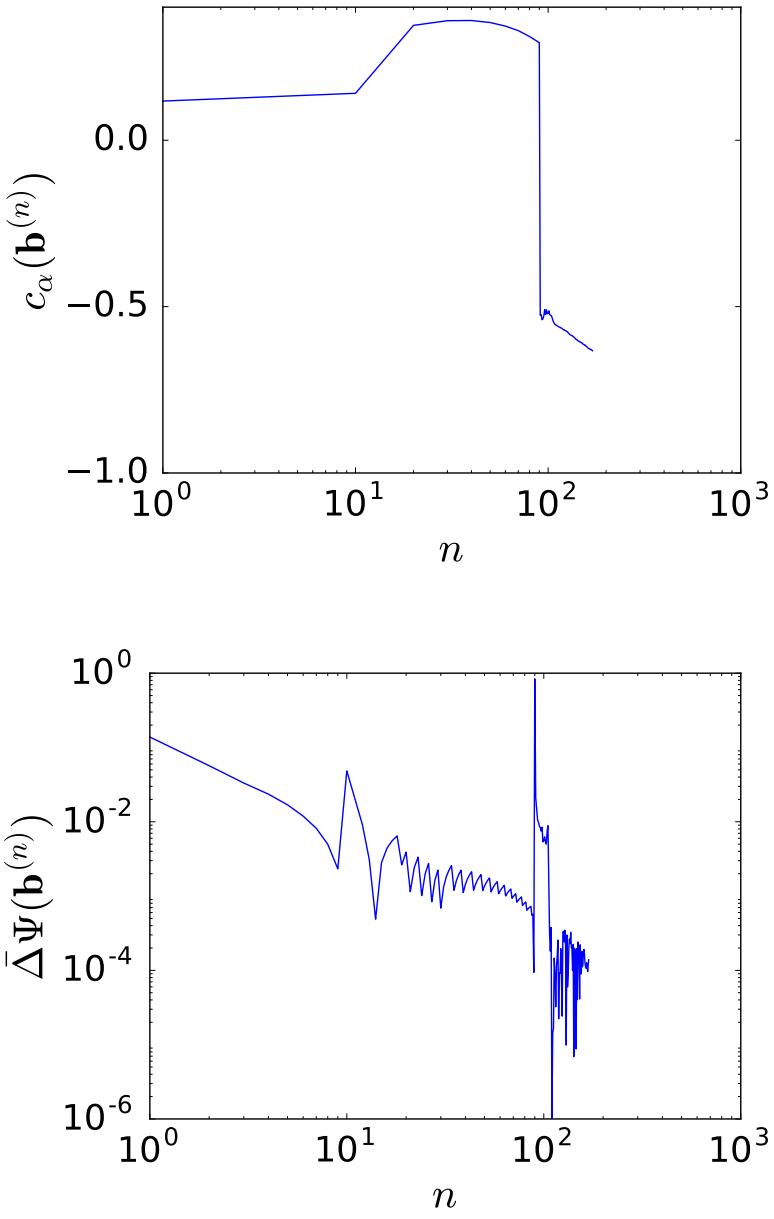

Figure 5.13: Convergence metrics $\bar{\Delta}\Psi(\mathbf{b}^{(n)})$ and $c_\alpha(\mathbf{b}^{(n)})$ as functions of iteration number n, obtained with $\epsilon = 0.0170$ for the DE-472 phantom data in the full-scan characterization study.

in equations (5.8) and (5.9), from ROIs in monochromatic energy reconstructions at 80 and 120 KeV, and select the value of ϵ that yields the lowest Θ and Σ. Using the strategy, we have determined $\epsilon = 0.0170$ and $\epsilon = 0.0111$ in the characterization study using the DE-472 and lung phantoms, respectively.

Reconstructed images

Using the program parameters, i.e., image pixel, spectra, matrices $\mathcal{A}^{[s]}$, and ϵ, determined, we reconstructed basis and monochromatic images of the DE-472 and lung phantoms.

DE-472 phantom results In Fig. 5.14, we display reconstructed basis images and their zoomed-in ROI images from the full-scan data of the DE-472 phantom. In Fig. 5.15, we display the monochromatic images at 40 and 120 KeV and their zoomed-in ROI images. The profiles plots of the monochromatic images are shown in Fig. 5.16.

Lung phantom results In Fig. 5.18, we display reconstructed basis images and their zoomed-in ROI images from the full-scan data of the lung phantom. In Fig. 5.19, we display the monochromatic images at 40 and 120 KeV and their zoomed-in ROI images. The profiles plots of the monochromatic images are shown in Fig. 5.20.

Analysis The water-basis image retains mostly the water and soft-tissue background, while high contrast inserts and bony structures appear largely in the bone-basis image. No significant cupping or band artifacts are visible in the monochromatic images, especially for the DE-472 phantom that contains high concentration iodine and calcium inserts. ROIs of the DE-472 phantom with a narrow display window show air-bubble contrast and discernible contrast inserts with the lowest concentration of iodine and calcium in the phantom. Meanwhile, ROIs of the lung phantom show details of the lung nodules in the dark background, with a display window to highlight these features.

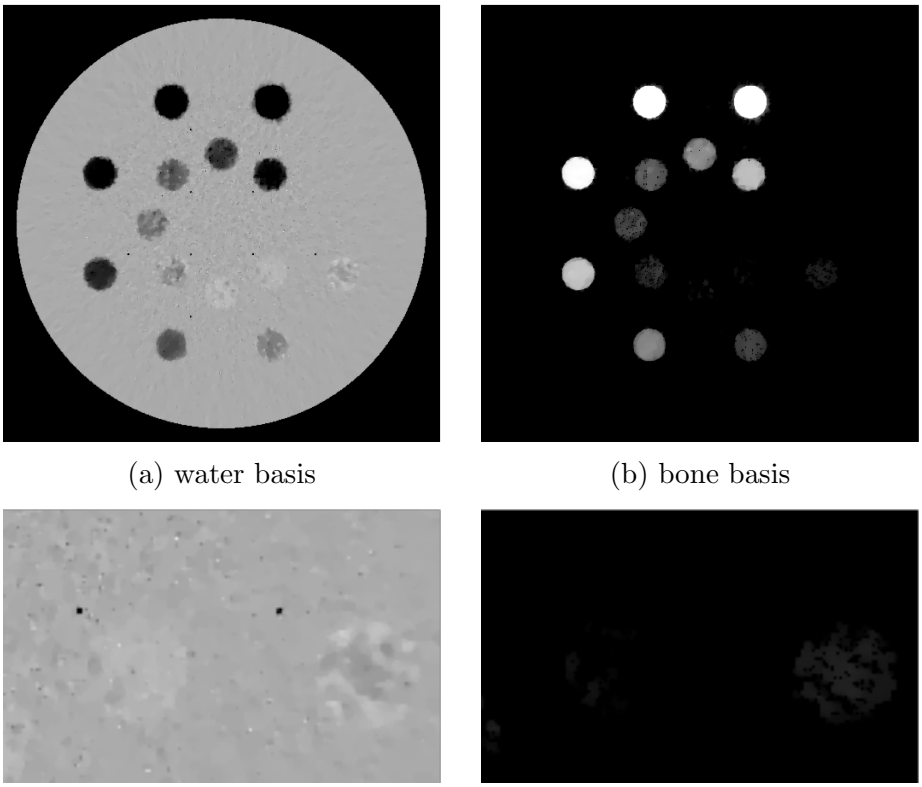

(a) water basis (b) bone basis

(c) water basis, zoomed-in (d) bone basis, zoomed-in

Figure 5.14: Water and bone basis ASD-NC-POCS images (row 1) and zoomed-in views (row 2) of the same ROI as indicated by the red boxes in row 1 of Fig. 5.6, from full-scan data of the DE-472 phantom, with a display windows of [0, 1.5] for both rows.

For acquiring a quantitative impression of the reconstructions, we also plot in Figs. 5.16 and 5.20 profiles of truth and reconstructed monochromatic images along the horizontal and vertical lines indicated in the Figs. 5.7 and 5.10. Overall, quantitative agreement in monochromatic images is observed for both phantoms, while some Gibbs effect can be observed in reconstructions of the DE-472 phantom, and the profiles reveal that the 40-KeV monochromatic images are of contrast higher than that of the 120-KeV counterparts.

It is of practical interest in inspecting how the reconstruction of monochromatic image evolves as iterations increase. Without loss of generality, we show in Figs. 5.17 and 5.21 reconstructions of 120-KeV monochromatic image at intermediate iterations for both phantoms. It appears that reconstructions at as early as iteration 50 can visually resemble the

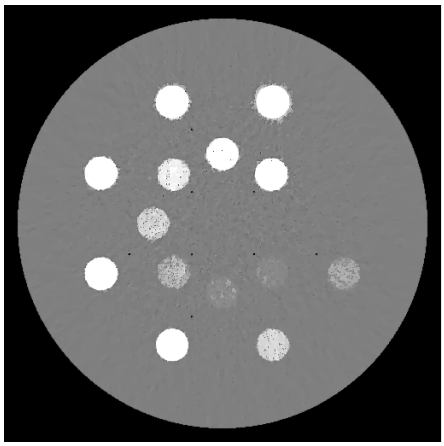

(a) 40-KeV image

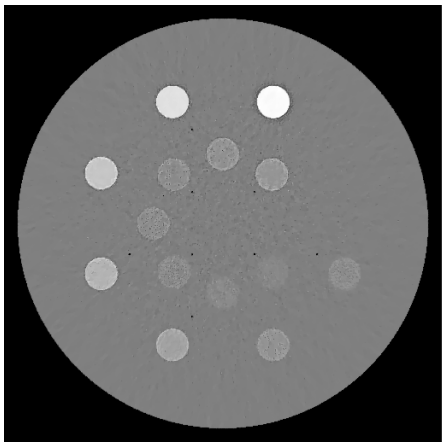

(b) 120-KeV image

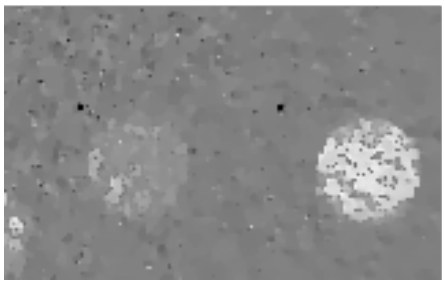

(c) 40-KeV zoomed-in

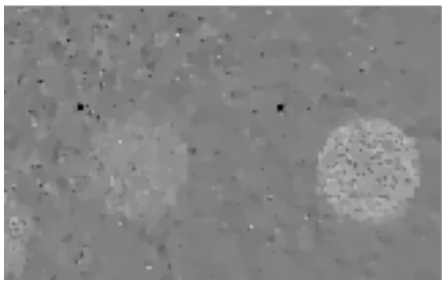

(d) 120-KeV zoomed-in

Figure 5.15: 40- and 120-KeV monochromatic ASD-NC-POCS images (row 1) and their zoomed-in views (row 2) of the same ROI as indicated by the red boxes in row 1 of Fig. 5.6, from full-scan data of the DE-472 phantom, with display windows of [-1000, 1000] HU (row 1) and [-500, 500] HU (row 2).

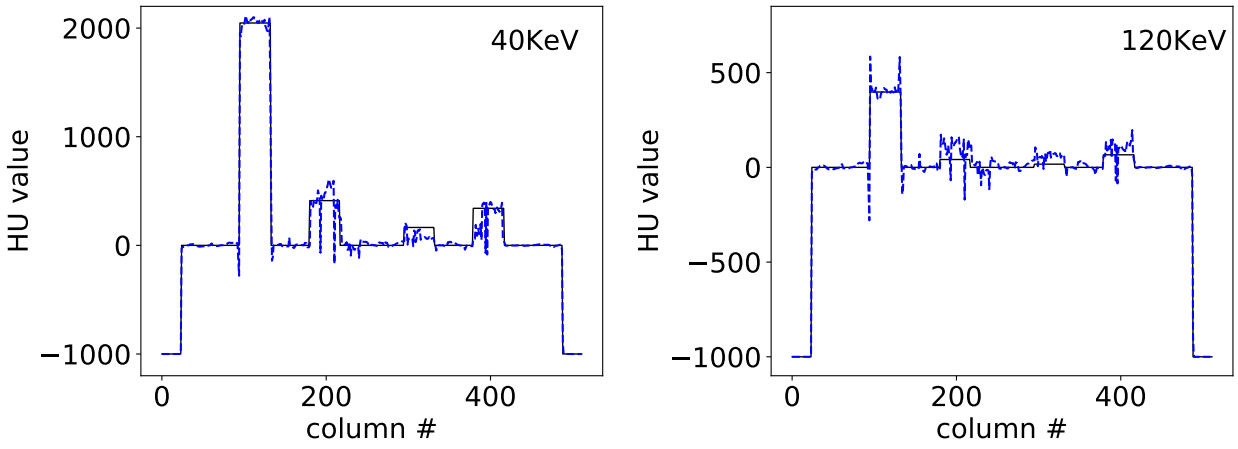

Figure 5.16: Profiles of ASD-NC-POCS reconstructed (blue dashed) and truth (black solid) monochromatic images at 40 and 120 KeV along the horizontal indicated in row 1 of Fig. 5.7 from full-scan data of the DE-472 phantom

respective convergent reconstructions. Similar observations can also be made for monochromatic energy images reconstructed at other energies.

5.5 Discussion

In this chapter, we have characterized the optimization-based reconstruction by using inconsistent simulation data from a full-scan configuration. Decomposition error and statistical noise were the two sources of inconsistencies in this characterization study, which are regarded as the dominant factors in multispectral CT reconstruction. The full-scan configuration was first employed in order to provide sufficient sampling conditions and to serve as the benchmark for non-standard scan configurations investigated in the next chapter. Further, an existing method including the data domain decomposition can be applied to the full-scan data that satisfied the ray-consistency condition, and be compared to the proposed method. The results suggest that converged solution to the optimization program might be obtained by using the ASD-NC-POCS algorithm. The reconstructed basis images showed good material separation, indicating the effectiveness of the decomposition model and the non-linear update step in the one-step reconstruction approach. Further, the monochromatic images were in good quantitative agreement with the truth images. Compared to the existing method using the data-domain decomposition and FBP-like algorithm, the ASD-NC-POCS algorithm can reconstruct images with suppressed noise levels in the images, especially for images with more uniform background and features. The intermediate iteration results for both phantoms suggest that images from iterations as early as 50 can already visually resemble the converged solutions, indicating application potential of the ASD-NC-POCS algorithm to practical situations.

Additional inconsistencies can be incorporated into the forward model to generate data that are closer to the real data. For example, estimated X-ray spectra data [130], instead of the exact ones used in generating the data, can be fed into the reconstruction. For real data

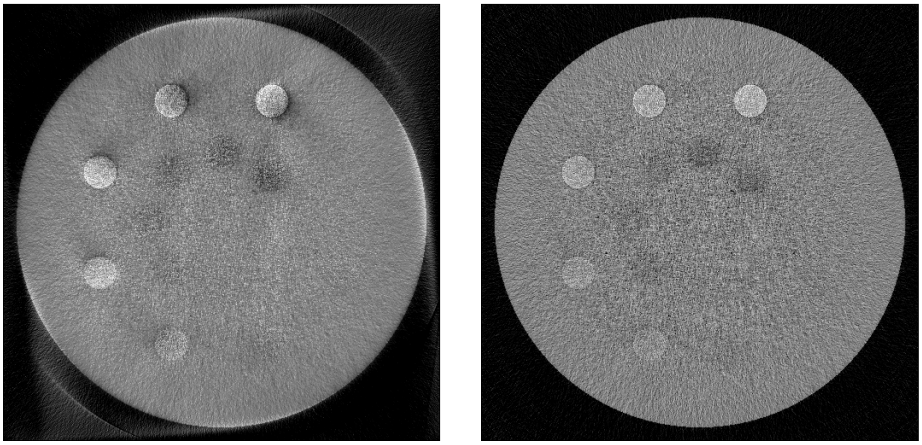

(a) iteration 2

(b) iteration 10

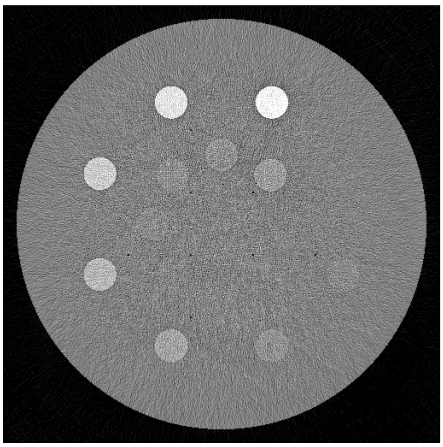

(c) iteration 30

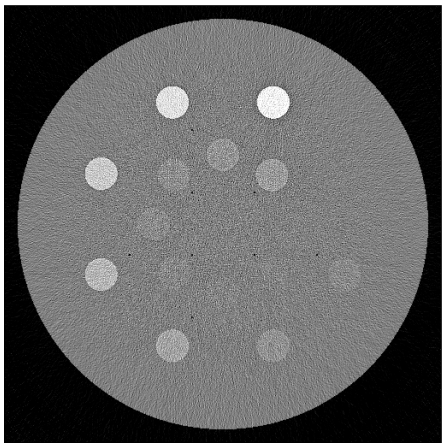

(d) iteration 50

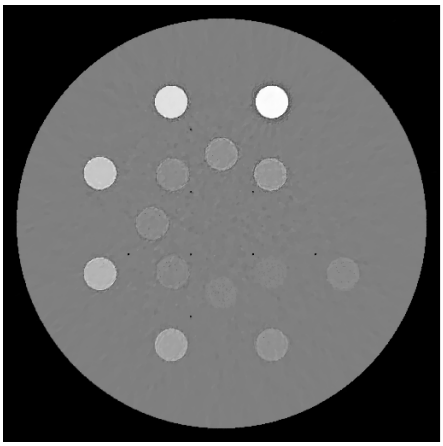

(e) iteration 110

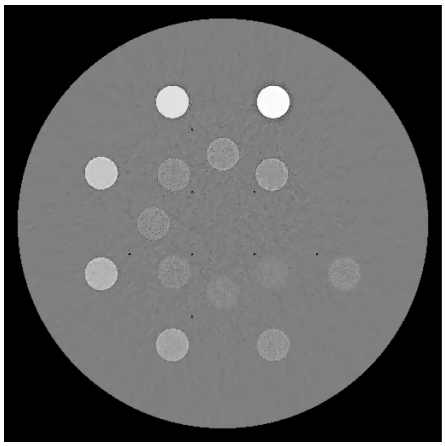

(f) $\mathbf{f}_{120\text{KeV}}$

Figure 5.17: 120-KeV monochromatic images of the DE-472 phantom from full-scan data at iterations 2, 10, 30, 50, and 110, along with the convergent reconstructions $\mathbf{f}_{120\text{KeV}}$. Display window: [-1000, 1000] HU.

(a) water basis

(b) bone basis

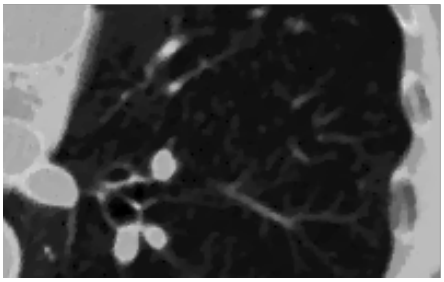

(c) water basis, zoomed-in

(d) bone basis, zoomed-in

Figure 5.18: Water and bone basis images (row 1) and zoomed-in views of ROI images (row 2) enclosed by boxes in row 1 from full-scan data of the DE-472 phantom, with a display windows of [0, 1.5] (row 1).

(a) 40-KeV image

(b) 120-KeV image

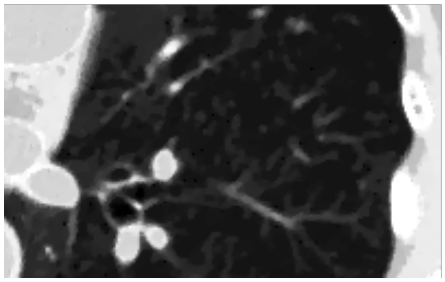

(c) 40-KeV zoomed-in

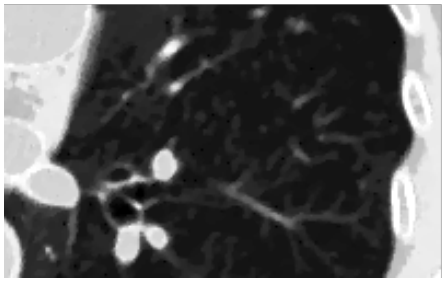

(d) 120-KeV zoomed-in

Figure 5.19: 40- and 120-KeV monochromatic images (row 1) and their zoomed-in views of ROI images (row 2) enclosed by boxes in row 1, from full-scan data of the DE-472 phantom, with display windows of [-1000, 1000] HU (row 1) and [-500, 500] HU (row 2).

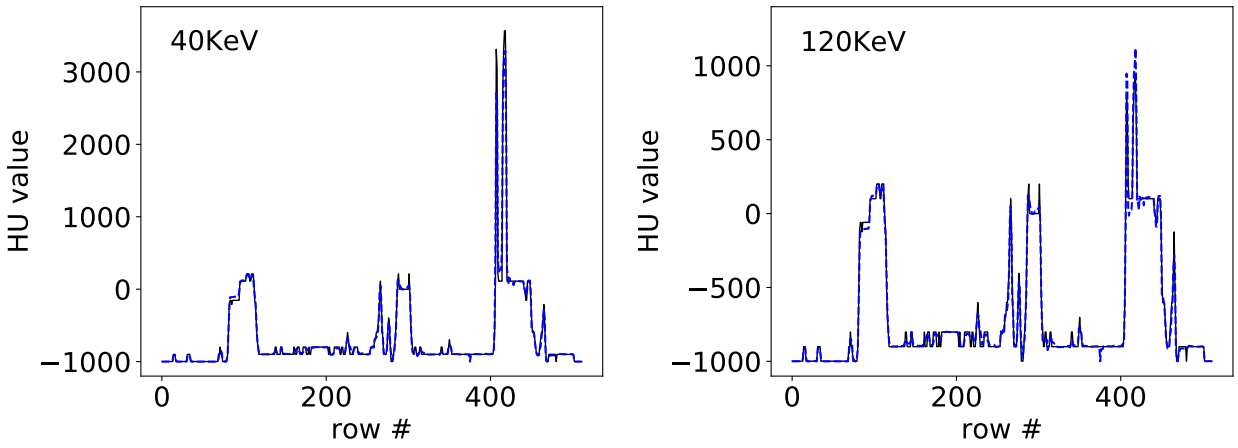

Figure 5.20: Profiles of reconstructed (blue dashed) and truth (black solid) monochromatic images at 40- and 120-KeV along the horizontal indicated in row 1 of Fig. 5.19 from full-scan data of the DE-472 phantom

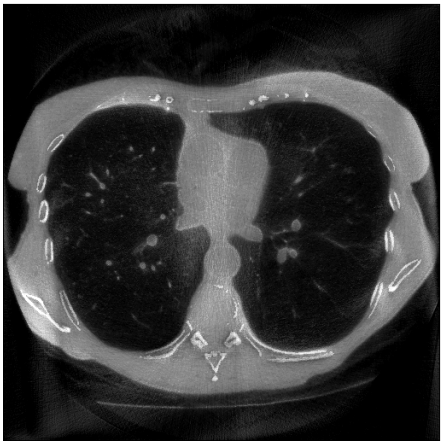

(a) iteration 2

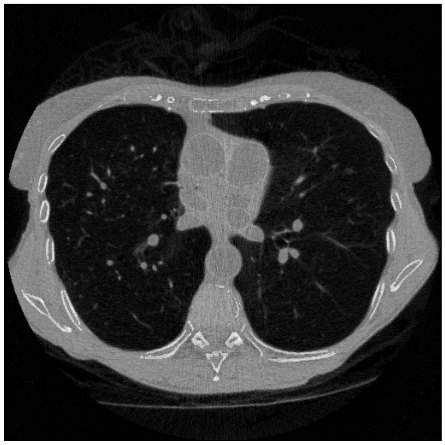

(b) iteration 10

(c) iteration 30

(d) iteration 50

(e) iteration 110

(f) $\mathbf{f}_{120\text{KeV}}$

Figure 5.21: 120-KeV monochromatic images of the lung phantom from full-scan data at iterations 2, 10, 30, 50, and 110, along with the convergent reconstructions $\mathbf{f}_{120\text{KeV}}$. Display window: [-1000, 1000] HU.

from a CT scanner, we often do not have the exact X-ray spectra of the system, which is the product of the incident X-ray beam and the detector energy response. Data can also be generated from a continuous-to-discrete model, causing potentially partial-volume effects in the image. Further, scattering would contaminate the data in a cone-beam geometry with a flat panel detector. Meanwhile, algorithms are available to decompose the measured KVp sinogram into basis sinogram more efficiently and handles the noise better with weighting schemes [82].

CHAPTER 6

NON-STANDARD SCAN CONFIGURATION SIMULATION STUDY

6.1 Introduction

One of the main goals of this dissertation work is to make multispectral CT applications more accessible, through enabling multispectral scan configurations with conventional CT systems. As we have demonstrated in the full-scan characterization study, multiple spectral data sets can be collected using a regular X-ray tube at different KVp's and a conventional energy-integrating detector, and reconstructed into basis images and monochromatic images. However, the full-scan configuration might not be desirable for clinical applications, since it almost doubles the radiation dose to the patient and the total scanning time, compared to a conventional CT scan. As a result, we propose four non-standard scan configurations, enabled by the ASD-NC-POCS algorithm, that might be of practical interest in multispectral CT.

One-step inversion approach for multispectral CT reconstruction gets rid of the ray-consistency condition when dealing with the non-linear model and no longer requires multiple measurements to be made for one ray with different X-ray spectra, as it combines the decomposition and reconstruction together. Consequently, we can design flexible configurations on how the multispectral data can be acquired, which are not possible with other methods where decomposition and reconstruction are treated as two isolated problems. In this work, the proposed optimization-based reconstruction method, especially the ASD-NC-POCS algorithm, is used and taken advantage of to enable the non-standard scan configurations for multispectral CT.

The non-standard scan configurations, categorized into two groups, are studied and characterized in this chapter. The first group of scan configurations involves changing the firing

patterns of the X-ray tube, compared to the full-scan configuration, and is thus referred to as the configurations with varying angular coverage. More sparse firing patterns are proposed, so that both dose and time can be reduced. The second group involves modification to the X-ray beam's illumination coverage at each projection and is referred to as the configurations with varying illumination coverages. Similarly, with reduced illumination coverages, the radiation dose is expected to be lowered as well.

Based on the full-scan characterization study in the previous chapter, we carry out the characterization studies with non-standard scan configurations, so that the scan configuration is the only variable and that the full-scan results can be used as the benchmark reference. Therefore, inconsistent data are generated from two digital phantoms, according to each configuration, and are reconstructed using the ASD-NC-POCS algorithm to basis image and monochromatic images for evaluation.

6.2 Study design

6.2.1 Data generation

Physical scanning configuration

Different scan configurations are being investigated in this chapter, but they all assume a 2D fan-beam geometry based on a OBI CBCT unit, with the same physical dimensions as used in the full scan. The source-to-center-of-rotation and source-to-detector distances are 1000 mm and 1500 mm, respectively, and a linear detector of 400 mm consisting of 1024 bins of 0.39 mm bin size is used. Table 6.1 summarizes the physical dimensions shared in all studies.

Table 6.1: Physical dimensions of the non-standard scan configurations.

Physical quantity	dimension
source-to-detector distance	1500 mm
source-to-center-of-rotation distance	1000 mm
FOV	265 mm
detector length	400 mm
detector bin size	0.39 mm

Spectra

Low and high KVp spectra at 80 and 140 KVp are used. Incident beam spectra are generated using the TASMICS worksheet and combined with the linear detector-energy response. A single X-ray spectra at each KVp is assumed for all rays in the spectral set, as no bow-tie filter, hence ray-dependence of the spectrum, is simulated. Fig. 6.1 shows the low (thin, blue line) and high (thick, red line) spectra after normalization.

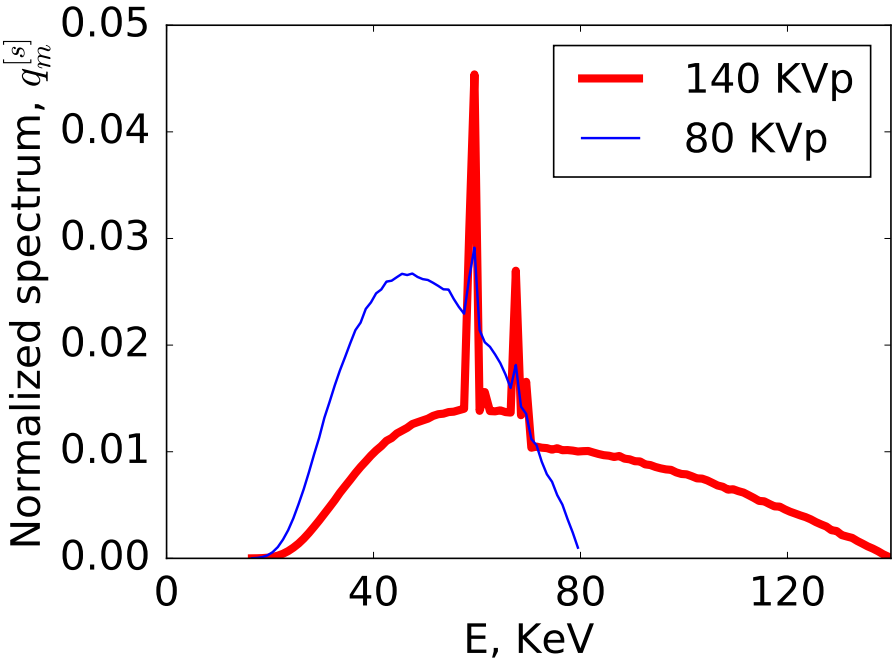

Figure 6.1: Normalized X-ray spectrum $q_m^{[s]}$. Low (thin, blue line) and high (thick, red line) energy spectra at 80 and 140 KVp are used in the verification study.

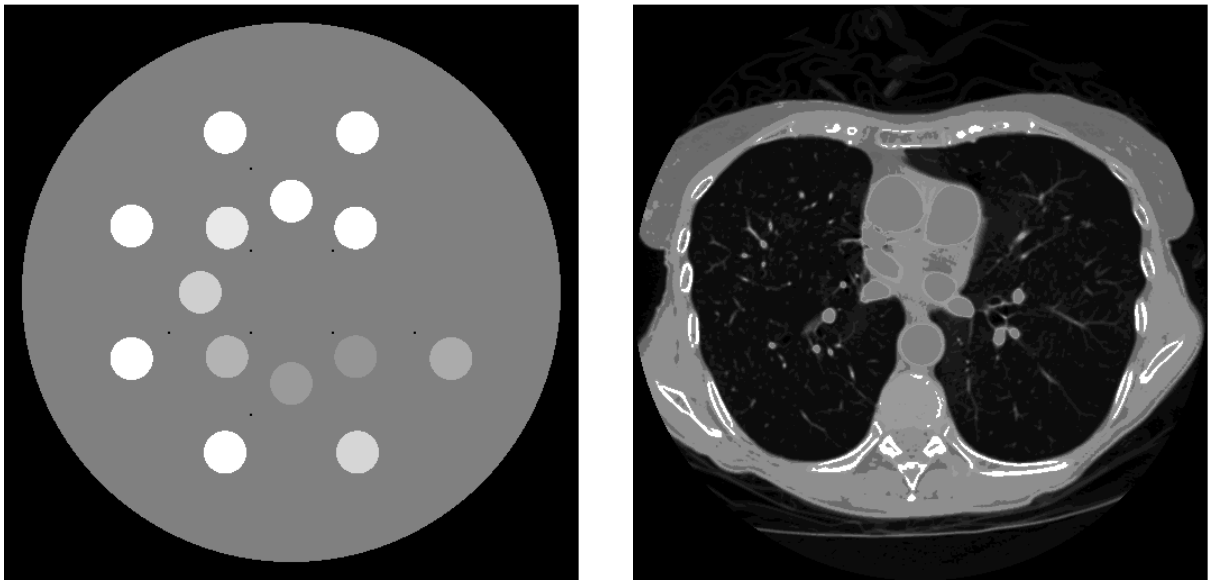

(a) DE-472 phantom (b) lung phantom

Figure 6.2: Monochromatic images of the DE-472 (a) and lung (b) phantoms as evaluated at 40 KeV, with display window of [-1000, 1000] HU.

Phantoms

The DE-472 phantom and lung phantom are used in the studies. Both phantoms are on a 512×512 array with 0.49-mm square pixels. The materials used in the phantoms are summarized in Table 5.2, while the phantoms are illustrated in Fig. 6.2.

Forward model

The DD data model with the monochromatic images in equation (2.13) is combined with the Poisson noise realization to generate the data as

$$\tilde{g}_j'^{[s]} = -\ln \frac{\sum_m \text{Poisson}\left[\phi\, q_m^{[s]} \exp\left(-\sum_i a_{ji}^{[s]} f_{im}'\right)\right]}{\phi \sum_m q_m^{[s]}}, \tag{6.1}$$

where the fluence level ϕ is scaled individually for each non-standard scan configuration to match the total dose level with the full-scan characterization study. For example, if a sparse-

view configuration is used with half the views from the full-scan configuration for each KVp scan, the fluence level is doubled from 2×10^4 to 4×10^4 photons per ray in the air scan.

6.2.2 Image reconstruction

We use the same reconstruction method as used in the full-scan characterization method. The non-convex optimization program is used for the image reconstruction as

$$\begin{aligned} \mathbf{b}^* = & \underset{\mathbf{b}}{\operatorname{argmin}} \sum_k ||\mathbf{b}_k||_{\mathrm{TV}} \\ \text{s. t.} \quad & D(\mathbf{g}(\mathbf{b}), \mathbf{g}_{\mathcal{M}}) \leq \epsilon, \\ & \mathbf{b} \succeq 0, \end{aligned} \tag{6.2}$$

where

$$D(\mathbf{g}(\mathbf{b}), \mathbf{g}_{\mathcal{M}}) = \left(\frac{\sum_s ||\mathbf{g}^{[s]}(\mathbf{b}) - \mathbf{g}^{[s]}_{\mathcal{M}}||_2^2}{\sum_s ||\mathbf{g}^{[s]}_{\mathcal{M}}||_2^2} \right)^{1/2},$$

and

$$g_j^{[s]}(\mathbf{b}) = -\ln \sum_m q_{jm}^{[s]} \exp\left(-\sum_k \mu_{km} \sum_i a_{ji}^{[s]} b_{ki} \right).$$

The ASD-NC-POCS algorithm in Algorithm 2 is used for reconstructing water and bone basis images, with the same algorithm parameters adopted in the full-scan study. Program parameters, such as image voxel size and X-ray spectra, are identical to those used in the data generation. The system matrices $A^{[s]}$ are different for each individual non-standard scan configuration, and will be discussed in each respective configuration. The data fidelity parameter ϵ is determined by use of the same strategy used in the full-scan study and described in Section 5.3.2. To summarize, "biases" and "standard deviations" within pre-defined ROIs for each phantom are calculated based on reconstructed monochromatic images

at 80 and 140 KeV, according to equations (5.6)-(5.9), for a number of ϵ values and the ϵ that yields the lowest Θ and Σ is selected.

In addition, the same practical convergence conditions are employed here as those in the full-scan characterization studies, since the same types of inconsistencies, i.e., decomposition error and statistical noise, are considered. Namely, the conditions are

$$\bar{D}(\mathbf{b}^{(n)}) < 10^{-3}, \tag{6.3}$$

$$\bar{\Delta}\Psi(\mathbf{b}^{(n)}) < 10^{-3}, \tag{6.4}$$

$$c_{\alpha}(\mathbf{b}^{(n)}) < -0.5. \tag{6.5}$$

6.3 Configurations with varying angular coverages

We first consider two non-standard scan configurations with varying angular coverages, referred to as the sparse-view and limited-angular-range configurations. In both cases, a reduced set of X-ray firing positions compared to the full-scan configuration is used, while the illumination coverage at each view is still the same. More importantly, the implementation of the two configurations does not require any hardware addition to existing CT systems with a conventional X-ray tube and an energy-integrating detector.

6.3.1 Sparse-view scan

Study parameters

In the sparse-view configuration, each of the low- and high-KVp data sets still has the same 2π coverage as in the full-scan case, but are sparsely sampled with 320 views evenly distributed. Instead of overlapping rays, the view angles from low- and high-KVp scans interlace with each other, as schematically shown in Fig. 6.3. This is equivalent to down-sampling from the full-scan configuration with alternating selections from the two KVp scans,

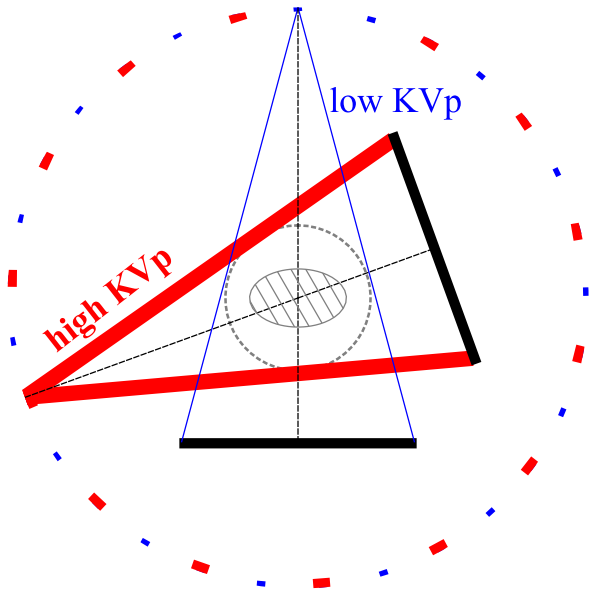

Figure 6.3: Sparse-view scan configurations where low- (thin, blue dot) and high- (thick, red dot) KVp data are collected at two sets of interlaced sparse views uniformly distributed over 2π.

e.g., views 0, 2, 4, ... from low KVp and views 1, 3, 5, ... from high KVp. Such configuration is of potential clinical interest for enabling fast and low-dose multispectral CT applications, while not requiring strict spatial registration of low- and high-KVp rays.

Dose reduction is one of the motivations for enabling the sparse-view scan configuration. However, for the purpose of characterizing the configuration and comparing to the full-scan benchmark, the statistical noise is kept the same in this study and we focus on any potential problems from sampling conditions. As a result, the fluence level is set at 4×10^4 photons per ray.

System matrices $\mathcal{A}^{[1]}$ and $\mathcal{A}^{[2]}$ are of identical dimensions with $J^{[1]} = J^{[2]} = 320 \times 1024$ and $I = 512 \times 512$. Using the same strategy detailed in the full-scan characterization study in Section 5.3.2, we select $\epsilon = 0.0116$ and 0.008, respectively, for the DE-472 and lung phantom studies below.

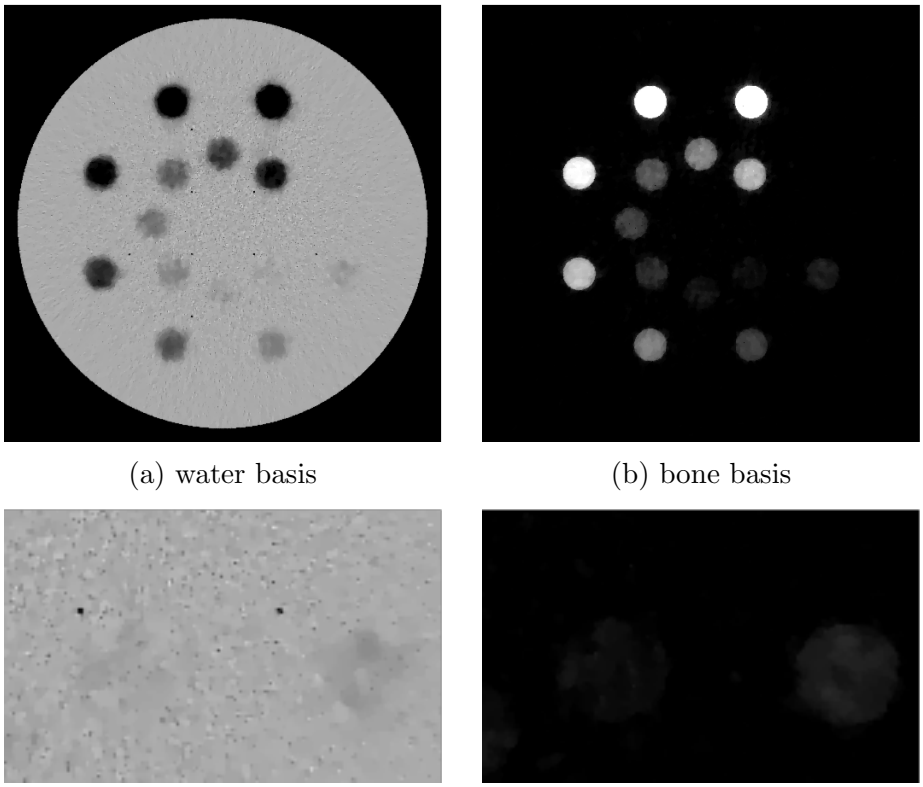

(a) water basis (b) bone basis

(c) water basis, zoomed-in (d) bone basis, zoomed-in

Figure 6.4: Water and bone basis ASD-NC-POCS images (row 1) and zoomed-in views (row 2) of the same ROI as indicated by the red boxes in row 1 of Fig. 5.6, from sparse-view-scan data of the DE-472 phantoms, with a display windows of [0, 1.5] for both rows.

Study results

We show in Figs. 6.4 and 6.5 reconstruction results of basis and monochromatic, respectively, images for the DE-472 phantom from data acquired with the sparse-view configuration, and Figs. 6.7 and 6.8 reconstruction results for the lung phantom from sparse-view scan data. Reconstructed basis images and monochromatic images at 40 and 120 KeV visually resemble their counterparts obtained from the full-scan data. Both basis images of each phantom show clear material separation, and the monochromatic images display an uniform background and no visible artifacts caused by non-linear spectral effect.

In addition to reconstruction visualization, we also plot in Figs. 6.6 and 6.9 profiles of the reconstructed and truth monochromatic images along the same horizontal and vertical

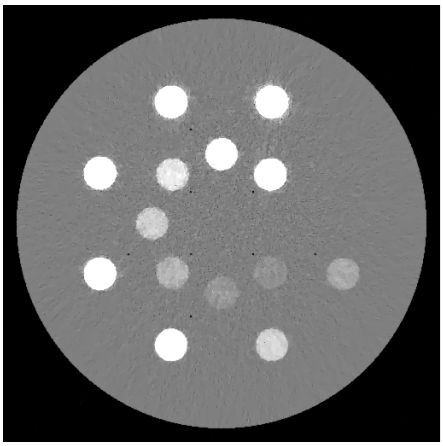

(a) 40-KeV image

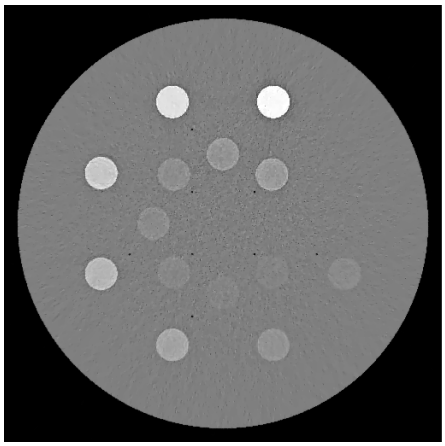

(b) 120-KeV image

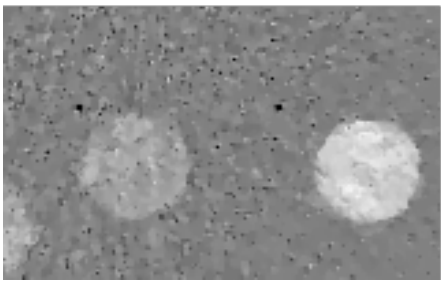

(c) 40-KeV zoomed-in

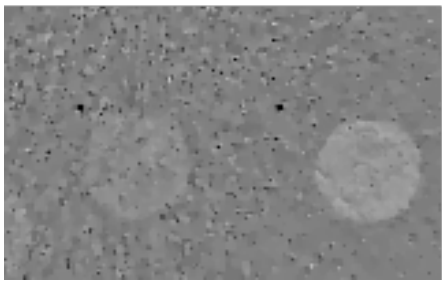

(d) 120-KeV zoomed-in

Figure 6.5: 40- and 120-KeV monochromatic ASD-NC-POCS images (row 1) and their zoomed-in views (row 2) of the same ROI as indicated by the red boxes in row 1 of Fig. 5.6, from sparse-view-scan data of the DE-472 phantoms, with display windows of [-1000, 1000] HU (row 1) and [-500, 500] HU (row 2).

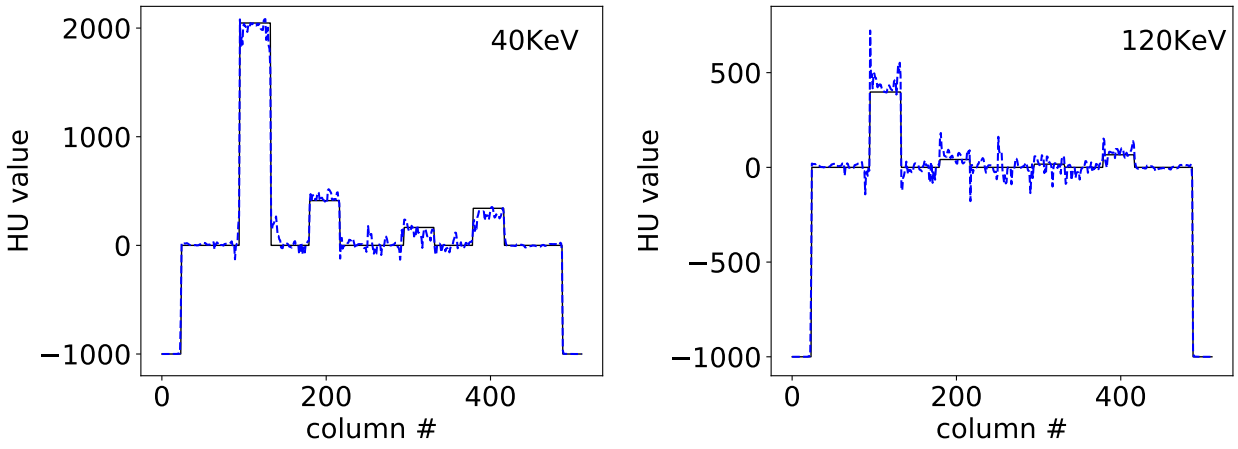

Figure 6.6: Profiles of ASD-NC-POCS reconstructed (blue dashed) and truth (black solid) monochromatic images at 40 and 120 KeV along the horizontal indicated in row 1 of Fig. 5.7 from sparse-view-scan data of the DE-472 phantoms

(a) water basis

(b) bone basis

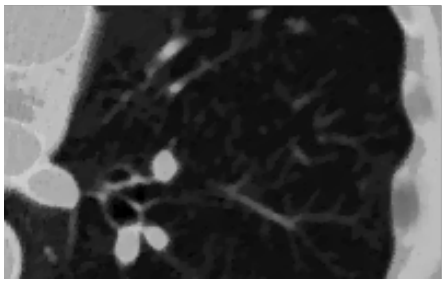

(c) water basis, zoomed-in

(d) bone basis, zoomed-in

Figure 6.7: Water and bone basis ASD-NC-POCS images (row 1) and zoomed-in views (row 2) of the same ROI as indicated by the red boxes in row 1 of Fig. 5.9, from sparse-view-scan data of the lung phantoms, with a display windows of [0, 1.5] for both rows.

(a) 40-KeV image

(b) 120-KeV image

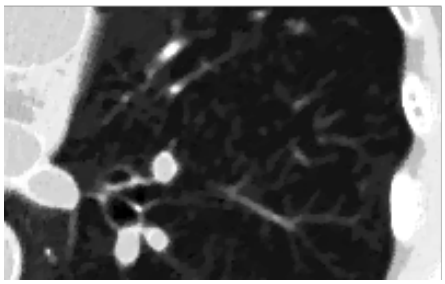

(c) 40-KeV zoomed-in

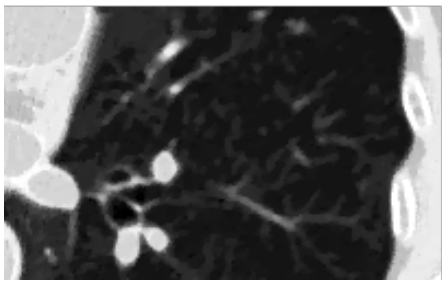

(d) 120-KeV zoomed-in

Figure 6.8: 40- and 120-KeV monochromatic ASD-NC-POCS images (row 1) and their zoomed-in views (row 2) of the same ROI as indicated by the red boxes in row 1 of Fig. 5.9, from sparse-view-scan data of the lung phantoms, with display windows of [-1000, 1000] HU (row 1) and [-500, 500] HU (row 2).

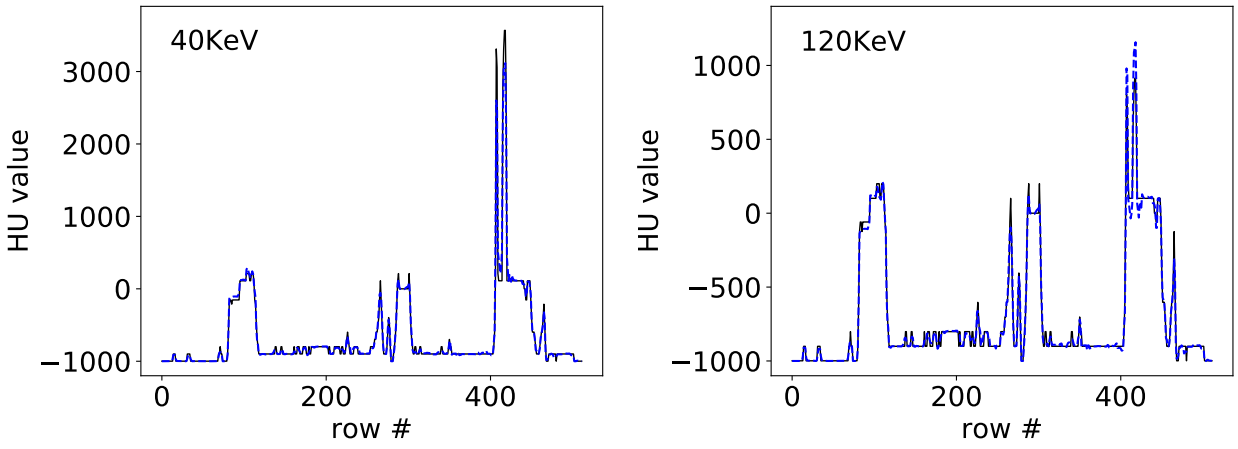

Figure 6.9: Profiles of ASD-NC-POCS reconstructed (blue dashed) and truth (black solid) monochromatic images at 40 and 120 KeV along the horizontal indicated in row 1 of Fig. 5.10 from sparse-view-scan data of the lung phantoms

lines indicated in the full-scan result in Figs. 5.7 and 5.10. It can be observed that for sparse-view-scan configuration, the agreement of monochromatic images reconstructed with the truth counterparts is comparable to that for the full-scan configuration in Fig. 5.20.

6.3.2 Limited-angular-range scan

Study parameters

In the limited-angular-range configuration, as shown in Fig. 6.10, each of the two adjacent angular spans covers 98°, thus forming a total of 196°-angular range, which corresponds to a short-scan angular range in this simulated OBI CBCT geometry under consideration. Low- or high-KVp data are generated individually at 174 views uniformly distributed over each of the two angular ranges, with a linear detector identical to that in the sparse-view configuration. Such configuration reduces the radiation dose and scan time significantly, compared to the full-scan configuration. More importantly, the reduced angular range makes it workflow-friendly and a viable option in clinical settings such as interventional radiology rooms.

The fluence level is set at 7.36×10^4 photons per ray to match the total dose level with the full-scan configurations. System matrices $\mathcal{A}^{[1]}$ and $\mathcal{A}^{[2]}$ are of identical dimensions with $J^{[1]} = J^{[2]} = 174 \times 1024$ and $I = 512 \times 512$. Again, using the strategy described in the full-scan study , we select $\epsilon = 0.0085$ and 0.0064, respectively, for the DE-472 and lung phantom studies below.

Study results

We show in Figs. 6.11 and 6.12 reconstruction results of basis and monochromatic, respectively, images for the DE-472 phantom from data acquired with the limited-angular-range configuration, and Figs. 6.14 and 6.15 reconstruction results for the lung phantom from

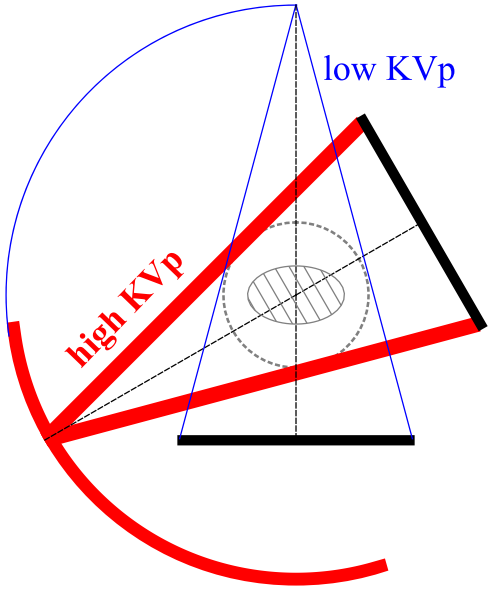

Figure 6.10: Limited-angular-range scan configurations, where low- (thin, blue line) and high- (thick, red line) KVp data are collected over two adjacent limited-angular ranges.

limited-angular-range scan data. Basis images and monochromatic image at 40 KeV for the DE-472 phantom show visible artifacts, due to the poor conditioning of the DD-data model for the limited-angular-range scan considered and the presence of high-concentration calcium and iodine inserts in the phantom. The monochromatic image at 120 KeV, as expected, reveals less artifacts. On the other hand, basis images and monochromatic images for the lung phantom appear to have artifacts much less prominent than those for the DE-472 phantom.

In addition to reconstruction visualization, we also plot in Figs. 6.13 and 6.16 profiles of the reconstructed and truth monochromatic images along the same horizontal and vertical lines indicated in the full-scan results in Figs. 5.15 and 5.19, which reveal quantitatively their differences. The lung-phantom reconstructions agree reasonably well with their truths for both configurations, whereas some differences between the DE-phantom reconstructions and truth counterparts can be observed especially for the limited-angular-range configuration.

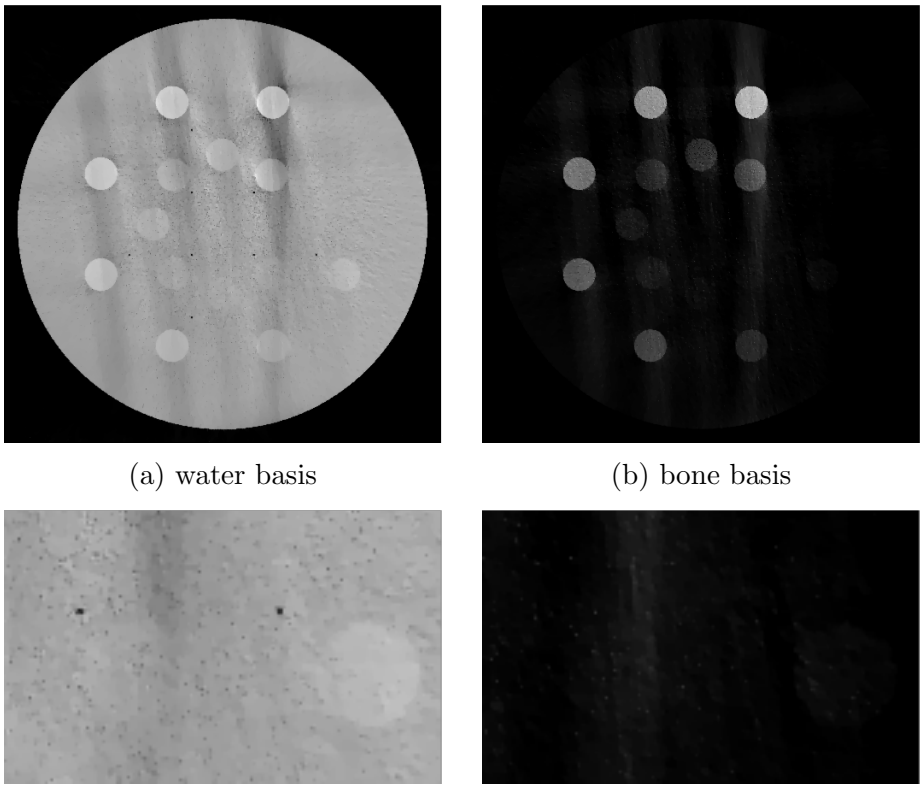

(a) water basis (b) bone basis

(c) water basis, zoomed-in (d) bone basis, zoomed-in

Figure 6.11: Water and bone basis ASD-NC-POCS images (row 1) and zoomed-in views (row 2) of the same ROI as indicated by the red boxes in row 1 of Fig. 5.6, from limited-angular-range-scan data of the DE-472 phantoms, with a display windows of [0, 1.5] for both rows.

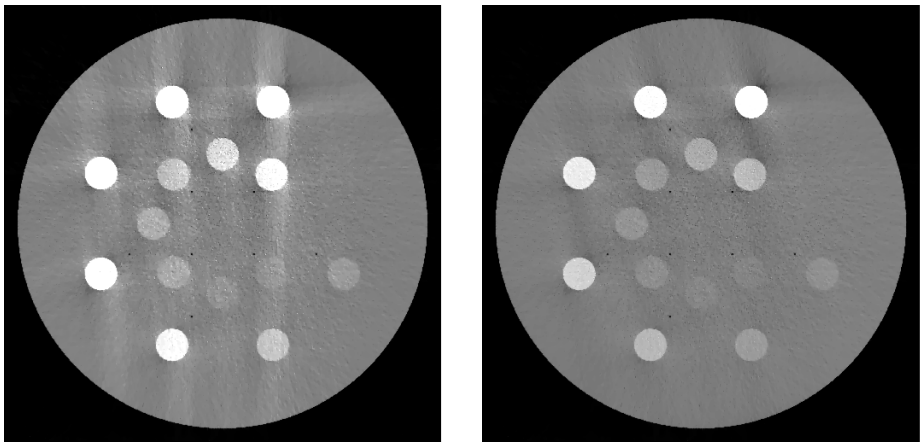

(a) 40-KeV image (b) 120-KeV image

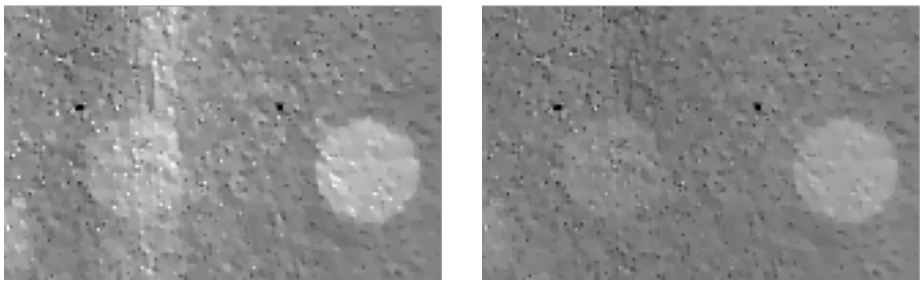

(c) 40-KeV zoomed-in (d) 120-KeV zoomed-in

Figure 6.12: 40- and 120-KeV monochromatic ASD-NC-POCS images (row 1) and their zoomed-in views (row 2) of the same ROI as indicated by the red boxes in row 1 of Fig. 5.6, from limited-angular-range-scan data of the DE-472 phantoms, with display windows of [-1000, 1000] HU (row 1) and [-500, 500] HU (row 2).

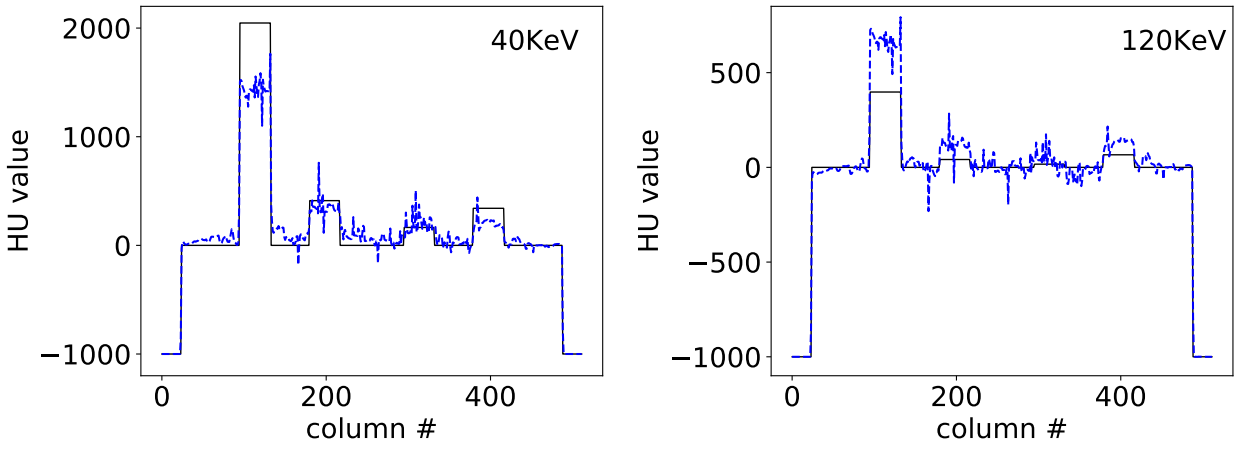

Figure 6.13: Profiles of ASD-NC-POCS reconstructed (blue dashed) and truth (black solid) monochromatic images at 40 and 120 KeV along the horizontal indicated in row 1 of Fig. 5.7 from limited-angular-range-scan data of the DE-472 phantoms

(a) water basis

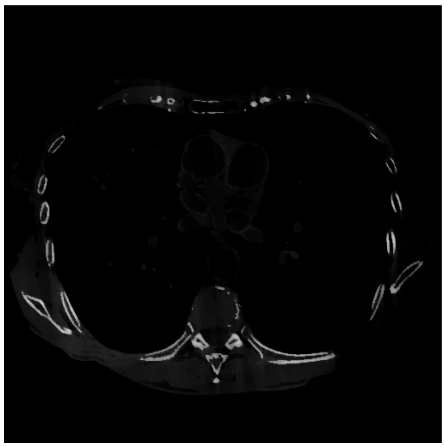

(b) bone basis

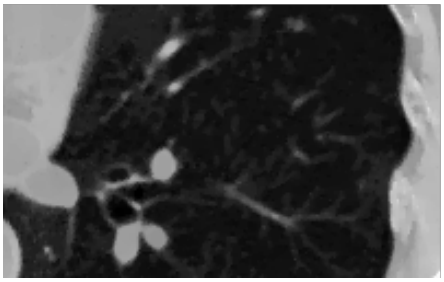

(c) water basis, zoomed-in

(d) bone basis, zoomed-in

Figure 6.14: Water and bone basis ASD-NC-POCS images (row 1) and zoomed-in views (row 2) of the same ROI as indicated by the red boxes in row 1 of Fig. 5.9, from limited-angular-range-scan data of the lung phantoms, with a display windows of [0, 1.5] for both rows.

(a) 40-KeV image

(b) 120-KeV image

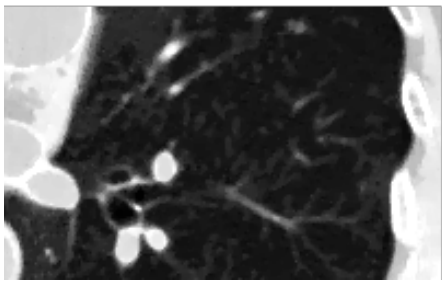

(c) 40-KeV zoomed-in

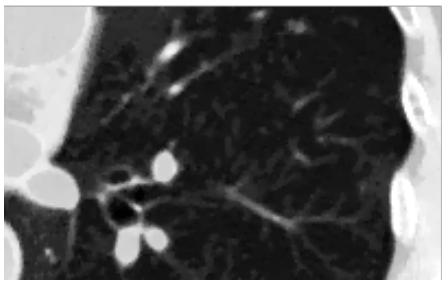

(d) 120-KeV zoomed-in

Figure 6.15: 40- and 120-KeV monochromatic ASD-NC-POCS images (row 1) and their zoomed-in views (row 2) of the same ROI as indicated by the red boxes in row 1 of Fig. 5.9, from limited-angular-range-scan data of the lung phantoms, with display windows of [-1000, 1000] HU (row 1) and [-500, 500] HU (row 2).

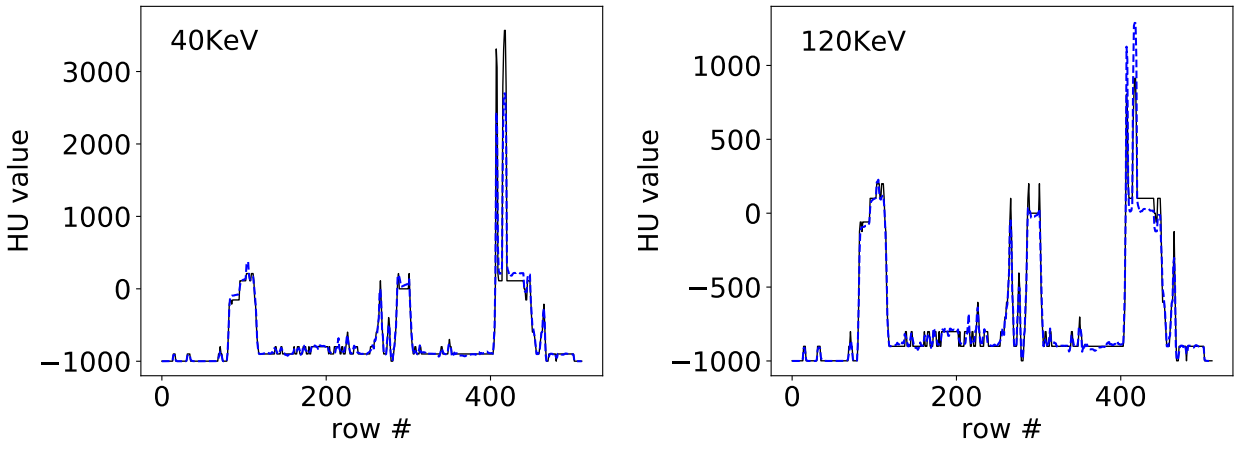

Figure 6.16: Profiles of ASD-NC-POCS reconstructed (blue dashed) and truth (black solid) monochromatic images at 40 and 120 KeV along the horizontal indicated in row 1 of Fig. 5.10 from limited-angular-range-scan data of the lung phantoms

6.4 Configurations with varying illumination coverages

We consider two additional configuration with varying illumination coverages, referred to as the split- and block-illumination configurations. The illumination coverage of the beam is reduced at each view, while the firing pattern of the X-ray tube is kept the same.

6.4.1 Split-illumination scan

Study parameters

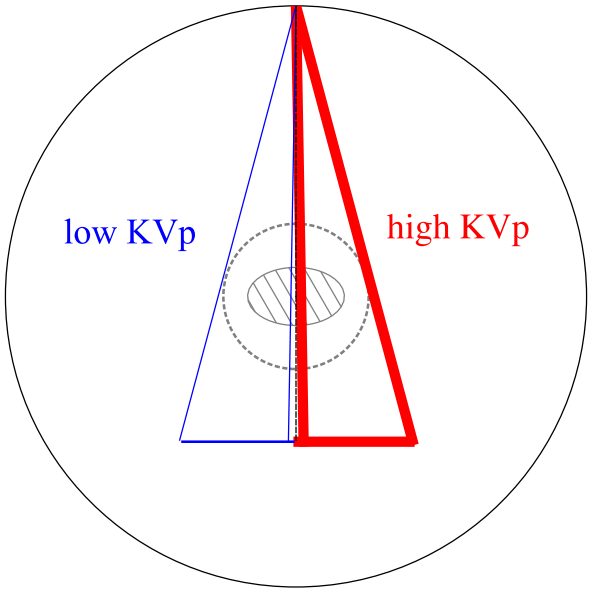

Figure 6.17: Split-illumination scan configuration, where low- (thin, blue line) and high- (thick, red line) KVp data are collected with two adjacent illumination coverages at each of the views uniformly distributed over 2π.

In the split-illumination configuration, the linear detector of 1024 bins and 400-mm length is divided into two adjacent segments of equal length with 512 bins and 200-mm length, as shown in Fig. 6.17. The low- and high-KVp beam illuminates each half of the two segments on the detector. As a result, system matrices $\mathcal{A}^{[1]}$ and $\mathcal{A}^{[2]}$ are of identical dimensions $J^{[1]} = J^{[2]} = 640 \times 512$ and $I = 512 \times 512$. Using the same strategy, we select $\epsilon = 0.0118$

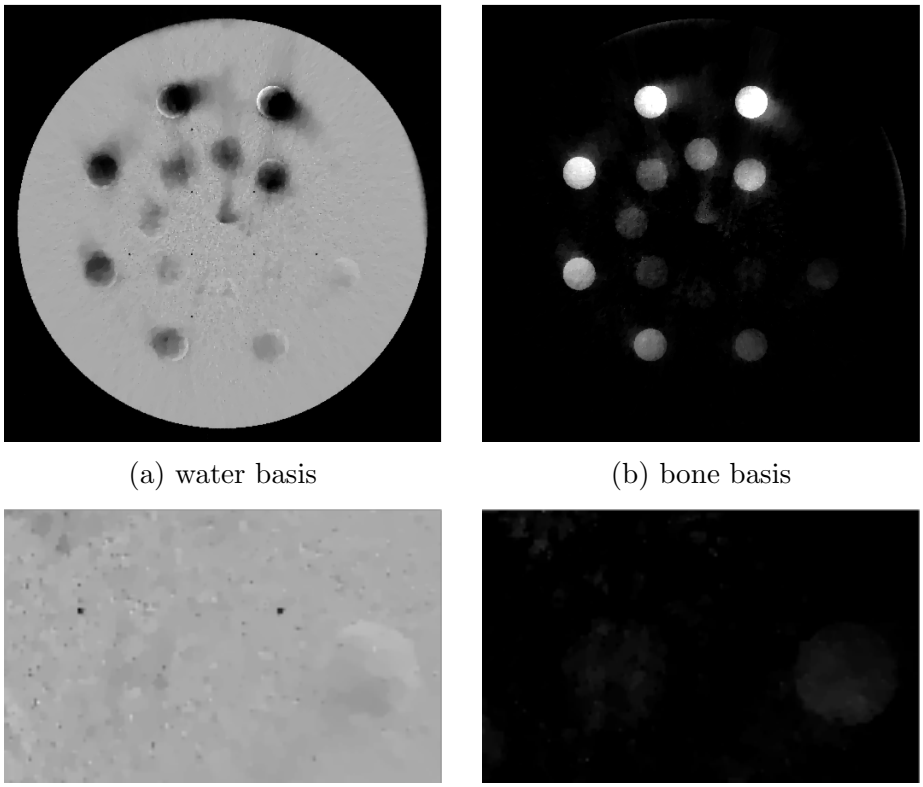

(a) water basis (b) bone basis

(c) water basis, zoomed-in (d) bone basis, zoomed-in

Figure 6.18: Water and bone basis ASD-NC-POCS images (row 1) and zoomed-in views (row 2) of the same ROI as indicated by the red boxes in row 1 of Fig. 5.6, from split-illumination-scan data of the DE-472 phantoms, with a display windows of [0, 1.5] for both rows.

and 0.008, respectively, for the DE-472 and lung phantom studies below.

Study results

We show in Figs. 6.18 and 6.19 reconstruction results of basis and monochromatic, respectively, images for the DE-472 phantom from data acquired with the split-illumination configuration, and Figs. 6.21 and 6.22 reconstruction results for the lung phantom from split-illumination scan data. For the DE-472 phantom, basis images and monochromatic image at 40 KeV show some visible artifacts, while the monochromatic image at 120 KeV reveals less artifacts. Conversely, basis images and monochromatic images for the lung phantom appear

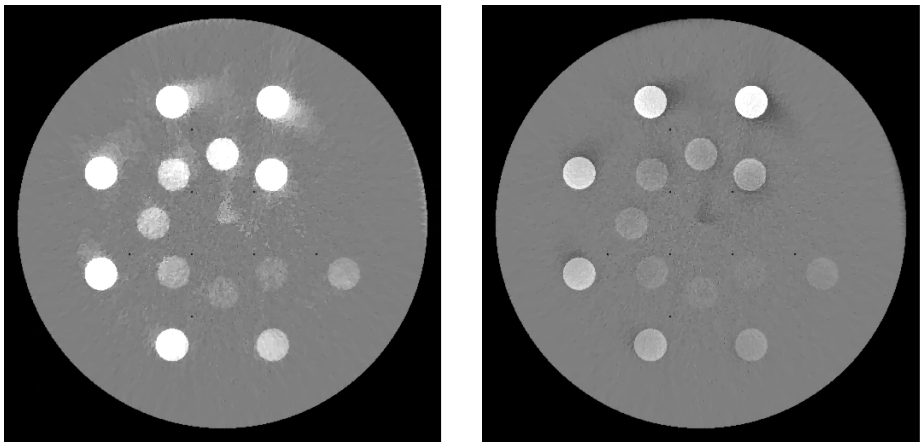

(a) 40-KeV image (b) 120-KeV image

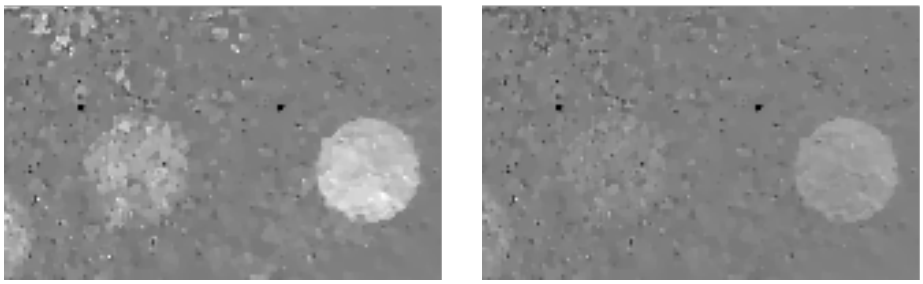

(c) 40-KeV zoomed-in (d) 120-KeV zoomed-in

Figure 6.19: 40- and 120-KeV monochromatic ASD-NC-POCS images (row 1) and their zoomed-in views (row 2) of the same ROI as indicated by the red boxes in row 1 of Fig. 5.6, from split-illumination-scan data of the DE-472 phantoms, with display windows of [-1000, 1000] HU (row 1) and [-500, 500] HU (row 2).

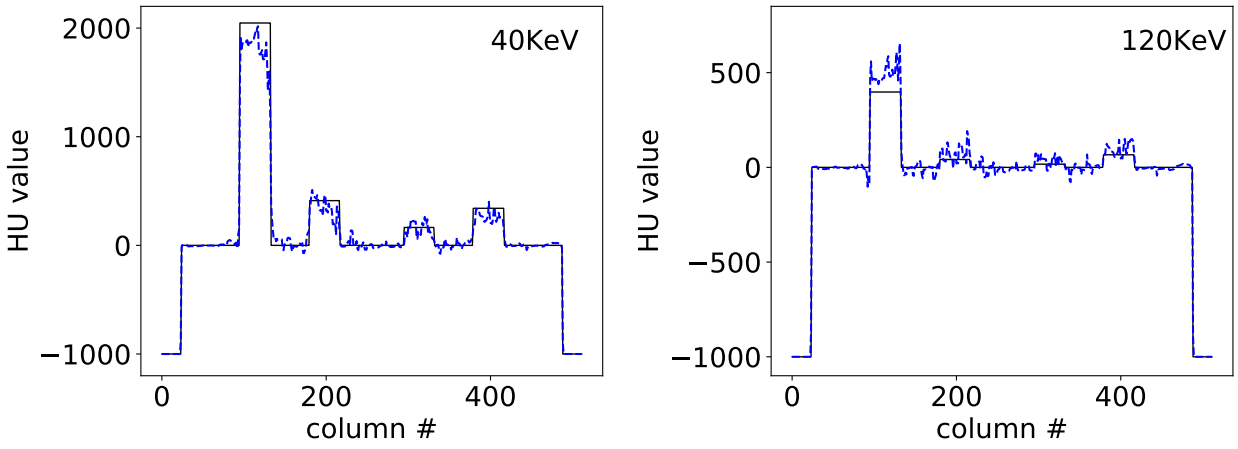

Figure 6.20: Profiles of ASD-NC-POCS reconstructed (blue dashed) and truth (black solid) monochromatic images at 40 and 120 KeV along the horizontal indicated in row 1 of Fig. 5.7 from split-illumination-scan data of the DE-472 phantoms

(a) water basis

(b) bone basis

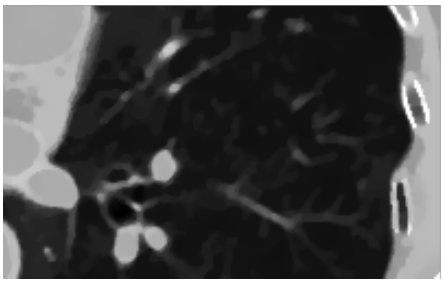

(c) water basis, zoomed-in

(d) bone basis, zoomed-in

Figure 6.21: Water and bone basis ASD-NC-POCS images (row 1) and zoomed-in views (row 2) of the same ROI as indicated by the red boxes in row 1 of Fig. 5.9, from split-illumination-scan data of the lung phantoms, with a display windows of [0, 1.5] for both rows.

(a) 40-KeV image

(b) 120-KeV image

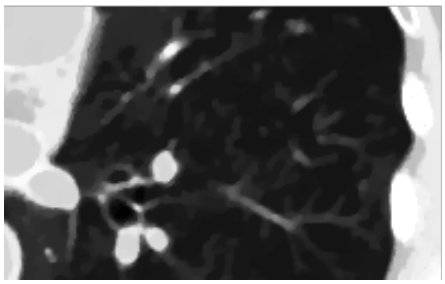

(c) 40-KeV zoomed-in

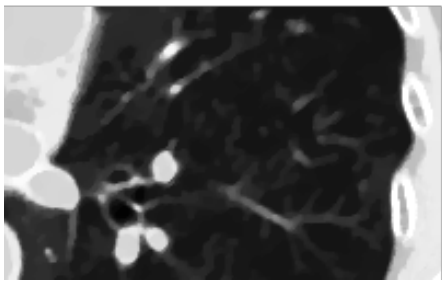

(d) 120-KeV zoomed-in

Figure 6.22: 40- and 120-KeV monochromatic ASD-NC-POCS images (row 1) and their zoomed-in views (row 2) of the same ROI as indicated by the red boxes in row 1 of Fig. 5.9, from split-illumination-scan data of the lung phantoms, with display windows of [-1000, 1000] HU (row 1) and [-500, 500] HU (row 2).

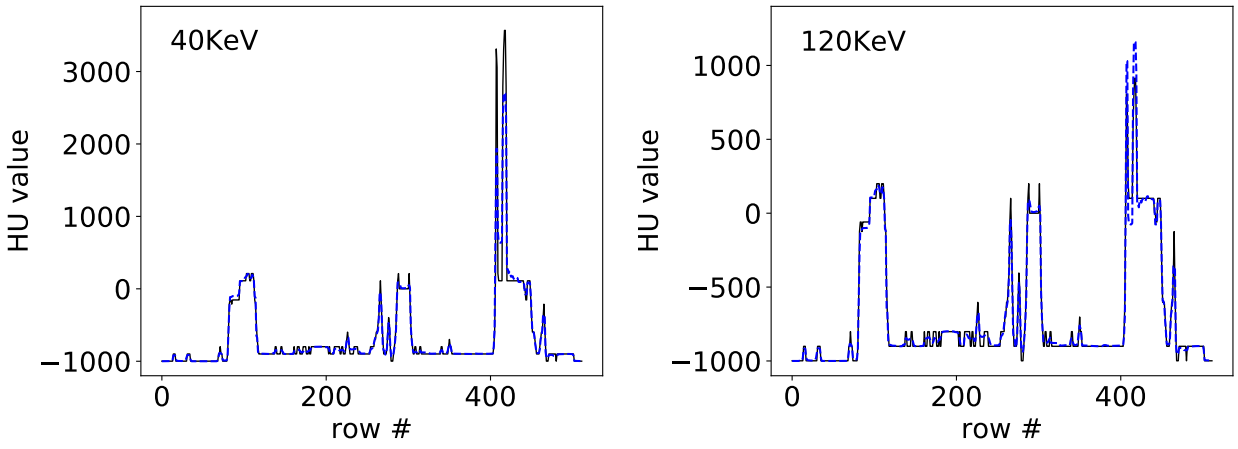

Figure 6.23: Profiles of ASD-NC-POCS reconstructed (blue dashed) and truth (black solid) monochromatic images at 40 and 120 KeV along the horizontal indicated in row 1 of Fig. 5.10 from split-illumination-scan data of the lung phantoms

to reveal little artifacts. In addition, we also plot in Figs. 6.20 and 6.23 profiles of the reconstructed and truth monochromatic images along the same horizontal and vertical lines in the full-scan results. It can be observed that while some quantitative difference between the reconstructed and truth monochromatic images for the DE-472 phantom can be observed, the truth and reconstructed monochromatic images agree reasonably well quantitatively for the lung phantom.

6.4.2 Block-illumination scan

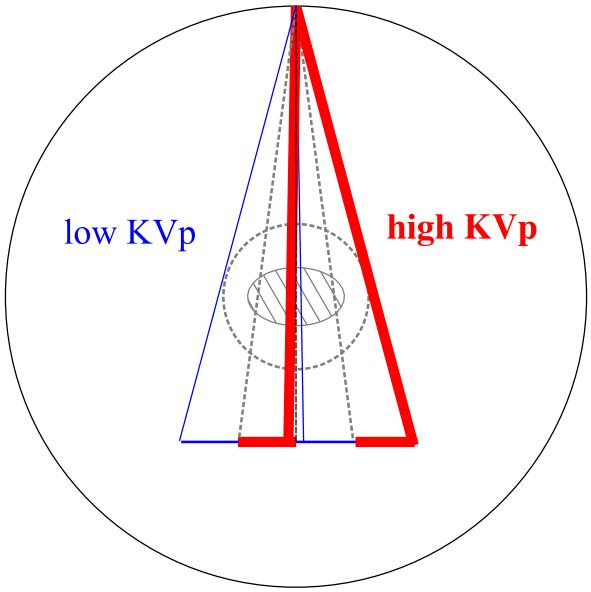

Figure 6.24: Block-illumination scan configurations, where low- (thin, blue line) and high- (thick, red line) KVp data are collected with multiple adjacent alternating illumination coverage at each of the views uniformly distributed over 2π.

Study parameters

In the block-illumination configuration, the linear detector is divided into two sets of interlaced, adjacent detector blocks of equal length, as shown in Fig. 6.24. Each detector block consists of 32 bins and 12.5-mm length. The low- or high- KVp beam illuminates one of

the two sets of detector blocks, respectively. Therefore, system matrices $\mathcal{A}^{[1]}$ and $\mathcal{A}^{[2]}$ are of identical dimensions $J^{[1]} = J^{[2]} = 640 \times 512$ and $I = 512 \times 512$. Using the same strategy, we select $\epsilon = 0.0121$ and 0.0089, respectively, for the DE-472 and lung phantom studies below.

Study results

We show in Figs. 6.25 and 6.26 reconstruction results of basis and monochromatic, respectively, images for the DE-472 phantom from data acquired with the block-illumination configuration, and Figs. 6.28 and 6.29 reconstruction results for the lung phantom from block-illumination scan data. Based upon the reconstruction results, observations similar to those for the split-illumination configuration can be made.

6.5 Discussion

In this chapter, we have investigated four non-standard scan configurations for acquiring multispectral CT data using simulation studies with inconsistent data. The non-standard configurations include different designs of scanning angular coverage and illumination coverage, each of which acquires only a port of the data from full-scan configuration. Therefore, these characterization studies with inconsistent data were continuations of the full-scan characterization study, which was used for benchmark reference, and the design of the studies mostly followed that of the full-scan study as well. The new configurations were considered because they can readily be implemented on a conventional CT scanner employing regular X-ray tubes and energy-integrating detectors, without invoking significant hardware additions or modifications to the scanner. The study results suggest that these configurations considered here can be enabled by the ASD-NC-POCS algorithm to yield monochromatic images comparable to those of the full-scan configuration.

The enabling effectiveness of the algorithm depends upon a number of factors, including sampling conditions and their impact on the data-model conditioning for a specific configura-

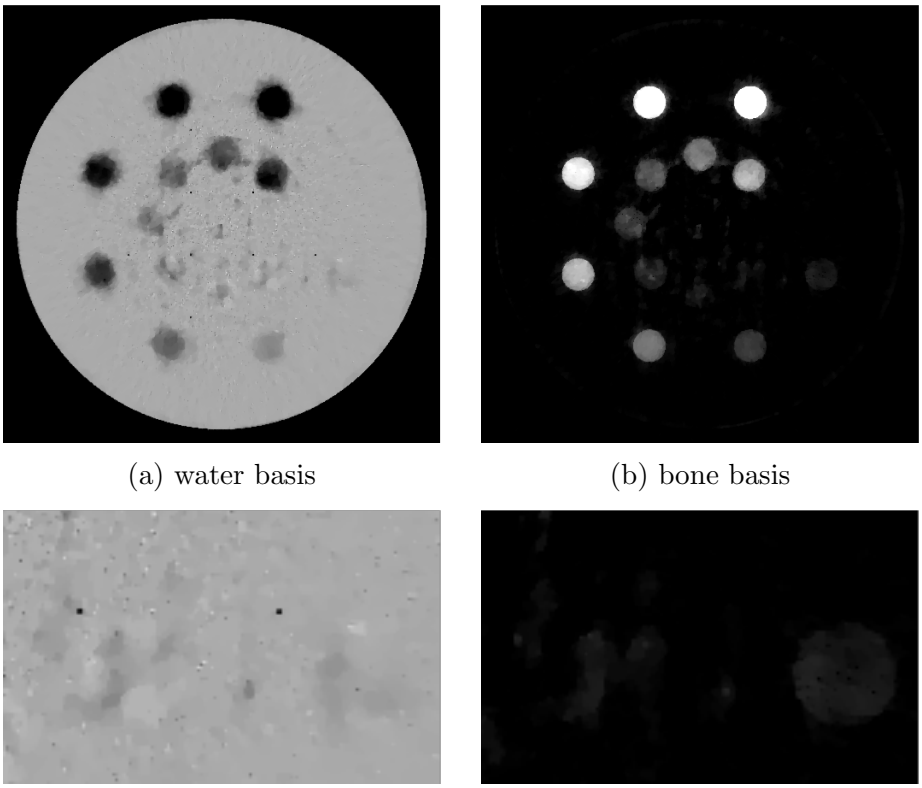

(a) water basis (b) bone basis

(c) water basis, zoomed-in (d) bone basis, zoomed-in

Figure 6.25: Water and bone basis ASD-NC-POCS images (row 1) and zoomed-in views (row 2) of the same ROI as indicated by the red boxes in row 1 of Fig. 5.6, from block-illumination-scan data of the DE-472 phantoms, with a display windows of [0, 1.5] for both rows.

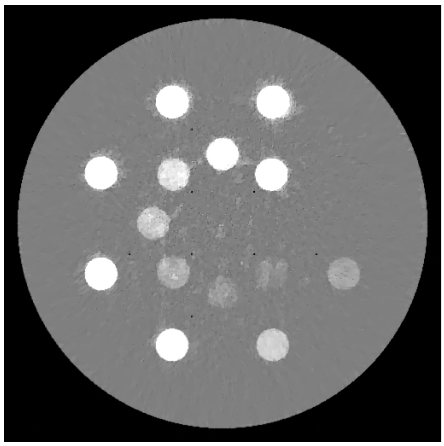

(a) 40-KeV image

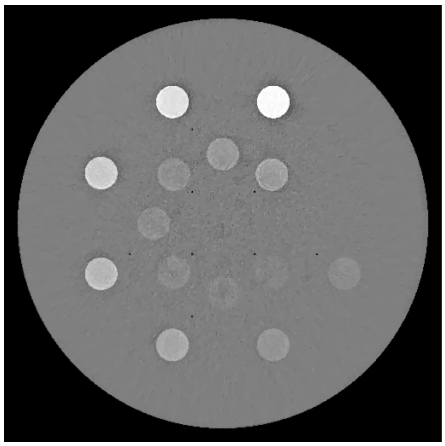

(b) 120-KeV image

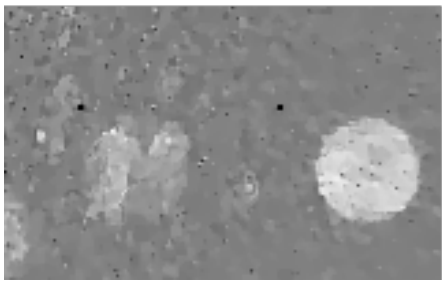

(c) 40-KeV zoomed-in

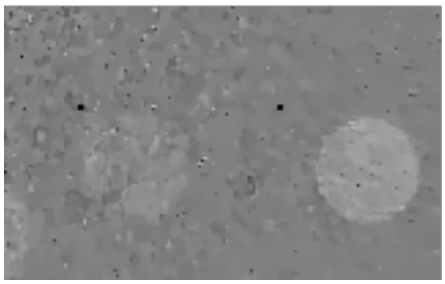

(d) 120-KeV zoomed-in

Figure 6.26: 40- and 120-KeV monochromatic ASD-NC-POCS images (row 1) and their zoomed-in views (row 2) of the same ROI as indicated by the red boxes in row 1 of Fig. 5.6, from block-illumination-scan data of the DE-472 phantoms, with display windows of [-1000, 1000] HU (row 1) and [-500, 500] HU (row 2).

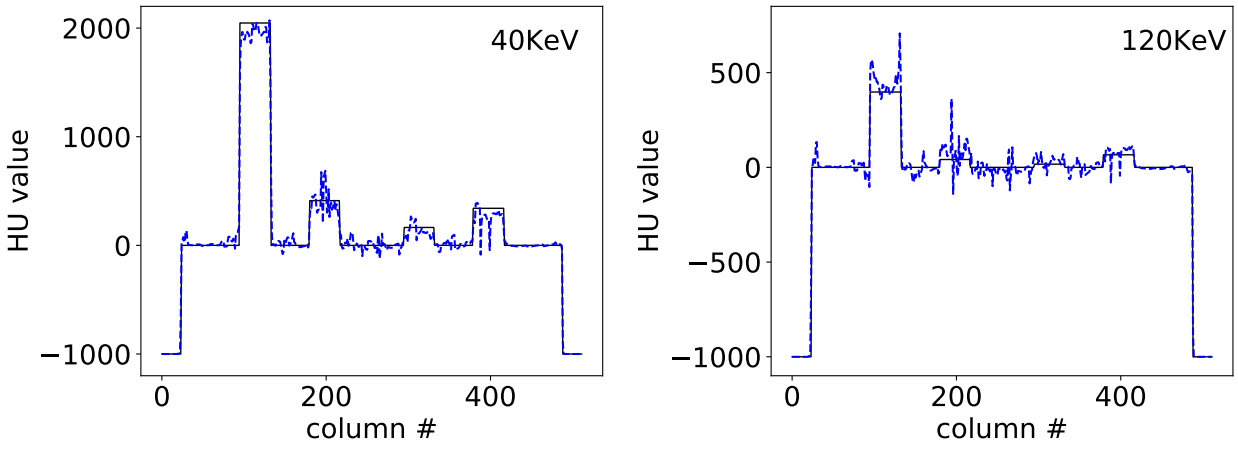

Figure 6.27: Profiles of ASD-NC-POCS reconstructed (blue dashed) and truth (black solid) monochromatic images at 40 and 120 KeV along the horizontal indicated in row 1 of Fig. 5.7 from block-illumination-scan data of the DE-472 phantoms

(a) water basis

(b) bone basis

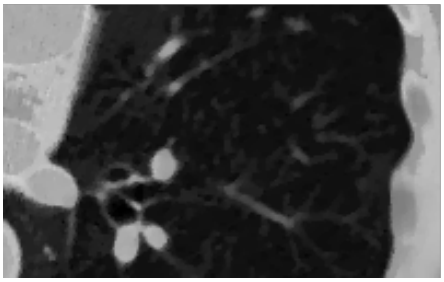

(c) water basis, zoomed-in

(d) bone basis, zoomed-in

Figure 6.28: Water and bone basis ASD-NC-POCS images (row 1) and zoomed-in views (row 2) of the same ROI as indicated by the red boxes in row 1 of Fig. 5.9, from block-illumination-scan data of the lung phantoms, with a display windows of [0, 1.5] for both rows.

(a) 40-KeV image

(b) 120-KeV image

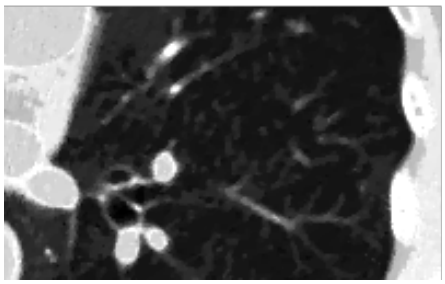

(c) 40-KeV zoomed-in

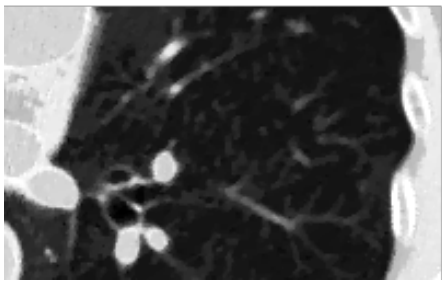

(d) 120-KeV zoomed-in

Figure 6.29: 40- and 120-KeV monochromatic ASD-NC-POCS images (row 1) and their zoomed-in views (row 2) of the same ROI as indicated by the red boxes in row 1 of Fig. 5.9, from block-illumination-scan data of the lung phantoms, with display windows of [-1000, 1000] HU (row 1) and [-500, 500] HU (row 2).

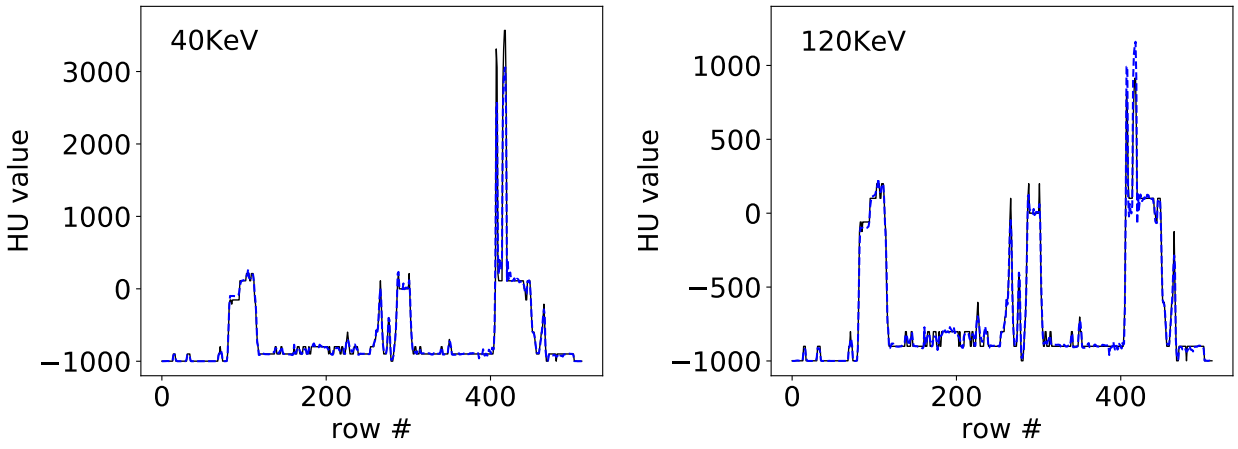

Figure 6.30: Profiles of ASD-NC-POCS reconstructed (blue dashed) and truth (black solid) monochromatic images at 40 and 120 KeV along the horizontal indicated in row 1 of Fig. 5.10 from block-illumination-scan data of the lung phantoms

tion, appropriateness of spectra used, anatomy complexity of subjects imaged, decomposition error, and data noise. In the presence of data inconsistencies such as decomposition error and statistical noise, it can be observed that banding artifacts near high contrast structures in DE-472-phantom images appear stronger understandably for the limited-angular-range configuration than for other configurations, suggesting that the effectiveness of the algorithm in enabling, e.g., a configuration with a considerably limited angular-range, decreases relative to that for other configurations. Additional image constraints other than the image-TV constraint can also be incorporated into the programs, which can be helpful in reducing the banding artifacts. For example, appropriate constraints on the basis component value pairs may be imposed to improve image reconstruction in multispectral CT [120]. On the other hand, the results show that reconstructions of the lung phantom appear to be robust for the configurations considered. Moreover, despite some visual artifacts, the monochromatic images obtained are quantitatively accurate and in good agreement with the truth.

Further investigations can include optimizing the design of the non-standard configurations. For the varying angular coverage configurations, we can further increase the sparsity of the view sampling, i.e., having less views for each KVp scan, in the sparse-view scan. Or else, we can increase the total angular coverage of the limited-angular-coverage scan to 2π or even large than 2π, as we will investigate in the next chapter. For the two varying illumination coverage configurations, the splitting location can be different than the exact middle point of the detector for the split-illumination scan. As a matter of fact, practical implementation of the configuration by blocking the beam in half often would not result in an exact middle point. For the block-illumination, the block size can be changed to evaluate its impact to the reconstruction results. It shall be noted that, by inserting beam blockers to realize the varying-illumination-coverage configurations, the spectra separation of the different spectra is different than what was modeled in the studies here. The "low" and "high" spectra should have the same KVp, but the "high" energy spectra, resulted from

the blocked part of the beam, are skewed toward the high energy due to filtration of the low energy photons. We can also carry out characterization studies with the more realistic spectra with beam blockers. Moreover, we can also incorporate more inconsistencies into the data generation step, in an effort to work toward the real data conditions and also to study the impact of different inconsistency, just as in the full-scan characterization study. Lastly, for the reconstruction method, data weighting can be tried to alleviate the artifacts in the split-illumination scan, as seen in Figs. 6.18 and 6.19, especially for splitting point being other than the middle and leading to offset-detector situation [62, 71]. Extrapolation can also be tried for the data from the varying-illumination-coverage scans, especially given that the low- and high-KVp data complement each other on the detector, providing reasonable estimates for the extrapolation already.

CHAPTER 7

REAL DATA STUDY

7.1 Introduction

After verification and characterization studies with simulation data, we move on to test the proposed reconstruction method and the ASD-NC-POCS algorithm on real data collected from diagnostic CT scanners. Specifically, we focus on the dual-energy CT data, which are clinically available with different implementations, and propose to apply the developed method on data collected from standard, full-scan configuration and also from the potentially fast, low-dose and lose cost single-KVp-switch configurations that are enabled by the algorithm.

7.1.1 Background on Dual-Energy CT

In dual-energy CT, material-basis and/or monochromatic-energy images are reconstructed from data sets collected with two different spectra. There exist four leading, distinctive methods currently for realizing dual-energy imaging in diagnostic CT: the first method, referred to as the single-KVp-switch method, uses a single X-ray source and single set of detectors to collect dual-energy data sets by performing two consecutive full-rotation scans in which the source KVp is switched following the first full-rotation scan; the second method, referred to as the fast-KVp-switch method, also uses a single X-ray source and a single detector for acquires dual-energy data sets only with one full-rotation scan in which the source invokes a fast KVp switch at each effective view of the full-rotation scan; the third method, referred to as the dual-source/detector method, employs two source-detector pairs of different spectra to collect dual-energy data sets within a full-rotation scan; and the fourth method, referred to as the dual-layer-detector method, adopts a single X-ray source and two-layer detectors with different energy responses to effectively different spectra for collecting

dual-energy data sets within a full-rotation scan.

All of the four methods require the performance of two or one full-rotation scans. In addition, the single-KVp-switch method, while easy to implement without hardware addition, has a relative low temporal imaging capability and doubled radiation dose of a regular full-rotation scan, as it carries out two full-rotation scans. The fast-KVp-switch and dual-source/detector methods, while having improved temporal imaging resolution over the single-KVp-switch method, in essence also perform two scans within one full rotation, and thus may also double radiation dose of a regular full-rotation scan. Furthermore, the fast-KVp-switch, dual-source/detector, and dual-layer-detector methods all require significant hardware addition to a regular diagnostic CT, thus considerably increasing CT system costs. Particularly, fast-KVp-switch method requires a unique, high performance X-ray tube capable of switching rapidly and repeatedly within a full rotation. The dual-source/detector method uses an additional pair of X-ray source and detector set, and the dual-layer-detector method uses a highly specialized detector technology. The cost of these perhaps is a leading reason for the lack of their adoption especially in non-diagnostic CT such as C-arm CT.

We investigate a new method for achieving fast, low-dose dual-energy imaging on current diagnostic and other CT systems without invoking significant hardware addition or modification to existing CT systems, including diagnostic and non-diagnostic (such as C-arm) CT scanners. The method is enabled by a one-step algorithm proposed for image reconstruction from dual-energy data. In the four existing methods described above, two measurements are made for each ray with two different spectra so that some of the existing algorithms can be applied to reconstruct basis or monochromatic images. In contrast, the one-step algorithm proposed can be applied to reconstructing images from data in which rays can be measured only with one of the two spectra. It is this unique property of the algorithm that enables the design of scanning configurations of potential for realizing fast, low-dose dual-energy imaging on current regular diagnostic CT systems without hardware addition or modification.

7.2 Scanning configurations

7.2.1 Full-scan configuration

The full-scan configuration for dual-energy CT is first used, in which each of the two sets of dual-energy data are collected from an object enclosed entirely in the scanner FOV over 2π. In this chapter, such configuration is also referred to as the *full-plus-full* scan configurations. The four existing methods described all adopt a full-scan configuration for acquisition of dual-energy data and may consequently suffer from some of the issues concerning temporal resolution, radiation dose, and system cost.

7.2.2 Partial-scan configurations

As a consistent theme of this dissertation work, one of the major goals for the development of optimization-based image reconstruction is to enable flexible scan configurations for acquiring multispectral CT. Therefore, in this chapter, we refer to a scan configuration as a partial-scan configuration in which each of the two dual-energy data sets is acquired from an object enclosed completely in the FOV of the scanner only over an angular range that is considerably less than 2π. Because of the reduced scan angular range from 2π, a partial-scan configuration can be exploited possibly for achieving improved temporal resolution and lowered radiation dose relative to those of a full-scan configuration. Most importantly, a partial-scan configuration can readily be realized on standard CT scanners by use of the standard single-KVp-switch technique without requiring additional hardware cost. Indeed, the single-KVp-switch technique has already be adopted in the existing slow-KVp-switch method in which the KVp is switched at the end of the first full rotation. As shown below, reconstruction algorithm can be devised for enabling a partial-scan configuration in dual-energy CT.

We use three parameters, α_0, α_1, and α_2 to specify a single-KVp-switch scan configu-

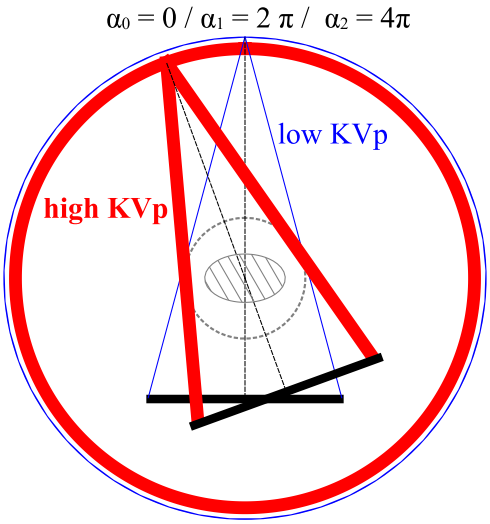

(a) full scan

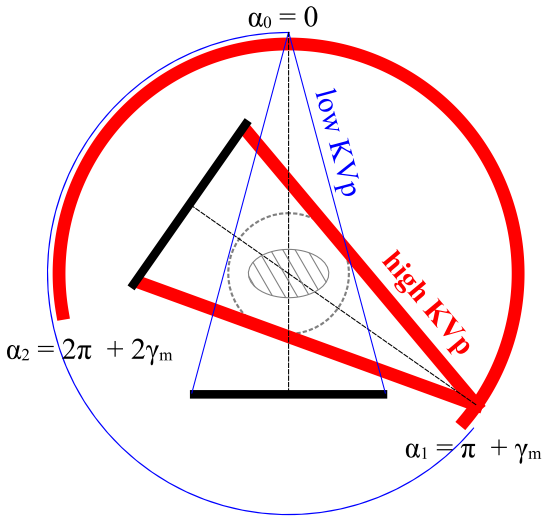

(b) short-plus-short scan

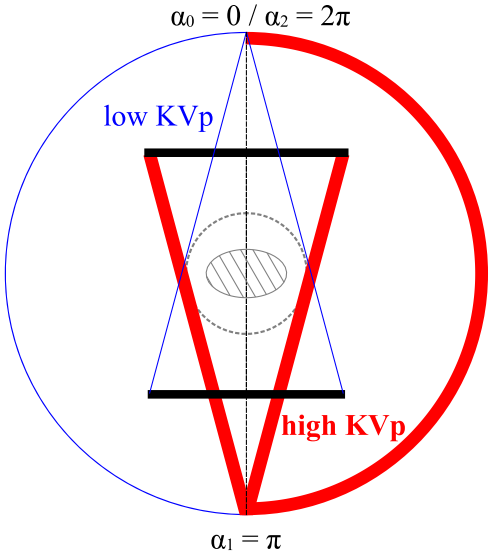

(c) half-plus-half scan

Figure 7.1: Full-plus-full (a), short-plus-short (b), and half-plus-half (c) scan configurations, where γ_m denotes the fan angle of a CT scanner. Dual-energy data sets are collected over the angle ranges with low- (thin, blue line) and high- (thick, red line) KVp X-rays. The dashed circle indicates the field of view of the scanner, which enclose completely the imaged object, denoted by the elliptical region.

ration, where α_0 and α_2 denote the starting and ending angles of the X-ray tube, and α_1 the angle at which the X-ray tube switches its KVp, thus collecting two sets of dual-energy data over angular ranges (α_0, α_1) and (α_1, α_2), respectively. In a full-scan configuration, $\alpha_1 - \alpha_0 = \alpha_2 - \alpha_1 = 2\pi$, while in a partial-scan configuration, $\alpha_1 - \alpha_0 < 2\pi$ and $\alpha_2 - \alpha_1 < 2\pi$. In this work, two single-KVp-switch scan configurations are investigated and demonstrated for dual-energy CT of potential practical significance in terms of reduced radiation dose, scanning time, and system cost. The first scan configuration of interest is referred to as the *short-plus-short* scan, as shown in Fig. 7.1b, in which the tube rotates a short-scan range in one KVp, before switching to another KVp setting and rotating for another short-scan range. Thus, two sets of dual-energy data are acquired with $\alpha_0 = 0$, $\alpha_1 = \pi + \gamma_m$, and $\alpha_2 = 2\pi + 2\gamma_m$, where γ_m is the fan angle of the CT scanner. The two KVp scans are adjacent to each on one end, and have an overlap of $2\gamma_m$ on the other end. The second scan configuration is referred to as the *half-plus-half* scan, as show in Fig. 7.1c, in which $\alpha_0 = 0$, $\alpha_1 = \pi$, and $\alpha_2 = 2\pi$. The X-ray tube is switched from one KVp to another at $\alpha_1 = \pi$, and the angular range of each KVp scan covers half of a full rotation. As a result, there is no angular overlap between the two KVp scans.

7.3 Data acquisition

7.3.1 Scanner

In the work, a clinical conventional CT scanner was used to acquire dual-energy data with 80 and 135 KVp in the circular/axial mode. The scanner has a FOV of 487 mm in diameter and a fan angle $\gamma_m = 49.2^\circ$. A curved detector consisting of 896 bins at each row is used for 1200 projections in one full rotation.

7.3.2 Phantoms

Two physical phantoms were scanned, the standard GAMMEX DE-472 dual-energy CT phantom [127] with calcium and iodine inserts, referred to as the *DE-472 phantom*, and an anthropomorphic head phantom with low contrast disks, referred to as the *head phantom*. Low and high spectra at 80 and 135 KVp were used, with bow-tie filters, to acquire dual-energy data. As a result, ray-dependent spectra are to be used in the reconstruction.

7.3.3 Techniques

Full-scan dual-energy data were first collected with two full rotations at 80 and 135 KVp, respectively. For each phantom, twenty full scans were repeated at each KVp with high mA setting and were then averaged to yield data sets with extremely low level of noise. Such high-dose, low-noise data were acquired to isolate image artifacts caused by sampling conditions, which could be buried in noises, and to establish the performance benchmark and references for quantitative evaluations. Table 7.1 summarizes the different mA setting used in the acquisition.

The dual-energy data for partial-scan configurations were subsequently obtained by extracting from the relevant portions from the full-scan data sets. Specifically, for the short-plus-short scan, 0-to-230°-rotation data from the 80-KVp scan and 230-to-460°-rotation data from the 135-KVp scan were extracted and joined together. Similarly, 0-to-π-rotation data from 80 KVp and π-to-2π-rotation data from 135 KVp were joined together to form the half-plus-half scan data.

Table 7.1: mA setting used to acquire phantom data at different KVp

	DE-472 phantom		head phantom	
	80 KVp	135 KVp	80 KVp	135 KVp
mA	450	250	450	250

7.4 Image reconstruction

In the section, we first describe the data model for dual-energy imaging from which the reconstruction problem is formulated as a non-convex (NC) optimization program. Because there is no mathematically exact solver for the NC program, we devise an heuristic algorithm for reconstructing basis and monochromatic-energy images from dual-energy data collected with full- and partial-scan configurations through numerically solving the program.

7.4.1 Data model for dual-energy imaging

In dual-energy CT imaging, $S = 2$ spectral data sets are measured with low ($s = 1$) and high ($s = 2$) KVp spectrum. Considering a two-basis decomposition model, one can express the data model for a ray measurement as

$$\begin{aligned} g_j^{[s]}(\mathbf{b}_1, \mathbf{b}_2) &= -\ln \sum_m q_{jm}^{[s]} \exp\left(-\sum_i a_{ji}^{[s]} f_{im}\right) \\ &= -\ln \sum_m q_{jm}^{[s]} \exp\left(-\sum_i a_{ji}^{[s]} \left(\mu_{1m} b_{1i} + \mu_{2m} b_{2i}\right)\right), \end{aligned}$$

where $j \in \{0, \cdots, J^{[s]} - 1\}$ is the ray index in either low or high KVp scan, $g_j^{[s]}(\mathbf{b}_1, \mathbf{b}_2)$ denotes the model data for the jth ray in scan s, $q_{jm}^{[s]}$ the ray-dependent, normalized X-ray spectrum, satisfying $\sum_m q_{jm}^{[s]} = 1$, at energy m for the jth ray in scan s, and $a_{ji}^{[s]}$ the intersection length of the jth ray in scan s with the ith voxel. The data model in equation (7.1) can be re-written as

$$g_j^{[s]}(\mathbf{b}_1, \mathbf{b}_2) = \bar{g}_j^{[s]}(\mathbf{b}_1, \mathbf{b}_2) + \Delta g_j^{[s]}(\mathbf{b}_1, \mathbf{b}_2), \tag{7.1}$$

where

$$\bar{g}_j^{[s]}(\mathbf{b}_1, \mathbf{b}_2) = \sum_i a_{ji}^{[s]} \left(\bar{\mu}_{j1}^{[s]} b_{1i} + \bar{\mu}_{j2}^{[s]} b_{2i} \right), \tag{7.2}$$

$$\Delta g_j^{[s]}(\mathbf{b}_1, \mathbf{b}_2) = -\ln \sum_m q_{jm}^{[s]} \exp\left(- \sum_i a_{ji}^{[s]} \left(\Delta\mu_{j1m}^{[s]} b_{1i} + \Delta\mu_{j2m}^{[s]} b_{2i} \right) \right), \tag{7.3}$$

are the linear and non-linear terms in the data model, in which

$$\bar{\mu}_{jk}^{[s]} = \sum_m q_{jm}^{[s]} \mu_{km}, \tag{7.4}$$

$$\Delta\mu_{jkm}^{[s]} = \mu_{km} - \bar{\mu}_{jk}^{[s]}. \tag{7.5}$$

are an energy-independent term, taken as the spectrum-weighted average of μ_{km} over energy, and the remaining error term that is still energy dependent [102,116], respectively, for $k = 1$ and 2.

For spectral set s, we form data vector $\mathbf{g}^{[s]}(\mathbf{b}_1, \mathbf{b}_2)$ of size $J^{[s]}$, with elements $g_j^{[s]}(\mathbf{b}_1, \mathbf{b}_2)$. Similarly, we can form additional data vectors $\bar{\mathbf{g}}^{[s]}(\mathbf{b}_1, \mathbf{b}_2)$ and $\Delta\mathbf{g}^{[s]}(\mathbf{b}_1, \mathbf{b}_2)$, for $s = 1$ and 2, in the same fashion as $\mathbf{g}^{[s]}(\mathbf{b}_1, \mathbf{b}_2)$, with $\bar{g}_j^{[s]}(\mathbf{b}_1, \mathbf{b}_2)$ and $\Delta g_j^{[s]}(\mathbf{b}_1, \mathbf{b}_2)$ in equation (7.2) and (7.3), respectively, as their elements. Also, let $\mathcal{A}^{[s]}$ denote the discrete X-ray transform matrix for scan s of dimension $J^{[s]} \times I$ with $a_{ji}^{[s]}$ as its element, and $\mathcal{U}_k^{[s]}$ a diagonal matrix of size $J^{[s]}$ with $\bar{\mu}_{jk}^{[s]}$ as its diagonal element. As a result, the DD-data model in equation (7.1) for an individual ray can be grouped into a matrix form for all of the rays from the low ($s = 1$) and high ($s = 2$) KVp scans as

$$\begin{aligned} \begin{pmatrix} \mathbf{g}^{[1]}(\mathbf{b}_1, \mathbf{b}_2) - \Delta\mathbf{g}^{[1]}(\mathbf{b}_1, \mathbf{b}_2) \\ \mathbf{g}^{[2]}(\mathbf{b}_1, \mathbf{b}_2) - \Delta\mathbf{g}^{[2]}(\mathbf{b}_1, \mathbf{b}_2) \end{pmatrix} &= \begin{pmatrix} \bar{\mathbf{g}}^{[1]}(\mathbf{b}_1, \mathbf{b}_2) \\ \bar{\mathbf{g}}^{[2]}(\mathbf{b}_1, \mathbf{b}_2) \end{pmatrix} \\ &= \begin{pmatrix} \mathcal{U}_1^{[1]} \mathcal{A}^{[1]}, & \mathcal{U}_2^{[1]} \mathcal{A}^{[1]} \\ \mathcal{U}_2^{[1]} \mathcal{A}^{[2]}, & \mathcal{U}_2^{[2]} \mathcal{A}^{[2]} \end{pmatrix} \begin{pmatrix} \mathbf{b}_1 \\ \mathbf{b}_2 \end{pmatrix}. \end{aligned} \tag{7.6}$$

7.4.2 Non-convex (NC) optimization program

We further form aggregated vectors

$$\bar{\mathbf{g}}(\mathbf{b}_1, \mathbf{b}_2) = (\bar{\mathbf{g}}^{[1]}(\mathbf{b}_1, \mathbf{b}_2)^\top, \bar{\mathbf{g}}^{[2]}(\mathbf{b}_1, \mathbf{b}_2)^\top)^\top,$$
$$\Delta\mathbf{g}(\mathbf{b}_1, \mathbf{b}_2) = (\Delta\mathbf{g}^{[1]}(\mathbf{b}_1, \mathbf{b}_2)^\top, \Delta\mathbf{g}^{[2]}(\mathbf{b}_1, \mathbf{b}_2)^\top)^\top,$$

and

$$\mathbf{g}_{\mathcal{M}} = (\mathbf{g}_{\mathcal{M}}^{[1]\top}, \mathbf{g}_{\mathcal{M}}^{[2]\top})^\top,$$

where $\mathbf{g}_{\mathcal{M}}^{[1]}$ and $\mathbf{g}_{\mathcal{M}}^{[2]}$ of sizes $J^{[1]}$ and $J^{[2]}$ denote measured data with spectra $s = 1$ and 2. Using the aggregated data vectors, we then formulate the basis images as a solution to the constrained optimization program designed as

$$\begin{aligned} (\mathbf{b}_1^*, \mathbf{b}_2^*) &= \underset{\mathbf{b}_1, \mathbf{b}_2}{\arg\min} \left(||\mathbf{b}_1||_{\mathrm{TV}} + ||\mathbf{b}_2||_{\mathrm{TV}} \right) \\ &\text{s. t.} \quad D\left(\bar{\mathbf{g}}(\mathbf{b}_1, \mathbf{b}_2),\, \mathbf{g}_{\mathcal{M}} - \Delta\mathbf{g}(\mathbf{b}_1, \mathbf{b}_2)\right) \leq \epsilon \\ &\qquad \mu_{1m}\mathbf{b}_1 + \mu_{2m}\mathbf{b}_2 \succeq 0, \end{aligned} \tag{7.7}$$

where $||\cdot||_{\mathrm{TV}}$ denotes image total-variation (TV) and the ℓ_2-norm data fidelity function is adopted as

$$D\left(\bar{\mathbf{g}}(\mathbf{b}_1, \mathbf{b}_2),\, \mathbf{g}_{\mathcal{M}} - \Delta\mathbf{g}(\mathbf{b}_1, \mathbf{b}_2)\right) = \frac{||\bar{\mathbf{g}}(\mathbf{b}_1, \mathbf{b}_2) - \mathbf{g}_{\mathcal{M}} + \Delta\mathbf{g}(\mathbf{b}_1, \mathbf{b}_2)||_2}{||\mathbf{g}_{\mathcal{M}}||_2} \tag{7.8}$$

$\epsilon > 0$ is the data constraint parameter. In addition, instead of a non-negativity constraint on the basis image, a non-negativity constraint is imposed on the monochromatic image at energy m. The optimization program in equation (7.7) is non-convex because $D\left(\bar{\mathbf{g}}(\mathbf{b}_1, \mathbf{b}_2),\, \mathbf{g}_{\mathcal{M}} - \Delta\mathbf{g}(\mathbf{b}_1, \mathbf{b}_2)\right) \leq \epsilon$ forms a non-convex set.

7.4.3 Reconstruction algorithm

In an attempt to solve the optimization program in equation (7.7), we first use the steepest descend (SD) procedure to reduce the convex term of the basis-image TV. On the other hand, there is no mathematically exact solver for globally minimizing $D\left(\bar{\mathbf{g}}(\mathbf{b}_1, \mathbf{b}_2),\, \mathbf{g}_{\mathcal{M}} - \Delta\mathbf{g}(\mathbf{b}_1, \mathbf{b}_2)\right)$. Instead, we consider a procedure for lowering the NC-data divergence: It can be observed that, if term $\Delta\mathbf{g}(\mathbf{b}_1, \mathbf{b}_2)$ can be estimated, the data divergence becomes convex and can thus be lowered by use of a procedure based upon the projection-onto-convex-sets (POCS). Therefore, we devise a procedure based upon the POCS updates for lowering the non-convex data divergence as

$$\mathbf{b}_k^{(n+1)} = \mathbf{b}_k^{(n)} + \gamma^{(n)}\, \bar{\mu}_{jk}^{[s]} \frac{g_{\mathcal{M}j}^{[s]} - \Delta g_j^{[s]}(\mathbf{b}_1^{(n)}, \mathbf{b}_2^{(n)}) - \bar{g}_j^{[s]}(\mathbf{b}_1^{(n)}, \mathbf{b}_2^{(n)})}{\left[(\bar{\mu}_{j1}^{[s]})^2 + (\bar{\mu}_{j2}^{[s]})^2\right] \mathbf{a}_j^{[s]\top} \mathbf{a}_j^{[s]}} \mathbf{a}_j^{[s]}, \tag{7.9}$$

where $k = 1$ and 2, and the correction for NC contribution $\Delta g_j^{[s]}(\mathbf{b}_1, \mathbf{b}_2)$ is estimated as

$$\Delta g_j^{[s]}(\mathbf{b}_1^{(n)}, \mathbf{b}_2^{(n)}) = -\ln \sum_m q_{jm}^{[s]} \exp\Big(-\mathbf{a}_j^{[s]\top} (\Delta\mu_{j1m}^{[s]} \mathbf{b}_1^{(n)} + \Delta\mu_{j2m}^{[s]} \mathbf{b}_2^{(n)})\Big), \tag{7.10}$$

where $j \in \{0, 1, ..., J^{[s]}\}$ for spectral set s.

Unlike the conventional POCS procedure, the update in equation (7.9) addresses the convexity of the data divergence by including NC term $\Delta g_j^{[s]}(\mathbf{b}_1^{(n)}, \mathbf{b}_2^{(n)})$, and is thus referred to as the NC-POCS procedure. Subsequently, we use the ASD-NC-POCS algorithm, as described in Algorithm 2, by combining SD and NC-POCS procedures that adaptively lowers image TV and data divergence. In the work, algorithm parameters $\gamma^{[n]}$, as well as $\alpha_k^{(n)}$ and N_{TV} (see Algorithm 2), are identical to those in the conventional ASD-POCS algorithm [57]

and the ASD-NC-POCS algorithm throughout the work, as

$$\begin{aligned}
&\gamma^{(n)} = 0.95\,\gamma^{(n-1)}, \quad \text{with} \quad \gamma^{(1)} = 1.0, \\
&\alpha_k^{(n)} = 0.8\,\alpha_k^{(n-1)}, \quad \text{with} \quad \alpha^{(1)} = 0.2\,\Delta_{\mathbf{b}}^{(1)}, \\
&N_{\text{TV}} = 20.
\end{aligned}$$

Further, we determine the program parameters as following. The image voxel size is set at 0.683 mm, as those used in a clinical scan, covering a square of 350 mm in the image space with an array of 512×512. The incident beam spectra at 80 and 135 KVp are first estimated from measurement and multiplied with the linear detector energy response. The resulting X-ray spectra, after normalization, are used in the reconstruction, particularly in estimating the non-linear term using equation (7.10). Since both spectra are ray-dependent due to the presence of bow-tie filters, the low and high KVp spectra at the central bin of the detector is shown in Fig. 7.2. Lastly, the data fidelity parameter ϵ is selected based on visual assessment. Since we no longer have the truth images in the real data study, the strategy we have been using in the simulation studies can not be applied here. Therefore, we use visual assessment, as an example, to select ϵ.

7.4.4 Necessary convergence conditions

While it cannot be shown mathematically whether the ASD-NC-POCS algorithm can mathematically solve the NC program in equation (7.7), two necessary convergence conditions can be obtained for the algorithm. Let

$$\begin{aligned}
\bar{D}(\mathbf{b}_1^{(n)}, \mathbf{b}_2^{(n)}) &= \left| D(\mathbf{g}(\mathbf{b}_1^{(n)}, \mathbf{b}_2^{(n)}), \mathbf{g}_{\mathcal{M}}) - \epsilon \right| / \epsilon \\
\Delta_{\text{TV}}(\mathbf{b}_1^{(n)}, \mathbf{b}_2^{(n)}) &= \frac{\left| (||\mathbf{b}_1^{(n+1)}||_{\text{TV}} + ||\mathbf{b}_2^{(n+1)}||_{\text{TV}}) - (||\mathbf{b}_1^{(n)}||_{\text{TV}} + ||\mathbf{b}_2^{(n)}||_{\text{TV}}) \right|}{\left| (||\mathbf{b}_1^{(n+1)}||_{\text{TV}} + ||\mathbf{b}_2^{(n+1)}||_{\text{TV}}) + (||\mathbf{b}_1^{(n)}||_{\text{TV}} + ||\mathbf{b}_2^{(n)}||_{\text{TV}}) \right|}.
\end{aligned} \tag{7.11}$$

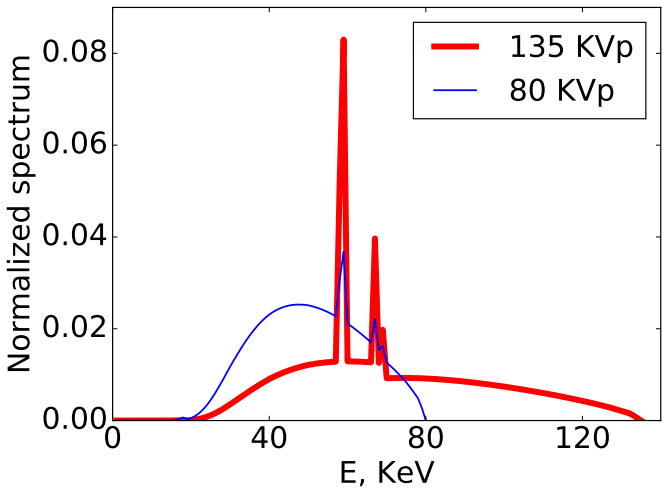

Figure 7.2: Normalized low (thin, blue line) and high (thick, red line) spectra at 80 and 135 KVp at the central bin.

The necessary mathematical convergence conditions for the ASD-NC-POCS algorithm can be obtained as

$$\begin{aligned} \bar{D}(\mathbf{b}_1^{(n)}, \mathbf{b}_2^{(n)}) &\to 0 \\ \Delta_{\mathrm{TV}}(\mathbf{b}_1^{(n)}, \mathbf{b}_2^{(n)}) &\to 0 \end{aligned} \tag{7.12}$$

as iteration number $n \to \infty$. The first condition makes sure that the convergent solution is feasible, as part of the KKT condition [122], whereas the second is for the optimality of the objective function. Because the mathematical convergence conditions cannot be met in practical reconstructions, they are used for devising the practical convergence conditions as

$$\begin{aligned} \bar{D}(\mathbf{b}_1^{(n)}, \mathbf{b}_2^{(n)}) &< 10^{-3}, \\ \Delta_{\mathrm{TV}}(\mathbf{b}_1^{(n)}, \mathbf{b}_2^{(n)}) &< 10^{-3}. \end{aligned}$$

7.4.5 Reference images

Several methods exist for image reconstruction from full-scan dual-energy data. When dual-energy data for a ray are measured with both the low- and high-KVp spectra, the ray-consistency condition is met and one of the methods first compensates approximately for

the non-linear effect by decomposition of measured data into X-ray transforms of individual basis images, i.e., basis sinogram, and then reconstructs basis images through the inversion of the X-ray transforms estimated [78, 82, 102–104].

In the work, we apply such data domain decomposition method to full-scan dual-energy data to yield basis and monochromatic images, and then use the images as references for the development guidance and reconstruction comparison of the ASD-NC-POCS algorithm. The same fix-point algorithm [102] used in the full-scan simulation study is used here for the data decomposition, and the FBP-like algorithm with a Hanning window is used to invert the X-ray transform from the full-scan data and reconstruction basis images. The reference images are reconstructed on a the same 512×512 image array with 0.683 mm square pixels.

7.5 Study results

7.5.1 Full-scan study

Reference images

We obtain reference images by use of the data-domain decomposition on the full-scan, dual-energy data and the FBP-like algorithm for reconstruction. We first show the convergence plot of the fix-point algorithm for the decomposition step, and then show reconstructed images using FBP-like analytic algorithm. A single ROI, matching that used in the full-scan simulations study for the digital DE-472 phantom, is selected for the DE-472 physical phantom images, while two separate ROIs are selected for the head phantom images, highlighting the low-contrast disks and the complicated bony regions in the phantom.

Convergence plots We show in Fig. 7.3 the convergence plot of the fix-point algorithm used in the data domain decomposition. Using the head phantom data as an example, the relative error between two consecutive updates are plotted as a function of iteration number

n. It is shown that after about 40 iterations, the changes in the consecutive updates are almost zero (only at the computer precision level), indicating that the algorithm finds the "fixed-point". The result from the DE-472 phantom is consistent with Fig. 7.3.

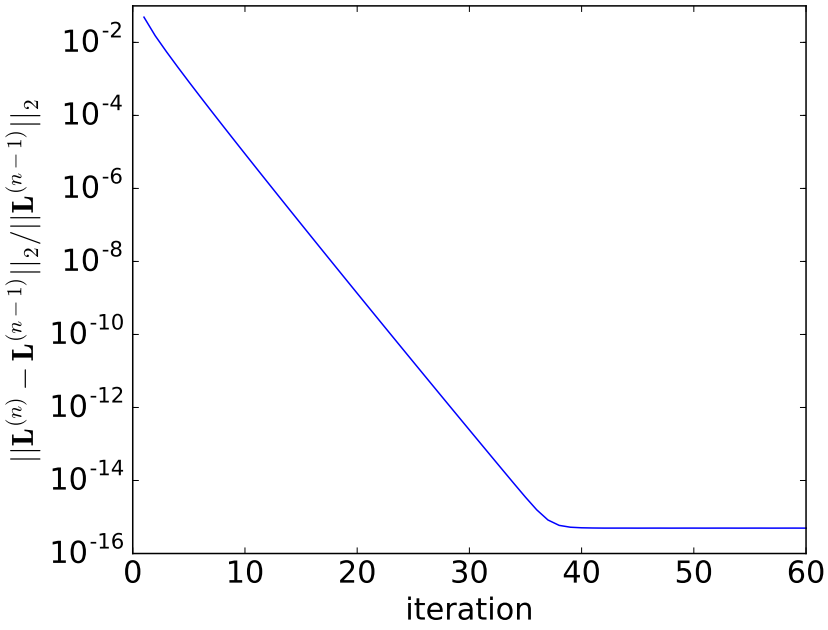

Figure 7.3: Relative error between consecutive updates as a function iteration n, using the fix-point algorithm for the data domain decomposition of the head phantom data in the full-scan characterization study. $\mathbf{L}$ denotes the vector concatenated from the two basis sinogram vector $\mathbf{L}_1$ and $\mathbf{L}_2$.

DE-472 phantom results In Fig. 7.4, we show reconstructed basis images and their zoomed-in views of ROI images, enclosed by the red rectangular boxes indicated in the full-size images in row 1. The ROI contains two contrast inserts with the lowest concentration of iodine and calcium in the phantom and two air bubbles. Good separation of water and bone bases can observed, with the uniform solid water background appearing bright in the water basis image and almost all contrast inserts bright in the bone basis image. Some dark bands can be observed in the water basis image, connecting and originating from the two inserts at the very top which are the two calcium inserts with the highest concentrations. Such artifacts can be caused by the residual non-linear effect from the polychromatic integral or

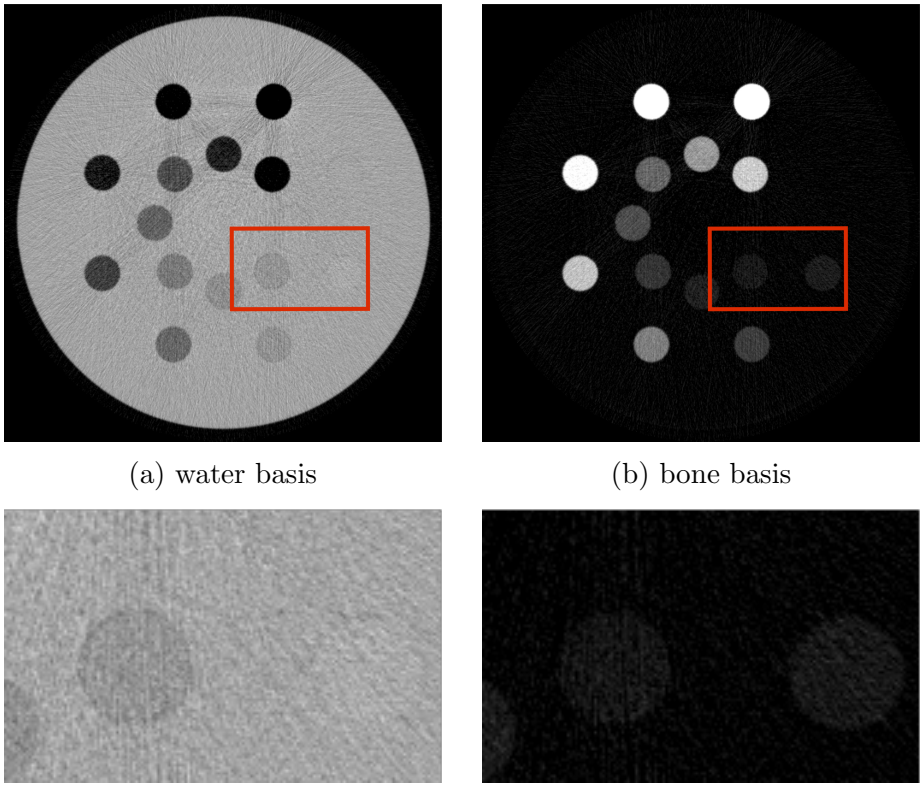

(a) water basis (b) bone basis

(c) water basis, zoomed-in (d) bone basis, zoomed-in

Figure 7.4: Water and bone basis reference images (row 1) and zoomed-in views (row 2) of the ROI as indicated by the red boxes in row 1, from the full-scan real data of the DE-472 phantom, with a display windows of [0, 1.5] for both rows.

the non-linear partial volume effect. The ROI image of the water basis shows these streaks expanding to the bottom half of the phantom.

In Fig. 7.5, we show reconstructed monochromatic images at 50 and 120 KeV and their zoomed-in views of the same ROI images. The 50-KeV image shows elevated contrast, compared the 120-KeV one, for all the contrast inserts except the two solid-water ones. With a narrow display window of [-200, 200] HU, the same banding artifacts, present in the water basis image, can be observed in the 50-KeV image, but not in the 120-KeV one. Both ROI images show discernible contrast level of the two inserts and air bubbles. Some streaks can also be observed in the 50-KeV ROI image, expanded from the banding artifacts above.

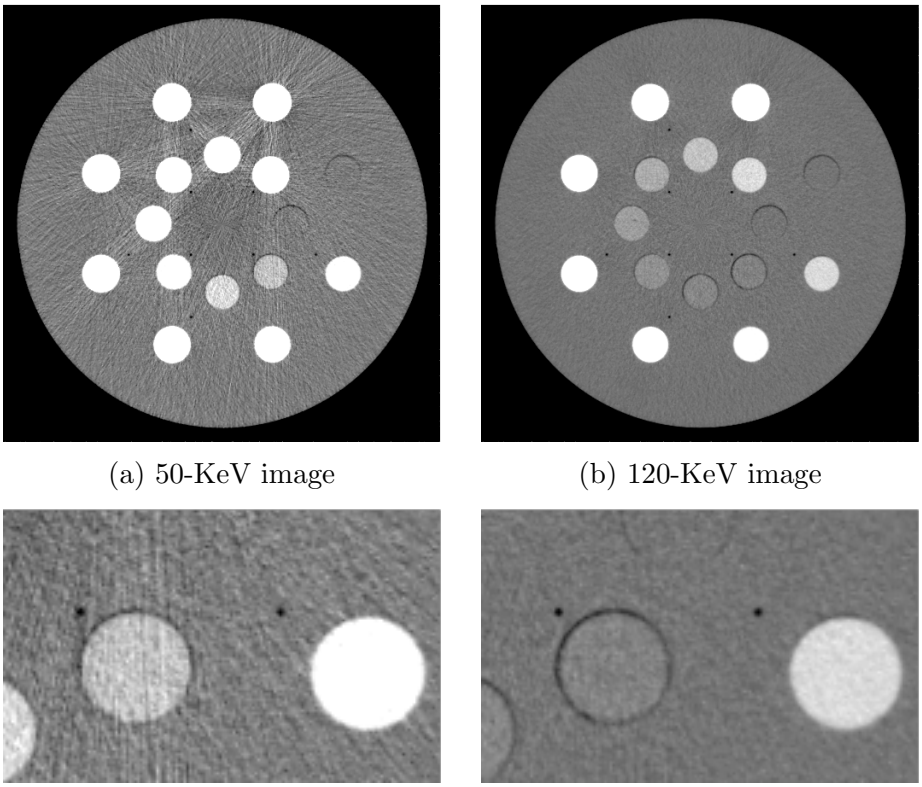

(a) 50-KeV image (b) 120-KeV image

(c) 50-KeV zoomed-in (d) 120-KeV zoomed-in

Figure 7.5: 50- and 120-KeV monochromatic reference images (row 1) and their zoomed-in views (row 2) of the same ROI as indicated by the red boxes in row 1 of Fig. 7.4, from the full-scan real data of the DE-472 phantom, with a display window of [-200, 200] HU for both rows.

Head phantom results In Fig. 7.6, we show reconstructed basis images and two sets of zoomed-in views of ROI images, enclosed by the red, solid-line boxes and green, dashed-line boxes indicated in the full-size images in row 1. Good separation of soft-tissue and bone materials into water and bone basis images can again be observed. The ROI images in row 2 (Figs. 7.6c and 7.6d) contain two low-contrast disks in the head phantom and show good contrast level with clear edges. The ROI images in row 3 (Figs. 7.6e and 7.6f) include bony structures that are near each other and show no visible artifacts.

In Fig. 7.7, we show reconstructed monochromatic images at 50 and 120 KeV and their zoomed-in views of the same ROI images. The 50-KeV image shows improved contrast for the disks, as corroborated by the ROI images in row 2, compared to the 120-KeV ones. The

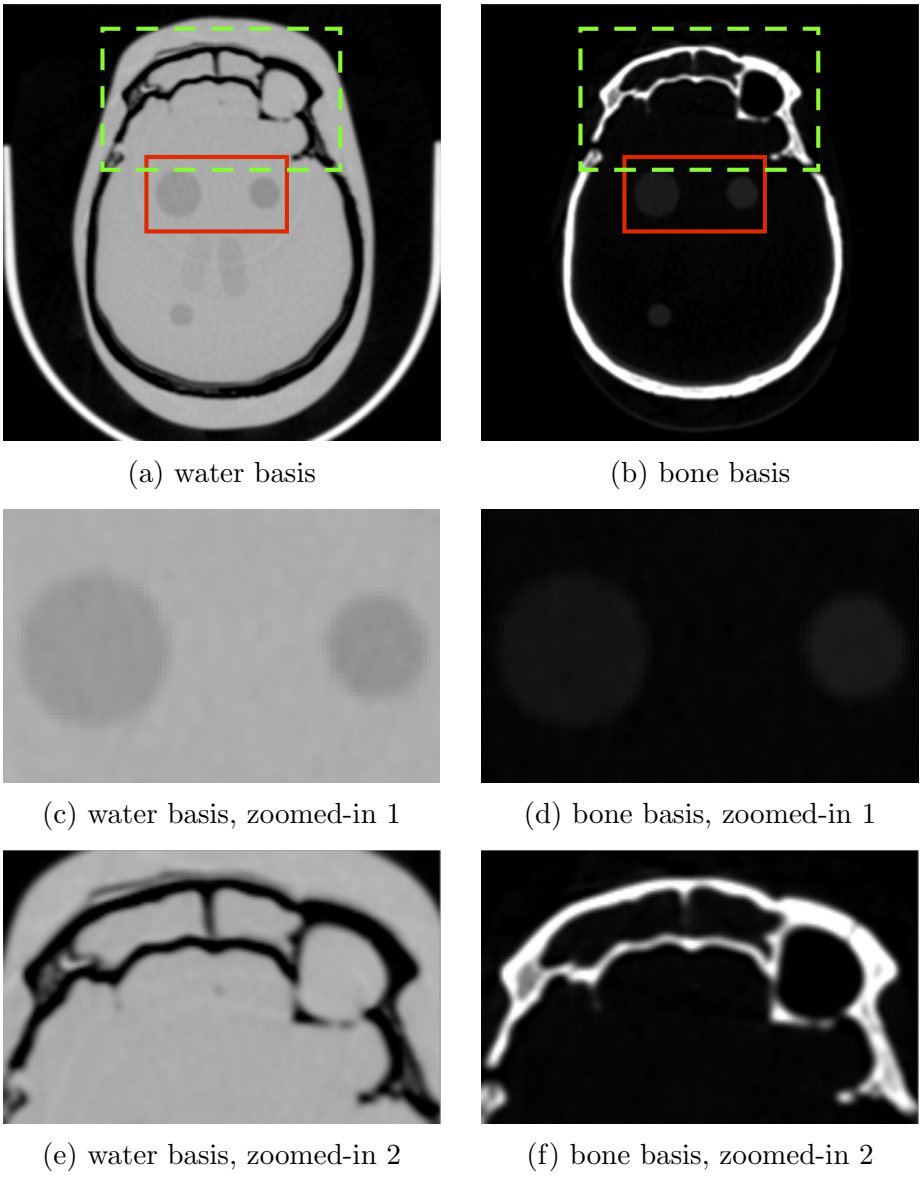

(a) water basis (b) bone basis

(c) water basis, zoomed-in 1 (d) bone basis, zoomed-in 1

(e) water basis, zoomed-in 2 (f) bone basis, zoomed-in 2

Figure 7.6: Water and bone basis reference images (row 1) and zoomed-in views (row 2 and 3) of the ROI as indicated by the red, solid-line boxes and green, dashed-line boxes in row 1, from the full-scan real data of the head phantoms, with a display windows of [0, 1.5] for both rows.

(a) 50-KeV image

(b) 120-KeV image

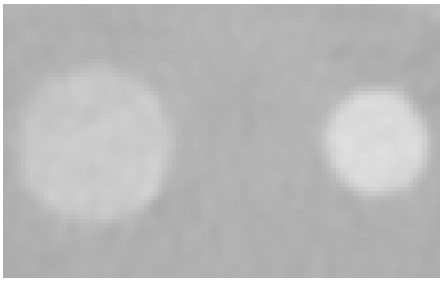

(c) 50-KeV zoomed-in 1

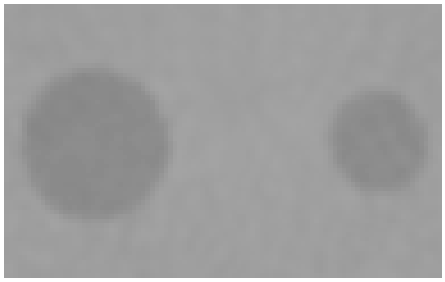

(d) 120-KeV zoomed-in 1

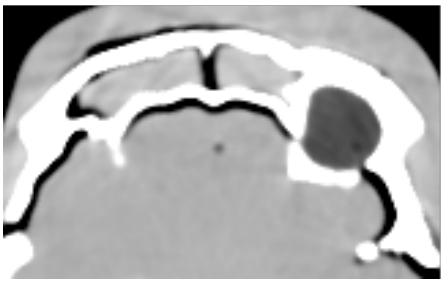

(e) 50-KeV zoomed-in 2

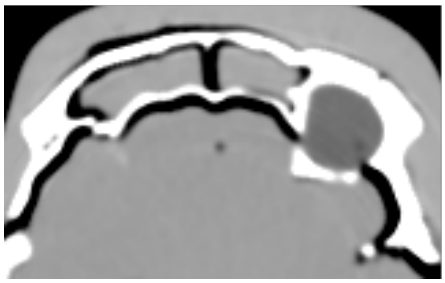

(f) 120-KeV zoomed-in 2

Figure 7.7: 50- and 120-KeV monochromatic reference images (row 1) and their zoomed-in views (row 2 and 3) of the same ROIs as indicated by the red, solid-line boxes and green, dashed-line boxes in row 1 of Fig. 7.6, from the full-scan real data of the head phantoms, with a display window of [-200, 200] HU for both rows.

50-KeV ROI images in row 3 show some streak artifacts inside the region enclosed by the high-contrast bones, typically caused by the residual non-linear BH effect, while the 120-KeV ROI show no such artifacts.

ASD-NC-POCS reconstruction

We then apply the ASD-NC-POCS algorithm on the same full-scan, dual-energy data. The full-scan study serves as a benchmark to show whether the ASD-NC-POCS algorithm can even achieve the level of performance of the existing methods, that is the reference images by the use of data-domain decomposition and FBP-like algorithm.

System matrices describing the two full-scan X-ray transform are denoted by $\mathcal{A}^{[1]}$ and $\mathcal{A}^{[2]}$, as in equation (7.6), and they have the same dimensions with $J^{[1]} = J^{[2]} = 1200 \times 896$ and $I = 512 \times 512$. We select parameter ϵ for yielding monochromatic images visually comparable to the reference images. As a result, $\epsilon = 0.0036$ and $\epsilon = 0.0040$ are selected for the DE-472 and head phantom reconstruction, respectively.

Demonstration of reconstruction convergence We first use a reconstruction from data of the full-scan configuration to demonstrate that the practical convergence conditions in equation (7.13) can be met by the ASD-NC-POCS algorithm. Without loss of generality, the reconstruction is carried out with $\epsilon = 0.0036$, and we display in Fig. 7.8 convergence metrics $\bar{D}(\mathbf{b}_1^{(n)}, \mathbf{b}_2^{(n)})$ and $\Delta_{\text{TV}}(\mathbf{b}_1^{(n)}, \mathbf{b}_2^{(n)})$ as functions of iteration number n. It can be observed that the ASD-NC-POCS algorithm converges to meet the practical convergence conditions.

DE-472 phantom results We show in Fig. 7.9 reconstructed basis images and their ROIs of the DE-472 phantom from full-scan data. The water basis image is visibly smoother than the corresponding reference image, due to the TV being applied directly on the basis images. The dark bands, as seen in Fig. 7.4a, are also reduced in the water basis image in Fig. 7.9a.

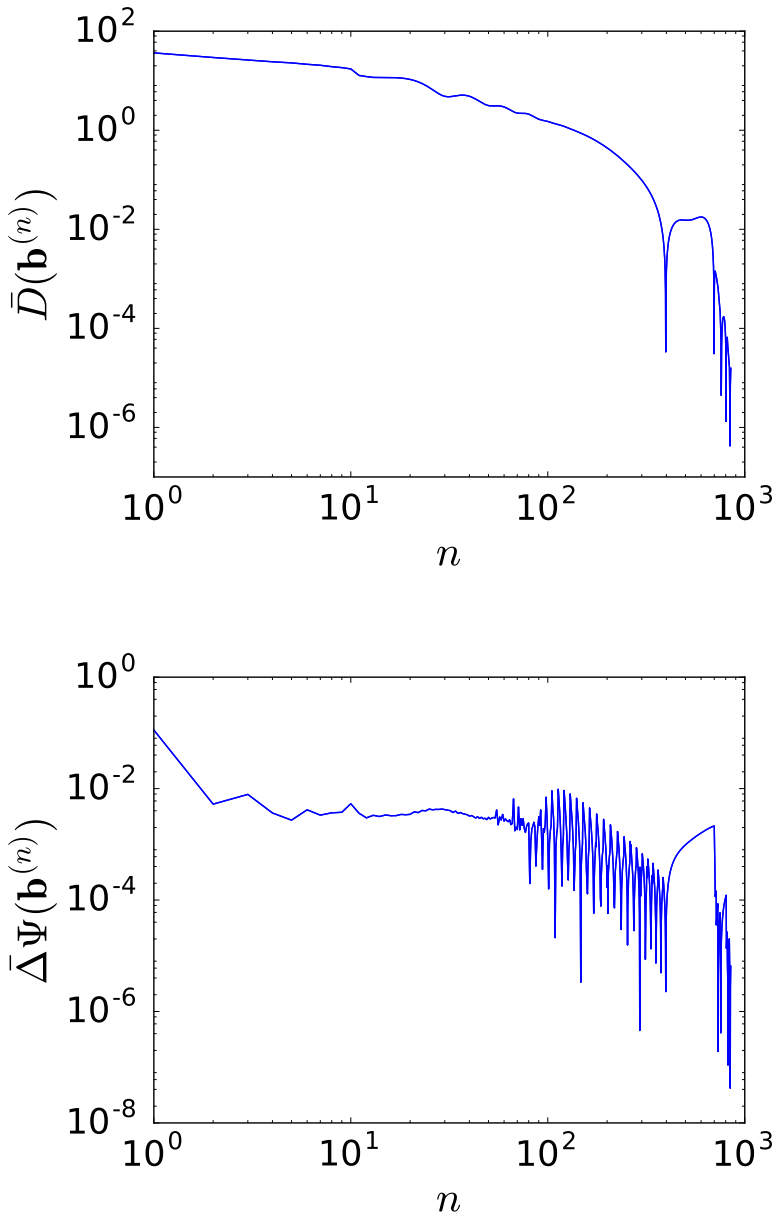

Figure 7.8: Convergence metrics $\bar{D}(\mathbf{b}_1^{(n)}, \mathbf{b}_2^{(n)})$ and $\Delta_{\text{TV}}(\mathbf{b}_1^{(n)}, \mathbf{b}_2^{(n)})$ as functions of iteration number n, obtained with $\epsilon = 0.0036$ for the DE-472 phantom data in the short-plus-short real data study.

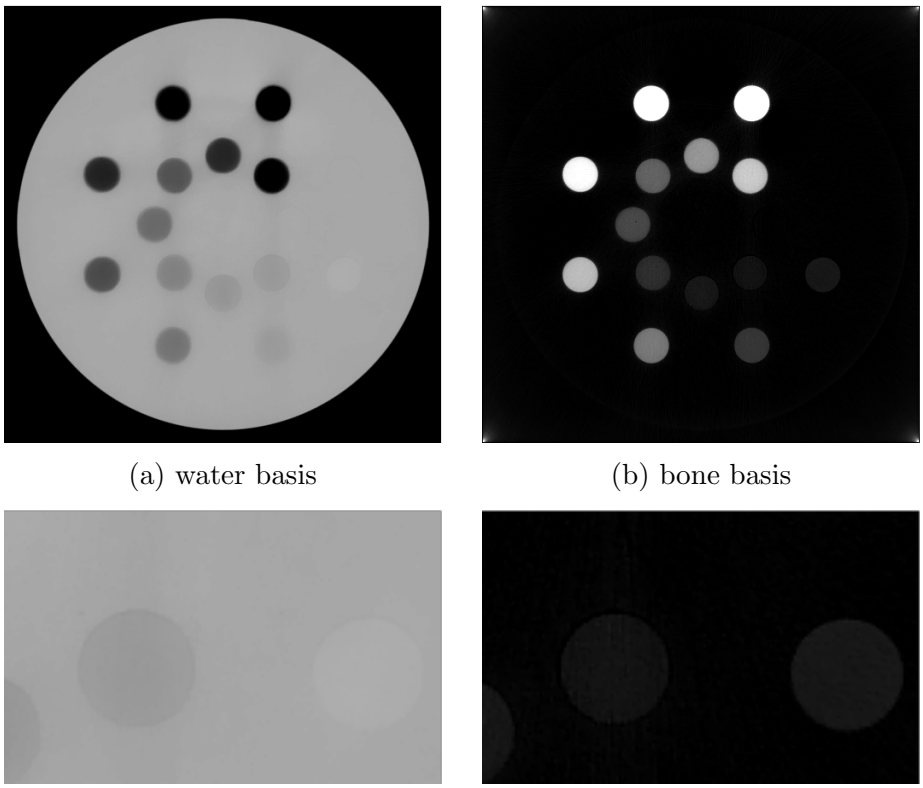

(a) water basis (b) bone basis

(c) water basis, zoomed-in (d) bone basis, zoomed-in

Figure 7.9: Water and bone basis ASD-NC-POCS images (row 1) and zoomed-in views (row 2) of the same ROI as indicated by the red boxes in row 1 of Fig. 7.4, from the full-scan real data of the DE-472 phantom, with a display windows of [0, 1.5] for both rows.

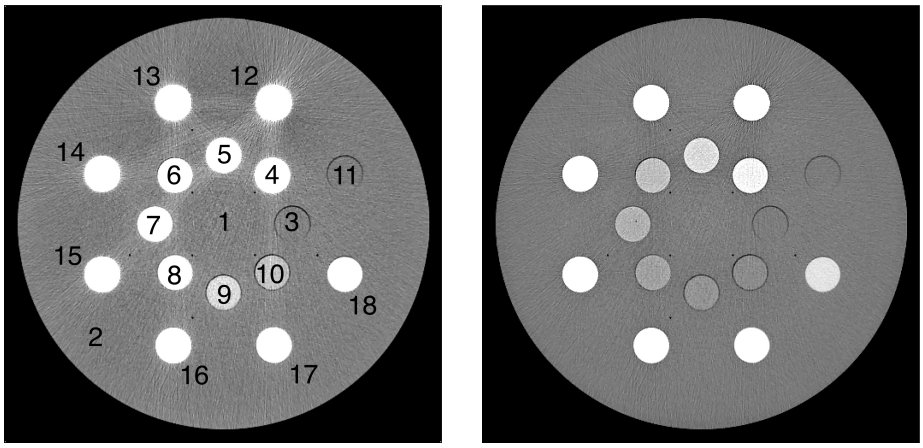

(a) 50-KeV image (b) 120-KeV image

(c) 50-KeV zoomed-in (d) 120-KeV zoomed-in

Figure 7.10: 50- and 120-KeV monochromatic ASD-NC-POCS images (row 1) and their zoomed-in views (row 2) of the same ROI as indicated by the red boxes in row 1 of Fig. 7.4, from the full-scan real data of the DE-472 phantom, with a display window of [-200, 200] HU for both rows.

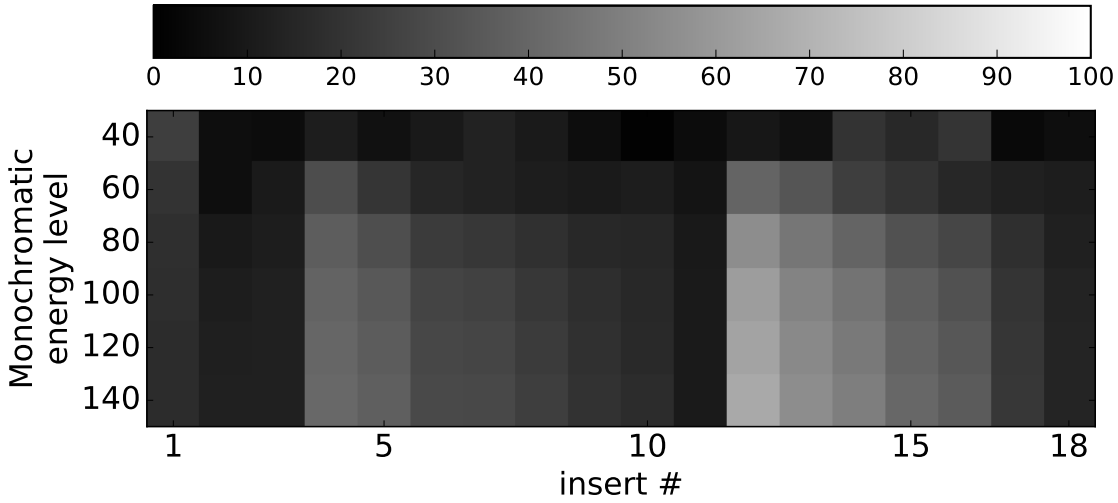

Figure 7.11: Bias map of ASD-NC-POCS images at different energy levels for each insert of the DE-472 phantom, compared to the reference images, from the full-scan real data.

The ROI images also appear smoother than their counter-parts in the reference images in Fig. 7.4.

The monochromatic images at 50 and 120 KeV in Fig. 7.10 look substantially similar to the reference images, however, with less conspicuous banding streak and smoother background in the 50-KeV image. The ROI images show similar level of contrast of the inserts with sharper edges. The streaks are still visible in the 50-KeV ROI image, even in the 120-KeV one as well, most likely due to the reduced noise fluctuation.

In addition, we calculate bias of each insert from the monochromatic images at 6 different energy levels, compared to the corresponding reference images at these energy levels. The bias for each insert is calculated with a formula similar to equation (5.6) as

$$\theta_{rm} = \frac{1}{I_r} \sum_i |f_{im} - f'_{im}|, \tag{7.13}$$

where f_{im} and f'_{im} denote the ith pixel value of the ASD-NC-POCS and reference, respectively, monochromatic image at energy m and I_r the number of pixels within insert r. We calculate for a total of 18 inserts, with 16 physical ones and 2 virtual inserts of the background in the center and at the peripheral, numbered from 1 to 18 as shown in Fig. 7.10. We plot the 2D bias map for the full-scan ASD-NC-POCS images in Fig. 7.11, with the colorbar at the top. All biases are under 100 HU and most of them are under 50 HU. The solid-water inserts (No. 1, 2, 3, 11) result in the lowest bias, compared to the reference images, while the iodine and calcium contrast inserts with the highest concentration (No. 4 and 12, respectively) give the highest biases.

Head phantom results We show in Fig. 7.12 reconstructed basis images and their ROIs of the head phantom from full-scan data. The basis images are similar to their counter-parts of the reference images, with smoother texture. Sharper edges can also be observed in the ROI images. The bone ROI image in row 2 (Fig. 7.12d) show slightly lower contrast of the

disks than the reference image (Fig. 7.6d).

The monochromatic images at 50 and 120 KeV in Fig. 7.13 are comparable to the reference images. The artifacts in the water basis ROI image in row 2 (Fig. 7.13e) show reduced streak artifacts and sharper edges than the reference one.

7.5.2 Short-plus-short scan study

We apply the ASD-NC-POCS algorithm to reconstruct basis and monochromatic images from partial-scan data, and demonstrate the potential of the algorithm in enabling new scanning configurations of practical significance in terms of scanning time, imaging dose, and system cost for dual-energy CT.

We first start with the short-plus-short scan, as shown in Fig. 7.1b, in which each of the low- and high-KVp data sets contains 764 views distributed over an arc spanning a short-scan range. At each view, the central slice of the detector array containing 896 detector bins is used for data reconstruction. As a result, system matrices $\mathcal{A}^{[1]}$ and $\mathcal{A}^{[2]}$ are of identical dimensions with $J^{[1]} = J^{[2]} = 764 \times 896$ and $I = 512 \times 512$. Furthermore, using the same strategy based on visual assessment, we select $\epsilon = 0.0036$ and $\epsilon = 0.0036$ for the DE-472 and head phantom, respectively.

DE-472 phantom results We show in Figs. 7.14 and 7.15 reconstructed basis and monochromatic images at 50 and 120 KeV, respectively, and their ROIs of the DE-472 phantom from short-plus-short scan data. The basis images are visibly comparable to their counter-parts in the full-scan results in Fig. 7.9. The inserts in the lower right corner (No. 10 and 17) seem to have lower contrast in the basis image, which is corroborated by the zoomed-in ROI of water basis in Fig. 7.14a. This could be due to over-smoothing of the basis images from the TV-minimization. However, the monochromatic images show no contrast loss and are very close to the full-scan results in Fig. 7.10.

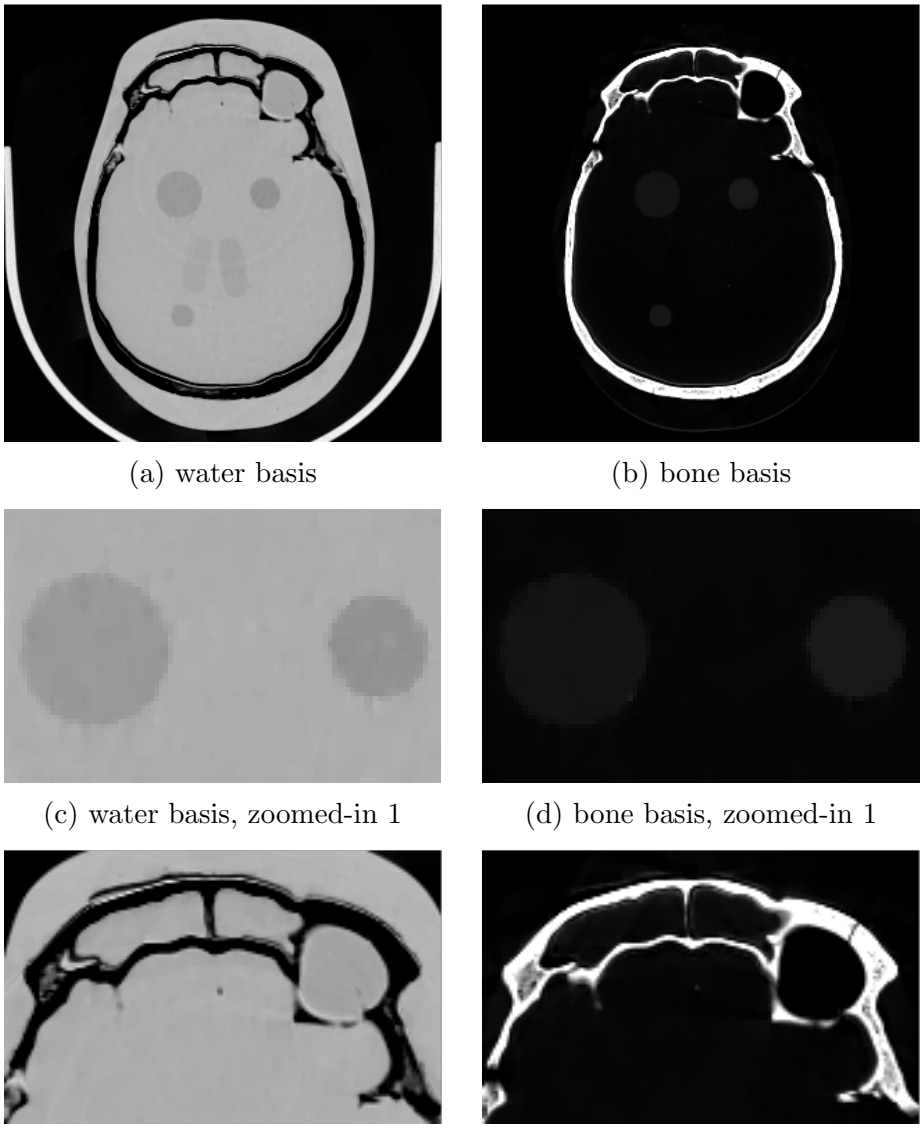

(a) water basis (b) bone basis

(c) water basis, zoomed-in 1 (d) bone basis, zoomed-in 1

(e) water basis, zoomed-in 2 (f) bone basis, zoomed-in 2

Figure 7.12: Water and bone basis ASD-NC-POCS images (row 1) and zoomed-in views (row 2 and 3) of the ROIs as indicated by the red, solid-line boxes and green, dashed-line boxes in row 1 of Fig. 7.6, from the full-scan real data of the head phantom, with a display windows of [0, 1.5] for both rows.

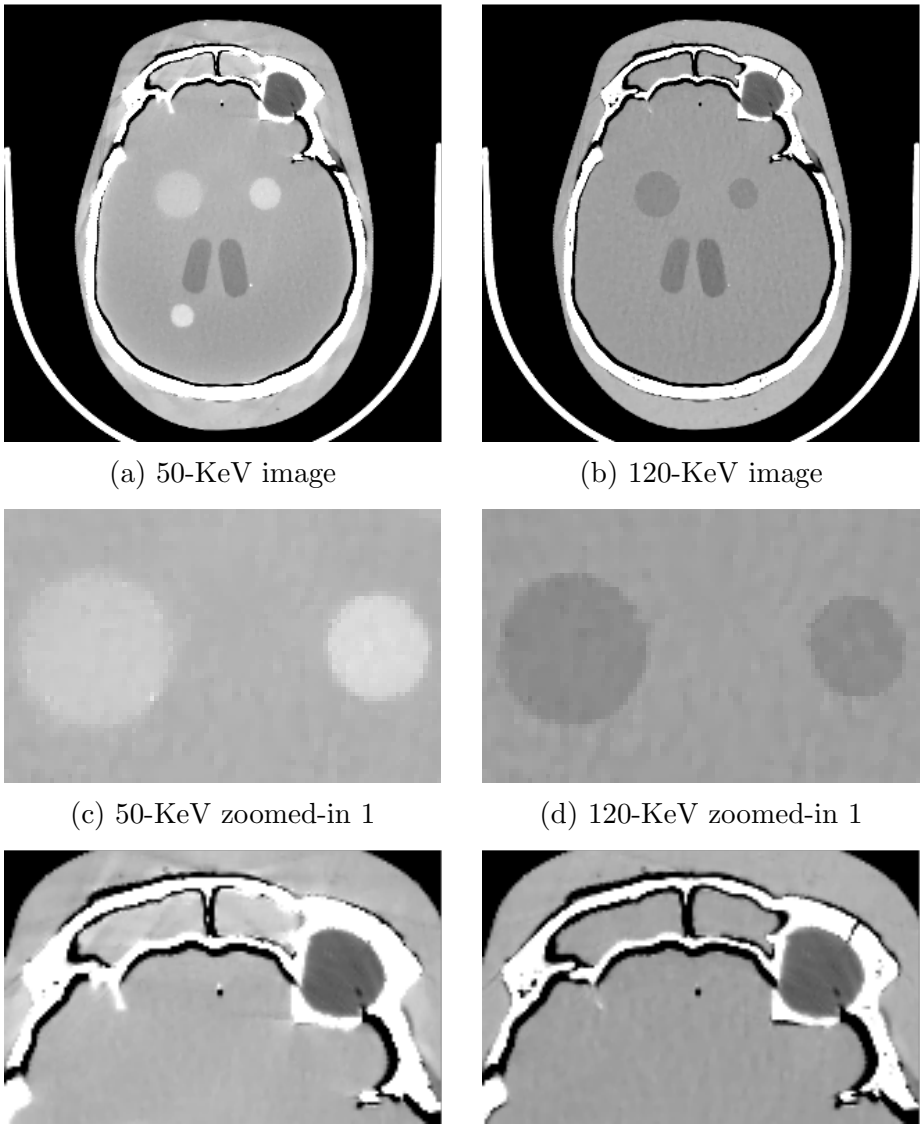

(a) 50-KeV image (b) 120-KeV image

(c) 50-KeV zoomed-in 1 (d) 120-KeV zoomed-in 1

(e) 50-KeV zoomed-in 2 (f) 120-KeV zoomed-in 2

Figure 7.13: 50- and 120-KeV monochromatic ASD-NC-POCS images (row 1) and their zoomed-in views (row 2 and 3) of the same ROIs as indicated by the red, solid-line boxes and green, dashed-line boxes in row 1 of Fig. 7.6, from the full-scan real data of the head phantom, with a display window of [-200, 200] HU for both rows.

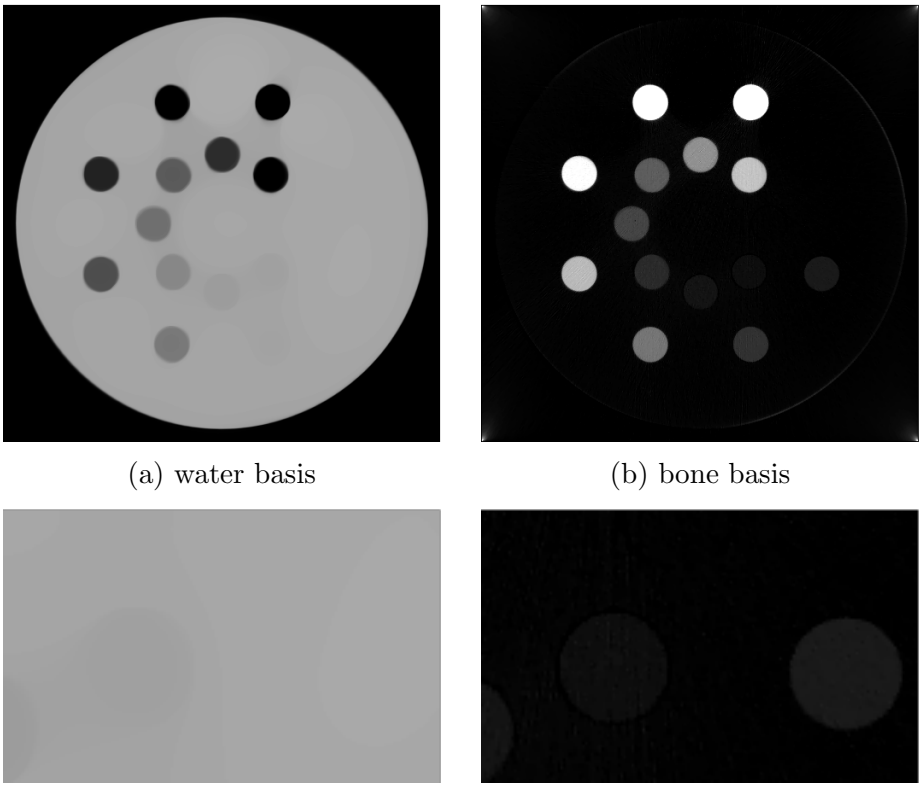

(a) water basis (b) bone basis

(c) water basis, zoomed-in (d) bone basis, zoomed-in

Figure 7.14: Water and bone basis ASD-NC-POCS images (row 1) and zoomed-in views (row 2) of the same ROI as indicated by the red boxes in row 1 of Fig. 7.4, from the short-plus-short scan real data of the DE-472 phantom, with a display windows of [0, 1.5] for both rows.

The bias map in Fig. 7.16 for the short-plus-short scan images show similar results, compared the one for the full-scan images in Fig. 7.11. However, elevated bias levels of the 40-KeV monochromatic images can be seen for most contrast inserts, which could be due to the over-smoothing of the water basis image.

Head phantom results We show in Figs. 7.17 and 7.18 reconstructed basis and monochromatic images at 50 and 120 KeV, respectively, and their ROIs of the head phantom from short-plus-short scan data. The basis images in row 1 are overall comparable to their counterparts in the full-scan results in Fig. 7.12. The larger disk on the left in the water basis ROI image in row 2 (Fig. 7.17c) show slightly distorted shape from a circle, which can be a result

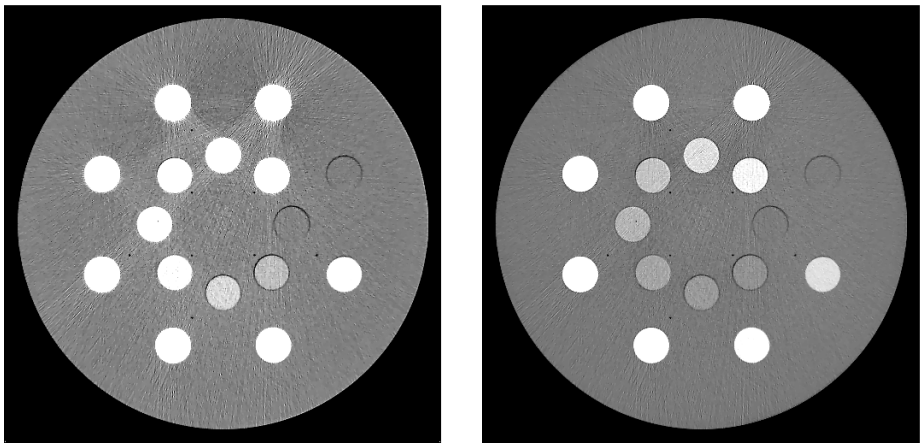

(a) 50-KeV image (b) 120-KeV image

(c) 50-KeV zoomed-in (d) 120-KeV zoomed-in

Figure 7.15: 50- and 120-KeV monochromatic ASD-NC-POCS images (row 1) and their zoomed-in views (row 2) of the same ROI as indicated by the red boxes in row 1 of Fig. 7.4, from the short-plus-short-scan real data of the DE-472 phantom, with a display window of [-200, 200] HU for both rows.

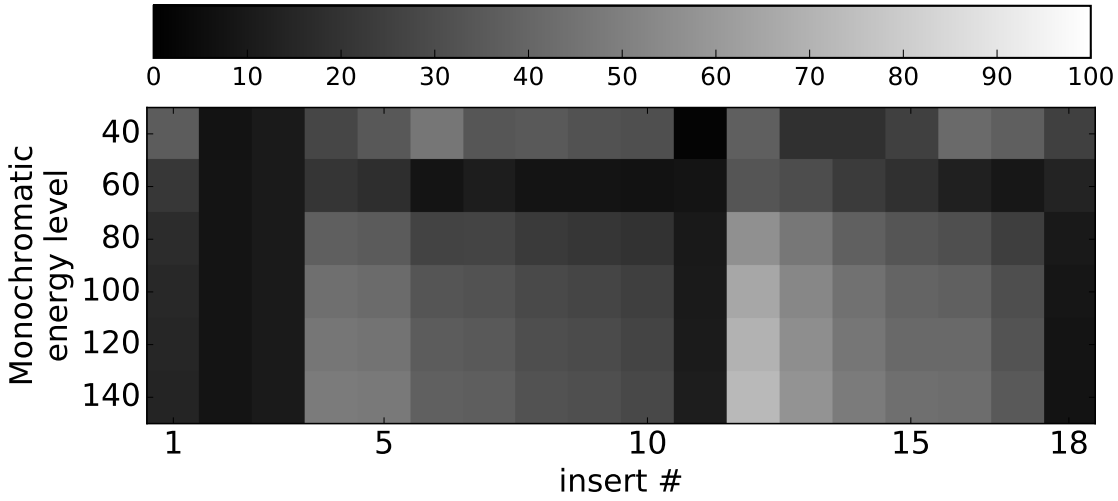

Figure 7.16: Bias map of ASD-NC-POCS images at different energy levels for each insert of the DE-472 phantom, compared to the references, from the short-plus-short scan real data.

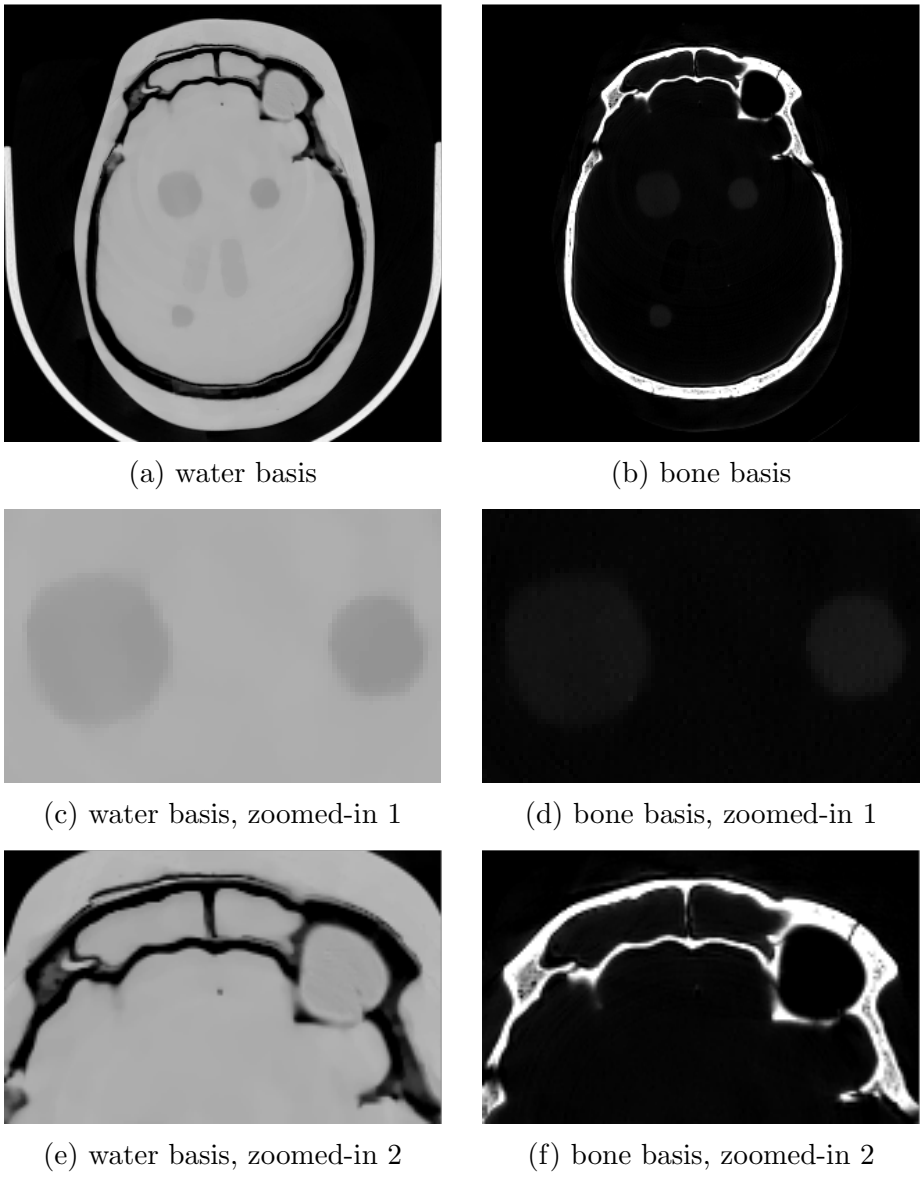

(a) water basis (b) bone basis

(c) water basis, zoomed-in 1 (d) bone basis, zoomed-in 1

(e) water basis, zoomed-in 2 (f) bone basis, zoomed-in 2

Figure 7.17: Water and bone basis ASD-NC-POCS images (row 1) and zoomed-in views (row 2 and 3) of the ROIs as indicated by the red, solid-line boxes and green, dashed-line boxes in row 1 of Fig. 7.6, from the short-plus-short-scan real data of the head phantom, with a display windows of [0, 1.5] for both rows.

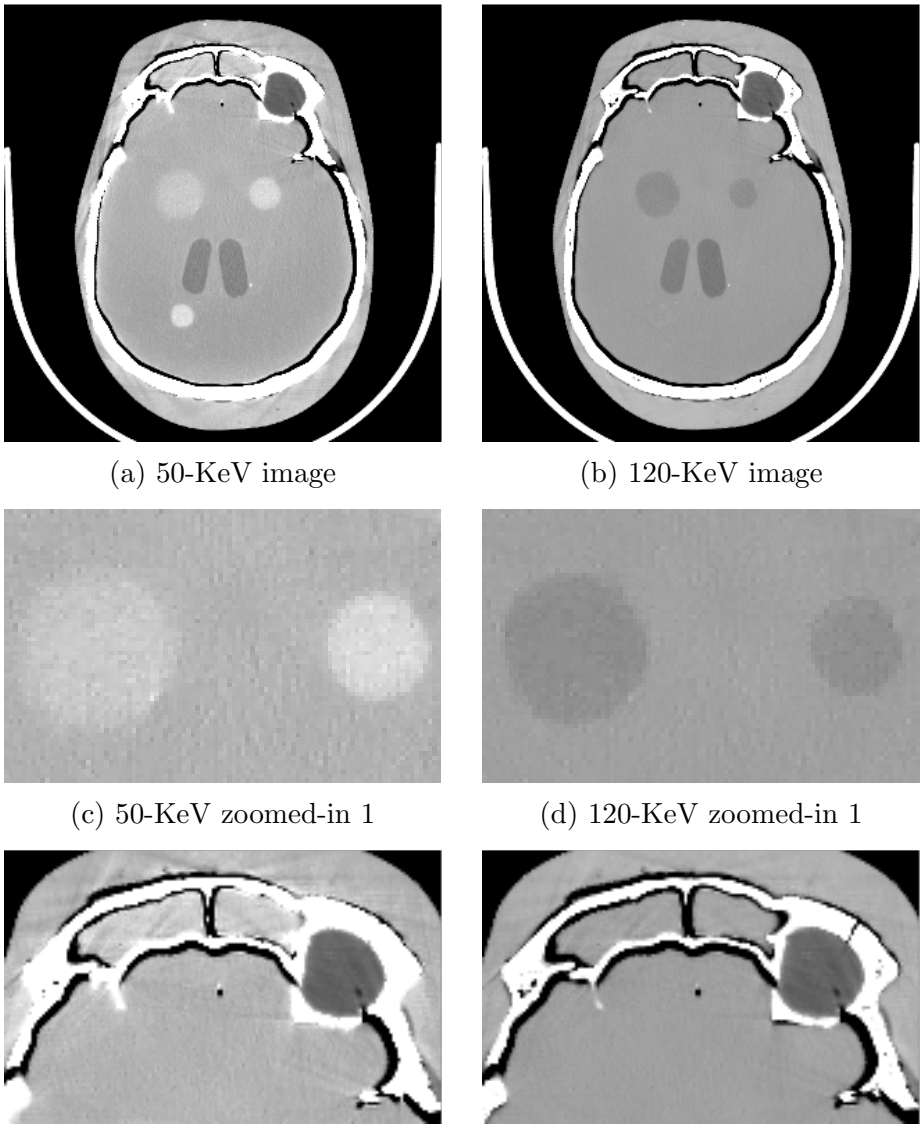

(a) 50-KeV image (b) 120-KeV image

(c) 50-KeV zoomed-in 1 (d) 120-KeV zoomed-in 1

(e) 50-KeV zoomed-in 2 (f) 120-KeV zoomed-in 2

Figure 7.18: 50- and 120-KeV monochromatic ASD-NC-POCS images (row 1) and their zoomed-in views (row 2 and 3) of the same ROIs as indicated by the red, solid-line boxes and green, dashed-line boxes in row 1 of Fig. 7.6, from the short-plus-short-scan real data of the head phantoms, with a display window of [-200, 200] HU for both rows.

of over-smoothing in the basis image. The ROI images in row 3 show no visible artifacts from the reduction of data, as compared to the full-scan results.

The monochromatic images are also visibly close to the full-scan images. The larger disk on the left in the 120-KeV ROI image in row 2 (Fig. 7.18d) show the same slightly distorted circular shape. In addition, the streaks in the 50-KeV ROI image in row 3 (Fig. 7.18e) are similar to those in the full-scan courter-part (Fig. 7.13e).

7.5.3 Half-plus-half scan study

Finally, we apply the ASD-NC-POCS algorithm to reconstruction basis image monochromatic images from the half-plus-half scan configuration, as shown on the left in Fig. 7.1c, where each of the low and high KVp data sets contains 600 views distributed over half a rotation. System matrices $\mathcal{A}^{[1]}$ and $\mathcal{A}^{[2]}$ are again of identical dimensions with $J^{[1]} = J^{[2]} = 600 \times 896$ and $I = 512 \times 512$. We select $\epsilon = 0.0034$ and $\epsilon = 0.0039$ for the DE-472 and head phantom reconstructions, respectively.

DE-472 phantom results We show in Figs. 7.19 and 7.20 reconstructed basis and monochromatic images at 50 and 120 KeV, respectively, and their ROIs of the DE-472 phantom from half-plus-half scan data. The basis images are overall comparable to the full-scan results in Fig. 7.9. The dark bands are more visible in the half-plus-half water basis image, and bright shades can be observed on the right side of the calcium insert on the top right corner (No. 12). The water basis ROI image in Fig. 7.19c shows a slightly distorted circular insert on the left. The monochromatic images show no additional artifacts. The banding artifacts in the 50-KeV image (Fig. 7.20a) are more conspicuous, together with the shading around the two calcium inserts on the top (No. 12 and 13). The 50- and 120-KeV ROI images from the half-plus-half scan are almost identical to those from the full-scan in Fig. 7.10. The bias map in Fig. 7.16 also show comparable results to the full-scan results, even for the 40-KeV

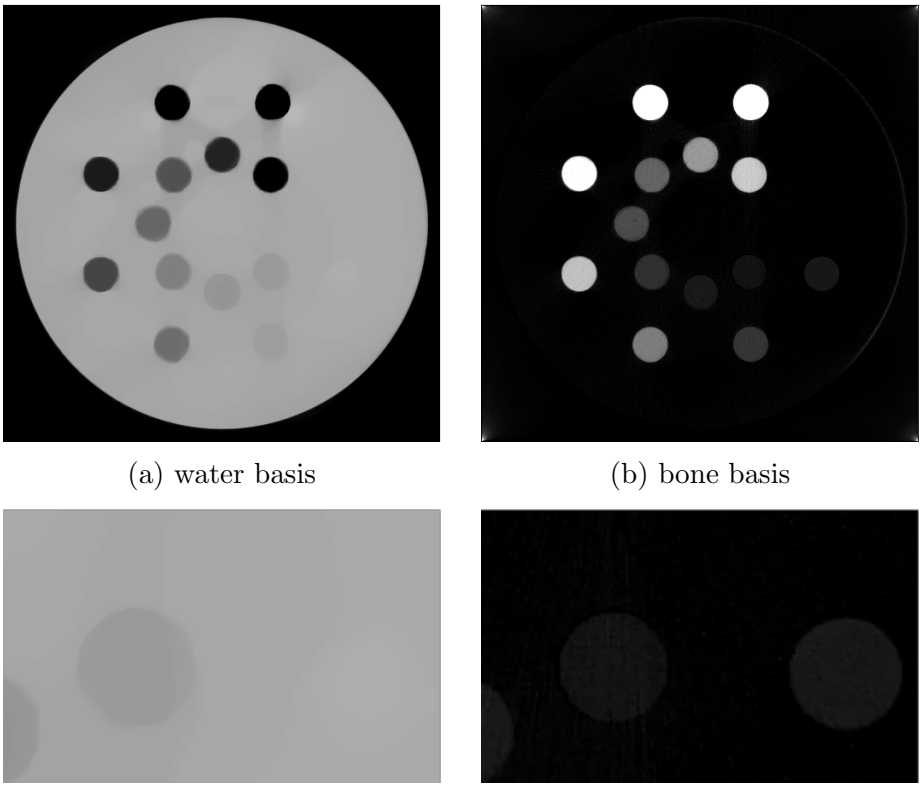

(a) water basis (b) bone basis

(c) water basis, zoomed-in (d) bone basis, zoomed-in

Figure 7.19: Water and bone basis ASD-NC-POCS images (row 1) and zoomed-in views (row 2) of the same ROI as indicated by the red boxes in row 1 of Fig. 7.4, from the half-plus-half-scan real data of the DE-472 phantom, with a display windows of [0, 1.5] for both rows.

images.

Head phantom results We show in Figs. 7.22 and 7.23 reconstructed basis and monochromatic images at 50 and 120 KeV, respectively, and their ROIs of the head phantom from half-plus-half scan data. The basis images in row 1 are similar to the the full-scan results, while the water basis image (Fig. 7.22a) shows some visible dark shades of certain oblique direction. The ROI images in row 1 show no visible artifacts. The water basis ROI image row 3 (Fig. 7.22e) show conspicuous dark shades of oblique angle. These shades are possibly caused by the half-plus-half sampling condition, as the direction corresponds to the angular positions of the tube where the KVp switching happens.

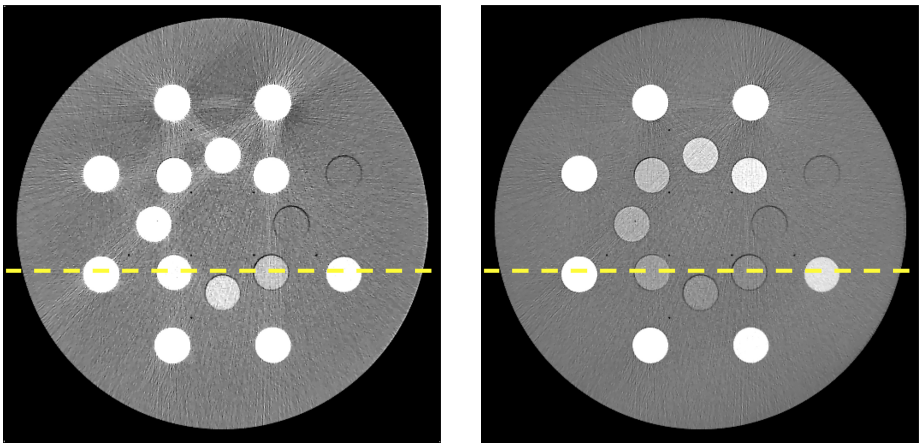

(a) 50-KeV image (b) 120-KeV image

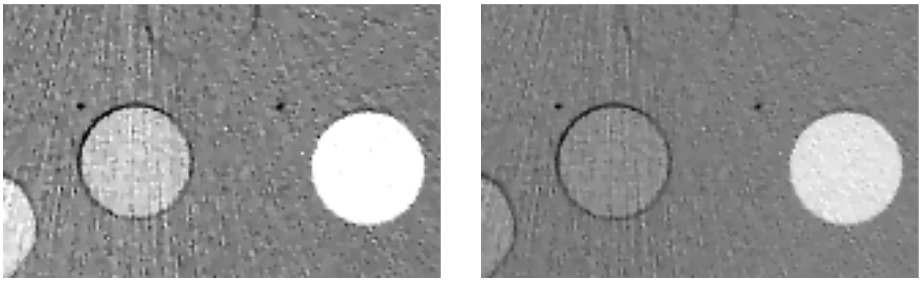

(c) 50-KeV zoomed-in (d) 120-KeV zoomed-in

Figure 7.20: 50- and 120-KeV monochromatic ASD-NC-POCS images (row 1) and their zoomed-in views (row 2) of the same ROI as indicated by the red boxes in row 1 of Fig. 7.4, from the half-plus-half scan real data of the DE-472 phantom, with a display window of [-200, 200] HU for both rows.

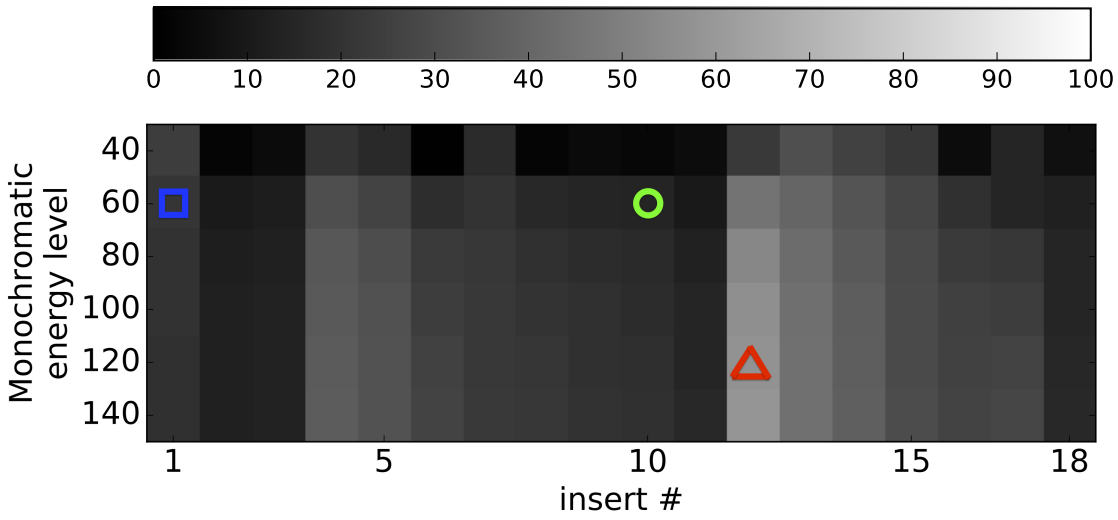

Figure 7.21: Bias map of ASD-NC-POCS images at different energy levels for each insert of the DE-472 phantom, compared to the references, from the half-plus-half scan real data.

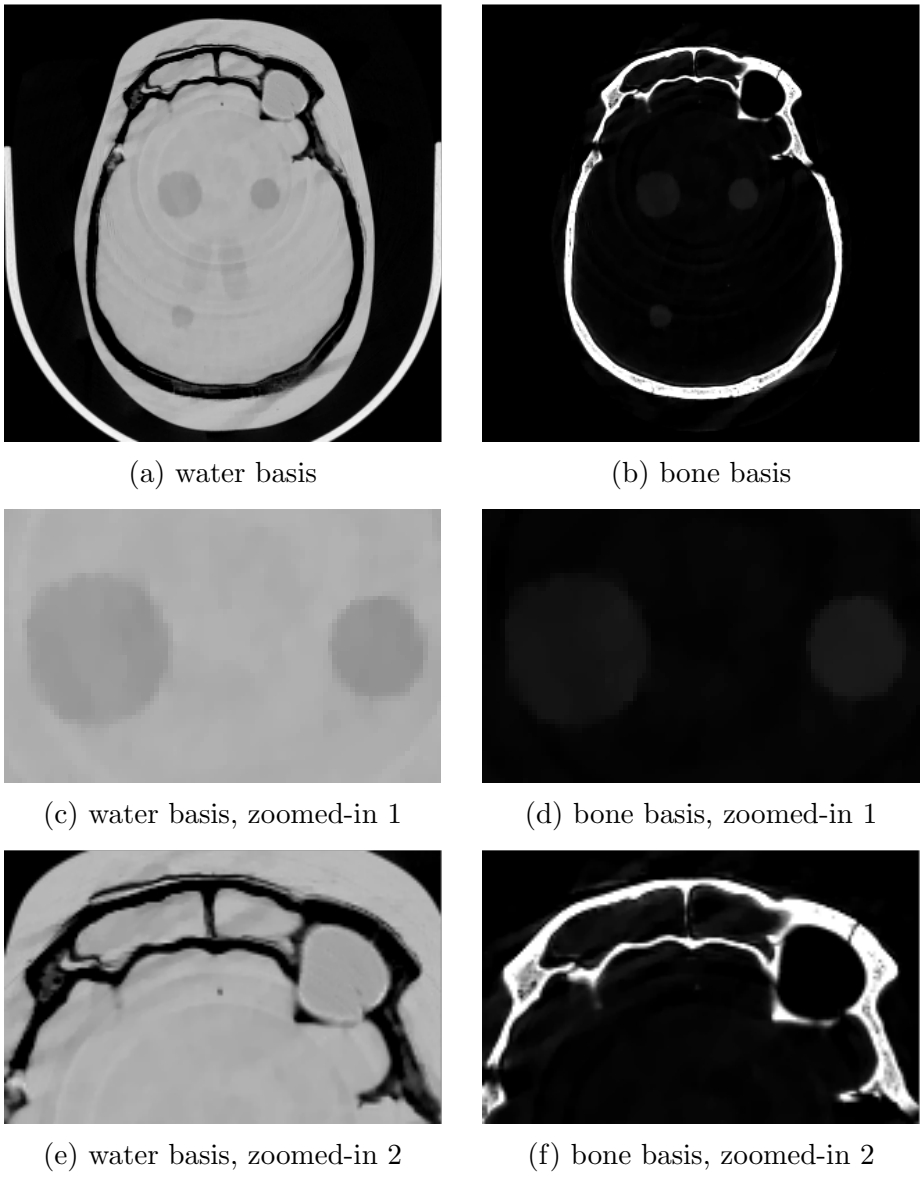

(a) water basis (b) bone basis

(c) water basis, zoomed-in 1 (d) bone basis, zoomed-in 1

(e) water basis, zoomed-in 2 (f) bone basis, zoomed-in 2

Figure 7.22: Water and bone basis ASD-NC-POCS images (row 1) and zoomed-in views (row 2 and 3) of the ROIs as indicated by the red, solid-line boxes and green, dashed-line boxes in row 1 of Fig. 7.6, from the half-plus-half scan real data of the head phantom, with a display windows of [0, 1.5] for both rows.

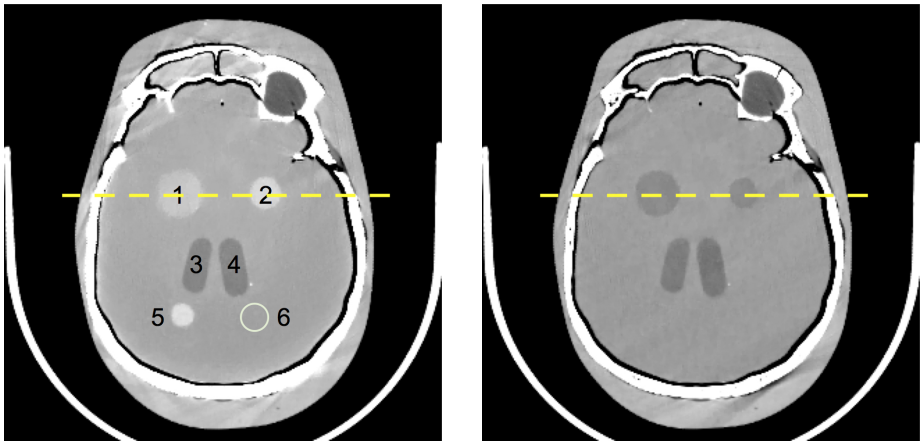

(a) 50-KeV image (b) 120-KeV image

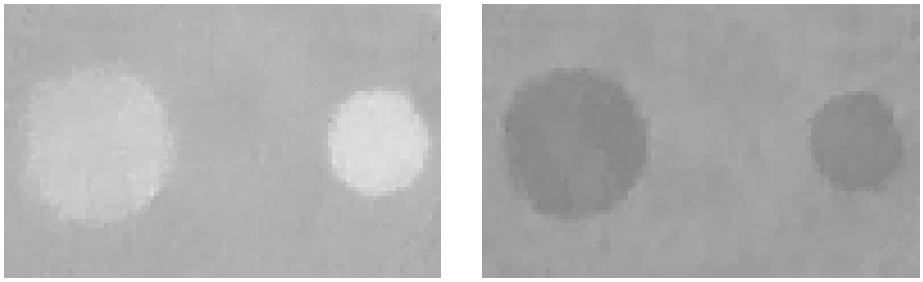

(c) 50-KeV zoomed-in 1 (d) 120-KeV zoomed-in 1

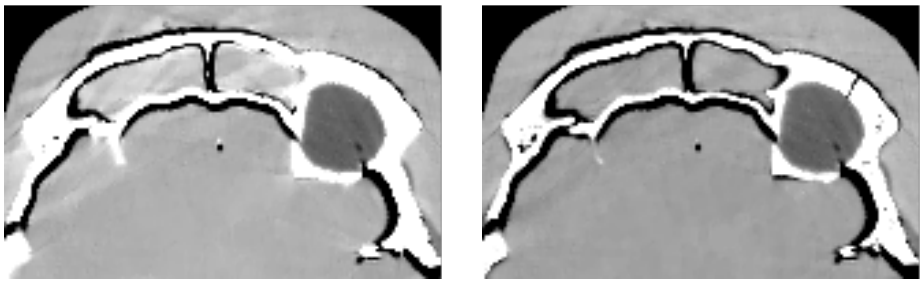

(e) 50-KeV zoomed-in 2 (f) 120-KeV zoomed-in 2

Figure 7.23: 50- and 120-KeV monochromatic ASD-NC-POCS images (row 1) and their zoomed-in views (row 2 and 3) of the same ROIs as indicated by the red, solid-line boxes and green, dashed-line boxes in row 1 of Fig. 7.6, from the half-plus-half scan real data of the head phantom, with a display window of [-200, 200] HU for both rows.

The monochromatic images also show the shading artifacts, in the form of bright streaks in the 50-KeV image and dark streaks in the 120-KeV image. The ROI images in row 2 show no visible artifacts and comparable contrast level of the disks to the full-scan result. The ROI images in row 3 show oblique streaks that are missing in the full-scan short-plus-short scan results. In the 120-KeV ROI image in row 3 (Fig. 7.23f), the dark streak, which originates from the bone on the lower left corner and goes through the bony regions, is conspicuous and obvious. Other than these streaks, the monochromatic images look visibly similar to their counter-parts in the full-scan results.

7.5.4 Comparing the scan configurations

We compare the three single-KVp-switch scan configurations investigated in this chapter, in terms of quantitative metrics such as bias and contrast level. Profiles of the monochromatic images are also plotted to compare the quantitative accuracy across different configurations.

DE-472 phantom

Using the DE-472 phantom, we pick three different locations on the bias map, corresponding to inserts 1, 10, and 12 at monochromatic images at 60, 60, and 120 KeV, respectively, as indicated on the bias maps of the half-plus-half scan results in Fig. 7.21. For each location, we plot the bias value for the three different scan configurations. As shown in Fig. 7.24, for either of the three locations selected, the variation of bias among the configurations is not big. Note that the bias does not have an increasing trend with the decreasing data quantity, from full-scan to short-plus-short and to half-plus-half scan. This could be due to the selection of parameter ϵ, which largely determines the reconstruction.

Further, we shown in Fig. 7.25 profiles plots and in Fig. 7.26 their zoomed-in sections across the yellow dashed line as indicated on the 50- and 120-KeV monochromatic images in Fig 7.20. Profiles of images from different scan configurations, including the reference image

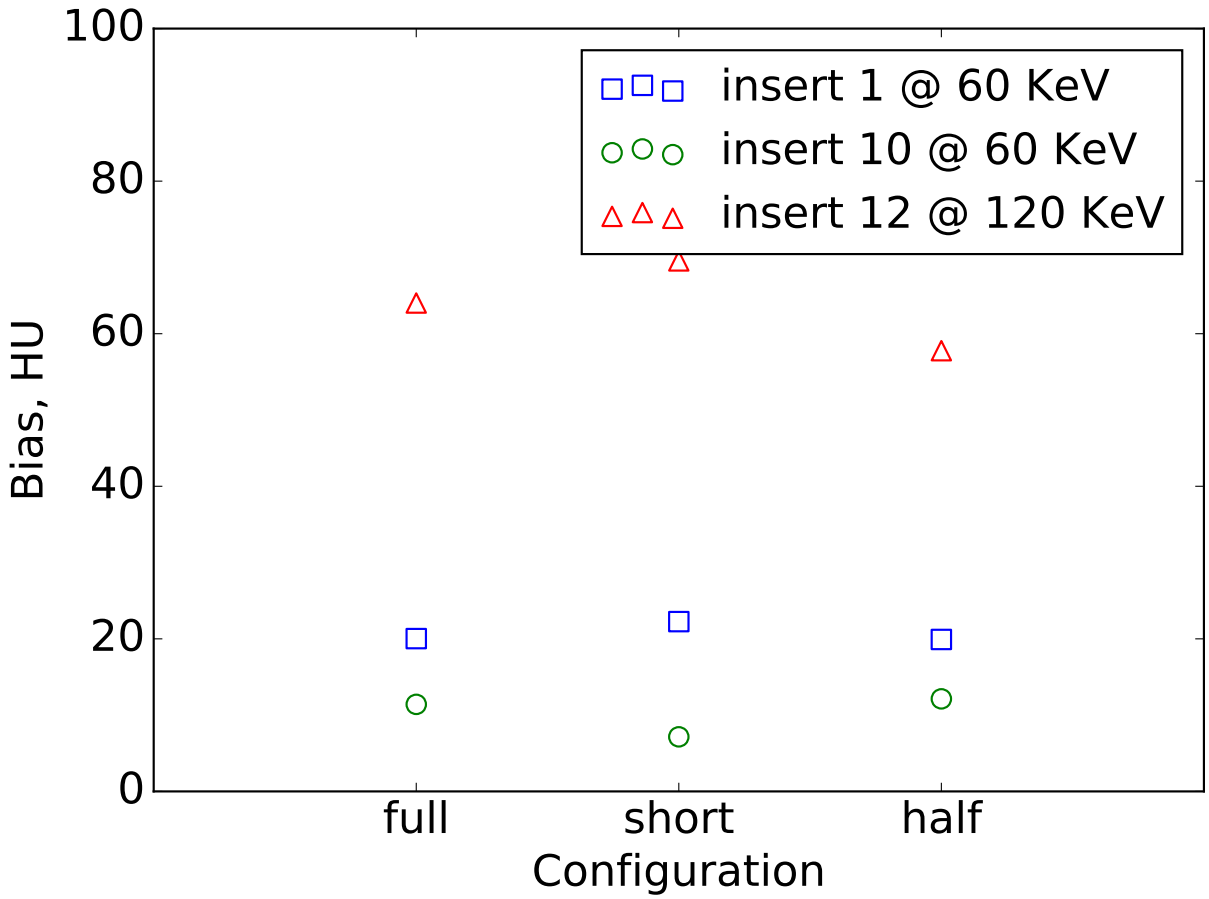

Figure 7.24: Bias at three locations on the bias map from the monochromatic images reconstructed from the full-, short-plus-short, and half-plus-half scan data. The variation among the different configuration is not big.

from the full-scan, are plotted overlapping each other. The results show good quantitative agreement among across all configurations.

In addition, we compare the performance of a material differentiation task between calcium and iodine using images reconstructed from full-scan data with the standard method, full-scan, short-plus-short-scan, and half-plus-half-scan data with the ASD-NC-POCS algorithm. A potential problem in separating calcium with iodine using the thresholding-based method is that there is an overlap of HU values between calcium and iodine in a single energy image. As shown in Fig. 7.27b, some of the calcium inserts (pointed to by blue arrows) in the 120-keV monochromatic image of the DE-472 phantom seem to have the same gray

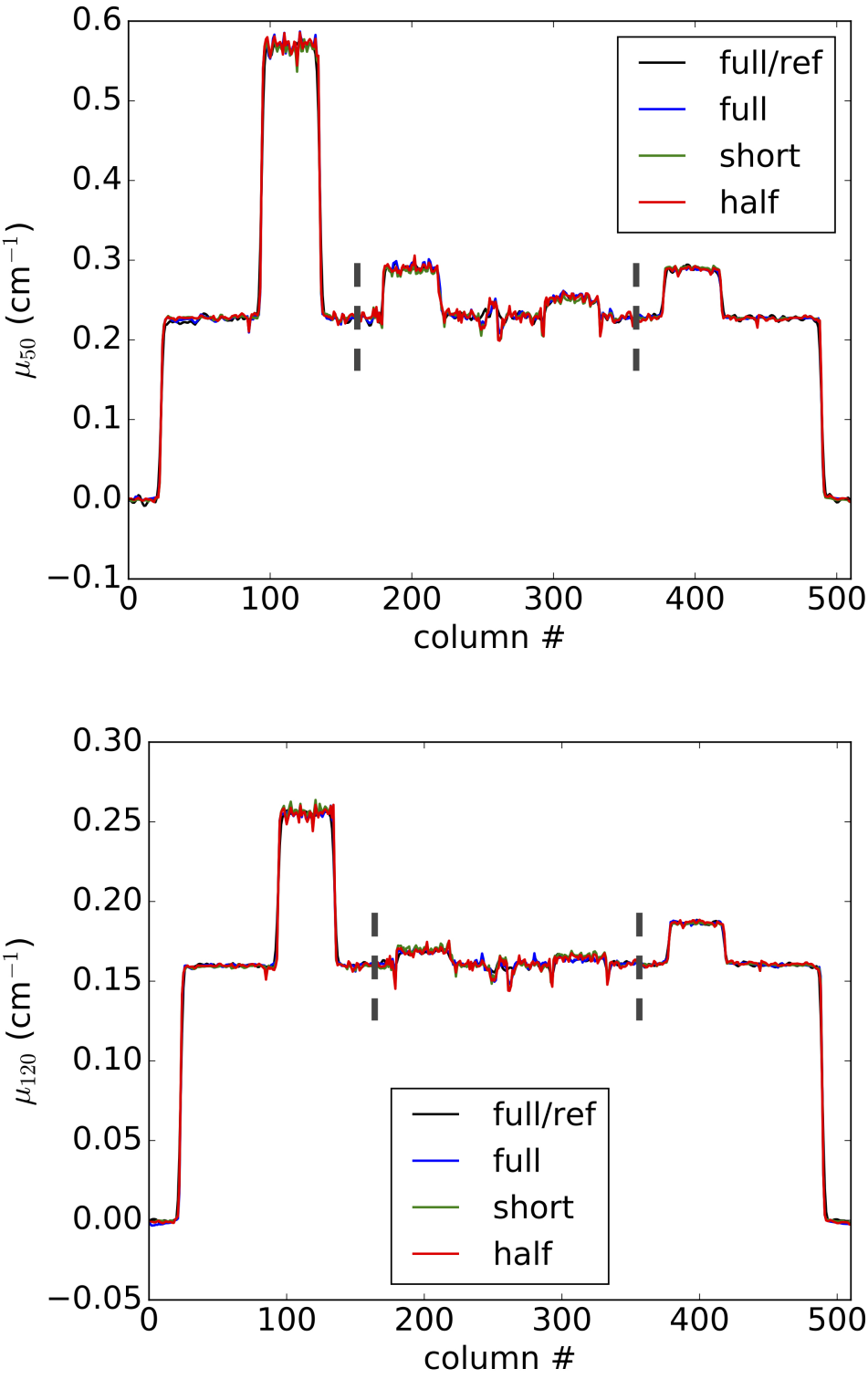

Figure 7.25: Profile plots of 50- (top) and 120-KeV (bottom) monochromatic images from all configurations across the yellow, dashed line in Fig. 7.20.

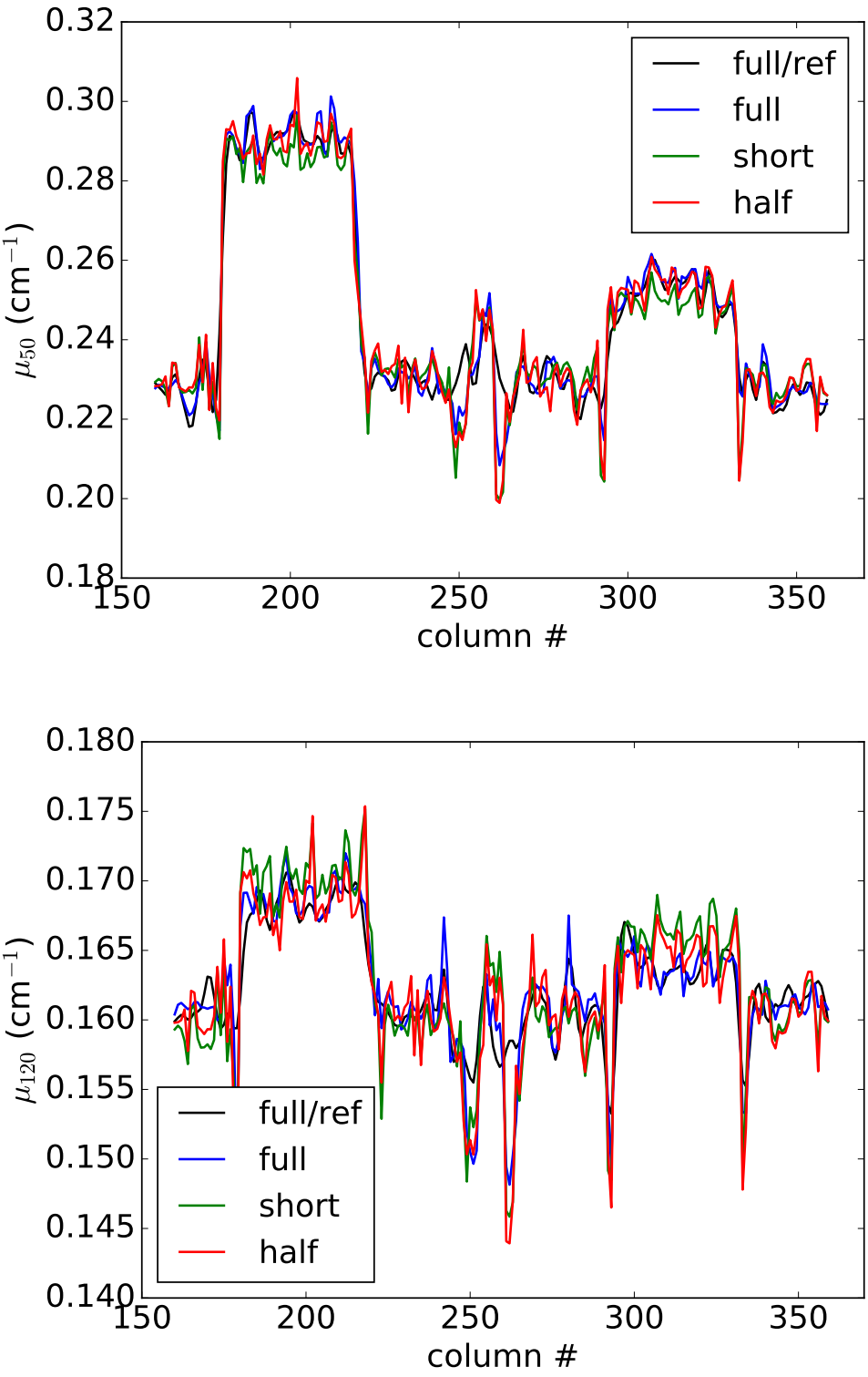

Figure 7.26: Zoomed-in section of the profile plots of 50- (top) and 120-KeV (bottom) monochromatic images from all configurations between the two vertical lines in Fig. 7.25.

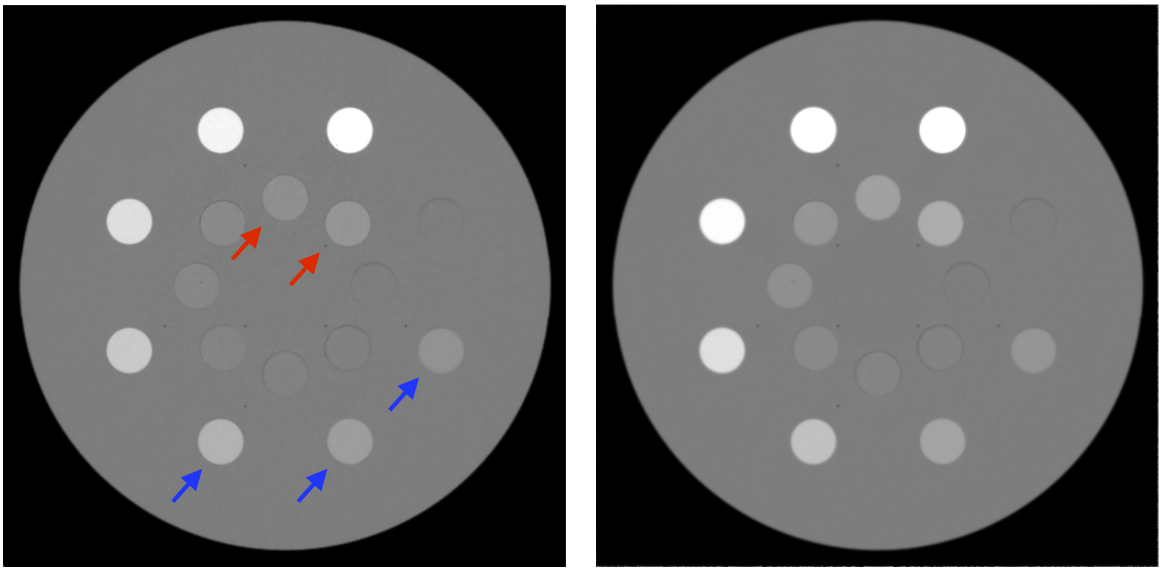

(a) 120 KeV monochromatic image, blue arrows (↑) indicate calcium inserts, and red arrows indicate (↑) iodine inserts.

(b) 80 KeV monochromatic image

Figure 7.27: Monochromatic images of the DE-472 phantom at 120 (a) and 80 (b) KeV. Calcium and iodine inserts of various concentration levels have an overlap in HU values in a single monochromatic image, while makes the thresholding-based separation difficult. However, by combining the HU values from two monochromatic images at low and high KeV levels, the calcium and iodine can be better separated.

level with some of the iodine inserts (pointed to by red arrows). Instead, calcium and iodine can be better differentiated by their distinct spectral response, i.e., their mass attenuation coefficient as a function of energy. With multispectral CT, we can compose monochromatic images at two different energy levels and use the HU value pair from the two monochromatic images at low and high energies to differentiate from each other. A scatter plot of the HU value pairs for each calcium and iodine inserts in the DE-472 phantom is shown in Fig. 7.28. For each insert, the mean pixel value within the insert is calculated based on 80 and 140-KeV monochromatic images, separately. Each data point on the scatter plot indicates one calcium or iodine insert of its unique concentration level. In Fig. 7.28, the square marker (■) corresponds to data points from iodine inserts and the triangle one (▲) from calcium inserts, and color of the marker indicates data points from the reference images (full-scan data with

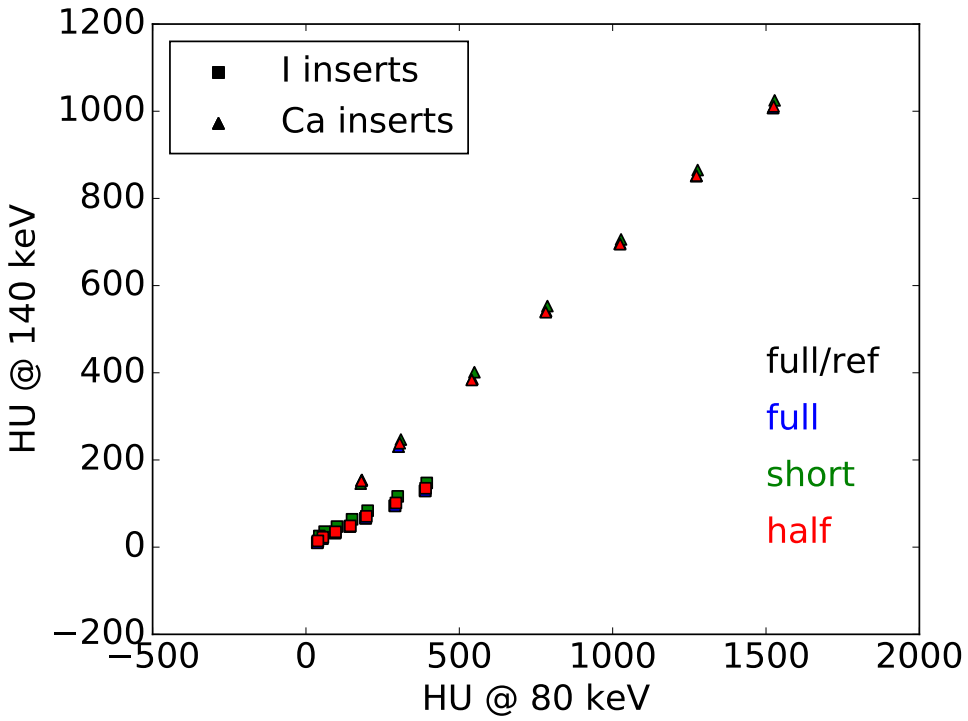

Figure 7.28: Scatter plot of HU value pairs of each calcium and iodine inserts in the DE-472 phantom monochromatic images composed at 80 and 140 KeV. The data points from different scan configurations, full, short-plus-short, and half-plus-half, are plotted on top of each other and overlapping the ons from the reference images. Iodine and calcium inserts are clearly separated on two straight lines in the scatter plot. Such separation is observed consistently across images from all scan configurations and reference images.

standard method) or ASD-NC-POCS images from full-scan, short-plus-short-scan, or half-plus-half-scan data. It can be observed that data points from iodine and calcium inserts are aligned along two straight lines in the scatter plot that are clearly separated, indicating a good performance of the material differentiation task between calcium and iodine. Further, the data points from full-scan, short-plus-short-scan, and half-plus-half-scan largely overlap with the ones from the reference images. Although some biases of the HU value can be observed (green markers from short-plus-short-scan data), such biases should barely impact the differentiation task, as the data points are still aligned along two straight lines that are clearly separated. As a result, the separation between iodine calcium is consistent across images from all scan configurations and reference images.

Head phantom

Next, using the head phantom, we compare the different configurations in terms of contrast level and profiles. We draw 6 ROIs on the head phantom, as shown in Fig. 7.23a, including five contrast disks (No. 1-5) and one background region (No. 6). The percentage contrast level for each of the five contrast disks are calculated as

$$\Delta_{rm} = \frac{\eta_{rm} - \eta_{6m}}{\eta_{6m}}, \tag{7.14}$$

where $r \in \{1, \cdots, 5\}$ and

$$\eta_{rm} = \frac{1}{I_r} \sum_i f_{im} \tag{7.15}$$

is the mean pixel value of monochromatic image at energy m for each ROI. The percentage contrast levels are calculated for monochromatic images reconstructed from data collected with the three configurations, as well as the reference images. We show in Fig. 7.29 the percentage contrast levels of 50- and 120-KeV monochromatic images, which again shows little variation both among the three different configurations and comparing to the reference images. Such observation is further corroborated by the profile plots in Fig. 7.30, along the yellow, dashed line as indicated in Fig. 7.23, and the zoomed-in sections between the two vertical lines in Fig. 7.31 focusing on the two low contrast disks.

7.6 Discussion

In this chapter, we have applied the developed optimization-based reconstruction and the ASD-NC-POCS algorithm on real data collected from a conventional diagnostic CT scanner. Further, two single-KVp-switch scan configurations, that are only enabled by the ASD-NC-POCS algorithm, were proposed and investigated. Two physical phantoms, one standard dual-energy phantom with contrast inserts and one anthropomorphic head phantom with

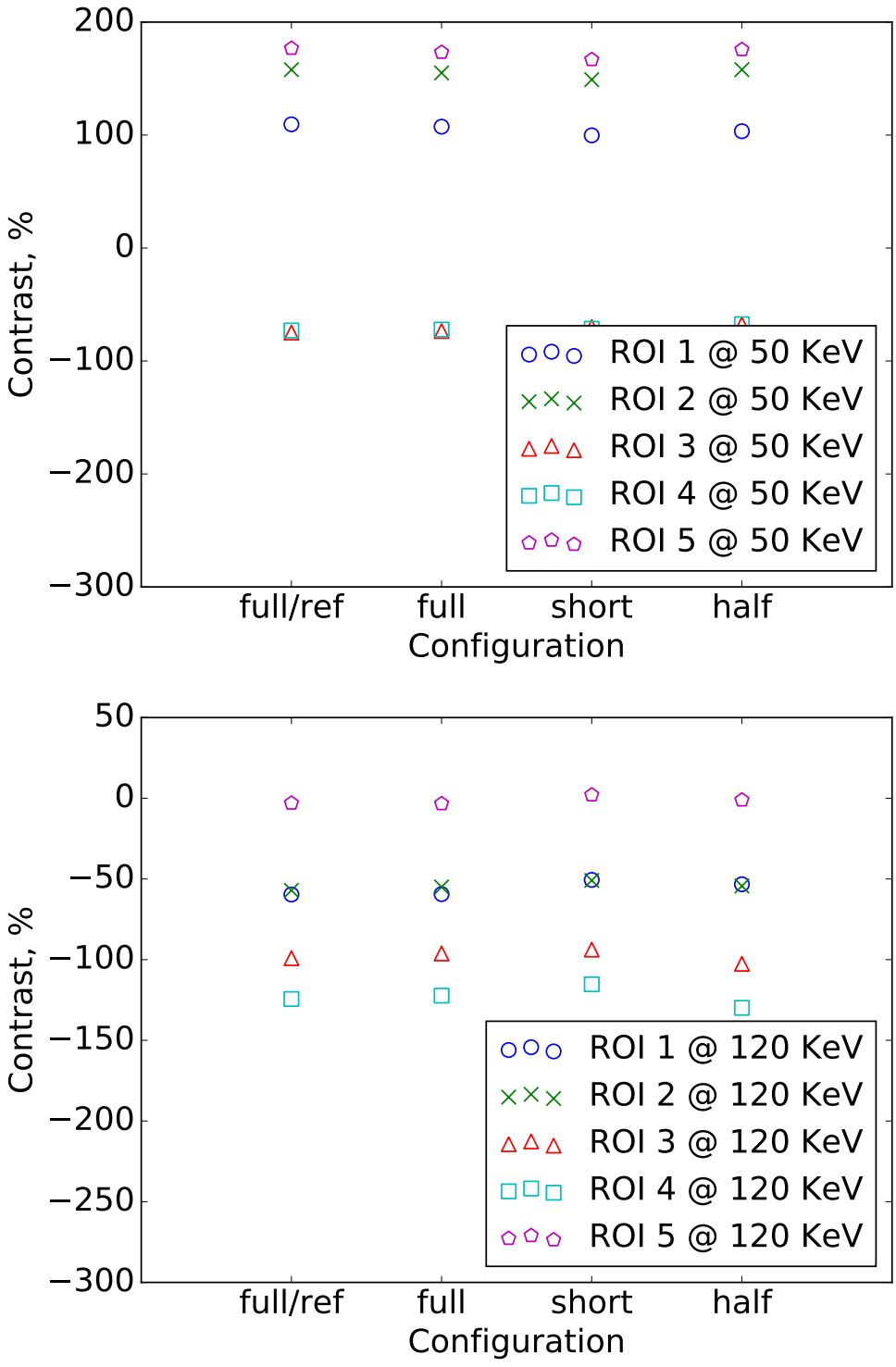

Figure 7.29: Percentage contrast levels from monochromatic images at 50 (top) and (120) KeV reconstructed from the full-, short-plus-short, and half-plus-half scan data, as well as the reference images.

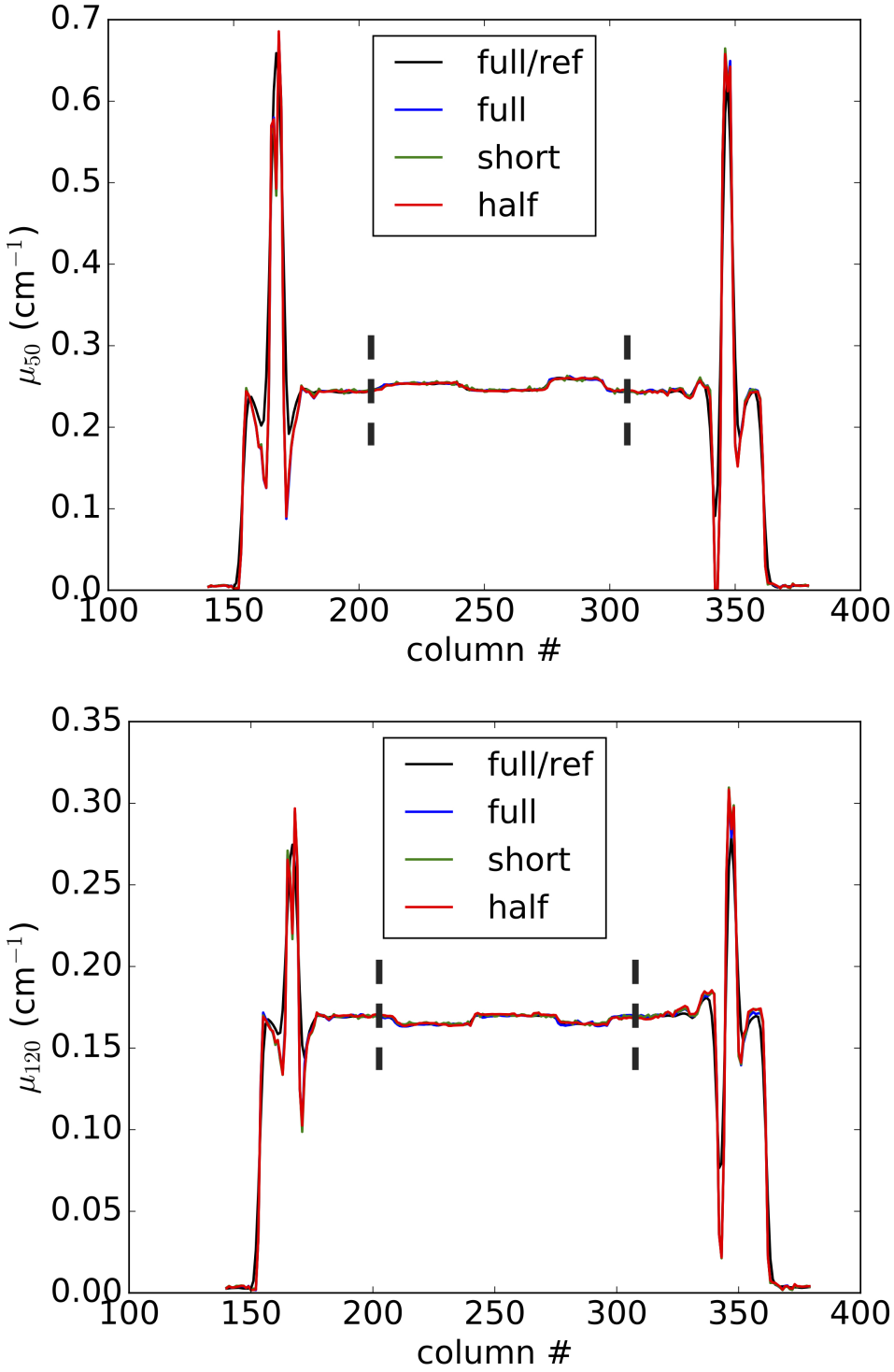

Figure 7.30: Profile plots of 50- (top) and 120-KeV (bottom) monochromatic images from all configurations across the yellow, dashed line in Fig. 7.23.

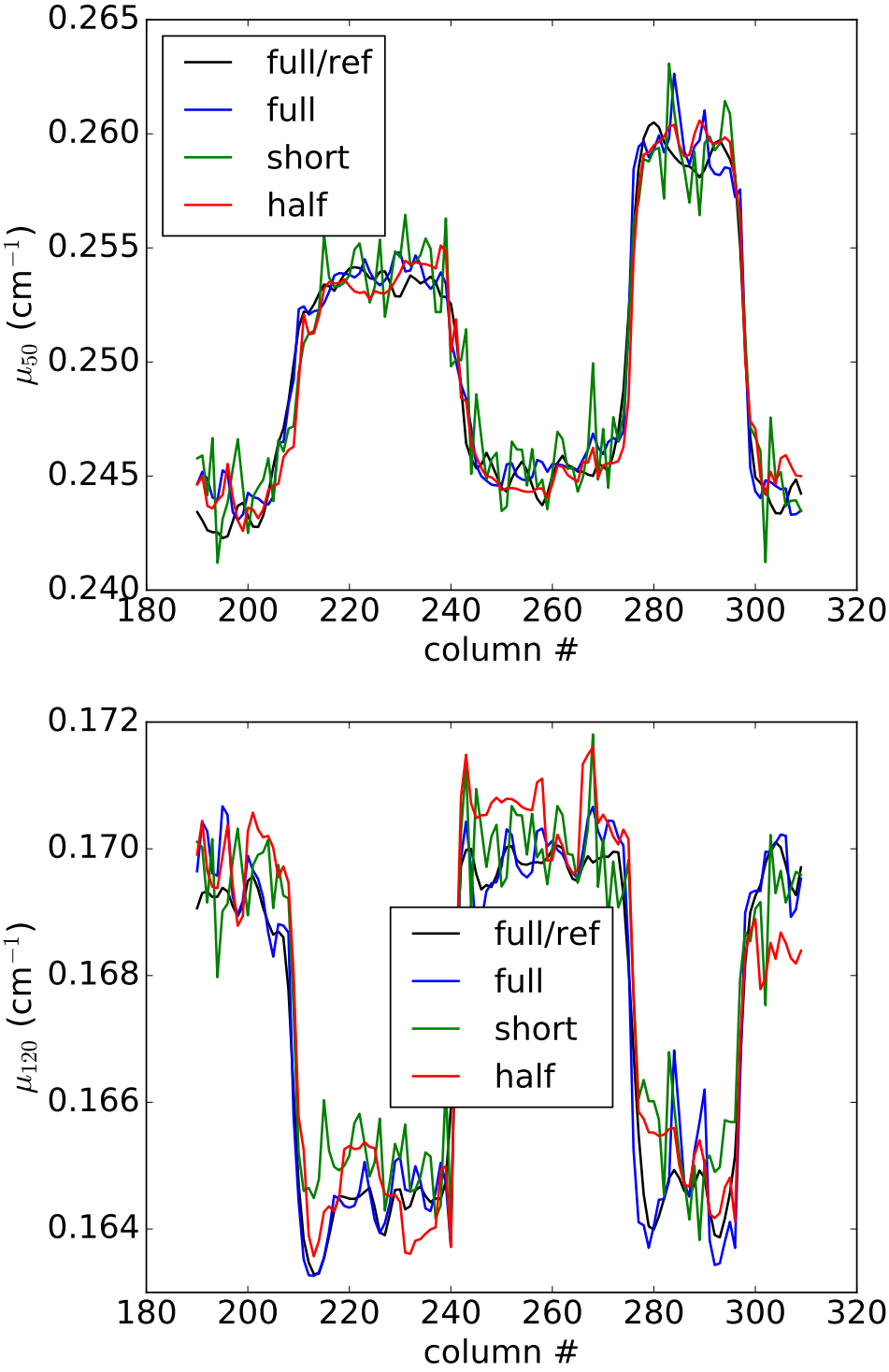

Figure 7.31: Zoomed-in sections of the profile plots of 50- (top) and 120-KeV (bottom) monochromatic images from all configurations between the two vertical lines Fig. 7.30.

contrast disks, were scanned using an Aquilion 16 diagnostic CT at 80 and 135 KVp. The full-scan data, two full rotations with one KVp for each rotation, were directly acquired from the scanner, and the partial-scan data were extracted from the full-scan data retrospectively. High mA settings were used, in addition to averaging 20 repeated scans, to get low-noise data, so that artifacts from sampling condition of the partial-scan configurations, such as the streaks of certain oblique angle seen in Fig. 7.23, would not be buried in noise. The image reconstruction was adapted for the dual-energy data with a two-basis decomposition model. A non-negativity constraint was applied on the monochromatic image, instead of the basis images.

The results suggest that, for the full-scan configuration, the ASD-NC-POCS algorithm can yield monochromatic images that are visually comparable to, and having sharper edges than, those from the existing method, which is the data-domain decomposition and FBP-like algorithm, making the proposed optimization-based reconstruction method match the performance bar in the standard, full-scan configuration. The monochromatic images from the half-plus-half scan showed some conspicuous streaks, that are possibly linked to the sampling condition of the scan configuration, while the short-plus-short images are visually very close the full-scan ones. Further, quantitative results from the enabled partial-scan configurations are comparable to the full-scan ones, in terms of bias of the inserts of the DE-472 phantom or contrast levels of the disks of the head phantom. Profile plots of monochromatic images show the same conclusion that good quantitative agreement were achieved among all three scan configurations. Using the DE-472 phantom, a material differentiation task between calcium and iodine is studied using monochromatic images at 80 and 140 KeV. The calcium and iodine inserts can be separated on two straight lines in the scatter plot, and such separation are consistent across the images from full- and partial-scan configurations as well as the reference images from the standard method. These results suggest clinical potentials of adopting the single-KVp-switch scan configurations, namely the short-plus-short

and half-plus-half configurations, for acquiring fast, low-dose, and low-cost dual-energy CT data.

Future investigations can be expanded in the following directions. First, we want to try physically acquiring data in the single-KVp-switch mode and modeling the beam modulation of the single switching phase in the reconstruction. The modeling part should not be very challenging, as the optimization-based approach can accommodate the physics of beam modulation. We can even start with just throwing out the views during the switching phase, especially in the short-plus-short scan configuration where there is an overlap of low- and high-KVp scans. To actually acquire data in the single-KVp-switch mode in a diagnostic CT, on the other side, requires collaboration with vendor engineers, but can be easily achieved with a bench-top system. Second, we want to reconstruct into 3D volumetric image from the cone-beam data. The investigations done so far are only given in the 2D cases for the central slices. We expect similar results with 3D reconstructions. After the cone-beam data, we also want to try scanning in helical mode, instead of circular/axial mode, to acquire the dual-energy data. Helical scanning provide a longer axial coverage and are often used in the clinical diagnostics. Although no ray-consistency condition is required for the proposed one-step approach, the decomposition of basis materials does rely on "scanning" the same object with both low and high KVp spectra. In helical mode, especially the full-scan configuration, such condition might be challenged. The partial-scan configurations have a better chance of recovery the basis image volumes, as bigger overlaps of low and high KVp data than the full-scan are obtained. In addition, the split- or block-illumination scan configuration, as shown in Figs. 6.17 and 6.24, might be of use in the helical, dual-energy scanning. Lastly, to validate the clinical utility of the proposed method, specific tasks shall be designed and optimized, e.g., relative to the optimization program parameter ϵ. In the current investigation, we demonstrate the selection of ϵ with visual assessment. This was done largely to remind that this parameter space is very important and shall not be neglected. A clinically relevant

task, such as classification or detection, together with a surrogate metric, can be designed to further validate the utility of the proposed method and the ASD-NC-POCS algorithm by carefully selecting ϵ that maximizes the surrogate metric.

CHAPTER 8

CONCLUSIONS

In this dissertation work, we have developed an optimization-based image reconstruction method for X-ray CT with multispectral data, with an emphasis on expanding the multispectral CT capability to existing conventional CT scanners and on enabling novel scan configurations of potential practical significance. Following a verification study, we characterized the proposed method by applying to simulation studies with both standard, full-scan configuration and non-standard, flexible scan configurations that are easy to implement on the conventional CT scanners with no or minimum hardware addition. Finally, we demonstrated the potential of the proposed method and algorithm by applying to real data collected from a diagnostic CT and enabling single-KVp-switch scan configurations for acquiring fast, low-dose, and low-cost dual-energy CT data.

In Chapters 2 and 3, we have established a DD data model in equation, based on which the optimization-based reconstruction was developed. The DD model, in which a basis decomposition model was incorporated, reduces the dimensionality of the unknown in the inverse problem and was separated into linear and non-linear terms, facilitating the development of the reconstruction algorithm. We have studied a non-convex optimization program, derived its KKT conditions, and proposed an heuristic algorithm numerically solving the program for image reconstruction in multispectral CT.

In Chapter 4, we have carried out a verification study to verify the numerical convergence of the ASD-NC-POCS algorithm and its computer implementation. The verification was essentially satisfied by an exact recovery of the truth basis images from which the consistent data were generated. The verification study by itself does not imply any utility of the proposed algorithm. However, it is an unavoidable step in the development of the reconstruction algorithms, as it makes sure that designed solutions by the optimization program could be achieved by the specific algorithm.

In Chapters 5 and 6, we have characterized the optimization-based reconstruction by using inconsistent simulation data from a full-scan configuration and investigated four non-standard configurations with different designs of varying angular or illumination coverages. Decomposition error and statistical noise were the two sources of inconsistencies in this characterization studies. The full-scan configuration was employed in order to serve as the benchmark for new non-standard scan configurations investigated, which were considered because they can readily be implemented on a conventional CT scanners with regular X-ray tubes and energy-integrating detectors, without invoking significant hardware additions or modifications to the scanner. The study results suggest that these configurations considered here can be enabled by the ASD-NC-POCS algorithm to yield monochromatic images comparable to those of the full-scan configuration.

Finally, in Chapter 7, we have applied the developed optimization-based reconstruction and the ASD-NC-POCS algorithm on real data collected from a conventional diagnostic CT scanner, and investigated two single-KVp-switch scan configurations, that are enabled by the ASD-NC-POCS algorithm. The proposed single-KVp-switch configurations for diagnostic CT can potentially acquire fast, low-dose, and low-cost dual-energy CT data. The results from two physical phantom data collected on a diagnostic CT scanner with very-low noise levels suggest that the reduction of data quantity in the single-KVp-switch configuration, from full rotation to short and half scan for each KVp scan, does not necessarily lead to compromises in image quality, especially in terms of quantitative metrics such as bias and contrast levels, and in a potential clinical task of separating calcium with iodine. It was also shown that the performance of the proposed ASD-NC-POCS algorithm can match that of an existing method, which is the data domain decomposition and FBP-like algorithm, in the case of full-scan configuration where ray-consistency condition is met.

In summary, optimization-based image reconstruction method can offer greatly flexibility in designing and enabling non-standard scan configurations for multispectral CT. While we

have demonstrated scan configuration enabling in dual-energy CT in the work, the algorithm can accommodate multiple ($S > 2$) spectral scans and/or a variety of configurations with different designs of source trajectory and/or illumination coverage tailored to specific applications. In addition, the data model and reconstruction method developed are also for cone-beam data and volumetric image reconstructions. While the study can hopefully provide insights into the design and implementation of scan configurations of practical interest in multispectral CT, it is the first step in expanding the multispectral scanning capability to existing conventional CT scanners and shall not be intended to show the truly application-specific utility of the proposed algorithm and scan configurations. Instead, future works are warranted to investigate, assess, and establish the utility of the algorithm and scanning configurations in carefully designed studies of application significance with task-specific metrics.

REFERENCES

[1] G. N. Hounsfield, "Computerized transverse axial scanning (tomography): Part 1. Description of system," *The British Journal of Radiology*, vol. 46, no. 552, pp. 1016–1022, Dec. 1973.

[2] G. N. Hounsfield, "The E.M.I. Scanner," *Proceedings of the Royal Society of London B: Biological Sciences*, vol. 195, no. 1119, pp. 281–289, Jan. 1977.

[3] A. M. Cormack, "Recollections of my work with computer assisted tomography," *Molecular and Cellular Biochemistry*, vol. 32, no. 2, pp. 57–61, Sep. 1980.

[4] J. Hsieh, *Computed Tomography: Principles, Design, Artifacts, and Recent Advances*. SPIE Press, 2003, google-Books-ID: JX_lLLXFHkC.

[5] W. A. Kalender, *Computed Tomography: Fundamentals, System Technology, Image Quality, Applications*. John Wiley & Sons, Jul. 2011, google-Books-ID: gfLWmR-joyPMC.

[6] M. Kaneko, K. Eguchi, H. Ohmatsu, R. Kakinuma, T. Naruke, K. Suemasu, and N. Moriyama, "Peripheral lung cancer: screening and detection with low-dose spiral CT versus radiography." *Radiology*, vol. 201, no. 3, pp. 798–802, Dec. 1996.

[7] S. J. Swensen, J. R. Jett, T. E. Hartman, D. E. Midthun, J. A. Sloan, A.-M. Sykes, G. L. Aughenbaugh, and M. A. Clemens, "Lung Cancer Screening with CT: Mayo Clinic Experience," *Radiology*, vol. 226, no. 3, pp. 756–761, Mar. 2003.

[8] T. M. Gluecker, C. D. Johnson, W. S. Harmsen, K. P. Offord, A. M. Harris, L. A. Wilson, and D. A. Ahlquist, "Colorectal Cancer Screening with CT Colonography, Colonoscopy, and Double-Contrast Barium Enema Examination: Prospective Assessment of Patient Perceptions and Preferences," *Radiology*, vol. 227, no. 2, pp. 378–384, May 2003.

[9] T. N. L. S. T. R. Team, "Reduced Lung-Cancer Mortality with Low-Dose Computed Tomographic Screening," *New England Journal of Medicine*, vol. 365, no. 5, pp. 395–409, Aug. 2011.

[10] M. J. Budoff, S. Achenbach, R. S. Blumenthal, J. J. Carr, J. G. Goldin, P. Greenland, A. D. Guerci, J. A. C. Lima, D. J. Rader, G. D. Rubin, L. J. Shaw, and S. E. Wiegers, "Assessment of Coronary Artery Disease by Cardiac Computed Tomography," *Circulation*, vol. 114, no. 16, pp. 1761–1791, Oct. 2006.

[11] M. J. Haydel, C. A. Preston, T. J. Mills, S. Luber, E. Blaudeau, and P. M. DeBlieux, "Indications for Computed Tomography in Patients with Minor Head Injury," *New England Journal of Medicine*, vol. 343, no. 2, pp. 100–105, Jul. 2000.

[12] J. Wilson, M. Korobkin, H. Genant, and E. Bovill, "Computed tomography of musculoskeletal disorders," *American Journal of Roentgenology*, vol. 131, no. 1, pp. 55–61, Jul. 1978.

[13] A. S. Agatston, W. R. Janowitz, F. J. Hildner, N. R. Zusmer, M. Viamonte, and R. Detrano, "Quantification of coronary artery calcium using ultrafast computed tomography," *Journal of the American College of Cardiology*, vol. 15, no. 4, pp. 827–832, Mar. 1990.

[14] M. G. P. Cavalcanti, J. W. Haller, and M. W. Vannier, "Three-dimensional computed tomography landmark measurement in craniofacial surgical planning: Experimental validation in vitro," *Journal of Oral and Maxillofacial Surgery*, vol. 57, no. 6, pp. 690–694, Jun. 1999.

[15] D. A. Jaffray, J. H. Siewerdsen, J. W. Wong, and A. A. Martinez, "Flat-panel cone-beam computed tomography for image-guided radiation therapy," *International Journal of Radiation Oncology*Biology*Physics*, vol. 53, no. 5, pp. 1337–1349, Aug. 2002.

[16] J. H. Siewerdsen, D. J. Moseley, S. Burch, S. K. Bisland, A. Bogaards, B. C. Wilson, and D. A. Jaffray, "Volume CT with a flat-panel detector on a mobile, isocentric C-arm: Pre-clinical investigation in guidance of minimally invasive surgery," *Medical Physics*, vol. 32, no. 1, pp. 241–254, Jan. 2005.

[17] K. A. Miles, "Perfusion imaging with computed tomography: brain and beyond," *European Radiology Supplements*, vol. 16, no. 7, pp. M37–M43, Nov. 2006.

[18] B. Jacobs, T. Beems, T. M. van der Vliet, R. R. Diaz-Arrastia, G. F. Borm, and P. E. Vos, "Computed Tomography and Outcome in Moderate and Severe Traumatic Brain Injury: Hematoma Volume and Midline Shift Revisited," *Journal of Neurotrauma*, vol. 28, no. 2, pp. 203–215, Feb. 2011.

[19] G. L. Raff, M. J. Gallagher, W. W. ONeill, and J. A. Goldstein, "Diagnostic Accuracy of Noninvasive Coronary Angiography Using 64-Slice Spiral Computed Tomography," *Journal of the American College of Cardiology*, vol. 46, no. 3, pp. 552–557, Aug. 2005.

[20] N. R. Mollet, F. Cademartiri, C. A. G. v. Mieghem, G. Runza, E. P. McFadden, T. Baks, P. W. Serruys, G. P. Krestin, and P. J. d. Feyter, "High-Resolution Spiral Computed Tomography Coronary Angiography in Patients Referred for Diagnostic Conventional Coronary Angiography," *Circulation*, vol. 112, no. 15, pp. 2318–2323, Oct. 2005.

[21] S. Achenbach, D. Ropers, A. Kuettner, T. Flohr, B. Ohnesorge, H. Bruder, H. Theessen, M. Karakaya, W. G. Daniel, W. Bautz, W. A. Kalender, and K. Anders, "Contrast-enhanced coronary artery visualization by dual-source computed tomography-Initial experience," *European Journal of Radiology*, vol. 57, no. 3, pp. 331–335, Mar. 2006.

[22] T. Uematsu, M. Sano, K. Homma, M. Shiina, and S. Kobayashi, "Three-Dimensional Helical CT of the Breast: Accuracy for Measuring Extent of Breast Cancer Candidates for Breast Conserving Surgery," *Breast Cancer Research and Treatment*, vol. 65, no. 3, pp. 249–257, Feb. 2001.

[23] J. M. Boone, T. R. Nelson, K. K. Lindfors, and J. A. Seibert, "Dedicated Breast CT: Radiation Dose and Image Quality Evaluation," *Radiology*, vol. 221, no. 3, pp. 657–667, Dec. 2001.

[24] S. Akashi-Tanaka, T. Fukutomi, N. Sato, and K. Miyakawa, "The role of computed tomography in the selection of breast cancer treatment," *Breast Cancer*, vol. 10, no. 3, p. 198, Jul. 2003.

[25] S. Sone, S. Takashima, F. Li, Z. Yang, T. Honda, Y. Maruyama, M. Hasegawa, T. Yamanda, K. Kubo, K. Hanamura, and K. Asakura, "Mass screening for lung cancer with mobile spiral computed tomography scanner," *The Lancet*, vol. 351, no. 9111, pp. 1242–1245, Apr. 1998.

[26] M. N. Gurcan, B. Sahiner, N. Petrick, H.-P. Chan, E. A. Kazerooni, P. N. Cascade, and L. Hadjiiski, "Lung nodule detection on thoracic computed tomography images: Preliminary evaluation of a computer-aided diagnosis system," *Medical Physics*, vol. 29, no. 11, pp. 2552–2558, Nov. 2002.

[27] T. Sobue, N. Moriyama, M. Kaneko, M. Kusumoto, T. Kobayashi, R. Tsuchiya, R. Kakinuma, H. Ohmatsu, K. Nagai, H. Nishiyama, E. Matsui, and K. Eguchi, "Screening for Lung Cancer With Low-Dose Helical Computed Tomography: Anti-Lung Cancer Association Project," *Journal of Clinical Oncology*, vol. 20, no. 4, pp. 911–920, Feb. 2002.

[28] P. B. Bach, J. R. Jett, U. Pastorino, M. S. Tockman, S. J. Swensen, and C. B. Begg, "Computed Tomography Screening and Lung Cancer Outcomes," *JAMA*, vol. 297, no. 9, pp. 953–961, Mar. 2007.

[29] R. Materne, B. E. V. Beers, A. M. Smith, I. Leconte, J. Jamart, J.-P. Dehoux, A. Keyeux, and Y. Horsmans, "Non-invasive quantification of liver perfusion with dynamic computed tomography and a dual-input one-compartmental model," *Clinical Science*, vol. 99, no. 6, pp. 517–525, Dec. 2000.

[30] C. Dromain, T. de Baere, J. Lumbroso, H. Caillet, A. Laplanche, V. Boige, M. Ducreux, P. Duvillard, D. Elias, M. Schlumberger, R. Sigal, and E. Baudin, "Detection of Liver Metastases From Endocrine Tumors: A Prospective Comparison of Somatostatin Receptor Scintigraphy, Computed Tomography, and Magnetic Resonance Imaging," *Journal of Clinical Oncology*, vol. 23, no. 1, pp. 70–78, Jan. 2005.

[31] N. F. Schwenzer, F. Springer, C. Schraml, N. Stefan, J. Machann, and F. Schick, "Non-invasive assessment and quantification of liver steatosis by ultrasound, computed

tomography and magnetic resonance," *Journal of Hepatology*, vol. 51, no. 3, pp. 433–445, Sep. 2009.

[32] A. P. Royster, H. M. Fenlon, P. D. Clarke, D. P. Nunes, and J. T. Ferrucci, "CT colonoscopy of colorectal neoplasms: two-dimensional and three-dimensional virtual-reality techniques with colonoscopic correlation." *American Journal of Roentgenology*, vol. 169, no. 5, pp. 1237–1242, Nov. 1997.

[33] D. P. Beall, B. J. Fortman, B. C. Lawler, and F. Regan, "Imaging Bowel Obstruction: A Comparison Between Fast Magnetic Resonance Imaging and Helical Computed Tomography," *Clinical Radiology*, vol. 57, no. 8, pp. 719–724, Aug. 2002.

[34] J. Sosna, M. M. Morrin, J. B. Kruskal, P. T. Lavin, M. P. Rosen, and V. Raptopoulos, "CT Colonography of Colorectal Polyps: A Metaanalysis," *American Journal of Roentgenology*, vol. 181, no. 6, pp. 1593–1598, Dec. 2003.

[35] G. D. Rubin, M. D. Dake, S. A. Napel, C. H. McDonnell, and R. B. Jeffrey, "Three-dimensional spiral CT angiography of the abdomen: initial clinical experience." *Radiology*, vol. 186, no. 1, pp. 147–152, Jan. 1993.

[36] U. J. Schoepf and P. Costello, "CT Angiography for Diagnosis of Pulmonary Embolism: State of the Art," *Radiology*, vol. 230, no. 2, pp. 329–337, Feb. 2004.

[37] L. Husmann, I. Valenta, O. Gaemperli, O. Adda, V. Treyer, C. A. Wyss, P. Veit-Haibach, F. Tatsugami, V. Schulthess, G. K, and P. A. Kaufmann, "Feasibility of low-dose coronary CT angiography: first experience with prospective ECG-gating," *European Heart Journal*, vol. 29, no. 2, pp. 191–197, Jan. 2008.

[38] N. Theumann, N. Favarger, P. Schnyder, and R. Meuli, "Wrist ligament injuries: value of post-arthrography computed tomography," *Skeletal Radiology*, vol. 30, no. 2, pp. 88–93, Mar. 2001.

[39] J. Harvey and A. West, "The role of computed tomography in musculoskeletal trauma," *Trauma*, vol. 14, no. 4, pp. 275–286, Oct. 2012.

[40] J. A. Carrino, A. Al Muhit, W. Zbijewski, G. K. Thawait, J. W. Stayman, N. Packard, R. Senn, D. Yang, D. H. Foos, J. Yorkston, and J. H. Siewerdsen, "Dedicated Cone-Beam CT System for Extremity Imaging," *Radiology*, vol. 270, no. 3, pp. 816–824, Nov. 2013.

[41] X. Pan, E. Y. Sidky, and M. Vannier, "Why do commercial CT scanners still employ traditional, filtered back-projection for image reconstruction?" *Inverse Problems*, vol. 25, no. 12, p. 123009, 2009.

[42] A. Katsevich, "Theoretically Exact Filtered Backprojection-Type Inversion Algorithm for Spiral CT," *SIAM Journal on Applied Mathematics*, vol. 62, no. 6, pp. 2012–2026, Jan. 2002.

[43] Y. Zou and X. Pan, "Exact image reconstruction on PI-lines from minimum data in helical cone-beam CT," *Physics in Medicine and Biology*, vol. 49, no. 6, p. 941, 2004.

[44] L. A. Feldkamp, L. C. Davis, and J. W. Kress, "Practical cone-beam algorithm," *JOSA A*, vol. 1, no. 6, pp. 612–619, Jun. 1984.

[45] A. C. Kak and M. Slaney, *Principles of Computerized Tomographic Imaging*. SIAM, 1988.

[46] H. Tuy, "An Inversion Formula for Cone-Beam Reconstruction," *SIAM Journal on Applied Mathematics*, vol. 43, no. 3, pp. 546–552, Jun. 1983.

[47] T. Khler, R. Proksa, C. Bontus, M. Grass, and J. Timmer, "Artifact analysis of approximate helical cone-beam CT reconstruction algorithms," *Medical Physics*, vol. 29, no. 1, pp. 51–64, Jan. 2002.

[48] T. Flohr, K. Stierstorfer, H. Bruder, J. Simon, A. Polacin, and S. Schaller, "Image reconstruction and image quality evaluation for a 16-slice CT scanner," *Medical Physics*, vol. 30, no. 5, pp. 832–845, May 2003.

[49] K. Taguchi, B.-S. S. Chiang, and M. D. Silver, "A new weighting scheme for cone-beam helical CT to reduce the image noise," *Physics in Medicine and Biology*, vol. 49, no. 11, p. 2351, 2004.

[50] X. Tang, J. Hsieh, R. A. Nilsen, S. Dutta, D. Samsonov, and A. Hagiwara, "A three-dimensional-weighted cone beam filtered backprojection (CB-FBP) algorithm for image reconstruction in volumetric CT-helical scanning," *Physics in Medicine and Biology*, vol. 51, no. 4, p. 855, 2006.

[51] R. Gordon, R. Bender, and G. T. Herman, "Algebraic Reconstruction Techniques (ART) for three-dimensional electron microscopy and X-ray photography," *Journal of Theoretical Biology*, vol. 29, no. 3, pp. 471–481, Dec. 1970.

[52] A. H. Andersen and A. C. Kak, "Simultaneous Algebraic Reconstruction Technique (SART): A Superior Implementation of the Art Algorithm," *Ultrasonic Imaging*, vol. 6, no. 1, pp. 81–94, Jan. 1984.

[53] A. P. Dempster, N. M. Laird, and D. B. Rubin, "Maximum Likelihood from Incomplete Data via the EM Algorithm," *Journal of the Royal Statistical Society. Series B (Methodological)*, vol. 39, no. 1, pp. 1–38, 1977.

[54] L. A. Shepp and Y. Vardi, "Maximum Likelihood Reconstruction for Emission Tomography," *IEEE Transactions on Medical Imaging*, vol. 1, no. 2, pp. 113–122, Oct. 1982.

[55] K. Lange and R. E. Carson, "EM reconstruction algorithms for emission and transmission tomography." *Journal of computer assisted tomography*, vol. 8, no. 2, pp. 306–316, Apr. 1984.

[56] J. A. Fessler and A. O. Hero, "Space-alternating generalized expectation-maximization algorithm," *IEEE Transactions on Signal Processing*, vol. 42, no. 10, pp. 2664–2677, Oct. 1994.

[57] E. Y. Sidky and X. Pan, "Image reconstruction in circular cone-beam computed tomography by constrained, total-variation minimization," *Physics in Medicine and Biology*, vol. 53, no. 17, p. 4777, 2008.

[58] E. Y. Sidky, J. H. Jorgensen, and X. Pan, "Convex optimization problem prototyping for image reconstruction in computed tomography with the Chambolle-Pock algorithm," *Physics in Medicine and Biology*, vol. 57, no. 10, p. 3065, 2012.

[59] S. Ramani and J. A. Fessler, "A splitting-based iterative algorithm for accelerated statistical X-ray CT reconstruction," *IEEE Transactions on Medical Imaging*, vol. 31, no. 3, pp. 677–688, Mar. 2012.

[60] O. Watzke and W. A. Kalender, "A pragmatic approach to metal artifact reduction in CT: merging of metal artifact reduced images," *European Radiology*, vol. 14, no. 5, pp. 849–856, May 2004.

[61] E. Meyer, R. Raupach, M. Lell, B. Schmidt, and M. Kachelrie, "Normalized metal artifact reduction (NMAR) in computed tomography," *Medical Physics*, vol. 37, no. 10, pp. 5482–5493, Oct. 2010.

[62] Z. Zhang, X. Han, E. Pearson, C. Pelizzari, E. Y. Sidky, and X. Pan, "Artifact reduction in short-scan CBCT by use of optimization-based reconstruction," *Physics in Medicine and Biology*, vol. 61, no. 9, p. 3387, 2016.

[63] D. Xia, D. A. Langan, S. B. Solomon, Z. Zhang, B. Chen, H. Lai, E. Y. Sidky, and X. Pan, "Optimization-based image reconstruction with artifact reduction in C-arm CBCT," *Physics in Medicine and Biology*, vol. 61, no. 20, p. 7300, 2016.

[64] B. D. Man, J. Nuyts, P. Dupont, G. Marchal, and P. Suetens, "An iterative maximum-likelihood polychromatic algorithm for CT," *IEEE Transactions on Medical Imaging*, vol. 20, no. 10, pp. 999–1008, Oct. 2001.

[65] I. Elbakri and J. Fessler, "Statistical image reconstruction for polyenergetic X-ray computed tomography," *IEEE Transactions on Medical Imaging*, vol. 21, no. 2, pp. 89–99, Feb. 2002.

[66] E. A. Pearson, S. Cho, C. A. Pelizzari, and X. Pan, "Non-circular cone beam CT trajectories: A preliminary investigation on a clinical scanner," in *IEEE Nuclear Science Symposuim Medical Imaging Conference*, Oct. 2010, pp. 3172–3175.

[67] A. Davis, E. Pearson, X. Pan, and C. Pelizzari, "WE-G-BRF-07: Non-Circular Scanning Trajectories with Varian Developer Mode," *Medical Physics*, vol. 41, no. 6, pp. 523–523, Jun. 2014.

[68] J. Bian, J. H. Siewerdsen, X. Han, E. Y. Sidky, J. L. Prince, C. A. Pelizzari, and X. Pan, "Evaluation of sparse-view reconstruction from flat-panel-detector cone-beam CT," *Physics in Medicine and Biology*, vol. 55, no. 22, p. 6575, 2010.

[69] X. Han, J. Bian, D. Eaker, T. Kline, E. Sidky, E. Ritman, and X. Pan, "Algorithm-Enabled Low-Dose Micro-CT Imaging," *IEEE Transactions on Medical Imaging*, vol. 30, no. 3, pp. 606–620, Mar. 2011.

[70] X. Han, J. Bian, E. L. Ritman, E. Y. Sidky, and X. Pan, "Optimization-based reconstruction of sparse images from few-view projections," *Physics in Medicine and Biology*, vol. 57, no. 16, p. 5245, 2012.

[71] J. Bian, J. Wang, X. Han, E. Y. Sidky, L. Shao, and X. Pan, "Optimization-based image reconstruction from sparse-view data in offset-detector CBCT," *Physics in Medicine and Biology*, vol. 58, no. 2, p. 205, 2013.

[72] J. Bian, K. Yang, J. M. Boone, X. Han, E. Y. Sidky, and X. Pan, "Investigation of iterative image reconstruction in low-dose breast CT," *Physics in Medicine and Biology*, vol. 59, no. 11, p. 2659, 2014.

[73] X. Han, E. Pearson, C. Pelizzari, H. Al-Hallaq, E. Y. Sidky, J. Bian, and X. Pan, "Algorithm-enabled exploration of image-quality potential of cone-beam CT in image-guided radiation therapy," *Physics in Medicine and Biology*, vol. 60, no. 12, p. 4601, 2015.

[74] E. Y. Sidky, C.-M. Kao, and X. Pan, "Accurate image reconstruction from few-views and limited-angle data in divergent-beam CT," *Journal of X-Ray Science and Technology*, vol. 14, no. 2, pp. 119–139, Jan. 2006.

[75] X. Jin, L. Li, Z. Chen, L. Zhang, and Y. Xing, "Anisotropic total variation for limited-angle CT reconstruction," in *IEEE Nuclear Science Symposuim Medical Imaging Conference*, Oct. 2010, pp. 2232–2238.

[76] F. Xu and K. Mueller, "Real-time 3d computed tomographic reconstruction using commodity graphics hardware," *Physics in Medicine and Biology*, vol. 52, no. 12, p. 3405, 2007.

[77] T. Zinsser and B. Keck, "Systematic performance optimization of cone-beam back-projection on the Kepler architecture," in *Proceedings of the 12th Fully Three-Dimensional Image Reconstruction in Radiology and Nuclear Medicine*, 2013, pp. 225–228.

[78] R. E. Alvarez and A. Macovski, "Energy-selective reconstructions in X-ray computerised tomography," *Physics in Medicine and Biology*, vol. 21, no. 5, p. 733, 1976.

[79] R. Carmi, G. Naveh, and A. Altman, "Material separation with dual-layer CT," in *2005 IEEE Nuclear Science Symposium Conference Record*, vol. 4, Oct. 2005, pp. 1876–1878.

[80] T. G. Flohr, C. H. McCollough, H. Bruder, M. Petersilka, K. Gruber, C. S, M. Grasruck, K. Stierstorfer, B. Krauss, R. Raupach, A. N. Primak, A. Kttner, S. Achenbach, C. Becker, A. Kopp, and B. M. Ohnesorge, "First performance evaluation of a dual-source CT (DSCT) system," *European Radiology*, vol. 16, no. 2, pp. 256–268, Dec. 2005.

[81] T. R. C. Johnson, B. Krau, M. Sedlmair, M. Grasruck, H. Bruder, D. Morhard, C. Fink, S. Weckbach, M. Lenhard, B. Schmidt, T. Flohr, M. F. Reiser, and C. R. Becker, "Material differentiation by dual energy CT: Initial experience," *European Radiology*, vol. 17, no. 6, pp. 1510–1517, Jun. 2007.

[82] E. Roessl and R. Proksa, "K-edge imaging in X-ray computed tomography using multi-bin photon counting detectors," *Physics in Medicine and Biology*, vol. 52, no. 15, p. 4679, 2007.

[83] J. P. Schlomka, E. Roessl, R. Dorscheid, S. Dill, G. Martens, T. Istel, C. Bumer, C. Herrmann, R. Steadman, G Zeitler, A. Livne, and R. Proksa, "Experimental feasibility of multi-energy photon-counting K-edge imaging in pre-clinical computed tomography," *Physics in Medicine and Biology*, vol. 53, no. 15, p. 4031, 2008.

[84] D. Xu, D. A. Langan, X. Wu, J. D. Pack, T. M. Benson, J. E. Tkaczky, and A. M. Schmitz, "Dual energy CT via fast kVp switching spectrum estimation," in *Proc. SPIE , Medical Imaging: Physics of Medical Imaging*, vol. 7258, 2009, pp. 72 583T–72 583T–10.

[85] K. Taguchi and J. S. Iwanczyk, "Vision 20/20: Single photon counting x-ray detectors in medical imaging," *Medical Physics*, vol. 40, no. 10, Oct. 2013.

[86] T. Johnson, C. Fink, S. O. Schnberg, and M. F. Reiser, *Dual Energy CT in Clinical Practice*. Springer Science & Business Media, Jan. 2011, google-Books-ID: Etvcnz0mjF4C.

[87] C. H. McCollough, S. Leng, L. Yu, and J. G. Fletcher, "Dual- and multi-energy CT: principles, technical approaches, and clinical applications," *Radiology*, vol. 276, no. 3, pp. 637–653, Aug. 2015.

[88] A. Pourmorteza, R. Symons, V. Sandfort, M. Mallek, M. K. Fuld, G. Henderson, E. C. Jones, A. A. Malayeri, L. R. Folio, and D. A. Bluemke, "Abdominal imaging with contrast-enhanced photon-counting CT: First human experience," *Radiology*, p. 152601, Feb. 2016.

[89] A. Graser, T. R. C. Johnson, H. Chandarana, and M. Macari, "Dual energy CT: preliminary observations and potential clinical applications in the abdomen," *European Radiology*, vol. 19, no. 1, p. 13, Jan. 2009.

[90] S. R. Pomerantz, S. Kamalian, D. Zhang, R. Gupta, O. Rapalino, D. V. Sahani, and M. H. Lev, "Virtual Monochromatic Reconstruction of Dual-Energy Unenhanced Head

CT at 6575 keV Maximizes Image Quality Compared with Conventional Polychromatic CT," *Radiology*, vol. 266, no. 1, pp. 318–325, Jan. 2013.

[91] Y. Yamada, M. Jinzaki, Y. Tanami, T. Abe, and S. Kuribayashi, "Virtual Monochromatic Spectral Imaging for the Evaluation of Hypovascular Hepatic Metastases: The Optimal Monochromatic Level With Fast Kilovoltage Switching Dual-Energy Computed Tomography," *Investigative Radiology*, vol. 47, no. 5, pp. 292–298, May 2012.

[92] B. Schulz, K. Kuehling, W. Kromen, P. Siebenhandl, M. J. Kerl, T. J. Vogl, and R. Bauer, "Automatic Bone Removal Technique in Whole-Body Dual-Energy CT Angiography: Performance and Image Quality," *American Journal of Roentgenology*, vol. 199, no. 5, pp. W646–W650, Nov. 2012.

[93] G. Pache, B. Krauss, P. Strohm, U. Saueressig, P. Blanke, S. Bulla, O. Schfer, P. Helwig, E. Kotter, M. Langer, and T. Baumann, "Dual-Energy CT Virtual Noncalcium Technique: Detecting Posttraumatic Bone Marrow LesionsFeasibility Study," *Radiology*, vol. 256, no. 2, pp. 617–624, Aug. 2010.

[94] S. F. Thieme, C. R. Becker, M. Hacker, K. Nikolaou, M. F. Reiser, and T. R. C. Johnson, "Dual energy CT for the assessment of lung perfusioncorrelation to scintigraphy," *European Journal of Radiology*, vol. 68, no. 3, pp. 369–374, Dec. 2008.

[95] S. F. Thieme, T. R. C. Johnson, M. F. Reiser, and K. Nikolaou, "Dual-Energy Lung Perfusion Computed Tomography: A Novel Pulmonary Functional Imaging Method," *Seminars in Ultrasound, CT and MRI*, vol. 31, no. 4, pp. 301–308, Aug. 2010.

[96] S. Ameli-Renani, F. Rahman, A. Nair, L. Ramsay, J. L. Bacon, A. Weller, H. K. Sokhi, A. Devaraj, B. Madden, and I. Vlahos, "Dual-Energy CT for Imaging of Pulmonary Hypertension: Challenges and Opportunities," *RadioGraphics*, vol. 34, no. 7, pp. 1769–1790, Nov. 2014.

[97] A. N. Primak, J. G. Fletcher, T. J. Vrtiska, O. P. Dzyubak, J. C. Lieske, M. E. Jackson, J. C. Williams Jr, and C. H. McCollough, "Noninvasive differentiation of uric acid versus nonuric acid kidney stones using dual-energy CT," *Academic Radiology*, vol. 14, no. 12, pp. 1441–1447, Dec. 2007.

[98] R. A. Brooks, "A quantitative theory of the Hounsfield unit and its application to dual energy scanning," *Journal of Computer Assisted Tomography*, vol. 1, no. 4, pp. 487–493, Oct. 1977.

[99] C. Maass, M. Baer, and M. Kachelriess, "Image-based dual energy CT using optimized precorrection functions: A practical new approach of material decomposition in image domain," *Medical Physics*, vol. 36, no. 8, pp. 3818–3829, Aug. 2009.

[100] P. R. S. Mendonca, P. Lamb, and D. V. Sahani, "A flexible method for multi-material decomposition of dual-energy CT images," *IEEE Transactions on Medical Imaging*, vol. 33, no. 1, pp. 99–116, Jan. 2014.

[101] S. Kuchenbecker, S. Faby, S. Sawall, M. Lell, and M. Kachelriess, "Dual energy CT: How well can pseudo-monochromatic imaging reduce metal artifacts?" *Medical Physics*, vol. 42, no. 2, pp. 1023–1036, Feb. 2015.

[102] Y. Zou and M. D. Silver, "Analysis of fast kV-switching in dual energy CT using a pre-reconstruction decomposition technique," in *Proc. SPIE, Medical Imaging: Physics of Medical Imaging*, vol. 6913, 2008, pp. 691 313–691 313–12.

[103] A. Sawatzky, Q. Xu, C. Schirra, and M. Anastasio, "Proximal ADMM for multi-channel image reconstruction in spectral X-ray CT," *IEEE Transactions on Medical Imaging*, vol. 33, no. 8, pp. 1657–1668, Aug. 2014.

[104] D. S. Rigie and P. J. LaRiviere, "Joint reconstruction of multi-channel, spectral CT data via constrained total nuclear variation minimization," *Physics in Medicine and Biology*, vol. 60, no. 5, p. 1741, Mar. 2015.

[105] C. Cai, T. Rodet, S. Legoupil, and A. Mohammad-Djafari, "A full-spectral Bayesian reconstruction approach based on the material decomposition model applied in dual-energy computed tomography," *Medical Physics*, vol. 40, no. 11, pp. n/a–n/a, Nov. 2013.

[106] Y. Long and J. Fessler, "Multi-material decomposition using statistical image reconstruction for spectral CT," *IEEE Transactions on Medical Imaging*, vol. 33, no. 8, pp. 1614–1626, Aug. 2014.

[107] R. Zhang, J.-B. Thibault, C. Bouman, K. Sauer, and J. Hsieh, "Model-based iterative reconstruction for dual-energy X-ray CT using a joint quadratic likelihood model," *IEEE Transactions on Medical Imaging*, vol. 33, no. 1, pp. 117–134, Jan. 2014.

[108] K. Nakada, K. Taguchi, G. S. K. Fung, and K. Amaya, "Joint estimation of tissue types and linear attenuation coefficients for photon counting CT," *Medical Physics*, vol. 42, no. 9, pp. 5329–5341, Sep. 2015.

[109] Y. Zhao, X. Zhao, and P. Zhang, "An extended algebraic reconstruction technique (E-ART) for dual spectral CT," *IEEE Transactions on Medical Imaging*, vol. 34, no. 3, pp. 761–768, Mar. 2015.

[110] R. F. Barber, E. Y. Sidky, T. G. Schmidt, and X. Pan, "An algorithm for constrained one-step inversion of spectral CT data," *Physics in Medicine and Biology*, vol. 61, no. 10, p. 3784, 2016.

[111] C. O. Schirra, B. Brendel, M. A. Anastasio, and E. Roessl, "Spectral CT: a technology primer for contrast agent development," *Contrast Media & Molecular Imaging*, vol. 9, no. 1, pp. 62–70, Feb. 2014.

[112] K. Taguchi, E. C. Frey, X. Wang, J. S. Iwanczyk, and W. C. Barber, "An analytical model of the effects of pulse pileup on the energy spectrum recorded by energy resolved

photon counting x-ray detectors," *Medical Physics*, vol. 37, no. 8, pp. 3957–3969, Aug. 2010.

[113] B. Chen, I. Reiser, J. C. Wessel, N. Malakhov, G. Wawrzyniak, N. E. Hartsough, T. Gandhi, C.-T. Chen, J. S. Iwanczyk, and W. C. Barber, "Si-strip photon counting detectors for contrast-enhanced spectral mammography," in *Proc. SPIE 9594, Medical Applications of Radiation Detectors V, 959406*, vol. 9594, 2015, pp. 959 406–959 406–8.

[114] D. Modgil, A. Smith, B. Chen, H.-J. Kim, W. C. Barber, C.-T. Chen, and I. Reiser, "Development of a photon counting detector response model using multiple transmission spectra," in *Proc. SPIE 10132, Medical Imaging 2017: Physics of Medical Imaging, 101323R*, vol. 10132, 2017, pp. 101 323R–101 323R–6.

[115] F. Natterer, "2. The Radon Transform and Related Transforms," in *The Mathematics of Computerized Tomography*, ser. Classics in Applied Mathematics. Society for Industrial and Applied Mathematics, Jan. 2001, pp. 9–53, dOI: 10.1137/1.9780898719284.ch2 DOI: 10.1137/1.9780898719284.ch2.

[116] X. Pan, B. Chen, Z. Zhang, E. Pearson, E. Sidky, and X. Han, "Optimization-based Reconstruction Exploiting Spectral Information in CT," in *The Third International Conference on Image Formation in X-Ray Computed Tomography*, 2014, pp. 228–232.

[117] M. S. Andersen and P. C. Hansen, "Generalized row-action methods for tomographic imaging," *Numerical Algorithms*, vol. 67, no. 1, pp. 121–144, Sep. 2014.

[118] S. Rose, M. S. Andersen, E. Y. Sidky, and X. Pan, "Noise properties of CT images reconstructed by use of constrained total-variation, data-discrepancy minimization," *Medical Physics*, vol. 42, no. 5, pp. 2690–2698, May 2015.

[119] B. Chen, Z. Zhang, X. Han, E. Sidky, and X. Pan, "Basis-image reconstruction directly from sparse-view data in spectral ct," in *2014 IEEE Nuclear Science Symposium and Medical Imaging Conference (NSS/MIC)*, 2014, pp. 1–3.

[120] B. Chen, Z. Zhang, E. Pearson, E. Sidky, and X. Pan, "An investigation of regularization for basis image reconstruction in spectral CT," in *2015 IEEE Nuclear Science Symposium and Medical Imaging Conference (NSS/MIC)*, Oct. 2015, pp. 1–3.

[121] B. Chen, Z. Zhang, E. Sidky, E. Pearson, C. Pelizzari, and X. Pan, "Basis-Image Reconstruction Directly from Limited-Angle Data Sets in Spectral CT," in *The 13th International Meeting on Fully Three-Dimensional Image Reconstruction in Radiology and Nuclear Medicine*, 2015, pp. 495–498.

[122] S. P. Boyd and L. Vandenberghe, *Convex Optimization*. Cambridge, UK ; New York: Cambridge University Press, 2004.

[123] A. Chambolle and T. Pock, "A first-order primal-dual algorithm for convex problems with applications to imaging," *Journal of Mathematical Imaging and Vision*, vol. 40, no. 1, pp. 120–145, Dec. 2010.

[124] A. Wirgin, "The inverse crime," *arXiv:math-ph/0401050*, Jan. 2004, arXiv: math-ph/0401050.

[125] J. Kaipio and E. Somersalo, "Statistical inverse problems: Discretization, model reduction and inverse crimes," *Journal of Computational and Applied Mathematics*, vol. 198, no. 2, pp. 493–504, Jan. 2007.

[126] A. M. Hernandez and J. M. Boone, "Tungsten anode spectral model using interpolating cubic splines: Unfiltered xray spectra from 20 kV to 640 kV," *Medical Physics*, vol. 41, no. 4, pp. 042 101–1–042 101–15, Apr. 2014.

[127] JRTAssociates, "Dual energy CT phantom - JRT Associates," 2015.

[128] J. Hubbell and S. Seltzer, "Tables of X-ray mass attenuation coefficients and mass energy-absorption coefficients (version 1.4)," 2004.

[129] M. Berger, J. Hubbell, S. Seltzer, J. Chang, J. Coursey, R. Sukumar, D. Zucker, and K. Olsen, "XCOM: Photon cross section database (version 1.5)," 2010.

[130] E. Y. Sidky, L. Yu, X. Pan, Y. Zou, and M. Vannier, "A robust method of x-ray source spectrum estimation from transmission measurements: Demonstrated on computer simulated, scatter-free transmission data," *Journal of Applied Physics*, vol. 97, pp. 124 701–124 701, Jun. 2005.